ANALYSIS OF TURBULENT FIELDS IN THE SUPERNOVA-DRIVEN INTERSTELLAR MEDIUM

JAMES FREDERICK HOLLINS

Thesis submitted for the degree of
Doctor of Philosophy

School of Mathematics, Statistics & Physics
Newcastle University
Newcastle upon Tyne
United Kingdom

2018

Acknowledgements

I would like to thank my supervision team – Prof. Anvar Shukurov, Dr. Graeme Sarson and Dr. Andrew Fletcher – who have provided a stimulating and collaborative working environment. They have been constructive in their criticism and supportive with both advice and resources. They have also provided me with opportunities to work on projects outside the immediate focus of my studies. I have always felt that they were interested in the project and valued its outcomes and have enjoyed the freedom to think and work autonomously.

Further, I thank Dr. Fred Gent for providing me with additional insight into the pencil-code, his work in developing its interstellar module and for his assistance with my own ISM simulations.

I wish to thank Dr. Luiz Felipe Santiago Rodrigues, Amit Seta and Cetin Can Evirgen, with whom I have had many fruitful conversations regarding the physics of the ISM and useful areas of investigation, which has both deepened my understanding of the ISM and informed my research.

I have been privileged to be part of the Astro-lunch seminar group, and was honoured to have been the organiser for a semester. Throughout the seminars, I gained more knowledge of different topics of astrophysical interest, and had the opportunity to present my work to a wider audience and practise talks before conferences.

In addition I have been fortunate to have shared offices with a wonderful group of friends, who have provided drama, amusement and insight in equal measure. I thank my office mates Dr. Pencheng Zheng, Aamir Khan, Liam Dobson, Ratish Ratnasingam, Alex Hindle, Jack Walton, Hadi Alshammari, and Laura Wadkin. Other graduate students and Post Docs who have made memorable contributions to my PHD studies are: Dr. Chris Hales, Dr. Irina Makarenko, Dr. Philipp Edelmann, Dr. Paolo Comaron, Chris Stafford, Dave Robertson, Steve Johnson, Tom Bland, Joe Matthews, Dr. Nick Loughlin, Dr. Rob Pattinson, Dr. Yameng Ji, Joe Reid, Em Rickisnon, Mae Mesgahnezhad, Sophie Harbisher, Francesca Fedele, Kate Marshall, Haley Moore, Robbie Bickerton, Matthew Robinson, and Jack Aiston.

I wish to thank the computing support officers Dr. Michael Beaty, John Nicholson, Dr. George Stagg, Christian Lawson-Perfect and Dr. Chris Graham, administrative staff Jackie Martin, Jackie Williams, Helen Green, Adele Fleck, Carol Andrew, Maria Adair, Georgina Kay-Black, Lauren Daley, Lauren Thompson and Michael McNally. Additionally, I wish to thank Dave McGeeny and Vicky Hall in MathsAid and Gail de-Blaquiere of the SAgE Faculty Office. I also thank Dr. Paul Bushby, Dr. Nick Parker, Prof. Robin Johnson, Prof. David Toms, Prof. Nikolaos Proukakis, Prof. Ian Moss, Prof. Carlo Barenghi, Dr. Andrew Baggaley, Dr. Toby Wood, Dr. Tamara Rogers, Dr. Clive Emary, Dr. Gerasimos Rigopoulos, Dr. Christopher Cambell, Dr. Colin Gillespie, Dr. Tom Nye, Dr. Phil Ansell, Dr. David Walshaw, Prof. John Matthews, Dr. Peter Avery, Dr. Jordan Stoyanov, Dr. James Ford, Prof. Peter Jorgenson, Dr. Michael White, Dr. Andrew Duncan, Dr.

Guyan Robertson, Dr. Rafael Bocklandt, Dr. Alina Vdovina and Dr. Oli King for their general assistance during my research and previously.

I acknowledge support of the staff and resources from; the Topsy and Rocket HPC clusters at Newcastle University, where my simulations were computed; the University of Saint Andrews who provided financial support to attend UKMHD 2018 in Saint Andrews, Scotland; the Royal Astronomical Society (RAS) and the International Astronomical (IAU) who both provided financial support to attend the XXXth general meeting of the IAU in Vienna, Austria; and my funding research council the Engineering and Physical Sciences Research Council.

In conclusion, I thank my internal examiner, Dr. Paul Bushby, and my external examiner Prof. Christoph Pfrommer for a challenging, intelligent and interesting viva.

Finally, I thank my parents and my family for their patience and support during my studies.

Abstract

I model the interstellar medium (ISM) randomly shocked and heated by supernova explosions (SNe), with the inclusion of differential rotation, gravity, radiative cooling and other parameters typical of the Solar neighbourhood. I perform correlation analysis of magnetohydrodynamic simulations detailed in Gent (2012); Gent et al. (2013a,b) in a $1 \times 1 \times 2\,\mathrm{kpc}^3$ domain, symmetric about the galactic mid-plane, and use Gaussian smoothing to obtain the mean fields. In these simulations, the nG seed magnetic field is amplified by dynamo action to strengths of μG. I have run and analysed a set of hydrodynamic simulations with similar parameters in a smaller domain, varying the supernova rate to investigate its impact on the structure and dynamics of the ISM.

The random magnetic field, density, and velocity have different correlation scales. The correlation time of the random velocity is comparable to the eddy turnover time, about 10^7 yr. The standard deviations of the components of the random magnetic field suggest the field is anisotropic, attributed to the global velocity shear from galactic differential rotation, and locally inhomogeneous outflow to the galactic halo. The correlation length of Faraday depth along the z-axis is greater than for electron density and vertical magnetic field. Uncertainties of the structure functions of synchrotron intensity rapidly increase with the scale, a feature which is hidden in power spectrum analysis.

I discuss methods to identify an optimal smoothing scale ℓ of the Gaussian kernel and the effects of this choice on the results. From spectral analysis of magnetic field, density and velocity, a suitable smoothing length for all three fields, $\ell = 75\,\mathrm{pc}$, is obtained. The properties of third-order statistical moments arising in connection of fluctuations of kinetic energy density in compressible flows and their physical interpretations are discussed. The mean magnetic field significantly alters the distributions of the kinetic energy in space and between scales, reducing the magnitude of the intermediate scale kinetic energy. This intermediate-scale kinetic energy is a useful diagnostic of the importance of SN-driven outflows.

Increasing the supernova rate results in greater abundances of both hot and cold gas, as a result of increased heating and the formation of more regions of cold, dense gas by increased compression. The increased number of supernovae results in greater turbulent pressures, which thicken the disk. The root-mean-square velocity is increased, attributed to stronger outflows driven by an increased number of buoyant bubbles of hot gas.

The depletion of the warm gas and the increased amount of cold gas results in a reduction in the correlation scale of the density fluctuations. The increased driving of motions also reduces the correlation length of the turbulent velocity. The increased supernova rate also results in a smaller correlation time. Further comparison to the eddy turnover time reveals that the eddy turnover time is most appropriate as an estimate of the correlation time in the horizontal directions.

Contents

List of Figures

List of Tables

Part I

Motivation and outline: the interstellar medium of galaxies

Chapter 1

Motivation

1.1 Outline of the work

1.1.1 Motivation for this work

As humanity has made observations beyond our planet, we have made many discoveries of both spectacular beauty and of scientific curiosity. From the nearby phenomena such as the auroras, comets and planets, to vast structures such as galaxies and galaxy clusters. The length- and time-scales contained in the observed universe are difficult to comprehend. Strange objects such as pulsars, black holes and supernovae are a challenge to properly explain. To describe the formation, function and evolution of astrophysical objects requires tools from other fields of physics such as general relativity, classical and fluid mechanics, electromagnetism, plasma physics, particle physics and quantum mechanics. The combination of both the development of mathematics and theory and improved measurements and observations have dramatically changed our understanding of objects in our own Solar system and those populating our own galaxy and external galaxies.

Successive generations of both ground and space based telescopes have enabled us to see further into space, and to capture features emitted at wavelengths outside of the visible range of the human eye, such as the radio spectrum, infrared and x-rays. The vast amounts of new data being collected allows for the testing of existing knowledge and the challenge of exploring new ideas to explain more recent discoveries. Of particular interest to this Thesis are the observations of the tenuous gas between the stars in our own Galaxy and external galaxies. This gas is observed to be turbulent and highly inhomogeneous, with strong small-scale motions and magnetic fields, in addition to large-scale features such as hot gas structures, clusters of massive stars and a galactic-scale magnetic field.

Despite the improvements in both technology and the methodology of observations, there still exist limitations. Observers are limited to line of sight measurements of galaxies. Along these lines of sight, assumptions must be made about the gas distribution and composition and the structure of

the magnetic field. In comparison to galactic time-scales, we are restricted to viewing a snapshot of galaxies. Measurements of evolution and motion must be inferred from the comparisons of galaxies at different stages of evolution.

Numerical models of galaxies in three dimensions can offer insight into their 3D composition, structure and evolution. These models are limited in terms of resolution and the physics that can be modelled because of computational resources. Additionally, there remains the challenge of comparing computational results to those from observations. However, the structure and evolution of astrophysical models of galaxies can be explored more easily and inexpensively compared to observations, and may be used to motivate areas of interest for future observations.

1.1.2 Structure and contents

In the rest of the introduction, I briefly describe galactic structure, highlighting particular features of interest and how these might be addressed in this work. Chapter 2 reviews some of the progress made to date with numerical models of the ISM, and discusses the significant differences in the physics detailed in each model.

The numerical model used to obtain my results is discussed in Chapter 3. The different runs analysed are listed in Chapter 4, along with their key features. The focus of this Thesis is the systematic analysis of 3D simulations of the ISM rather than updating aspects of existing numerical models. However, to provide full context for the outcomes to the reader, I shall highlight the physical components of the model and discuss the necessary omissions and numerical limitations.

The new results I have obtained are described in Chapters 5– 8. These include data from two sets of simulations, the second of which were run by myself over a period of six months. The key difference is that the first set include a seed magnetic field and allow for dynamo action. Additionally, the second set were performed in a smaller domain in order to perform a faster exploration of the parameter space. Results from the first set of simulations are discussed in Chapters 5 and Chapters 6, whilst Chapters 7 and Chapters 8 contains results from the second set. Comparisons are made between the runs in each set in order to determine the impact of model parameters on the physical characteristics of the ISM. A summary of my results, conclusions and discussion of future direction of the research are contained in Chapters 9.

Collaborative and previous work

Some of the work presented in this Thesis is the result of collaboration, some of which has been published or submitted for publication. The Thesis contains material published in (Hollins et al., 2017, ApJ, 850, 4) and submitted to MNRAS (Hollins et al., 2018, arXiv:1809.01098), in which I am lead author with co-authors Dr. G. R. Sarson, Prof. A. Shukurov, Dr. A. Fletcher and Dr. F. A. Gent. Material from the former is included in Chapter 5. Appendix A contains an important result I derived that is used in the latter paper, with material from this paper included in Chapter 6 and

Appendix B. The numerical simulation code refinement, testing and modelling for the simulations discussed in both papers was performed by Dr. F. A. Gent, with full details given in Gent (2012); Gent et al. (2013b,a). The simulations discussed in Chapters 7 and 8 and were performed by myself, with testing and refinement performed in collaboration with Dr. F. A. Gent and Dr. G. R. Sarson.

I am a co-author on two papers. The first has been submitted to GAFD for the PENCIL CODE special issue, with Dr. F. A. Gent the lead author, and Prof. M-M. Mac Low, Dr. M. J. Käpylä, Dr. G. R. Sarson as the other co-authors (Gent et al., 2018, arXiv:1806.01570). This paper is referenced in Chapter 3 and details refinements to the modelling of supernova explosions in the PENCIL CODE[1]. The second paper has been submitted to MNRAS, with Prof. A. Shukurov the lead author, and Dr. L. F. S. Rodrigues, Dr. P. J. Bushby, Dr. J. P. Rachen as the other co-authors (Shukurov et al., 2018, arXiv:1809.03595). This paper presents the GALMAG[2] software package that is used to model large-scale magnetic fields in spiral galaxies using mean-field dynamo theory. In Appendix D, I demonstrate the solution, which I obtained with assistance from Prof. A. Shukurov and Dr. P. J. Bushby, for the spherical free decay modes used in the modelling of the mean magnetic field in the halo.

1.2 Introduction to galaxies

The distribution of galaxies across the universe is inhomogeneous, with most galaxies residing within either groups or clusters. Within these associations, galaxies of various types interact gravitationally. The distinction between groups and clusters is arbitrary but it is useful to define a cluster to be an association containing more than 50 members which lie within two magnitudes of the third brightest galaxy in the association (Binney & Tremaine, 1987).

Clusters of galaxies occupy regions of space of order 1–a few mega-parsecs (Mpc) and contain up to thousands of galaxies. Groups of galaxies span regions of space of order 1 Mpc. Our own galaxy, the Milky Way, resides within a collection of approximately 40 galaxies, termed the Local Group. The Milky Way shall be denoted the Galaxy to distinguish it from other galaxies, which shall be referred to in lower case.

1.2.1 Galaxies and their classification

All galaxies within a cluster interact with the surrounding intergalactic material but they contain powerful internal forces and structure, which can be sufficient to dominate the internal dynamics, irrespective of the surrounding environment.

The classification of galaxies was attempted by Edwin Hubble. In Hubble (1926), galaxies are categorised as follows; elliptical (E), spiral (S), barred spiral (SB) and irregular (Irr), with

[1] http://pencil-code.nordita.org/
[2] https://github.com/luizfelippesr/galmag

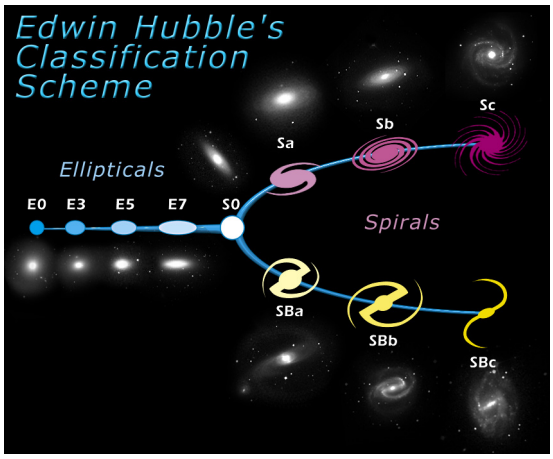

Figure 1.1: The Hubble tuning fork diagram for the classification of galaxies, courtesy of the European Space Agency (ESA) https://www.spacetelescope.org/images/heic9902o/. Galaxies are classified as follows; Elliptical (E), Spiral (S), Barred Spiral (SB) and lenticular (S0).

only 3% of galaxies categorised as irregular. A diagram detailing these classifications is shown in Figure 1.1.

The elliptical galaxies, on the left of Hubble's diagram, are those which appear smooth and structureless. Elliptical galaxies vary from round to highly elliptical in shape. At the junction of elliptical and spiral galaxies is a class of galaxies known as lenticulars, designated S0 or SB0 if they are barred. Lenticular galaxies are characterised by a bulge or spheroidal component, surrounded by a disk that contains no gas, dust or bright young stars. The right of Hubble's diagram bifurcates into spiral and barred spiral galaxies. Spiral galaxies are characterised by a spheroidal component surrounded by a prominent disk composed of stars, gas and dust. The disk contains spiral arms; filaments of stars, gas and dust in which the star formation rate is high compared to the inter-arm regions. Barred spiral galaxies contain an elongated central structure, termed a bar, interior to the spiral arms connected to the ends of the bar. Irregular galaxies are those which do not conform to a particular pattern in the Hubble diagram (Hubble, 1926; Mihalas & Binney, 1981; Binney & Tremaine, 1987).

A more physically motivated revision of these classifications was proposed by Cappellari et al. (2011) based on the kinematic properties of galaxies, using data from the ATLAS^{3D} astronomical survey. This classification based on kinematics reduces the influence of viewing angle on the categorisation of galaxies. In addition, this classification also gives insight into the influence of kinematic properties of galaxies on their morphology.

The slow rotating galaxies are elliptical, with the slowest rotators being the most spherical. In faster rotating elliptical galaxies, there are multiple stellar disks which counter-rotate, or rotate with different axes of rotation. This action reduces the flattening of the disk perpendicular to the axis of rotation. Faster rotating galaxies, rotating in one direction about a single axis of rotation, appear as flat, elliptical galaxies and disk galaxies, with disk galaxies being the fastest rotating.

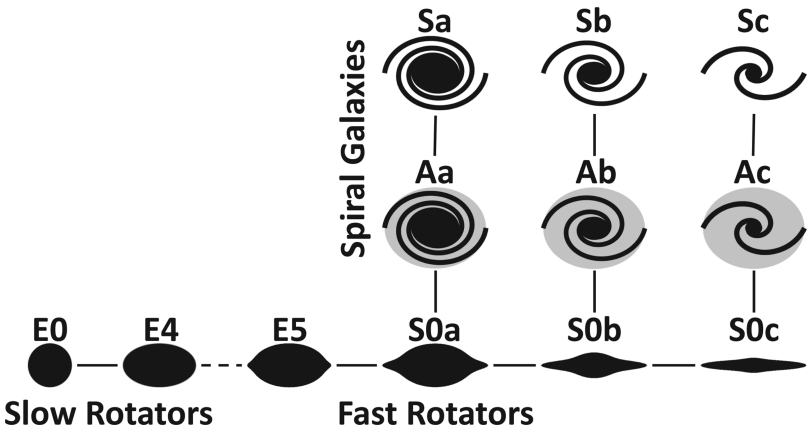

Figure 1.2: The classification diagram from Cappellari et al. (2011), based on the revised categorisation from the ATLAS^{3D} survey data. Elliptical galaxies are characterised by slower rotation rates, whilst disk galaxies rotate faster. Increasing rotation rate results in higher angular momentum, which reduces the size of the spherical bulge and results in a more flat galaxy.

Lenticular galaxies contain a flattened disk component but no dust or gas, whilst spiral galaxies contain gas-rich disks. In addition, there is an intermediate class of disk galaxies with gas-poor disks termed 'anaemic' spirals, proposed in van den Bergh (1976), where the present star formation rate is low.

The survey in Cappellari et al. (2011) explored relatively low density environments, in which the proportion of elliptical galaxies was approximately 4%, with the exception of the Virgo core where the elliptical population is about 20%.

The strength and structure of galactic magnetic fields are affected by the rotation rate and stellar density. In the long term, the aim of the simulations discussed in this Thesis is to model the ISM in any type of galaxy. At present, the model is constructed to simulate the ISM of spiral galaxies, using parameters associated with the Solar neighbourhood, since the most comprehensive observational data is for the Galaxy. The numerical models are tested by comparisons between their output and observations of the Solar neighbourhood.

From observations, it is concluded that the Milky Way is a spiral galaxy with a disk and spheroidal bulge. The radius of the bulge is of order 2–3 kpc, with the disk extending in the Galactic plane to radii of $\sim$ 25–30 kpc, approximately 400–600 pc in effective thickness (Ferrière, 2001). There is some evidence to suggest that our Galaxy is a barred galaxy (Binney & Tremaine, 1987). Most of the mass in the Galaxy is in the form of dark matter and stars, with 90% of the visible mass in the Galaxy located in stellar populations (Ferrière, 2001). Either side of the disk, there is a spherical region extending to approximately 30 kpc in radius termed the Galactic Halo. The gas in the halo is generally hotter and more diffuse than the gas in the disk.

The Sun is located within the disk, approximately 8.5 kpc from the centre of the Galaxy (Ferrière, 2001). At the galactocentric radius of the Sun, the Galaxy rotates at 230 km s^{-1}. Near

Figure 1.3: Examples of spiral galaxies the whirlpool galaxy (M51) and the barred spiral galaxy (NGC2903); courtesy of NASA's astronomy picture of the day (https://apod.nasa.gov/apod/ap130224.html and https://apod.nasa.gov/apod/ap150410.html respectively).

to the centre of the Galaxy, the orbit of the ISM is shorter, which induces a shear in the azimuthal direction due to the differential rotation rate with radius. The shear and rotation within galaxies are dependent on radius, and also vary between different galaxies. These features strongly determine the morphology of galaxies and are thought to influence the strength and structure of their magnetic fields.

1.2.2 Introduction to the interstellar medium

The space between the stars is occupied with a dilute mixture of atoms, molecules, dust grains and charged particles, termed the interstellar medium (ISM). The gas consists of 90.8 % by number [70.4 % by mass] hydrogen, 9.1 % [28.1 %] helium, with small amounts of heavier elements. Observations of the ISM suggest most of the heavier elements exist within dust grains (Ferrière, 2001). The interstellar gas is tenuous, with a number density of 1 hydrogen atom per cubic centimetre, compared to a number density of 10^{27} molecules per cubic centimetre in air at sea level.

The interstellar gas spans multiple orders of magnitude in both density and temperature and is often described using a multiphase approach, with each phase having distinct properties. A model describing the cold ($T \sim 10^2$ K) and warm ($T \sim 10^4$ K) phases was proposed in Field et al. (1969). This approach was extended with the inclusion of a hot phase ($T \sim 10^6$ K) by McKee & Ostriker (1977). The hot gas is produced by supernova explosions; the structure of the hot gas was described in Cox & Smith (1974). The description of the multi-phase ISM in pressure equilibrium has persisted with small refinements (Cox, 2005).

Different physical processes in the ISM, such as star formation, turbulent flows, galactic winds and fountains, the behaviour of magnetic fields and the propagation of cosmic rays, are strongly influenced by the multi-phase structure. The coldest, most dense structures in the ISM are clouds of molecular gas, which contain most of the dense gas and occupy a negligible fraction of the

volume (Solomon et al., 1987; Spitzer, 1990; McKee, 1995). Star formation occurs in molecular clouds via the gravitational collapse of the most dense regions of these clouds (Blitz, 1993; Williams et al., 2000). The cooling time of the warm gas is much greater than the interval between the passing of supernova shocks and so contains persistent transient states that do not relax to pressure equilibrium (Kalberla & Kerp, 2009, and references therein). Energy input from supernova explosions (SNe) and stellar winds help to maintain the complex structure by driving turbulence, with SNe being the larger contribution (Mac Low & Klessen, 2004, and references therein). The hot gas structures are produced and maintained by supernovae and the buoyant hot gas can rise from the disk into the halo. The spatial and temporal clustering of SNe result in the formation of superbubbles which drive outflows of hot gas termed galactic winds or fountain flows (Shapiro & Field, 1976; Bregman, 1980). Such outflows reduce the filling factor of the hot gas at the mid-plane to values close to 10% (Norman & Ikeuchi, 1989). Thus the turbulent motions, the multi-phase structure and the disk-halo interaction in the ISM are strongly linked.

In the Galaxy, the ISM contains 10–15% of the visible matter in the disk (Ferrière, 2001). Despite this the ISM play a very important role in the evolution of the Galaxy. Stars are formed from the gravitational collapse of interstellar matter. These stars return material to the ISM during their lifetimes, particularly at the end of their evolution, which is enriched with heavier elements formed from the thermonuclear processes that occurred within these stars. Successive generations of stars form from the enriched interstellar material (Lequeux, 2005). The ISM also supports the amplification of a magnetic field with the length-scale of the mean field comparable to the size of the galaxy (Brandenburg & Subramanian, 2005). The magnetic field confines the cosmic rays to the Galaxy and is dynamically important in regions where its energy density is comparable to the thermal or the turbulent energy density (Draine, 2011). The cosmic rays contribute an extra source of pressure in the ISM, which is in equilibrium with the thermal, turbulent and magnetic pressures. Cosmic rays also drive winds from the disk, which further regulate star formation (Pfrommer et al., 2017). Thermal and turbulent pressure, resulting from heating and shock waves, along with magnetic and cosmic-ray pressure support the disk against gravitational collapse.

1.3 Supernova explosions

Throughout this thesis, I consider the modelling of turbulence in the ISM driven by supernova explosions (SNe). These are classified into two types, I and II, depending on the presence of hydrogen in their optical spectra (Weiler & Sramek, 1988), with further subclasses within each type.

Each SNe releases $E_{\rm SN} \approx 10^{51}$ erg of energy. After the explosion, the matter in the expanding bubble of gas is referred to as the supernova remnant. Supernova remnants contain hot, overpressured gas and expand initially at supersonic speeds. As the remnants evolve, they transfer energy to their surroundings, eventually merging with the ISM when the pressure inside the supernova

remnant drops to values comparable to the surrounding gas. The almost random times and locations at which SNe occur results in random forcing of the ISM which leads to turbulence in the gas. The types of supernovae considered and the mechanisms describing their evolution are described below.

1.3.1 Type Ia supernovae

Type Ia supernovae originate from white dwarves, evolved stars which have used most of their hydrogen and are composed of heavier elements, such as carbon and oxygen. If the mass of these stars exceeds the Chandrasekhar limit of $\sim 1.4 M_{\odot}$ (Chandrasekhar, 1931), usually through accretion from a companion star in a binary system (Whelan & Iben, 1973), the core of the star becomes unstable leading to an explosion. In such explosions, the star is completely destroyed. The supernova remnant interacts only with the interstellar medium since there is little or no circumstellar material in such star systems.

Type Ia supernovae occur in all types of galaxies and those that occur in spiral galaxies do not show any strong preference for occurring in the spiral arms (Filippenko, 1997). Type Ia supernovae which explode in the more diffuse gas away from of the mid-plane may expand to radii of a few hundred parsecs and provide an additional source of heat to the galactic disk.

1.3.2 Core collapse supernovae

Type II, Ib and Ic supernovae have not been detected in elliptical galaxies and are rarely seen in S0 galaxies. These occur in or near spiral arms in disk galaxies. Core collapse supernovae occur more frequently than Type Ia supernovae in the these regions. These originate from massive stars with mass $M > 8 M_{\odot}$ whose evolution ends with the collapse of their cores under self-gravity.

Type II supernovae are characterised by the presence of hydrogen in their optical spectra. Type Ib and Ic supernovae lack hydrogen (and helium in the case of Type Ic) in their optical spectra. The loss of hydrogen and helium envelopes from the progenitor stars is attributed to either accretion to companion stars or stellar winds (Filippenko, 1997).

For the purposes of modelling the interactions of supernova remnants with the ISM, it is necessary only to note the spatial and temporal distributions of such events and the mass and energy injected into the ISM by them. These are determined by the distributions of the stars from which the SNe originate. Consequently, I shall refer to Type Ia supernovae as Type I and all core collapse supernovae as Type II throughout the thesis.

1.3.3 Evolution of a supernova

Supernova explosions eject a mass $M_{\rm ej}$ with a kinetic energy of 10^{51} erg. The mass ejected depends on the star from which the SNe originates, which are released with a range of velocities, with the fastest material at the edge of the explosion. The rms velocity of the ejected material is far greater

than the sound speed in the surrounding gas, and so a shock is driven in the surrounding medium. Additionally, the density within the remnant is much greater than in the surroundings. As a result, the remnant expands ballistically at near constant velocity. This stage is referred to as the 'free expansion phase'. During the early times of the expansion, the shock wave propagating outward into the ISM is the only shock of interest (Draine, 2011).

The density of the expanding ejected mass drops as r^{-3}, resulting in a pressure drop inside the remnant. Once the pressure of the surrounding gas exceeds the thermal pressure of the remnant, a reverse shock is driven into the ejecta. The reverse shock slows and heats the ejecta as it propagates inward. Once the reverse shock reaches the centre of the remnant, the free-expansion phase ends and the interior of the remnant is very hot. The pressure in the supernova interior is far higher in the surrounding medium. The hot gas emits radiation but radiative losses are small because the densities are low. The supernova remnant now enters the Sedov-Taylor phase. This phase can be modelled by a point explosion injecting only energy into a surrounding medium of uniform density. The mass of the ejected material, pressure in the medium and radiative losses are neglected (Draine, 2011).

Sedov (1959) and Taylor (1950) independently derived the solution for the radius of an expanding spherical shock from a point explosion, which provides a good approximation of the expansion of supernova remnants during this phase

$$R_s = \kappa E_{\rm SN}^{1/5} \rho_0^{-1/5} t^{2/5}, \tag{1.1}$$

where R_s is the radius of the supernova remnant, ρ_0 is the uniform surrounding density and t is the time since the explosion.

As the post-shock temperature decreases, the radiative cooling of the gas increases via line emission due to the collisional excitation of ions. After sufficient time, radiative cooling of the gas immediately behind the shock is greater than the cooling by expansion. The gas tries to lose pressure but is pushed up against the shock by the interior gas, whose high temperature and low density results in negligible cooling on the timescales considered here. The compression of the gas at the edge of the remnant shock results in higher density and increased cooling. This cooling results in the formation of a thin shell of cool material immediately behind the shock, with the very hot interior gas filling the remnant (Dyson & Williams, 1997). During this stage, the propagation of the shock is no longer maintained by thermal energy but instead by the momentum of the gas (Lequeux, 2005). This is called the snowplough phase.

The supernova remnant merges into the interstellar medium when the shock velocity is of the same order as the velocity dispersion in the ISM $\sim 10\,\mathrm{km\,s^{-1}}$. The kinetic energy of the remnant is transferred to the surroundings. The interior gas remains hot with temperatures of 10^5 to $10^6\,\mathrm{K}$, which spreads out into the surroundings, contributing to the hot phase of the ISM (Lequeux, 2005). The numerical modelling of supernova remnants and their expansion is discussed in Chapter 2.

Chapter 2

A summary of Interstellar Modelling

2.1 Introduction

Significant work over the last three decades has been undertaken to describe the physics of the multi-phase ISM using numerical simulations. This work began with the simulations of Chiang & Prendergast (1985) and was proceeded by many others including Rosen et al. (1993); Rosen & Bregman (1995); Vázquez-Semadeni et al. (1995); Passot et al. (1995); Rosen et al. (1996); Korpi et al. (1999b,a); Gazol-Patiño & Passot (1999); Wada & Norman (1999); de Avillez (2000); Wada & Norman (2001); de Avillez & Mac Low (2001); de Avillez & Berry (2001); Wada et al. (2002); de Avillez & Mac Low (2002); de Avillez & Breitschwerdt (2004); Balsara et al. (2004); Slyz et al. (2005); Mac Low et al. (2005); de Avillez & Breitschwerdt (2005a,b); Balsara & Kim (2005); Joung & Mac Low (2006); Wada & Norman (2007); de Avillez & Breitschwerdt (2007); Gressel et al. (2008a,b); Joung et al. (2009, 2012); Hill et al. (2012); de Avillez & Breitschwerdt (2012b,a); Gent et al. (2013b,a); Walch et al. (2015); Girichidis et al. (2016a,b); Simpson et al. (2016); Pardi et al. (2017); Gatto et al. (2017); Kim & Ostriker (2017, 2018); Girichidis et al. (2018a,b).

Numerical models of the interstellar medium are computationally expensive, requiring of the order of 10^5 cpu hours per 100 Myr on high-performance computing clusters using current codes. Processes in the ISM span from kpc to sub-parsec spatial scales (see de Avillez & Breitschwerdt, 2007), with time-scales on the order of Myr to Gyr (see Gent et al., 2013a), and occur over a broad range of densities, from 10^{-4} to $10^3\,\mathrm{cm}^{-3}$, and temperatures, from 10 to 10^7 K, (see Hill et al., 2012).

The formation of cold, dense molecular clouds results in star formation via the collapse of their cores, driven by thermal and gravitational instabilities on larger scales. The massive stars that form (of mass $> 8\mathrm{M}_\odot$) drive turbulence in the ISM via stellar winds and supernova explosions (see Gatto et al., 2017). No single numerical model is able to fully capture all scales, physical processes and parameters that are of importance.

I shall present a summary of the current and previous numerical models, highlighting the physics they capture or omit. Particular attention is paid to the physics of most relevance to the work in this Thesis.

2.2 Star formation

Star formation is not considered directly in the simulations used in this Thesis. However, it is worth discussing here because modelling the dynamical effects of star formation on the ISM is an important future consideration.

Compression of interstellar gas results in dense clouds. Small regions of high density form within these clouds, which collapse to form protostellar cores. These cores become unstable, causing further collapse which ignites the cores under pressure, forming stars (Mac Low & Klessen, 2004). The dense clouds typically have length scales of a few parsecs. As a region of the cloud collapses, the scales involved rapidly become much smaller. These scales are tiny compared to other important galactic processes such as disk-halo interactions and rotation. Hence, it is not currently practical to include such detailed physics in ISM simulations whilst also modelling the larger-scale dynamics.

Hydrodynamic and magnetohydrodynamic simulations of molecular clouds, incorporating turbulence and self-gravity, were made by Klessen et al. (2000) and Heitsch et al. (2001). Turbulence is driven at the scale of the molecular clouds with Gaussian velocity fluctuations. These simulations investigate the formation of high density, gravitationally collapsing regions which are expected to lead to the formation of stars. The formation of stars was not directly modelled in these simulations, whose resolution is larger than the lengthscales of star formation. Supersonic turbulence of sufficient strength to globally support clouds against collapse will usually cause local collapse. Magnetic fields are unable to completely support molecular clouds against local collapse, with the strength and driving wavelength of the turbulence governing the behaviour of the cloud. However, magnetic pressure behind shocks decreases local density enhancements, which results in longer timescales for local collapses (Girichidis et al., 2018b). In addition, sufficiently strong magnetic fields can organise the flow into sheets, resulting in clustered star formation Klessen et al. (2000). In the ISM, SNe drive turbulence at scales of up to 100 pc, and so it is not yet practical to include such detailed physics of molecular clouds in kiloparsec-scale ISM simulations.

Thermal instabilities may also contribute to the formation of high density structures within the ISM. Brandenburg et al. (2007) model the effects of thermal instability in a turbulent ISM. Forced turbulence was required since thermal instabilities do not produce sustained turbulent flows. The domain size was 200 pc with a resolution below 1 pc. The formation of the densest regions is dominated by turbulent compression, with cooling times much larger than the turnover time of the turbulence.

Simulations including star formation in a numerical domain 1.28 kpc in size were performed

by Slyz et al. (2005), with a resolution of 10 or 20 pc. The lowest temperatures permitted by their choice of cooling function were 300 K, and the highest densities achieved were $n \sim 10^2\,\mathrm{cm}^{-3}$. The simulations investigated the effects of self-gravity, which was found to be less important than feedback processes for star formation. However, self-gravity of the gas caused high density regions to become more spherical. The addition of self-gravity also resulted in the further compression of high density regions, which resulted in an extended high density tail in the density PDF. Since self-gravity is much less important than turbulent effects on scales 1 pc or greater, it can be safely ignored in the simulations analysed in this Thesis.

It is possible to implement an approximation of star formation in ISM simulations via sink particles. Such an approach involves selecting sites for star formation where the density exceeds a threshold value, the flow is converging, and the site is a local gravitational potential minimum (see Kim & Ostriker, 2017). At such sink particles, gas is accreted onto the particle until a threshold mass is reached, after which a parameterised star formation model is used to determine the properties of the newly formed star. Stellar winds for each star can be included using stellar evolution models, as shown by Gatto et al. (2017). This approach only allows for the creation of massive stars and so only yields the sites of core collapse SNe. Type I supernovae would still have to be modelled via parameterisation.

These simulations have been performed using ideal MHD codes, running for simulation times of a few 100 Myr. Simulations modelling the action of mean-field magnetic dynamo in the ISM require run time in excess of 1 Gyr. Hence, the implementation of sink particles, and the associated increased computing cost required, via solving Poisson's equation to determine the accretion of mass, may not be currently practical in such models.

To summarise, the modelling of molecular clouds and their gravitational collapse resulting in star formation requires resolutions below 1 pc. Self-gravity is important only within the dense structures within these clouds. As a result, accurately modelling these effects is not within the scope of current kiloparsec-scale ISM simulations and a parameterised approach is required to include these effects. Sink particles are a promising alternative but are computationally expensive and have, to the author's knowledge, only been used within ideal MHD simulations. The effects of modelling star formation using sink particles within non-ideal MHD codes remains to be tested.

2.3 Disk and spiral arms

A global simulation of a spiral galaxy requires a radial extent of 10 kpc, with a minimum height of roughly double that in order to fully capture the halo. For computational efficiency, authors either adopt a low vertical extent (Dobbs & Price, 2008; Hanasz et al., 2009; Kulesza-Żydzik et al., 2009; Dobbs & Pringle, 2010) or use a 2-dimensional domain (Slyz et al., 2003). Such models typically employ resolutions of 100 pc or greater. Physical processes in the ISM, such as the injection of energy via supernovae, can only be included via parameterisation. An isothermal ISM is usually

imposed, with heating and cooling in the gas ignored. Dobbs & Price (2008) implement cold and warm phases in their simulations but do not consider any interaction between the phases.

Such simulations are able to explore global galactic phenomena. For example, Slyz et al. (2003) are able to recreate spiral arm structures consistent with observations, with random, forced turbulence driving density perturbations. Dobbs & Pringle (2010) are able to replicate spiral arm structures through multiple spiral excitation mechanisms.

Similar work has been able to replicate magnetic structures on a galactic scale. In Dobbs & Price (2008), the magnetic field is amplified in the spiral arms, which then acts to smooth the structure within both the spiral arms and interarm regions. The amplitude of spiral shocks is also reduced. In the simulations of Kulesza-Żydzik et al. (2009), magnetic arms develop inside the gaseous spiral arms before being shifted to the interarm regions. There is amplification of the magnetic field, however no dynamo mechanism is considered. A cosmic-ray driven dynamo in Hanasz et al. (2009) is shown to amplify galactic magnetic fields up to equipartition strength, seeded by weak magnetic dipoles and cosmic-rays supplied by supernova remnants. The amplified magnetic field has structure on large-scales in both the disk and halo component.

Numerical simulations of galaxies which include magnetic fields are able to amplify magnetic fields via a turbulent dynamo, provided the strength of the turbulence and the spatial resolution in these models are both sufficient. The choice of resolution is important since these models do not include explicit magnetic diffusion. Simulations of magnetic field amplification via a dynamo driven by feedback were investigated by Rieder & Teyssier (2016) using the RAMSES code. Both dwarf galaxies and Milky Way-like galaxies were considered. For dwarf galaxies, supernova feedback is able to drive a small-scale dynamo, with growth rates comparable to the rotation rate for their higher resolution runs. In Milky Way-like galaxies, the inclusion of radiative feedback from dust grains was necessary to drive the dynamo, with the growth rate of the magnetic field increasing with opacity.

A small-scale dynamo is found within simulations of isolated disk galaxies in $10^{11} M_{\odot}$ haloes by Pakmor et al. (2016), using the moving-mesh AREPO code. The simulations include cosmic rays, with different cosmic-ray diffusion processes examined. In the simulations with isotropic and anisotropic cosmic-ray diffusion, an initial seed field of strength 10^{-10} G is amplified to strengths of $10^{-2}\,\mu$G over a time-scale of 300 Myr. After the initial amplification by a small-scale dynamo, the magnetic field strength continues to increase until saturation at around 1 Gyr, whilst the azimuthal component begins to dominate, suggesting amplification via a large-scale dynamo. The typical magnetic field strength is of order 1 G in the run with anisotropic diffusion, in contrast to strengths of order 0.1 G in the run with isotropic diffusion.

As a result of the low vertical extent of such simulations, the vertical mutliphase structure of the disk-halo system is not fully explored within these global simulations. In addition, the turbulent velocity and thermal distribution of the gas cannot be explored directly and must be introduced as model parameters. However, global simulations are useful both for the understanding

the amplification and structure of magnetic fields in galaxies, both small and large-scale, and the exploration of large scale effects that are beyond the scope of localised ISM simulations, such as spiral shocks and the differences between the spiral arms and interarm regions. The results of global simulations may help with the choice of parameters for the inclusion of such effects in local ISM simulations.

2.4 The supernova-driven interstellar medium

This thesis considers the modelling of the ISM on scales greater than molecular clouds but smaller than the size of a galaxy. Supernova explosions are considered as the primary mechanism for the driving of turbulence.

The first investigation of the evolution of a supernova in an inhomogeneous gas was performed by Cowie et al. (1981). Subsequent higher resolution runs performed by Cioffi et al. (1988) investigating the adiabatic and snowplough phases of the expansions of a supernova, finding the need for refinement to the classic Sedov-Taylor solution. The modelling of multiple supernova explosions, as a sequence of explosions in an OB association, in superbubbles was performed by Tomisaka (1998). Three dimensional simulations of the turbulent ISM including multiple SNe were first performed by Korpi et al. (1999b) and de Avillez (2000) independently. In this section, I will detail the important numerical and physical elements of various models of ISM turbulence, highlighting the impacts of these features on the results obtained.

2.4.1 Modelling and distribution of supernovae

The sites for the injection of supernovae are selected uniformally in a horizontal plane, using a Gaussian or exponential distribution in height, with the peak of the distribution at the mid-plane, $z = 0$. Once the location is selected, a sphere of mass, energy and/or a divergent velocity profile is injected. The radius of the sphere needs to be sufficiently large to resolve thermal and velocity gradients, and so is typically at least a few gridpoints. With a typical resolution of a few pc, this corresponds to an injection radius of several pc. At this radius, the supernova will be in the late Sedov-Taylor phase or early snowplough phase some thousands of years after the explosion (Dyson & Williams, 1997). The gas is expelled by thermal pressure or kinetic energy from the interior of the supernova remnant to form a supersonic shell, which heats the ISM and drives turbulent motions. The modelling of the evolution of supernova remnants can encounter problems. The use of kinetic energy rather than thermal energy to drive the evolution of the remnant is hindered by the lack of resolution. In addition, cooling of the gas can dissipate energy before the shell is formed. To avoid radiative losses in the first few time steps after an explosion, Joung & Mac Low (2006) inject SNe at radii such that $60\,M_{\odot}$ is enveloped in the explosion site. The injection radii vary between 7 and 50 pc. This avoids high energy losses at $T > 10^8$ K from a small injection site, whilst also avoiding higher masses which result in thermal energy heating remnants

to temperatures of only $T \lesssim 10^6\,\mathrm{K}$. Walch et al. (2015) use an injection mass $M_{\mathrm{inj}} = 800\,M_{\odot}$ with radii $R_{\mathrm{inj}} \gtrsim 4\,\Delta x = 15.6\,\mathrm{pc}$.

The addition of Type II supernova clustering results in SNe occurring in more diffuse, higher temperature environments which result in lower radiative losses. Korpi et al. (1999a) include clustering by selecting sites in z with an exponential distribution, with the exclusion of sites in the horizontal plane where the density is less than the average in the plane. This results in 70% of Type II located in clusters. de Avillez (2000) and de Avillez & Breitschwerdt (2004) include clustering via locating 60% of Type II SNe in supperbubbles, using the observational estimates of Cowie et al. (1979). The clustering of 60% of Type II SNe in supperbubbles is also employed in both Joung & Mac Low (2006) and Joung et al. (2009). A simplified approach is used in which the superbubble is injected with the assumption that all the supernovae in the OB association explode at the same location, spaced equally over the superbubble lifetime of 40 Myr. A similar prescription is included in Walch et al. (2015) and subsequent simulations.

2.4.2 Shock handling

The ISM is highly compressible, with large amounts of the gas travelling at supersonic speeds. The strongest shocks are driven by SNe, which initially produce motions in the gas orders of magnitude greater than the sound speed. Simulations of a single supernova remnant require high resolution and very short time-steps (Cowie et al., 1981). On the time-scales of interest for this Thesis, hundreds, possibly thousands of SNe, occur which constrain the spatial and temporal resolution that can be used for modelling each individual SNe. Consequently, it is necessary to use approximations which capture the essential physics and structure of each remnant.

Many ISM models currently employ adaptive mesh refinement (AMR), with shocks handled by the increasing of the resolution local to the strongest gradients in density, temperature and velocity (see de Avillez, 2000; Mac Low & Klessen, 2004; Joung & Mac Low, 2006; Gressel et al., 2008a; Walch et al., 2015, as examples). Increasing the spatial resolution requires a smaller time-step and so this procedure has high computational overheads. An alternative approach is to apply enhanced viscosities and diffusivities where there are strong convergent flows. This approach is discussed in Korpi et al. (1999b); Gent (2012) and Gent et al. (2013b). This removes discontinuities but also broadens the shock profiles to scales of 10–20 pc and so care must be taken to ensure the correct modelling of physical processes, particularly on small scales.

2.4.3 Reynolds and Prandtl numbers

The characteristic values of the kinetic and magnetic Reynolds numbers (Re and Rm) and the magnetic Prandtl number (Pm) are much larger than those currently available to numerical simulations. An estimate of $\mathrm{Re} \simeq 10^7$ and kinematic viscosity $\nu \simeq 3 \times 10^{17}\,\mathrm{cm^2\,s^{-1}}$ in the cold, neutral medium is obtained in Lequeux (2005). Brandenburg & Subramanian (2005) obtain $\mathrm{Pm} \sim 10^{11}$

and Rm $\sim 10^{18}$, with an associated value of magnetic diffusivity $\eta \sim 10^7\,\mathrm{cm^2\,s^{-1}}$, using parameters typical for the Galaxy.

There exist uncertainties with these estimates, particularly regarding the differences between viscosity and the thermal and magnetic diffusivities in the cold, warm and hot phases. However, it is clear that the values of Re, Rm and Pm are far greater, with far lower values of ν and η, than those that can be achieved numerically.

Given the relatively low diffusivities in the ISM, most authors choose to treat any diffusive coefficients as approximately zero (see de Avillez, 2000; Mac Low & Klessen, 2004; Joung & Mac Low, 2006; Walch et al., 2015, as examples). In such ideal MHD codes, the magnetic field is frozen into the fluid. Whilst no explicit viscosity or diffusion is included, there is numerical diffusion which is controlled by the grid scale. These models typically utilise AMR codes and so the numerical diffusion varies locally with the resolution.

Bulk viscosities and diffusivities are used in the simulations of Korpi et al. (1999b); Gressel et al. (2008a) and Gent et al. (2013b). These values are orders of magnitude larger than those expected in the physical ISM. The values available are limited by the resolution employed but the use of bulk diffusivities ensures a consistent diffusion throughout the domain.

The effective Reynolds numbers are often not discussed by authors. However it is expected that these Reynolds numbers, and the magnetic Prandtl number, are much lower than the estimates in the ISM. The low magnetic Reynolds and Prandtl numbers may help to explain the lack of turbulent dynamo action within kpc-scale ISM simulations.

Despite this, numerical models are able to replicate large scale features in the ISM such as the size of supernova remnants, superbubbles and the thickness of the disk. There exist uncertainties when describing the small scale structures such as clouds of cold gas, the supernova remnants and the dispersions of velocity, density, temperature and magnetic field.

2.4.4 Stratification

In spiral galaxies, the matter is flattened into a disk. The morphology is determined by the rate and form of the rotation of the galaxy. Near the centre of the galaxy, there is a bulge whose density and dynamics differ from that of the disk. The dynamics in the disk region of spiral is the concern of this Thesis.

The gas in the disk is stratified vertically. Estimates for the Solar neighbourhood by Clemens et al. (1988) suggest the Gaussian scale height of the cold, molecular gas is 80 pc. The exponential scale height of the warm gas is estimated to be $\sim$ 390–1000 pc. The hot gas is more difficult to isolate and uncertainties exist in the observed scale height of the hot gas, with estimates ranging from approximately 1 kpc to 5 kpc Ferrière (2001).

Stratification can be ignored providing the vertical extent of the domain is smaller than the thickness of the disk (Balsara et al., 2004; Balsara & Kim, 2005; Pardi et al., 2017). Balsara et al. (2004) performed simulations with 8, 12 and 40 times the Galactic SN rate, with the initial density

typical of the mid-plane. For higher SN rates, a thermal runaway is triggered, resulting in higher pressures and an overheated ISM. Pardi et al. (2017) performed simulations with a similar sized domain using a SN rate similar to the Galactic rate, varying the strength of the initial magnetic field imposed. In the runs with high initial magnetic fields, of strengths of a few μG, a multi-phase ISM does not develop. Instead, the medium remains dominated by warm gas at densities close to the values at the mid-plane.

These problems can be avoided in kpc-scale ISM simulations via stratification. Increased pressure from SNe is released via blow outs of hot, high pressure bubbles and diffuse convection. A multiphase structure is established despite the presence of strong magnetic fields with the hot gas dominant at large heights, resulting from outflows of hot gas from the mid-plane and Type I supernovae exploding at large heights in more diffuse gas.

The inclusion of a stratified ISM is detailed in Korpi et al. (1999b,a). They found the hot gas is transported away from the mid-plane in supperbubbles due to clustering of SNe or SNe exploding inside existing remnants. de Avillez (2000); de Avillez & Berry (2001) also model the stratified ISM, with hot gas transported into the halo by both supperbubbles and chimneys of hot gas. The transport of hot gas expands the disk, reducing the mean temperature and density at the mid-plane. A layer of cold gas with thickness 10–20 pc remains at the mid-plane.

The gravitational potential, dominated by the stellar mass near the mid-plane, results in a vertical density and pressure gradient. This potential depends on the galaxy but most ISM simulations use parameters for the Solar neighbourhood, since the estimates are better understood. Thus, the results of such simulations are easier to benchmark.

It is natural for the hot gas to rise and cool and for the cold gas to fall towards the mid-plane, with the warm gas occupying the intermediate spaces. Observational estimates of the scale heights suggest the requirement of a vertical extent of at least ± 1 kpc to reasonably model the interaction between the cold and warm gas.

It is less clear as to the precise vertical domain required to fully model the hot gas. With a vertical extent of up to 2 kpc, as used by Gressel et al. (2008a), there is a net outflow of hot gas. Without any mechanism to recycle the outflowing gas, these losses eventually exhaust the disk of gas. Korpi et al. (1999b,a) found this limited the useful runtime of their simulations to a few hundred Myr.

Using a vertical extent of ± 4 kpc, de Avillez (2000) found the hot gas occupies 100% of the volume for $|z| \geq 2.5$ kpc. This extent is not sufficient to observe the cooling and recycling of the hot gas back to the disk. A vertical extent of ± 5 kpc is used subsequently by Joung & Mac Low (2006); Joung et al. (2009); Walch et al. (2015), whereas de Avillez & Mac Low (2001); de Avillez & Berry (2001); de Avillez & Breitschwerdt (2004, 2005a); Hill et al. (2012) use a vertical extent of ± 10 kpc. These also find the ISM above heights of $|z| = 2.5$ kpc is composed almost entirely of hot gas for column densities and supernova rates comparable to the Solar neighbourhood. These models all exclude cosmic rays and many exclude magnetic fields, resulting in thinner disks than

those determined by observations. The addition of magnetic fields and cosmic rays is expected to result in a thicker disk and an increase scale height of the hot gas.

Magnetic tension is known to inhibit outflows of hot gas. The stratified, 3D simulations of Tomisaka (1998) place an upper limit of the magnetic field strength of $B = 5\,\mu$G for this confinement, in the absence of turbulence. In the turbulent ISM, the magnetic field becomes disordered and the ISM contain pockets of diffuse gas which increase the likelihood of hot gas blow outs (see e.g. Korpi et al., 1999a; de Avillez & Breitschwerdt, 2004, 2005b).

2.4.5 Galactic fountain

The build up of thermal and turbulent pressure from SNe in the disk results in strong vertical flows of hot gas into the halo. This gas reaches heights of order 1 kpc, before radiative cooling results in the formation of cool clouds which then return to the disk. The convective and radiative mechanism is termed the 'galactic fountain' (Shapiro & Field, 1976; Bregman, 1980).

The most critical factor in the correct modelling of the temperature distribution of the halo is the vertical extent of the simulation domain (see Hill et al., 2012). Joung et al. (2009) perform simulations in box $(0.5\,\mathrm{kpc})^2 \times 10\,\mathrm{kpc}$ in size with no outflow enforced at the vertical boundaries. During these runs, hot gas from Type Ia above $|z| = 0.5\,\mathrm{kpc}$ rapidly rises during the first few Myr. After the passage of the blast wave, the pressure inside drops, leading to a constant inflow of hot, high-pressure gas. This results in an unphysical ram pressure which heats the gas above $|z| = 1\,\mathrm{kpc}$ to temperatures of 10^7 K. This problem is discussed in greater detail in Joung et al. (2012).

In both de Avillez & Breitschwerdt (2004) and Hill et al. (2012), a vertical extent of 10 kpc is utilised, with horizontal extents of 1 kpc and 0.5 kpc respectively. In de Avillez & Breitschwerdt (2004), the disk-halo cycle is established on time scales of 100 Myr, with some dependence on the supernova rate. The flow of matter into the halo acts as a pressure valve on the hot gas, ensuring the warm phase remains most prevalent in the disk regardless of supernova rate.

In Hill et al. (2012), the initial supernovae at heights $|z| \approx 1\,\mathrm{kpc}$ produce shocks as a result of the low ambient densities. These shocks propagate away from the mid-plane, escaping the domain after 20 Myr and heat the whole volume. The resulting densities in the halo are of order $10^{-6}\,\mathrm{cm}^{-3}$, compared to observational estimates of $10^{-4}\,\mathrm{cm}^{-3}$. After 100 Myr, the ejected material returns to the disk, resulting in a second pair of shocks, which propagate towards the vertical extents of the domain. After this pair of shocks passes through the medium, the densities in the halo are more consistent with observations. This second pair of shocks heats the gas in the halo ($z \gtrsim 0.3\,\mathrm{kpc}$) to temperatures of 10^6 K. A layer of thermally unstable gas of temperature 10^5 forms at heights $0.5 \leq |z| \leq 3\,\mathrm{kpc}$, whilst the warm gas of temperature 10^4 dominates close to the mid-plane.

Spatially and temporally correlated SNe can drive fountain flows of warm gas, as shown by Kim & Ostriker (2018). Vertical flows of warm gas with mean velocity 60–80 $\mathrm{km\,s}^{-1}$ result from the propagation of superbubbles produced by the correlated SNe through layers of cold and warm gas. As supernova feedback reduces star formation by the depletion of gas from the disk, the

driving of warm outflows from SNe becomes weaker and the warm gas at heights 1–2 kpc falls back the the disk.

It is clear that a large vertical extent, of order 10 kpc, is required to fully model fountain flows of hot gas and the resulting temperature distribution of the halo, with an extent of at least 2 kpc required for warm fountain flows. Simulations of the ISM in sufficiently tall domains have been able to explore these flows and achieve some agreement with observations. However, such simulations require a greater horizontal extent to fully model the hot gas outflows at larger heights (see Section 2.4.6). In the simulations outlined in Chapter 4, the vertical extent of 1 kpc used does not allow for exploration of fountain flows. However, as detailed below, these runs are able to fulfil the purpose of capturing the physics of the ISM near the mid-plane, excluding fountain flows, without any effects introduced via periodic boundary conditions.

2.4.6 Horizontal extent

Whilst much work has been performed to determine the required vertical extent for capturing fountain flows, much less work has been undertaken to find the necessary horizontal scales of ISM simulations. Simulations which employ large heights ($L_z \gtrsim 5$ kpc) typically use a horizontal scale of $L_x = L_y = 0.5$–1 kpc (see de Avillez & Mac Low, 2002; de Avillez & Breitschwerdt, 2004; Joung & Mac Low, 2006; Hill et al., 2012; Walch et al., 2015, as examples).

Periodic boundary conditions in both x and y are routinely used, with shearing periodic boundary conditions required in x if shear is implemented. As a result, it is important to use a sufficiently large horizontal scale to avoid introducing unphysical effects from periodic boundaries.

The correlation length of the velocity has been shown to increase with height (see Korpi et al., 1999b; Gent et al., 2013b). In particular, the simulations of Gent et al. (2013b) performed with a horizontal area of $1 \times 1\,\mathrm{kpc}^2$ found that near the vertical edge of the box, the velocity components are correlated at scales comparable to the horizontal scale. This is linked to the expansion of rising bubbles and chimneys of hot gas (see Korpi et al., 1999b). Additionally, the typical diameter of supernova shells increase to 0.4–0.6 kpc at heights of $|z| \simeq 1$ kpc. This can have significant impact on the results at $|z| \gtrsim 1$ kpc. Recent simulations using large heights report within a few kiloparsecs of the midplane (e.g. Hill et al., 2012; Walch et al., 2015).

Consequently, to fully explore larger heights in ISM simulations, for example to better model fountain flows, the domains used must be extended in all three dimensions. Such simulations would be much more computationally expensive than the current generation of runs. One method for increasing computational efficiency would be to use a more coarse resolution at large heights, such as detailed in de Avillez & Mac Low (2002) and Hill et al. (2012). This can be justified since the most detail is required around the sites of supernovae explosions, whose vertical distributions have scale heights of order 0.1 kpc.

2.4.7 Rotation

Most ISM codes that employ AMR do not include rotation, although both rotation and shear are included in the simulations of Gressel et al. (2008a,b) using the Nirvana code [1]. Neglecting both solid body and differential rotation is not essential for the modelling of temperature and density distributions in the ISM. Additionally, the characteristic velocities and Mach numbers in different phases of the ISM can be described without the presence of rotation.

However, rotation is a key component of disk galaxies on a global scale. The rapid rotation of spiral galaxies results in their flat shape and differential rotation is responsible for the spiral structure. Interstellar gas is locally affected by the Coriolis force and shear in the azimuthal direction. Observations suggest the structure of the magnetic field is strongly influenced by the spiral arms (see Fletcher et al., 2011). In regions of M51, analysis of turbulent correlation scales parallel and perpendicular to the local mean field suggest the presence of anisotropy in the magnetic field possibly to shear (see Houde et al., 2013). Thus, the inclusion of rotation is necessary for the organisation of the mean magnetic field and for the modelling of any resulting anisotropies.

Both solid body and differential rotation are necessary for mean field dynamo action, see Section 2.4.8, which requires both anisotropic turbulence and large-scale flows.

2.4.8 Magnetic fields

Galactic magnetic fields have typical strengths of order μG, resulting in magnetic energy densities of order 10^{-12}—$10^{-11}\,\mathrm{erg\,cm^{-3}}$. This is comparable to the kinetic energy density of the turbulent gas motions (see Beck, 2016) and so cannot be neglected by realistic models. Whilst hydrodynamic models can provide useful insights into the driving of turbulent gas motions by supernovae and exploration of parameters, magnetic fields must be included to form a more complete picture.

The vertical scale height is increased by magnetic pressure. The Lorentz force and magnetic tension modifies the velocity, which in turn affects the density of interstellar gas. Ohmic heating and electrical conductivity provides additional sources of heating which impacts the thermal distribution of the gas. In addition, cosmic rays cannot be included in ISM models without the presence of magnetic fields.

Two approaches are employed for the implementation of magnetic fields. The first involves initialising magnetic fields with strengths comparable to those from observations. The other method is to start with a weak seed field, which is then amplified by a dynamo. Both approaches are discussed below.

Strong initial fields

The addition of strong magnetic fields have been investigated in Korpi et al. (1999b), Mac Low et al. (2005), de Avillez & Breitschwerdt (2005a) and Hill et al. (2012). These impose an initial

[1] http://nirvana-code.aip.de/

horizontal field, proportional to the square root of density and run these simulations over a relatively short timescale. Korpi et al. (1999b) utilise an initial mean field strength of $0.1\,\mu$G, whereas Mac Low et al. (2005) and de Avillez & Breitschwerdt (2005a) use initial field strengths of order $1\,\mu$G. In contrast, Hill et al. (2012) explore the effects of initial field strengths in the range 1.3–13 μG.

The magnetic field is amplified initially, reaching equilibrium after a few 10 Myr. No turbulent field is included initially but is allowed to develop by turbulent action on the mean field. The distributions of the turbulent fields with respect to density and temperature, and the comparative strength to the mean field are reported in Mac Low et al. (2005), de Avillez & Breitschwerdt (2005a) and Hill et al. (2012). These simulations are run for only a few hundred Myr, beyond which it is expected that the mean field would begin to dissipate since the lack of rotation results in the absence of any restoring force for the mean field. The properties of these fields on longer timescales are not reported and so their realism may be questioned.

Dynamo action

Conversely, simulations of dynamo action in the ISM start with a weak seed field, with typical strengths of nG, and amplify the magnetic field until it reaches a steady state, typically with strengths of a few μG, comparable to observations. Fluctuation dynamo action evolves on timescales of 10 Myr, whilst mean field models require run times of 1 Gyr or greater. The impact of the mean magnetic field in such simulations can be investigated via comparisons between different stages of the dynamo. Hydrodynamic steady state is achieved after a few hundred Myr, where the magnetic field is still weak and so any differences between the early and late stages of the dynamo can be attributed to the magnetic field.

Gressel et al. (2008b) performed simulations in a box $0.8 \times 0.8 \times 4.267\,\mathrm{kpc}^3$ in size. They explored the effects of supernova rate and rotation rate on dynamo action, whilst retaining a constant shear parameter $q = -1$. The inclusion of shear was found to be necessary for the amplification of magnetic fields in their model (see Gressel et al., 2008a). In their simulations, the rotation frequency is the critical parameter allowing the dynamo to operate, with a required rotation rate of $\Omega > 25\,\mathrm{km\,s^{-1}\,kpc^{-1}}$. The turbulent component of the magnetic field is 2–3 stronger than the regular component, in agreement with observations, although no turbulent dynamo is present in the model.

Gent et al. (2013a) were also able to amplify a weak seed field via dynamo action in a box $1.0 \times 1.0 \times 2.2\,\mathrm{kpc}^3$ in size using the PENCIL code. The model employs the same shear parameter as in Gressel et al. (2008b), using a rotation rate of $\Omega = 50\,\mathrm{km\,s^{-1}\,kpc^{-1}}$ for computational efficiency. Despite the higher rotation, the simulation required a timescale of 1.6 Gyr for the dynamo to saturate. In contrast to observations, the regular field is approximately twice the strength of the turbulent field. Again, no fluctuation dynamo is discussed because of the low magnetic Reynolds number in the simulation.

Simulations to explore the small-scale, or fluctuation, dynamo in the ISM have been performed by Balsara et al. (2004) and Balsara & Kim (2005) in a domain $200^3\,\mathrm{pc}^3$ in size, with a resolution of approximately 1 pc. Such a domain size allows for supernova explosions to drive turbulence, rather than parameterised driving. The initial magnetic energy is 2×10^6 lower than the thermal energy. They found a small-scale dynamo amplifies the magnetic field from strengths of order $10^{-3}\,\mu$G to strengths of order $10^{-1}\,\mu$G on timescales of a few 10 Myr, comparable to the eddy turnover time, although the models do not achieve saturation because of the very short run time. Additionally, no mean field is generated because of the very short run times and lack of rotation.

Several simulations have been able to enhance magnetic fields via dynamo action. However, no simulation has been able to convincingly accommodate both mean-field and turbulent dynamo action simultaneously. Mean-field dynamo models require both extents of 1 kpc and shear, whilst turbulent dynamos necessitate high magnetic Reynolds numbers which are not currently reported in kpc-scale ISM models. Small-scale magnetic fields are amplified on much shorter timescales than mean-fields. The modification of the turbulent motions by small-scale field could act to inhibit the mean-field dynamo, which can only be investigated by models which admit both mechanisms.

2.4.9 Stellar winds

Stellar winds also contribute energy to the ISM. The most significant stellar winds originate from massive, hot, young O type stars (Draine, 2011). Their impact on the ISM is expected to be less important than supernova explosions (Mac Low & Klessen, 2004). However, stellar winds provide an additional mechanism for stellar feedback which regulates star formation rates.

In the simulations of Gatto et al. (2017), stellar winds are included via the tracking of the evolution of massive stars. The evolution is assumed to start from the beginning of the main sequence of each star. The age and initial mass of the star is used to determine the appropriate stellar wind model for each star. Stellar winds were found to reduce star formation and increase the thickness of the disk in the absence of supernovae. The inclusion of both stellar winds in addition to supernova explosions resulted in a thinner disk compared to as a result of reduced star formation. Stellar winds are insufficient on their own to create a hot, volume-filling phase. Supernovae are found to be the dominant mechanism for the maintenance of this phase.

2.4.10 Cosmic rays

Cosmic rays are high-energy charged particles travelling at relativistic speeds. With typical magnetic field strength of $1\,\mu$G and cosmic ray energy of 1GeV, the Larmor radius of cosmic rays as they propagate through the ISM is 10^{12} cm, significantly less than the expected correlation length of ISM turbulence, 10^{20} cm. Thus, cosmic rays in the ISM closely propagate along magnetic field lines and their galactic distribution depends importantly on the galactic magnetic field (see Cesarsky, 1980).

The estimated energy density of cosmic rays in the interstellar medium is similar to the kinetic, thermal and magnetic energy densities. Thus, the global properties of the ISM are expected to be significantly affected by the cosmic rays.

Cosmic rays can strongly influence the bulk motions of interstellar gas, despite the gas not being fully ionized. The interaction of cosmic rays with the ISM is a non-linear process, usually considered in a simplified form via a diffusion-advection equation, neglecting the streaming of cosmic rays

$$\frac{\partial e_{\rm cr}}{\partial t} + \nabla \cdot (e_{\rm cr} \boldsymbol{u}) = -p_{\rm cr} \nabla \cdot \boldsymbol{u} + \nabla \cdot (\hat{K} \nabla e_{\rm cr}) + Q_{\rm cr}, \tag{2.1}$$

$$p_{\rm cr} = (\gamma_{\rm cr} - 1) e_{\rm cr}, \tag{2.2}$$

where $\boldsymbol{u}$ is the gas velocity, $e_{\rm cr}$ is the cosmic ray energy, $p_{\rm cr}$ the cosmic ray pressure, $\hat{K}$ the cosmic ray diffusion tensor. The cosmic rays are injected via a source term $Q_{\rm cr}$ such as SNe.

Magnetohydrodynamic simulations of the local ISM including cosmic rays have been performed by Girichidis et al. (2016b) in a domain $2 \times 2 \times 20\,{\rm kpc}^3$ in size. They investigate the effects of the injection of thermal energy, $E_{\rm th} = f_{\rm th} E_{\rm SN}$ and cosmic-ray energy, $E_{\rm cr} = f_{\rm cr} E_{\rm SN}$, per SN, with $f_{\rm th} = 0.9$–1.0 and $f_{\rm cr} = 0$–0.1. These values are constant within each model discussed. The inclusion of cosmic rays increases the scale height of the galactic disk and support outflows from the disk, in addition to those driven by supernovae. These outflows are of cooler, more dense gas, travelling at slower speeds than those driven by supernovae. The additional cosmic-ray energy most strongly affects the gas outside the disk, in the halo. Thermal energy from supernovae dominates the structure near the mid-plane.

The impact of cosmic rays on the outflows in the ISM were also investigated in the MHD simulations of Simpson et al. (2016), using the moving-mesh code AREPO. The domain size used is $1 \times 1 \times 10\,{\rm kpc}^3$. As in Girichidis et al. (2016b), $f_{\rm cr} = 0.1$ in the models which included cosmic rays. However, they also investigated the effects of including isotropic and anisotropic cosmic-ray diffusion, and the inclusion of kinetic energy injection $E_{\rm kin} = f_{\rm kin} E_{\rm SN}$, where $f_{\rm kin} = 0.3$, but with no injection of cosmic rays. The non-thermal pressure contribution from cosmic rays increases the disk scale height and reduces the formation of dense gas. The inclusion of cosmic-ray diffusion is required to drive gas to significant heights from the mid-plane, with the mass-loss rates comparable to the star formation rate. The exception to this is their 'random-driving' purely thermal SNe model in which the selection of SNe sites is decoupled from dense gas regions. Similar to Girichidis et al. (2016b), the cosmic-ray driven outflows are smoother, more dense and travel at slower velocities than those produced in their 'random-driving' model. The choice of cosmic-ray diffusion impacts the cosmic-ray driven outflows. In the model with anisotropic diffusion, the outflows are weaker and their onset is delayed, as compared to the isotropic diffusion model. This results from the trapping of CR energy at the mid-plane by the magnetic field, which

is initially oriented parallel to the disk. As the magnetic field is altered by turbulence, this effect is reduced and the anisotropic diffusion model at late times evolves similarly to the model with isotropic diffusion.

Subsequent MHD simulations including cosmic rays have been performed by Girichidis et al. (2018a) in a box $0.5 \times 0.5 \times 10\,\mathrm{kpc}^3$ in size. The simulations contained a nG seed magnetic field, which was amplified to strengths of $0.1\,\mu$G by local compression and small-scale dynamo action. The range of prescribed values of the diffusion coefficient of the cosmic rays $\hat{K}$ investigated varied between 10^{27}–$10^{29}\,\mathrm{cm}^2\,\mathrm{s}^{-1}$ parallel and 10^{25}–$10^{27}\,\mathrm{cm}^2\,\mathrm{s}^{-1}$ perpendicular to magnetic field lines. As for Girichidis et al. (2016b), 10% of the SN energy is injected in the cosmic rays. The cosmic-ray pressure dominates at the mid-plane and at heights $|z| > 1\,\mathrm{kpc}$, with pressure equilibrium between thermal energy and cosmic-ray pressure at intermediate heights. Similar to Girichidis et al. (2016b), the cosmic-ray driven outflows are much smoother, cooler and more dense than those driven by thermal pressure. These cooler outflows extend into the region where cosmic rays dominate, leading to a reduced volume filling factor in the hot gas, compared to runs in which cosmic rays are omitted.

The inclusion of cosmic rays within an MHD model of the ISM containing magnetic fields, amplified by both fluctuation and mean-field dynamo action, to strengths comparable with those observed has yet to be investigated. The action of these magnetic fields may result in increased confinement of cosmic rays to the disk, resulting in increased cosmic ray pressure near the mid-plane.

2.4.11 Parker Instability

The magnetic Rayleigh-Taylor instability in the interstellar gas, enhanced by cosmic rays, is termed the Parker instability (Parker, 1966, 1967, 1969). Numerical experiments of the Parker instability using the PENCIL code have been performed by Rodrigues et al. (2016) in a domain $6\,\mathrm{kpc} \times 12\,\mathrm{kpc} \times 3.5\,\mathrm{kpc}$ in the x, y and z directions, centred about the galactic mid-plane. The initial state is an isothermal disk under magnetohydrostatic equilibrium, in which the variation of the relative contributions of the gas, magnetic field and cosmic rays to the total initial pressure is investigated. The system is allowed to evolve passively from the initial state, with no imposed sources of magnetic field or cosmic rays. Their results are in good agreement with linearised studies of the Parker instability. The sensitivity of the results to the initial cosmic-ray pressure highlights the importance of the inclusion of cosmic rays for studying the Parker instability.

2.5 Summary

A large array of numerical models have been used to describe the interstellar environment. The direct comparison of numerical models is difficult as they include different physical processes and cover different spatial and temporal scales. Limitations in computational power require careful

selection of physics, domain size and resolution in order to correctly model the astrophysical features that each simulation aims to investigate. For example, star formation requires high resolution which limits the overall size of the domain. Modelling on the scale of the spiral arms necessitates a much lower resolution and parameterisation of the driving of turbulence. The study of galactic dynamo action requires high magnetic Reynolds for the turbulent dynamo, whilst mean-field dynamos require large-scale shear flows and anisotropic turbulence. To establish a comprehensive set of numerical results, a set of models on overlapping scales encompassing the critical features on each of these scales is required.

Part II

Modelling the supernova driven interstellar medium

Chapter 3

Equations and numerical implementation

This chapter discusses the numerical methods used for the simulations in this Thesis. The numerical implementation of the MHD models were first detailed in Mee (2007); Gent (2012); Gent et al. (2013b), but I have included a discussion of the numerical methods here for both the benefit of understanding the results I have obtained from the MHD models, highlighted in Chapters 5 and 6, and for the purposes of discussing the changes made for my own hydrodynamic models.

3.1 Basic equations

The model solves numerically a system of equations using the PENCIL CODE, which is designed for fully non-linear, compressible magnetohydrodynamic (MHD) simulations. Cosmic rays are omitted here and will be added in later simulations.

The basic equations are the mass conservation equation, the Navier–Stokes equation, the heat equation, and the induction equation. The Navier–Stokes equation in (3.2) is written in a rotating frame. The induction equation is written in the appropriate gauge;

$$\frac{D\rho}{Dt} = -\rho\nabla\cdot\boldsymbol{u} + \dot{\rho}_{\rm SN} + \zeta_D\nabla^2\rho + \nabla\zeta_D\cdot\nabla\rho, \tag{3.1}$$

$$\begin{aligned}\frac{D\boldsymbol{u}}{Dt} =& -\rho^{-1}\nabla\dot{\sigma}_{\rm SN,kin} - c_s^2\nabla(s/c_{\rm P} + \ln\rho) - \nabla\Phi - Su_x\hat{\boldsymbol{y}} - 2\boldsymbol{\Omega}\times\boldsymbol{u} \\ &+\rho^{-1}\boldsymbol{j}\times\boldsymbol{B} + \nu(\nabla^2\boldsymbol{u} + \tfrac{1}{3}\nabla\nabla\cdot\boldsymbol{u} + 2\boldsymbol{W}\cdot\nabla\ln\rho) + \zeta_\nu(\nabla\nabla\cdot\boldsymbol{u}),\end{aligned} \tag{3.2}$$

$$\begin{aligned}\rho T\frac{Ds}{Dt} =& \dot{\sigma}_{\rm SN,th} + \rho\Gamma - \rho^2\Lambda + \nabla\cdot(c_{\rm P}\rho\chi\nabla T) + \eta\mu_0\boldsymbol{j}^2 \\ &+ 2\rho\nu|\boldsymbol{W}|^2 + \zeta_\chi(\rho T\nabla^2 s + \nabla\rho T\cdot\nabla s) + \rho T\nabla\zeta_\chi\cdot\nabla s,\end{aligned} \tag{3.3}$$

$$\frac{D\boldsymbol{A}}{Dt} = \boldsymbol{u}\times\boldsymbol{B} - SA_y\hat{\boldsymbol{x}} - Sx\frac{\partial\boldsymbol{A}}{\partial y} + (\eta+\zeta_\nu)\nabla^2\boldsymbol{A} + \nabla\cdot\boldsymbol{A}(\nabla\eta + \nabla\zeta_\nu), \tag{3.4}$$

where ρ, s and T are the mass density, specific entropy and temperature of the gas, with $\boldsymbol{u}$ the perturbation velocity from the background rotation profile. The induction equation is solved in terms of the magnetic vector potential $\boldsymbol{A}$ such that $\boldsymbol{B} = \nabla \times \boldsymbol{A}$, where $\boldsymbol{B}$ is the magnetic field. This ensures $\nabla \cdot \boldsymbol{B} = 0$. In addition $\boldsymbol{j} = \nabla \times \boldsymbol{B}$ is the current density, c_s the adiabatic sound speed and c_P the specific heat capacity at constant pressure. The velocity shear rate, S, is associated with the Galactic differential rotation at the angular velocity $\boldsymbol{\Omega}$, aligned with the z-axis.

The advective derivative includes transport by an imposed shear flow, $\boldsymbol{U} = (0, Sx, 0)$, in the local Cartesian frame

$$\frac{D}{Dt} = \frac{\partial}{\partial t} + (\boldsymbol{U} + \boldsymbol{u}) \cdot \nabla. \tag{3.5}$$

This linear shear flow is used to model the Galactic differential rotation in the local frame, where $S = r\partial\Omega/\partial r$ is the shear rate in terms of the galactocentric distance r. For the Solar neighbourhood, $\Omega_0 = -S = 25\,\mathrm{km\,s^{-1}\,kpc^{-1}}$.

It should be noted that while $\boldsymbol{u}$ is the velocity deviation from the background shear profile $\boldsymbol{U}$, there exists a mean component of $\boldsymbol{u}$, primarily from vertical outflows of hot gas. The mean flow is obtained from $\boldsymbol{u}$ via averaging with a Gaussian kernel, with the random velocity obtained via subtraction of this mean flow from the perturbation velocity. Further details are provided in Chapters 5 and 6.

The Navier–Stokes equation includes the Coriolis effect $2\boldsymbol{\Omega} \times \boldsymbol{u}$, the Lorentz force $\rho^{-1}\boldsymbol{j} \times \boldsymbol{B}$, the acceleration due to the gravitational potential produced by stars and dark matter, $\nabla\Phi$, and viscous terms with the viscosity ν, shock-capturing viscosity ζ_ν and the rate of strain tensor $\boldsymbol{W}$, whose components are as follows;

$$2W_{ij} = \frac{\partial u_i}{\partial x_j} + \frac{\partial u_j}{\partial x_i} - \frac{2}{3}\delta_{ij}\nabla \cdot \boldsymbol{u}. \tag{3.6}$$

The implementation of shock-capturing viscosity and diffusivities are discussed in Section 3.4. Using the gravitational potential as obtained in Kuijken & Gilmore (1989a,b), the vertical acceleration in the Solar neighbourhood is calculated as follows;

$$g_z = -\frac{\partial\Phi}{\partial z} = -\frac{a_1}{\sqrt{z^2 + z_1^2}} - a_2\frac{z}{z_2}, \tag{3.7}$$

where $a_1 = 4.4 \times 10^{-14}\,\mathrm{km\,s^{-1}}$, $a_2 = 1.7 \times 10^{-14}\,\mathrm{km\,s^{-1}}$, $z_1 = 200\,\mathrm{pc}$ and $z_2 = 1\,\mathrm{kpc}$.

Energy input from SNe drives the system, with $\dot{\sigma}_\mathrm{SN,kin}$ in (3.2) and $\dot{\sigma}_\mathrm{SN,th}$ in (3.3) the rates of kinetic and thermal energy per unit volume respectively. The total energy injected per SN is $E_\mathrm{SN} = 10^{51}\,\mathrm{erg}$, split between thermal and kinetic energy. The SN energy is injected within the density distribution within the injection sphere. The selection of supernova sites and the initial radius of each SN remnant are discussed in Section 3.2. The ejecta mass of each SN is included via the source term $\dot{\rho}_\mathrm{SN}$ in (3.1). Further details are provided in Section 3.2.

The heat equation (3.3) includes heat conduction, viscous heating associated with $|\boldsymbol{W}|$, Ohmic heating $\eta\mu_0\boldsymbol{j}^2$ and shock-capturing thermal diffusivity ζ_χ. $K = c_\mathrm{P}\rho\chi$ is the heat conductivity with χ the thermal diffusivity, $|\boldsymbol{W}|$ is the determinant of $\boldsymbol{W}$ and μ_0 is the vacuum permeability. Additionally, (3.3) contains a thermal energy source from photoelectric heating, $\rho\Gamma$, and energy losses from optically thin radiative cooling, $\rho^2\Lambda$. The photoelectric heating and radiative cooling functions are further discussed in Section 3.3. The heat equation is solved for entropy rather than temperature. All thermodynamic quantities are therefore formulated in terms of s and ρ.

The induction equation includes magnetic diffusivity, η, and shock-capturing magnetic diffusivity, ζ_η.

The ISM is modelled as an ideal gas, with thermal pressure calculated as

$$p = \rho RT, \tag{3.8}$$

where $R = \frac{k_\mathrm{B}}{\mu m_\mathrm{p}}$ is the gas constant, with k_B the Boltzmann constant, μ the mean molecular weight and m_p the proton mass. The choice of μ, discussed in Section 3.8 and Appendix C, assumes a constant level of ionisation. The effect of mean molecular weight is applied indirectly via the temperature dependent cooling and the specific heat capacities c_v and c_P. Electrons and ions are not modelled directly in these simulations because of the complexity. Nonetheless, it would be reasonable to consider different values of μ, depending on the level of ionisation. Future work could consider a temperature dependent level of ionisation, which would result in a temperature dependent value of μ. The expectation is that the thermal pressure in both the cold and warm gas would be reduced, and would be increased in the hot gas.

Self-gravity of the gas is neglected since, with the exception of the very cold molecular gas which I do not attempt to model, it can safely be ignored with the resolution employed. Simulations with higher resolution would be required to model the higher densities and the associated cooling rates.

Were self-gravity to be included, it would be important on scales below the Jeans length

$$\lambda_\mathrm{J} \approx \sqrt{\frac{k_\mathrm{B}Tr^3}{GM\mu}}, \tag{3.9}$$

where the gravitational energy $GM\mu/r$ becomes dominant over the thermal energy per particle $k_\mathrm{B}T$ within a cloud of gas with radius r. If the density within a cloud of cold gas becomes sufficiently high that λ_J locally is less than the grid scale Δ, then it can not be resolved. To prevent this, Dobbs et al. (2011) located their SNe where the ISM becomes sufficiently self-gravitating. This is also used to regulate the SN rate.

3.2 Injection of supernovae

Both Type I and Type II SNe are included in these simulations, varying only in vertical distribution and frequency. The frequencies correspond to those in the Solar neighbourhood, with a rate of $0.02\,\mathrm{yr}^{-1}$ for the whole Galaxy (see Tammann et al., 1994, as an example). Type I SNe occur with a surface density of $\nu_{\mathrm{I}} = 4\,\mathrm{Myr}^{-1}\,\mathrm{kpc}^{-2}$. The surface density of Type II is $\nu_{\mathrm{II}} = 25\,\mathrm{Myr}^{-1}\,\mathrm{kpc}^{-2}$, with fluctuations of order 10%, compared to the average rate, in an interval of order 10 Myr. It is natural to introduce such fluctuations and there is some evidence that these fluctuations enhance dynamo action in MHD models (Balsara et al., 2004).

The SN energy is split between thermal and kinetic energy, in order to reduce energy and temperature losses at early stages of SN evolution. Thermal energy density is distributed within the SN site as $\exp[-(r/r_{\mathrm{SN}})^6]$, where r is the local spherical radius and r_{SN} the size of the injected SN bubble. Kinetic energy is included within the spherical shell via a spherically symmetric velocity field $u_r \propto \exp[-(r/r_{\mathrm{SN}})^6]$. The injection site is placed midway between grid points to avoid a discontinuity in $\boldsymbol{u}$. An ejecta mass of $4M_{\odot}$ is also included, with an $\exp[-(r/r_{\mathrm{SN}})^6]$ density profile. As a result of the turbulent environment, there are large density inhomogeneities and random motions within injection regions. Hence, the kinetic energy injected varies between SN injection regions, which also varies the total energy injected within each injection region.

In each run, the total energy injected in each remnant is recorded to allow for the accounting of the rate of energy injection. The range of energy injection per SN is

$$0.5 < E_{\mathrm{SN}} < 1.5 \times 10^{51}\,\mathrm{erg}, \tag{3.10}$$

with an average injected energy of 0.9×10^{51} erg per SN.

The SN locations are distributed normally in height, with a uniform horizontal distribution. The scale heights of Type 1 and Type II SNe are $h_{\mathrm{I}} = 0.325\,\mathrm{kpc}$ and $h_{\mathrm{II}} = 0.09\,\mathrm{kpc}$ respectively. The mass source term in (3.1) is implemented as

$$\dot{\rho}_{\mathrm{SN}} \simeq 4\left(\frac{\nu_{\mathrm{I}}}{2h_{\mathrm{I}}} + \frac{\nu_{\mathrm{II}}}{2h_{\mathrm{II}}}\right)[M_{\odot}\,\mathrm{kpc}^{-3}\,\mathrm{Myr}^{-1}], \tag{3.11}$$

with a mass injection of $4M_{\odot}$ per SN. The mean kinetic and thermal energy sources included in (3.2) and (3.3) are as follows;

$$\dot{\sigma}_{\mathrm{SN,kin}} \simeq f_{\mathrm{kin}} E_{\mathrm{SN}}\left(\frac{\nu_{\mathrm{I}}}{2h_{\mathrm{I}}} + \frac{\nu_{\mathrm{II}}}{2h_{\mathrm{II}}}\right)[\mathrm{erg}\,\mathrm{kpc}^{-3}\,\mathrm{Myr}^{-1}], \tag{3.12}$$

$$\dot{\sigma}_{\mathrm{SN,th}} \simeq f_{\mathrm{th}} E_{\mathrm{SN}}\left(\frac{\nu_{\mathrm{I}}}{2h_{\mathrm{I}}} + \frac{\nu_{\mathrm{II}}}{2h_{\mathrm{II}}}\right)[\mathrm{erg}\,\mathrm{kpc}^{-3}\,\mathrm{Myr}^{-1}], \tag{3.13}$$

where f_{kin} and f_{th} are the fractions of the total SN energy injected as kinetic energy and thermal energy respectively.

Table 3.1: The parameterisation for the radiative cooling function, $\Lambda = \Lambda_k T^{\beta_k}$, using the cooling function of Wolfire et al. (1995) for $T < 10^5$ K and the cooling function of Sarazin & White (1987) for $T > 10^5$ K – for $T < 10$ K, $\Lambda = 0$.

T_k [K]	Λ_k [erg g^{-2} s^{-1} cm^3 K$^{-\beta_k}$]	β_k
10	3.70×10^{16}	2.12
141	9.46×10^{18}	1.00
313	1.18×10^{20}	0.56
6102	1.10×10^{10}	3.21
10^5	1.24×10^{27}	−0.20
2.88×10^5	2.39×10^{42}	−3.00
4.73×10^5	4.00×10^{26}	−0.22
2.11×10^6	1.53×10^{44}	−3.00
3.98×10^6	1.61×10^{22}	0.33
2.00×10^7	9.23×10^{20}	0.50

The final constraints applied to the selection of SN sites are to reject any site where the temperature would exceed 10^{10} K, or the number density at the injection site exceeds 2 cm^{-3}. The latter constraint is implemented to guarantee the injected thermal energy is not lost to radiative cooling before it is converted to kinetic energy in the surrounding gas. More sophisticated prescriptions, such as those employed by Korpi et al. (1999b); de Avillez (2000); Joung & Mac Low (2006); Gressel et al. (2008a); Walch et al. (2015), were found to unnecessary for the present purposes.

The initial radius of a SN remnant in a numerical simulation must span at least two gridpoints. With a numerical resolution of 4 pc, this minimum radius is 7 pc since the injection origin is set between grid points. The initial size of the remnant must be such that the temperature is between 10^6 K and 10^8 K. At both higher and lower temperatures, adiabatic expansion cannot be established because of excessive radiative losses. The injection radius is adjusted such that it contains $60 M_\odot$ of gas, following the work of Joung & Mac Low (2006). The distribution of injection radii appears lognormal, with $r_{\rm SN} > 75$ pc occurring infrequently. The modal value of $r_{\rm SN}$ is close to 10 pc, corresponding to the Sedov-Taylor phase of SN expansion. Uniform density within the injection site is not imposed, unlike in Joung & Mac Low (2006), since mass redistribution within the remnant is not required. Additionally, the redistribution of mass within SN remnants could introduce unintended effects in MHD simulations.

3.3 Heating and Cooling Functions

I use a parameterisation for the optically thin cooling function in (3.3), of the piecewise form $\Lambda = \Lambda_k T^{\beta_k}$, within a set of temperature ranges $T_k \leq T < T_{k+1}$. The values of T_k and Λ_k are listed in Table 3.1. The parameterisation consists of two parts. For $T < 10^5$ K, the cooling function fitted by

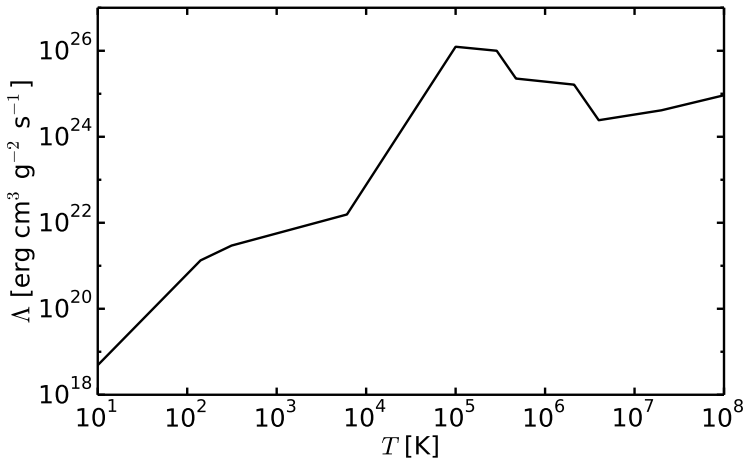

Figure 3.1: The cooling function, with the parameters listed in Table 3.1.

Sánchez-Salcedo et al. (2002) to the equilibrium pressure-density relation of Wolfire et al. (1995) is used. The cooling function of Slyz et al. (2005), adapted from the cooling curve in Sarazin & White (1987), is employed for higher temperatures. The cooling rate is dependent on the elemental abundances in the gas. The elemental abundances used in the cooling curve from Sánchez-Salcedo et al. (2002) are listed in Table 2 of Wolfire et al. (1995). The cooling curve from Sarazin & White (1987) assumes Solar abundances, based on the estimates from Meyer (1979).

This cooling function is also used in the dynamo simulations of Gressel et al. (2008a). It has two thermally unstable regions; the gas is isobarically unstable ($\beta_k < 1$) for $313 < T < 6102\,\mathrm{K}$, whilst for $T > 10^5\,\mathrm{K}$, the gas is isochorically ($\beta_k < 0$) or isentropically ($\beta_k < -1.5$) unstable.

The cooling function of Sarazin & White (1987), extended to lower temperatures with the cooling function adopted by Rosen & Bregman (1995), was used by Slyz et al. (2005) in their simulations modelling star formation in the ISM.

The values listed in Table 3.1 differ slightly from those in Sánchez-Salcedo et al. (2002). The slight modifications are to ensure continuity in the cooling function (see Gent et al., 2013b). The cooling function is shown in Figure 3.1.

Photoelectric heating by stellar far-ultraviolet (FUV) radiation is included in (3.3), based on the calculations of Wolfire et al. (1995), declining exponentially away from the mid-plane with a length-scale comparable to the height of the disk

$$\Gamma = \Gamma_0 \exp(-|z|/300\,\mathrm{pc}), \quad \Gamma_0 = 0.0147\,\mathrm{erg\,g^{-1}\,s^{-1}}. \tag{3.14}$$

This heating is applied for $T < 2 \times 10^4\,\mathrm{K}$, since the efficiency of the photoelectric heating of dust grains and Polycyclic Aromatic Hydrocarbons (PAHs) via UV photons is significantly reduced at higher temperatures (Wolfire et al., 1995). Similar photoelectric heating is applied by both Joung & Mac Low (2006) and Hill et al. (2012).

3.4 Numerical Methods and Shock Capturing

The model is performed in a three dimensional Cartesian grid $L_x = 1.024 \times L_y = 1.024 \times L_z = 2.172\,\mathrm{kpc}^3$ ($1.536 \times 1.536 \times 2.172\,\mathrm{kpc}^3$ for the larger domain) in size. The radial and azimuthal scales are 1.024 kpc, with a vertical scale of 1.086 kpc either side of the mid-plane. Relative to the characteristic radial and vertical Galactic length-scales of order 10 kpc, this domain occupies a small region of the Galactic disk extending vertically into the lower region of the halo. With an integral scale of the fluctuations $l_0 \simeq 50$–$100\,\mathrm{pc}$, as described in Chapter 5, the box encompasses approximately 100–400 correlation cells horizontally and about 2000–16000 cells in the entire domain. Thus, statistically reliable results can be obtained within the current domain size.

A vertical extent of 1 kpc includes approximately ten scale heights of the cold $\mathrm{H\,I}$ gas, two scale heights of the warm, diffuse $\mathrm{H\,I}$ gas and one scale height of the ionized hydrogen. A height of 1 kpc is insufficient to contain one scale height of the hot gas or capture the Galactic halo. This extent is strictly controlled by the horizontal size. Periodic boundary conditions are often employed horizontally in ISM simulations, which can significantly influence the outflow speed at heights exceeding the horizontal extent of the domain (see Gent et al., 2013b). Non-periodic boundary conditions are considered vertically, usually allowing for outflow from the domain. In addition, the typical size of supernova shells increases to 0.4–0.6 kpc at heights of $|z| \simeq 1\,\mathrm{kpc}$. Thus the domain is sufficient in size to fulfil the purpose of capturing the physics of the ISM near the mid-plane, excluding fountain flows, without any effects introduced via periodic horizontal boundary conditions. It would be ideal to extend the vertical domain in the future, in order to capture fountain flows, or at least to better model the vertical structure. However, this would require the extension of the horizontal extent to ensure the dynamics of the flows are still captured reliably without any artefacts from periodic, or sheared periodic in the x–direction, boundary conditions.

The number of grid points used in the model is $256 \times 256 \times 544$ ($384 \times 384 \times 544$ in the larger domain), corresponding to a resolution of $\Delta = \Delta x = \Delta y = \Delta z = 4\,\mathrm{pc}$. This numerical resolution has been chosen carefully to accurately reproduce the known expansion laws and reasonably approximate the internal structure of an isolated supernova, subject to radiative losses, until the radial expansion speed of the shell becomes comparable to the adiabatic sound speed in the surrounding ISM (Appendix B of Gent et al., 2013b). A third order Runge-Kutta scheme is used for time stepping, with a sixth-order finite difference scheme used for spatial vector operations.

The Courant-Friedrichs-Lewy (CFL) condition necessitates the numerical time step to be shorter than the crossing time over the mesh length Δ for each transport process involved. In addition to the 'classic' Courant time step, calculated from the ratio of the grid scale to the advective terms

$$\Delta t < c_{\delta t} \frac{\Delta^2}{\max(c_s, u, U)},$$

the PENCIL CODE also includes the Courant time step based on the diffusive processes

$$\Delta t < c_{\delta t,\mathrm{v}} \frac{\Delta^2}{\max(\nu, \gamma\chi, \eta)},$$

where $c_{\delta t} = c_{\delta t,\mathrm{v}} = 0.25$ in the simulations described in this thesis.

Additionally, the von Neumann stability condition requires the time step to be sufficiently small in order to ensure the errors of a numerical scheme are bounded. For a typical diffusion process, this time step constraint may be written as

$$\Delta t < \frac{c\Delta^2}{\alpha},$$

where α is the diffusion coefficient and c is a constant, usually $c \leq \frac{1}{2}$ (Fletcher, 1991).

Both conditions impose lower limits for the kinematic viscosity ν, thermal conductivity K and magnetic diffusivity η. Given the spatial and temporal resolutions in the model, the necessary minimum values are unavoidably much higher than the realistic values. It is important to avoid using values of ν, χ and η that are much higher than necessary. The typical perturbation gas speeds in the cold and warm phases are of order $10\,\mathrm{km\,s^{-1}}$, and so the viscosity and thermal diffusivity are set proportional to the square root of temperature, which is proportional to the local sound speed, with $\nu = \nu_1\sqrt{T/T_0}$, $\chi = \chi_1\sqrt{T/T_0}$ and $\eta = \eta_1\sqrt{T/T_0}$. The values used are $T_0 = 44.74127\,\mathrm{K}$, $\nu_1 \approx 4.2\times10^{-3}\,\mathrm{km\,s^{-1}\,kpc}$, $\chi_1 \approx 9.2\times10^{-4}\,\mathrm{km\,s^{-1}\,kpc}$ and $\eta_1 \approx 1.2\times10^{-3}\,\mathrm{km\,s^{-1}\,kpc}$. The use of $T^{1/2}$ for the temperature dependence of the diffusivities is for numerical convenience. In a fully ionised gas, the magnetic diffusivity scales with temperature as $T^{-3/2}$ (Cohen et al., 1950; Spitzer & Härm, 1953). However, the above prescriptions for the viscosity and the diffusivities represent a useful compromise, in which unnecessarily high diffusivities in the cold and warm gas are avoided, whilst also ensuring the maximum grid Reynolds, Péclet and magnetic Reynolds numbers do not exceed order unity in the hot gas.

Shock-capturing mass, momentum, heat and magnetic diffusivities are included in order to fully resolve the strong shocks pervasive throughout the ISM. The shock-capturing diffusivities ζ_D, ζ_ν, ζ_χ and ζ_η are defined as

$$\zeta_D = \begin{cases} c_D \Delta x^2 \max_5 |\nabla\cdot\boldsymbol{u}|, & \text{if } \nabla\cdot\boldsymbol{u} < 0, \\ 0, & \text{otherwise,} \end{cases} \tag{3.15}$$

with similar expressions for ζ_ν, ζ_χ and ζ_η but with c_D, c_χ and c_η respectively. The maximum value occurring within the five nearest mesh points in any direction is denoted by $\max_5$. c_D, $c_\nu = c_\chi$ and c_η are dimensionless constants set empirically to 1, 10 and 5 respectively. Hence, the shock-capturing diffusivities are confined to regions where the flow converges and are proportional to the maximum velocity divergence in the local region. The shock-capturing diffusivities spread the

shocks over a sufficient number of grid points, typically 4. The results from tests of the expansion of an isolated supernova remnant are described in detail in Gent (2012, Appendix A) and Gent et al. (2018). These results are shown to be reasonably accurate, particularly the conversion of thermal energy to kinetic energy in supernova remnants.

Shock-capturing diffusivites broaden the shock profiles and increases the spread of density around the shocks. This could impact the statistical properties of the small-scale physics, such as the correlation scales, particularly the scale of the density fluctuations despite these length-scales being typically significantly longer than $5\Delta = 20\,\mathrm{pc}$. Additionally, the gas inside SN remnants cools at a faster rate because of the smoothed density profile. Following the approach outlined in Gent et al. (2013b, Appendix B), the following numerical scheme is applied to reduce gas cooling within SN remnants and confine the extreme cooling to the shock fronts. This is prescribed by the multiplication of the factor

$$\xi = \exp\left(-C|\nabla\zeta_\chi|^2\right), \tag{3.16}$$

to the term $(\Gamma - \rho\Lambda)T^{-1}$, where ζ_χ is the shock-capturing thermal diffusivity. Outside of the shock regions, $\xi \approx 1$, reducing to zero within strong shocks. The parameter $C \approx 0.01$ is empirically set to ensure numerical stability with minimal change to the basic physics. The accurate modelling of a single SN remnant with the inclusion of artificial diffusion terms has been verified in Gent et al. (2013b, Appendix B).

The cooling function is susceptible to thermal instability, hence the thermal diffusivity χ must be sufficiently large to resolve the most unstable normal modes

$$\chi \geq \frac{1-\beta}{\gamma\tau_{\mathrm{cool}}}\left(\frac{\Delta}{2\pi}\right)^2, \tag{3.17}$$

where $\beta = 0.56$ is the exponent of the cooling function in the thermally unstable range ($313 < T < 6102\,\mathrm{K}$, see Table 3.1), $\gamma = 5/3$ is the adiabatic index and τ_{cool} is the radiative cooling time. The cooling time is usually in excess of order 1 Myr (see Gent, 2012, Chapter 7). Additionally, Gent et al. (2013b) demonstrate any thermal instabilities in the model are well resolved at the grid scale.

3.5 Boundary Conditions

Within the horizontal scale modelled, arm-interarm variations can be neglected and the horizontal structure can be regarded as statistically homogeneous. Thus, in the azimuthal (y) direction, periodic boundary conditions are applied. Differential rotation is included via shear in the local radial (x) direction and so shearing periodic boundary conditions are used in x (see Wisdom & Tremaine, 1988; Hawley et al., 1995). In the shearing box, the horizontal periodicity conditions for a variable

f are as follows

$$\begin{aligned} f(x,y,z) &= f(x+L_x, y-\delta y(t), z) \qquad \text{(boundary in } x\text{)}, \\ f(x,y,z) &= f(x, y+L_y, z) \qquad\qquad\ \ \text{(boundary in } y\text{)}, \end{aligned} \tag{3.18}$$

where $\delta y(t) = \mathrm{mod}[q\Omega L_x t, L_y]$ is the time-varying offset between the shearing boundaries in x (mapped to the range $0 \leq \delta y < L_y$).

By comparison, the vertical boundary conditions are much less trivial. Supernova heating within a few kiloparsecs of the mid-plane results in outflows of hot gas from the disk to the halo. The vertical extent of the halo is of order 10 kpc, with non-trivial physical processes occurring at this height, particularly with the escape of cosmic rays and the galactic wind. From the results of de Avillez & Breitschwerdt (2007); Joung et al. (2009) among others, a vertical extent greater than ± 5 kpc is required for the hot gas to cool and return to the mid-plane. A height of 10 kpc, or 20 kpc as employed by Hill et al. (2012), excludes significant mass loss but the computational expense is considerable. MHD runs, particularly those modelling a mean-field dynamo, require simulation times of order 1 Gyr. Hence, it is desirable to restrict the domain to the minimum height with which the physics can be reliably modelled. A vertical extent of 2 kpc is employed by Gressel et al. (2008a,b) but with half the resolution and so only a quarter of the resources are required. A vertical boundary of ± 1 kpc results in no adequate physical process for the cooling and return of hot gas, so the mass loss needs to be addressed carefully. Further discussion of the mass loss is detailed in Section 3.6.

The formulation of boundary conditions must allow for the flow of matter and energy, whilst also minimising any artefacts that could impact on the interior physics. The use of stress-free, open boundary conditions on the vertical boundaries would be the most appropriate, requiring the vanishing of horizontal stresses, with constant vertical first derivatives at the boundaries in density, entropy and vertical velocity. The boundary conditions are numerically implemented with the use of 'ghost' zones; three outer grid planes allowing for the derivatives at the boundary to be calculated in the same way as at the interior points. The values of the variables in the ghost zones near the vertical boundaries specified by the values at the interior points near the opposite boundary.

The handling of shocks in the ISM becomes increasingly difficult as these approach the vertical boundaries. In both the computational domain and the periodic boundaries, the shocks are absorbed into the surrounding medium, which limits the magnitude of the momentum and energy within each shock. When a shock approaches the vertical boundaries, the strong gradients can be extrapolated into the ghost zones. This results in the artificial enhancement of such structures, which may lead to numerical instabilities. The modified boundary conditions, with the adjustments to ensure numerical stability, are detailed below.

Mass

Weak negative gradients are imposed in the ghost zones in order to prevent artificial mass sources in the ghost zones. The extrapolation of density into the ghost zones is computed as follows

$$\rho(x,y,\pm Z \pm k\Delta) = (1-\Delta/0.1\,\mathrm{kpc})\rho(x,y,\pm Z \pm (k-1)\Delta), \tag{3.19}$$

at all horizontal co-ordinates x and y, with the boundary surfaces denoted $z = \pm Z$ and the ghost zones $z = \pm Z \pm k\Delta$, with $k = 1, 2, 3$. The positive sign refers to the top boundary, whilst the negative sign refers to the lower boundary. This results in the gradual reduction of gas density in the ghost zones.

Temperature

Gas temperature in the ghost zones is kept equal to the boundary temperature, in order to prevent artificial enhancement of spikes in the temperature

$$T(x,y,\pm Z \pm k\Delta) = T(x,y,\pm Z). \tag{3.20}$$

This allows the temperature fluctuations in the ghost zones to be influenced by the interior physics. Since the code solves for entropy, this boundary condition is implemented for entropy, with the density variation in (3.19).

Velocity

If the flow is directed outwards, then the vertical velocity in the ghost zones is kept equal to the value at the boundary

$$u_z(x,y,\pm Z \pm k\Delta) = u_z(x,y,\pm Z), \quad u_z(x,y,\pm Z) \gtrless 0. \tag{3.21}$$

The rapid cooling of gas near the boundary can result in a drop in pressure, which results in the flow of gas away from the boundary. To allow for inward flows of gas $u_z(x,y,\pm Z \pm k\Delta) \lesseqgtr 0$, the following prescription is applied:

$$\text{if} \quad |u_z(x,y,\pm Z \mp \Delta)| < |u_z(x,y,\pm Z)|,$$

set

$$u_z(x,y,\pm Z \pm \Delta) = \tfrac{1}{2}[u_z(x,y,\pm Z) + u_z(x,y,\pm Z \mp \Delta)], \tag{3.22}$$

otherwise;

$$u_z(x,y,\pm Z \pm \Delta) = 2u_z(x,y,\pm Z) - u_z(x,y,\pm Z \mp \Delta). \tag{3.23}$$

In each case, the vertical velocity in the outer two ghost zones is computed as follows

$$u_z(x,y,\pm Z \pm k\Delta) = 2u_z(x,y,\pm Z \pm (k-1)\Delta) - u_z(x,y,\pm Z \pm (k-2)\Delta). \tag{3.24}$$

This ensures the inward velocity in the ghost zones is smaller than the value at the boundary. These boundary conditions for u_z allow for the flow of gas across the vertical boundaries, whilst guaranteeing the velocity is determined by the dynamics in the interior.

Symmetrical boundary conditions are applied for the horizontal velocity components in order to exclude horizontal stresses;

$$u_x(x,y,\pm Z \pm k\Delta) = u_x(x,y,\pm Z \mp k\Delta), \tag{3.25}$$

with a similar condition for u_y.

Magnetic field

For the MHD models, two sets of vertical boundary conditions are considered: vertical field and open. Since the induction equation in (3.4) is solved for the vector potential $\boldsymbol{A}$, the boundary conditions are prescribed in terms of $\boldsymbol{A}$. The vertical field condition is designed to prevent external flux. Flux across the periodic horizontal boundaries conserves the magnetic energy. The addition of magnetic energy from non-physical boundary effects must be excluded in order to correctly identify the presence of a dynamo, which is ensured by implementing zero flux on the vertical boundaries. For the horizontal components of $\boldsymbol{A}$

$$A_x(x,y,\pm Z \pm k\Delta) = A_x(x,y,\pm Z \mp k\Delta), \tag{3.26}$$

with a similar condition for A_y. For the vertical component

$$A_z(x,y,\pm Z \pm k\Delta) = -A_z(x,y,\pm Z \mp k\Delta), \tag{3.27}$$

which ensures

$$\frac{\partial A_x}{\partial z} = \frac{\partial A_y}{\partial z} = A_z = 0 = B_x = B_y, \tag{3.28}$$

on the vertical boundaries. B_z can differ from zero. These boundary conditions result in the formation of a boundary layer in which the non-zero horizontal fields near to the upper and lower surfaces must vanish non-physically.

Open vertical boundary conditions allow for external flux but maintain the vertical structure of the magnetic field up to the vertical boundaries. These boundary conditions were applied by Gressel et al. (2008a) in a domain extending to $\pm 2\,\mathrm{kpc}$ in z, arguing that any effects from the external flux were negligible. Since the outward flow of gas across the vertical surfaces is dominant compared to the inward flow, the outward magnetic flux is expected to be greater than the inward

flux. A simulation with open vertical magnetic boundary conditions is discussed in Gent (2012). In this simulation, the Poynting flux on the vertical boundaries is monitored. The total outward flux is found to be two orders of magnitude greater than the inward flux. Thus, any artificial amplification of magnetic field by boundary effects may be ignored.

The open vertical boundary condition for the horizontal magnetic vector potential components is prescribed as

$$A_x(x,y,\pm Z \pm k\Delta) = 2A_x(x,y,\pm Z \pm (k-1)\Delta) - A_x(x,y,\pm Z \pm (k-2)\Delta), \tag{3.29}$$

with a similar condition for A_y. For the vertical component

$$A_z(x,y,\pm Z \pm k\Delta) = A_z(x,y,\pm Z \mp k\Delta). \tag{3.30}$$

Thus, on the vertical boundary

$$\frac{\partial^2 A_x}{\partial z^2} = \frac{\partial^2 A_y}{\partial z^2} = \frac{\partial A_z}{\partial z} = 0 = \frac{\partial B_x}{\partial z} = \frac{\partial B_y}{\partial z}, \tag{3.31}$$

$\partial B_z/\partial z$ can differ from zero on the boundary.

3.6 Mass loss

The mass loss rate through the top and bottom boundaries is about $10^{-3}\,\mathrm{M_\odot\,yr^{-1}}$, so $10^6\,\mathrm{M_\odot}$ is lost in 1 Gyr, as compared to the total gas mass of $10^7\,\mathrm{M_\odot}$ in the computational domain. This mass loss would correspond to a total mass loss rate of $1\,\mathrm{M_\odot\,yr^{-1}}$ for a galactic disk of radius 15 kpc, assuming the Galaxy is in a steady state, comparable to the observed mass loss in the Galaxy. The open boundary conditions allow for inflow as well as outflow, albeit in an ad hoc way (see Section 3.5), which mitigates the mass loss through the boundaries. This modest mass loss is compensated by calculating the total net mass loss and redistributing the mass throughout the domain, proportional to the local density. This replacement rate is roughly 10^{-7} of the total ISM mass on each occasion. Given the preservation of the local ratios in density, there should be minimal impact on any density gradients and the dynamics in the model. Additionally, any structures in temperature, velocity and energy should not be sensitive to the mass redistribution. This allows for the preservation of the simulation over times of order 1 Gyr with minimal impact on the properties of the dynamics in the simulation.

Extending the simulation to to at least ± 5 kpc vertically would significantly reduce the mass loss through the vertical boundaries and allow for recycling of gas to the disk, removing the requirement for the artificial replacement of mass. Such an approach will increase the computational expense, however decreased resolution at larger heights would be acceptable, reducing the increase in computational cost. As detailed in Section 2.4.6, the reliability of the results at larger heights

may be questionable, although most authors using large vertical extents report within a few kiloparsecs of the mid-plane. However, the replacement of mass detailed above provides a reasonable compromise since any impact on the dynamics is minimal whilst ensuring the gas is not depleted over the long simulation times considered here (see Gent, 2012, Appendix C).

3.7 Initial Conditions

The initial density distribution corresponds to an isothermal hydrostatic equilibrium in the gravity field given in (3.7);

$$\rho(z) = \rho_0 \exp\left[a_1\left(z_1 - \sqrt{z_1^2 - z^2} - \frac{a_1}{2a_2}\frac{z^2}{z_1}\right)\right], \tag{3.32}$$

where $\rho_0 = 3.0 \times 10^{24}\,\mathrm{g\,cm^{-3}}$, accounting only for atomic gas. No models contain cosmic rays and some do not contain magnetic fields, which provide about one quarter each of the total pressure in the ISM; the remaining contributions are from thermal and turbulent pressure. Thus, the gas scale heights are anticipated to be smaller than those from observations.

Density-dependent heating and cooling results in the gas no longer being isothermal after the start of the simulation. Thus the profile in (3.32) is not a hydrostatic distribution. A non-uniform initial temperature profile is imposed to maintain a nearly static equilibrium, which also avoids long initial transients;

$$T(z) = \frac{T_0}{z_1}\left(\sqrt{z_1^2 + z^2} + \frac{a_1}{2a_2}\frac{z^2}{z_2}\right), \tag{3.33}$$

where T_0 is calculated from

$$\Gamma(0) = \rho_0 \Lambda(T_0) \approx 0.0147\,\mathrm{erg\,g^{-1}\,s^{-1}}. \tag{3.34}$$

In the MHD models, the initial seed field used is $\boldsymbol{B} = (0, B_I n(z), 0)$, where $B_I = 0.05\,\mu\mathrm{G\,cm^3}$ and $n(z)$ follows the same distribution as (3.32) but with $n_0 = 1.8\,\mathrm{cm^{-3}}$. This results in an initial mean rms value of $\langle B_{\mathrm{rms}} \rangle_V \simeq 0.001\,\mu\mathrm{G}$, where $\langle \cdot \rangle_V$ denotes averaging over the whole volume. This initial magnetic field imposes a net horizontal flux in the y-direction. Analysis of snapshots from the MHD models show that this flux is a conserved quantity, with the periodic boundary conditions in the y-direction used in these simulations.

The initial profile used is an unstable equilibrium because of differential heating and cooling in the stratified gas. This results in collapse of the gas towards the mid-plane and oscillations. The establishing of a new equilibrium requires a build up of turbulent and thermal pressure, after which an extended period of time is required to allow for the dissipation of oscillations in the disk in order for the disk to become statistically steady.

To avoid these transients, Gressel et al. (2008a) adjust the initial condition such that the vertical profiles of density and pressure are computed to ensure both hydrostatic equilibrium and the balance of radiative heating and cooling. Whilst the contribution of heating to the long term dy-

namics is relatively small, this does add an unphysical element to the model. Another approach, which remains to be tested, would be to begin with an isothermal, hydrostatic equilibrium by switching off heating and cooling until thermal and turbulent pressure are sufficient to support the gas against gravitational collapse. This would result in a reduced duration of transients, increasing the efficiency of the code.

3.8 Updated Code

The hydrodynamic simulations performed by myself use very similar code to the model described above, with the obvious exclusion of magnetic fields. This allows for more convenient comparison between the different supernova rates, without requiring the consideration of effects introduced by the magnetic field. To reduce computational expense, the domain size was altered to $0.720 \times 0.720 \times 2.240\,\mathrm{kpc}^3$, with $180 \times 180 \times 560$ grid points used, corresponding to the same 4 pc resolution as for the previous models. In this domain, about 50–200 correlation cells are included in the horizontal direction, with about 1000–8000 correlation cells contained in the simulation volume. Modest refinements were made to the specified code units, which resulted in some minor changes to the derived, as shown in Appendix C. The exceptions are the unit temperature and unit specific entropy.

Refinements were made with the injection of SNe into the simulation. For greater numerical stability, the minimum injection radius is increased to $5\Delta = 20\,\mathrm{pc}$, whilst the energy injected is purely thermal. The change to purely thermal energy injection is more similar to the prescription used by other authors. This change is not anticipated to significantly impact the results as a large percentage of the thermal energy injected in each SNe is quickly transferred as kinetic energy into the surrounding gas. Further details are provided in Gent et al. (2018).

Further testing and refinement revealed the damping of the cooling term $(\Gamma - \rho\Lambda)T^{-1}$, as shown in (3.16) was no longer required for either numerical stability or accuracy of the solution, provided calculation of the viscous heating time is included in the limit for the time-step, and so this term is switched off. This removes any artificial limit on the cooling and the density of the gas within shocks.

The viscosity is calculated with the same temperature dependence as previously, but with $\nu_1 \approx 3.9 \times 10^{-3}\,\mathrm{km\,s^{-1}\,kpc}$ and $T_0 = 36.63718\,\mathrm{K}$. The thermal diffusivity is calculated in terms of the local temperature as $\chi = \chi_1 (T/T_0)^{0.335}$, with $\chi_1 \approx 4.54 \times 10^{-3}\,\mathrm{km\,s^{-1}\,kpc}$. The shock-capturing diffusivities and the viscosity are calculated as previously.

Based on the percentage abundances of hydrogen and helium in the Solar neighbourhood (see Ferrière, 2001), the mean molecular weight has been adjusted from $\mu = 0.62$ to $\mu = 0.531$. This has resulted in the careful calculation for the adjusted unit temperature, which has also significantly changed the value of the unit specific entropy (see Appendix C).

Chapter 4

Models Explored

4.1 Summary of models

I have analysed four HD and three MHD models, which are listed in Table 4.1, together with the important input parameters and domain dimensions. All models used an equidistant grid with 4 pc resolution and utilise shear rates based on a flat rotation curve, $q = +1$, such that $S = -q\Omega = -\Omega$. The model names are listed in Column 1.

The models H1$\Omega_{\rm ref}$, B1Ω and B2Ω are expanded upon in Gent (2012), Gent et al. (2013a) and Gent et al. (2013b). B1Ω and B1ΩOoL utilise parameters corresponding to those of the Solar neighbourhood with using alternative vertical boundary conditions for the magnetic field. B1ΩOoL also uses a larger domain than the 'standard' model B1Ω. The comparisons between B1Ω and B1ΩOoL are used to test the sensitivity of the model to simulation volume. H1$\Omega_{\rm ref}$ is identical to B1Ω, with the exception of magnetic field. This model is used as a reference model in order to test the new HD runs. Each of these models have supernova distributions and rates, $\dot{\sigma}$, equivalent to the Solar neighbourhood. B2Ω is identical to B1Ω but with twice the rotation rate, see Column 4. This model was originally used in order to test the sensitivity of the mean-field dynamo to the rotation rate. The increased rotation rate enhances the dynamo and results in the earlier saturation of the mean magnetic field (see Gent, 2012; Gent et al., 2013a).

The HD models H1$\Omega_{\dot{\sigma}=0.5}$, H1$\Omega_{\dot{\sigma}=1.0}$ and H1$\Omega_{\dot{\sigma}=1.5}$ are used to test the impact of the supernova rate. The rates used are listed in Column 5. These models use a smaller horizontal extent $L_{\rm horiz} = L_x = L_y$ than the previous models for computational efficiency, see Column 2. The vertical extents L_z on either side of the mid-plane, at $z = 0$ pc, are similar for all models (see Column 3).

The inclusion of a magnetic field is listed in Column 6, with the vertical boundary condition on the magnetic vector potential highlighted in Column 7. Column 8 indicates in which sections of the thesis the results of each model are discussed.

Such computational runs are expensive, necessitating parallel processing on around 280 nodes. To run for 100 Myr, approximately 100000 cpu hours are required. As a result, only three models

Table 4.1: The dimensions and important input parameters of the model explored. The names are listed in Column 1. Column: (2) horizontal extent $L_{\rm horiz}$; (3) vertical extent L_z; (4) galactic rotation rate Ω; (5) galactic supernova rate $\dot{\sigma}$; (6) magnetic field $\boldsymbol{B}$; (7) vertical boundary condition on the magnetic potential $\boldsymbol{A}$; (8) Section where result from each model are listed.

(1)	(2)	(3)	(4)	(5)	(6)	(7)	(8)
Models	$L_{\rm horiz}$ [kpc]	L_z [kpc]	Ω [Ω_0]	$\dot{\sigma}$ [$\dot{\sigma}_0$]	$\boldsymbol{B}\neq 0$	bcz($\boldsymbol{A}$)	Sections
B1Ω	1.024	1.086	1	1.0	yes	vertical	5
B1ΩOoL	1.532	1.278	1	1.0	yes	open	5
B2Ω	1.024	1.086	2	1.0	yes	vertical	5, 6
H1$\Omega_{\rm ref}$	1.024	1.118	1	1.0	no	—	7
H1$\Omega_{\dot{\sigma}=0.5}$	0.72	1.118	1	0.5	no	—	7, 8
H1$\Omega_{\dot{\sigma}=1.0}$	0.72	1.118	1	1.0	no	—	7, 8
H1$\Omega_{\dot{\sigma}=1.5}$	0.72	1.118	1	1.5	no	—	7, 8

are started from $t = 0$, since run times of the order of 1 Gyr are needed. For the magnetic runs, B1Ω was initially run to 400 Myr. Further snapshots for this run were also generated, which are used to test in comparison to B1ΩOoL. B2Ω was then started from this snapshot and evolved to 1.7 Gyr. The mean-field dynamo reaches a non-linear stage at 1.1 Gyr. B1Ω was then restarted from this snapshot and ran for a further 400 Myr to examine the saturated magnetic field. This was required since the estimated time for the dynamo to saturate in B1Ω was 2 Gyr. B1ΩOoL was run to 600 Myr.

For the new hydrodynamic runs, H1$\Omega_{\dot{\sigma}=1.0}$ was evolved until 300 Myr, at which the model has reached a statistical steady state, and then ran further until 600 Myr. The models H1$\Omega_{\dot{\sigma}=1.5}$ and H1$\Omega_{\dot{\sigma}=0.5}$ were started from the snapshot 300 Myr, with both models continued for 400 Myr. The first 100 Myr were required in order to remove any transient effects and ensure each model returns to a statistically steady state.

4.2 Summary statistics of the models

Summary statistics for the models shown in Table 4.1 are displayed in Table 4.2. In this section, angular brackets indicate averages over eleven snapshots from the statistically steady state of each model, with brackets indicating the spatial fluctuations over the composite snapshots. For models B1Ω and B2Ω, this refers to the period after the saturation of the magnetic field, which occurs at a much later time than the hydrodynamical steady state. For all other models, the hydrodynamical steady state is used. Results from the kinematic stage of B1Ω are used for comparison with B1ΩOoL; this is listed as B1Ω(k) in the table.

The sound speed is computed in terms of the temperature using the equation of state, as de-

Table 4.2: The models discussed in Table 4.1 (Column 1), with important summary statistics listed as follows; (9) average sound speed $\langle c_s \rangle$, (10) average kinematic viscosity $\langle \nu \rangle$, (11) average grid Reynolds number $\langle \mathrm{Re}_\Delta \rangle$, (12) average root mean square velocity $\langle u' \rangle$, (13) average random velocity $\langle u' \rangle$, (14) average kinetic energy density $\langle e_{\mathrm{kin}} \rangle$, (15) average thermal energy density $\langle e_{\mathrm{th}} \rangle$, (16) average magnetic energy density $\langle e_{\mathrm{B}} \rangle$, and (17) time span over which the models have been in steady state (hydrodynamic for all models except B1Ω and B2Ω where the magnetic steady state is used). The values listed in brackets are the corresponding standard deviations over the snapshots considered.

(1)	(9)	(10)	(11)	(12)	(13)	(14)	(15)	(16)	(17)
Model	$\langle c_s \rangle$ $[\mathrm{km\,s^{-1}}]$	$\langle \nu \rangle$	$\langle \mathrm{Re}_\Delta \rangle$	$\langle u_{\mathrm{rms}} \rangle$ $[\mathrm{km\,s^{-1}}]$	$\langle u' \rangle$ $[\mathrm{km\,s^{-1}}]$	$\langle e_{\mathrm{th}} \rangle$ $[E_{\mathrm{SN}}\,\mathrm{kpc^{-3}}]$	$\langle e_{\mathrm{kin}} \rangle$ $[E_{\mathrm{SN}}\,\mathrm{kpc^{-3}}]$	$\langle e_{\mathrm{B}} \rangle$ $[E_{\mathrm{SN}}\,\mathrm{kpc^{-3}}]$	Δt $[\tau]$
B1Ω	23 (22)	0.09	0.63	13 (10)	7 (8)	25 (94)	5 (14)	5 (7)	1.7
B2Ω	22 (21)	0.09	0.59	11 (9)	6 (7)	26 (99)	5 (13)	7 (10)	1.8
B1Ω(k)	80 (94)	0.32	0.87	48 (54)	23 (24)	26 (64)	10 (25)	0.06 (0.29)	4.9
B1ΩOoL	27 (25)	0.11	0.65	16 (14)	7 (7)	23 (98)	4 (18)	0.04 (0.18)	1.3
$\mathrm{H1\Omega_{ref}}$	43 (55)	0.17	0.91	31 (36)	15 (19)	27 (70)	8 (19)	—	9.1
$\mathrm{H1\Omega_{\sigma=0.5}}$	181 (163)	0.72	0.83	96 (79)	34 (27)	20 (24)	9 (44)	—	14.4
$\mathrm{H1\Omega_{\sigma=1.0}}$	274 (188)	1.10	0.95	199 (135)	54 (44)	31 (37)	17 (68)	—	23.1
$\mathrm{H1\Omega_{\sigma=1.5}}$	303 (193)	1.21	1.00	233 (148)	59 (53)	34 (37)	21 (84)	—	24.9

scribed in (C.1). The viscosity ν is set proportional to the sound speed and the mean value is shown in table $\langle\nu\rangle = \nu_1\langle c_s\rangle$, where $\nu_1 = 0.004$. The values of $\langle c_s\rangle$ and $\langle\nu\rangle$ are shown in Columns 9 and 10.

The mesh Reynolds number, defined as $\mathrm{Re}_\Delta = \mathrm{u}\Delta/\nu$, is discussed. The characteristic value for each model $\langle\mathrm{Re}_\Delta\rangle = \Delta\langle\mathrm{u_{rms}/c_s}\rangle/\nu_1$ is listed in Column 11. The resolution is 4 pc for all models. The numerical resolution is considered sufficient provided the mesh Reynolds number does not exceed a particular value (typically between 1 and 10). The mean values $\langle\mathrm{Re}_\Delta\rangle$ are close to 1 in all models, although the values of Re_Δ can be much higher at certain locations. However, it is guaranteed in all models that $u\Delta/\nu < 5$ through the combination of the shock enhanced diffusion and the temperature dependent bulk diffusion.

The values of $\langle u_{\rm rms}\rangle$ listed in Column 12 are obtained from the perturbation velocity $\boldsymbol{u}$, from which only the galactic rotation $\boldsymbol{U}$ is subtracted. In Column 13, $\langle u'\rangle$ is calculated from the random velocity $\boldsymbol{u}'$, where the mean velocity $\langle\boldsymbol{u}\rangle_\ell$, as defined in (6.11) is subtracted from the perturbation velocity $\boldsymbol{u}$.

The averages of the thermal $e_{\rm th} = \rho e$, kinetic $e_{\rm kin} = \frac{1}{2}\rho u^2$ and magnetic energies $e_{\rm B} = \frac{1}{8\pi}B^2$ are listed in Columns 14, 15 and 16 respectively. These energies are normalised by the supernova energy $E_{\rm SN} = 10^{51}$ erg, with the kinetic energy calculated using the perturbation velocity. For B1ΩOoL and B1Ω(k), $e_{\rm B}$ is calculated from the magnetic field in the kinematic stage of the mean-field dynamo, whereas for B1Ω and B2Ω, $e_{\rm B}$ is calculated from the statistical steady state of the magnetic field.

The timespan Δt, normalised by $\tau = L_{\rm horiz}/\langle u'\rangle$, refers to how long each model has been in steady state, where $L_{\rm horiz} = L_x = L_y$ is the horizontal size of the domain and $\langle u'\rangle$ is the root-mean-square of the turbulent velocity. The models B1Ω and B2Ω have been in hydrodynamical steady state for much longer than the Δt listed, since the values in column 17 refer to the periods at which the magnetic field is also in statistical steady state.

Part III

Turbulent fields in the magnetised ISM

Chapter 5

Spatial and temporal correlation analysis

5.1 Study of Correlation Lengths

The interstellar medium of a spiral galaxy is a complex, multiphase, random system, driven by the input of thermal and kinetic energy from supernova explosions and stellar winds (e.g., Mac Low & Klessen, 2004; Elmegreen & Scalo, 2004; Scalo & Elmegreen, 2004; Mac Low et al., 2005; de Avillez & Breitschwerdt, 2005a; Federrath et al., 2010; Hill et al., 2012). Its statistical analysis, including that of interstellar turbulence, is complicated by the multi-phase structure, where the diversity of physical processes predominant in different phases causes strong inhomogeneity. Furthermore, interstellar turbulence is transonic or supersonic (Bykov & Toptygin, 1987; Vázquez-Semadeni, 2015). The compressibility of the ISM and the abundance of random shock waves lead to spatial and temporal intermittency of the random velocity and magnetic fields and of the density fluctuations. Dynamo action adds further complexity by producing intermittent random magnetic fields (Wilkin et al., 2007).

Observational studies of such an inhomogeneous, complex random system are severely limited by the fact that observable quantities are integrals along the line-of-sight, so that many physically significant statistical features become hidden. When observed at a low resolution, the interstellar medium can be satisfactorily described in terms of Gaussian random fields, but recent observations have revealed a plethora of density structures in neutral hydrogen, mostly planar or filamentary (Heiles & Troland, 2003; Makarenko et al., 2015; Wang et al., 2016, and references therein). Statistical analysis of such random fields cannot be restricted to the standard tools of the theory of Gaussian random functions (and related ones, such as log-normal and χ^2 functions), where the probability distribution and second-order correlation functions provide a complete description. However, correlation analysis remains an important first step, where the form of the correlation function, the correlation length (or time) and the mean-square variations of a variable are the most

important quantities explored.

There are numerous and diverse estimates of the integral (correlation) scale of interstellar turbulence l_0 (see also Haverkorn & Spangler, 2013). The autocorrelation function of the line-of-sight H_I cloud velocities obtained in the Milky Way by Kaplan (1966) leads to $l_0 \simeq 80\,\mathrm{pc}$. Lazaryan & Shutenkov (1990) found $l_0 \simeq 50\,\mathrm{pc}$ from the fluctuations in synchrotron intensity. Ohno & Shibata (1993) used differences in Faraday rotation between neighbouring pulsars to obtain $10 < l_0 < 100\,\mathrm{pc}$. Minter & Spangler (1996) yielded $l_0 \simeq 4\,\mathrm{pc}$ from the structure functions of the variations in the Faraday rotation and emission measures across extended extragalactic radio sources. Structure functions of the Faraday rotation of extragalactic sources (Haverkorn et al., 2004, 2006, 2008) and their degree of depolarization (Haverkorn et al., 2008) give $l_0 \simeq 1\,\mathrm{pc}$ in the Milky Way's spiral arms. $l_0 < 20\,\mathrm{pc}$ was found by an analysis of low-frequency synchrotron intensity fluctuations from a large region of the Galactic disk by Iacobelli et al. (2013). In the Large Magellanic Cloud, the structure function of the Faraday rotation of more distant sources gave $l_0 \simeq 90\,\mathrm{pc}$ (Gaensler et al., 2005). In the galaxy M51 Fletcher et al. (2011) obtained $l_0 \simeq 50\,\mathrm{pc}$ from the depolarization of diffuse emission, whilst Houde et al. (2013) found $l_0 \simeq 65\,\mathrm{pc}$ from the dispersion of radio polarization angles. These estimates are strikingly different, perhaps not surprisingly. They have been obtained from diverse tracers, and it is not surprising that the correlation length of the gas velocities, Faraday rotation measure and synchrotron fluctuations differ (the latter being non-linear functions of the fluctuating quantities). A relation between the correlation length of the product of random individual variables and those of the multipliers depends on their detailed statistical properties (e.g., §6.2 in Stepanov et al., 2014). The aim here is to clarify this relation. This would be difficult to do with observational data, at least at present.

Interpretations of observations of polarized synchrotron emission and its Faraday rotation suggest that a significant fraction of the polarization may be due to anisotropy of the random magnetic field. The correlation between the mean Faraday rotation and its standard deviation along the Galactic disc, found by Brown & Taylor (2001), was the earliest indication of an anisotropic random field. Subsequent models of various components of Milky Way emission along the Galactic disk (Jaffe et al., 2010, 2011, 2013) and across the entire sky (Jansson & Farrar, 2012b,a) required the inclusion of an anisotropic random magnetic field in order to fit the observations. In other galaxies, modeling of pre- and post-shock polarized emission in the barred galaxies NGC1097 and NGC1365 (Beck et al., 2005) and the spiral galaxy M51 (Fletcher et al., 2011), the dispersion of polarization angles in M51 (Houde et al., 2013), comparison of the observed polarized emission and Faraday rotation in M33 (Stepanov et al., 2014), and modelling depolarization in M51 (Shneider et al., 2014), have all indicated the presence of anisotropic random fields. Extracting the degree of anisotropy from the observations, though, is difficult.

In M51, Fletcher et al. (2011) estimate that the ratio of the standard deviations of the random magnetic field components in orthogonal directions is $\sigma_x/\sigma_y \simeq 2$ and Houde et al. (2013) obtained a ratio of correlation lengths along and perpendicular to the local mean-field direction of $l_\parallel/l_\perp \simeq$

1.8. As with observational estimates for l_0, it is appropriate to carefully examine the possible anisotropy of the random magnetic field.

Correlation lengths obtained from comprehensive numerical simulations of the multi-phase ISM exhibit less diversity than the observational results. Joung & Mac Low (2006) obtain a gas density spectrum with a peak at 20 pc, whereas most kinetic energy is contained at scales 20–40 pc. Gent et al. (2013b) calculate $l_0 = 100$ pc for the random velocity field in the mid-plane of the galaxy, also from hydrodynamic simulations. In the MHD simulations of de Avillez & Breitschwerdt (2007), $l_0 = 70$ pc for the random velocity field. This scale fluctuates strongly with time. From correlation analysis of the vertical component of random velocity, Korpi et al. (1999b) obtained an estimate of $l_0 = 30$ pc for the warm gas at all heights, whereas in the hot gas l_0 increases from 20 pc in the mid-plane to 60 pc at $|z| = 150$ pc.

Simulations of the SN-regulated ISM have become sufficiently realistic to treat them as numerical experiments. It is then natural to use the numerical models to address these questions before the more difficult observational exploration. In particular, the autocorrelation and cross-correlation functions of the random (i.e., small-scale; see §5.2) velocity and magnetic fields and density fluctuations, as well as the Faraday depth and synchrotron intensity can be made.

However complex, the simulations of the ISM can hardly be considered as trustworthy representations of the ISM in its whole complexity. Therefore, the goal of the analysis is not to achieve quantitative agreement with observations in every detail (although the general agreement is quite remarkable) but rather to identify those physical processes that shape the simulated ISM and are likely to be important in reality.

Turbulent flows are often represented in spectral space, using Fourier transforms of the physical variables. Such transforms are straightforward in infinite or periodic spaces. However, simulations of the ISM are performed in relatively small domains, only containing of order one thousand correlation cells, not simply-periodic because of the open (or similar) boundary conditions at the top and bottom of the domain, and statistically inhomogeneous because of the stratification (e.g. Korpi et al., 1999b,a; Gent et al., 2013b). Furthermore, it is difficult to estimate reliably the statistical uncertainty of the Fourier transforms.

This work employs correlation analysis (e.g., Monin & Yaglom, 2007a) and for the most part, local isotropy in the horizontal (xy) plane is assumed but this assumption is assessed in Section 5.5.

5.2 The structure and correlation functions

The calculations start with the second-order structure functions $D(l)$, which are more robust than the correlation functions, $C(l)$, with respect to errors (§13.1 in Monin & Yaglom, 2007a):

$$D(l) = \langle [f(\boldsymbol{x}+\boldsymbol{l}) - f(\boldsymbol{x})]^2 \rangle_{xy}, \tag{5.1}$$

where $\boldsymbol{x}$ a given position in the (x,y)-plane, $\boldsymbol{l}$ a horizontal offset with $l = |\boldsymbol{l}|$ and $\langle\rangle_{xy}$ denotes a horizontal average. Analysis is restricted to horizontal planes with no offsets in the z-direction, because of the stratification in z.

Since periodic (or sheared periodic) functions in x and y are analysed, the maximum offsets considered in the x and y directions are half the domain sizes in each direction. Hence, we consider offsets in the range $0 \leq l_x \leq L_x/2$, $0 \leq l_y \leq L_y/2$. Using $D(l)$, the autocorrelation function $C(l)$ is obtained as

$$C(l) = 1 - \frac{D(l)}{2\sigma^2}, \tag{5.2}$$

where $2\sigma^2$ is the value of $D(l)$ at which the random function $f(\boldsymbol{x})$ is no longer correlated, and σ is the dispersion (r.m.s. value) of $f(\boldsymbol{x})$. The choice of $2\sigma^2$ in a finite domain is not always obvious (see below). In terms of $C(l)$, the correlation length l_0 is defined as

$$l_0 = \int_0^\infty C(l)\,\mathrm{d}l. \tag{5.3}$$

The magnitude of the implied correlation length is very sensitive to the range of integration and to the behaviour of the correlation function at large l. An exponentially small tail in $C(l)$ can make a significant contribution to l_0, when integrated over a large domain.

To address this problem, the structure functions are fitted with one of the following analytic forms (as discussed below), thereby obtaining estimates of σ^2 and L_0 (and hence l_0):

$$D(l) = 2\sigma^2\left[1 - \exp\left(-\frac{l}{L_0}\right)\right], \qquad l_0 = L_0, \tag{5.4}$$

$$D(l) = 2\sigma^2\left[1 - \exp\left(-\frac{l^2}{2L_0^2}\right)\right], \qquad l_0 = \sqrt{\frac{\pi}{2}}L_0. \tag{5.5}$$

Since the governing equations contain second-order derivatives in spatial coordinates, the spatial variations must be smooth random functions of position, so that $\mathrm{d}C/\mathrm{d}l = 0$ at $l = 0$ for spatial correlations. However, the fact that only the first time derivatives appear in the governing equations implies that the time variations only needs to be continuous, so that $\mathrm{d}C/\mathrm{d}\tau \neq 0$ for $\tau = 0$ may be expected for time correlations (as considered in §5.4), with τ the time lag.

This difference is observed in the computed structure and correlation functions, and so we use equation (5.4) for time correlations and equation (5.5) for spatial correlations. Some of the spatial autocorrelation functions discussed below (most notably those for the density fluctuations) exhibit an oscillatory behaviour at larger offsets; in such cases, equation (5.5) is augmented to

$$D(l) = 2\sigma^2\left[1 - \exp\left(-\frac{l^2}{2L_0^2}\right)\cos(kl)\right], \tag{5.6}$$

with $k = al + b$, where a and b are two additional parameters determined by the zeros in the correlation function.

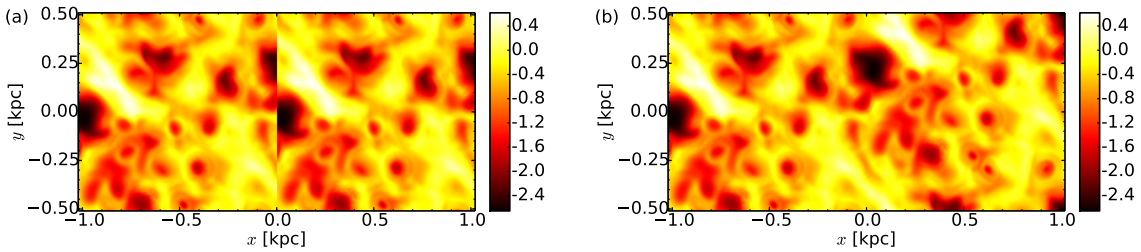

Figure 5.1: Aligned domains of logarithm of gas number density ($\log n$), at $z = 2\,\mathrm{pc}$, $t = 1.55\,\mathrm{Gyr}$; **(a)** before and **(b)** after shifting the right-hand domain by δy to account for the shearing boundary. The boundary between the two copies of the computational domain is here located at $x = 0$.

The correlation lengths l_0 are presented in Tables 5.1 and 5.3. To confirm the importance of using fitted correlation functions, the correlation lengths $\tilde{l}_0$ obtained by integration of the directly calculated $C(l)$, over the range $0 \leq l \leq 500\,\mathrm{pc}$, are also presented in this table. The values differ by up to a factor of 2, with the differences being greatest for density fluctuations (where the form in equation (5.6) was used); the agreement for random magnetic field and velocity (where the form in equation (5.5) was used) is closer.

The data used in this analysis is 12 snapshots from the simulation B1Ω in the range $1.4 \leq t \leq 1.675\,\mathrm{Gyr}$. The results from these snapshots are reported in Sections 5.3, 5.5, 5.6. The analysis is also performed on 12 snapshots in the same timespan from B2Ω to test for the effects of the rotation rate on the correlation statistics. Any differences between the two runs are reported in Section 5.7.

To investigate if the correlation statistics are independent from the horizontal extent, comparisons between the results from 21 snapshots in B1Ω in the range $0.4 \leq t \leq 0.61$, and 12 snapshots in the range $0.336 \leq t \leq 0.6\,\mathrm{Gyr}$ from B1ΩOoL. The differences between these two runs are also discussed in Section 5.7. The mean-field dynamo in both runs is in the kinematic stage within the time ranges discussed.

To improve the reliability of the statistics, the averaging involved in the calculation of the structure functions is performed within layers at $|z| \leq 50\,\mathrm{pc}$ and $350 \leq |z| \leq 450\,\mathrm{pc}$ over 26 grid planes for each snapshot, and then the structure functions are further averaged over the snapshots. The uncertainty of the resulting values of the structure functions is rather small (of order 10^{-3} in terms of the relative error) because of the large number of data-point pairs available even at large values of l. The structure and correlation functions in the figures below are shown with error bars representing *not* their uncertainty but the standard deviation of the individual measurements around the mean.

5.2.1 Accounting for shearing boundaries

When calculating the increments in the structure function, pairs of points separated by the periodic boundaries in x and y are used. In order to conveniently include pairs of points located on different

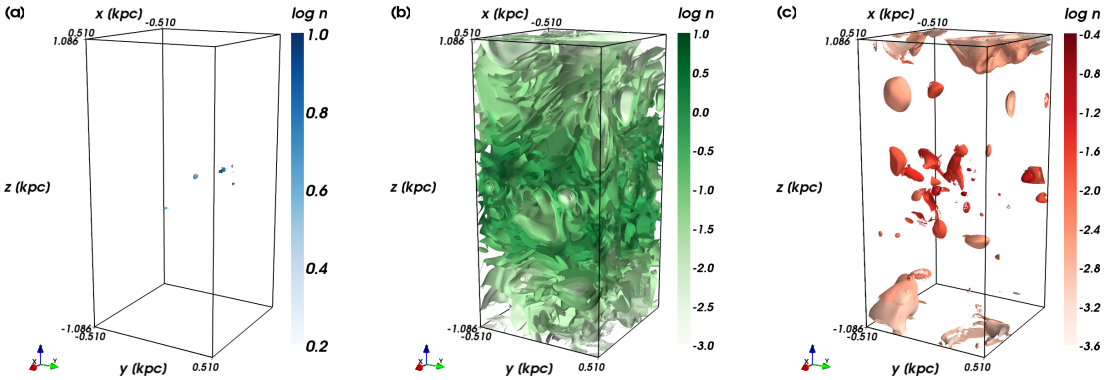

Figure 5.2: Plots of $\log n$ in the **(a)** cold, **(b)** warm and **(c)** hot phases from the model B1Ω. The data is from the snapshot at $t = 1.425\,\mathrm{Gyr}$.

sides of the periodic boundary in x, the computational domain is extended in the x-direction by its copy and shift it by $\delta y(t)$ to remove the discontinuity between the two domains, as shown in Figure 5.1.

5.2.2 Calculations within phases

Both B1Ω and B2Ω exhibit three distinct states of the gas corresponding to local maxima in the probability distribution function (PDF) of the specific entropy s. Gas parameters in those states are similar to the three main phases of the ISM. Following Gent et al. (2013b), the cold phase is defined as that having $s \leq 3.7 \times 10^8\,\mathrm{erg\,K^{-1}}$, the hot phase has $s \geq 23.2 \times 10^8\,\mathrm{erg\,K^{-1}}$, with the warm phase in between. The three phases have very different physical properties, including the random velocity and magnetic fields, as well as differing in their mean temperature and density. Therefore, our analysis is carried out for each phase separately. For this purpose, only grid points corresponding to a given phase are retained in the data cubes containing each physical variable, with the other points masked out. This allows us to do the averaging required in the computation of the structure functions over disjoint regions in the physical space.

The analysis focusses on the warm phase initially, with the results from this phase demonstrated in Sections 5.3.1, 5.3.2 and 5.3.3, since the warm phase occupies the majority of the simulation domain (80%–90% of the simulation volume). In contrast to the warm phase, the cold and hot phases exist as isolated regions within the heights considered in the analysis presented in this chapter ($|z| \leq 400\,\mathrm{pc}$). Hence, the the results for the cold and hot phases, discussed briefly in Section 5.3.4, are limited by only being able to obtain reliable statistics within small regions, as confirmed in Figures 5.6 and 5.7. A separate analysis for each ISM phase, even if feasible with simulated data with a higher resolution than the data used here, may not be possible in observations. Therefore, the statistical properties of the simulated ISM without separation by phase are

Table 5.1: The root-mean-square (rms) values of the fluctuations, their magnitude relative to the mean and correlation lengths of the fluctuations in gas density, speed and magnetic field for the warm gas at the midplane $z = 0$ and at $|z| = 400\,\mathrm{pc}$. The mean field is obtained using Gaussian smoothing (see Section 6.2.1), using a smoothing length of $\ell = 50\,\mathrm{pc}$. Two values of the correlation lengths are provided, l_0 obtained from a fitted form of the structure function as described in §5.2, and $\tilde{l}_0$ derived by integrating the calculated correlation function within the available range, $0 \leq l \leq 500\,\mathrm{pc}$; the difference demonstrates how important is the fitting to obtain a reliable estimate of l_0.

	n' [cm^{-3}]		u' [kms^{-1}]		b [μG]	
$\lvert z\rvert$ [pc]	0	400	0	400	0	400
rms	0.306 ± 0.001	0.0604 ± 0.0001	8.10 ± 0.03	2.84 ± 0.01	0.587 ± 0.002	0.483 ± 0.001
rms relative	0.49 ± 0.03	0.49 ± 0.03	1.0 ± 0.1	0.49 ± 0.11	0.58 ± 0.04	0.39 ± 0.05
l_0 [pc]	53 ± 5	37 ± 2	60 ± 3	87 ± 3	44 ± 2	64 ± 2
$\tilde{l}_0$ [pc]	24 ± 1	27 ± 2	50 ± 1	81 ± 1	41 ± 1	55 ± 1

also discussed in Section 5.3.4. The results are shown in Table 5.3.

5.3 Spatial correlations

As described above, the spatial structure and correlation functions for the random magnetic and velocity fields and the fluctuations in the gas number density separately for the warm and hot gas are calculated. The correlation functions are then used to estimate the correlation lengths of these variables. Spatial correlations of the Faraday depth and synchrotron emissivity are discussed in §5.6.

The results are shown in Table 5.1 and Figure 5.3 for the density fluctuations, Figure 5.4 for the random speed and the magnitude of the random magnetic field. The structure functions used to obtain the autocorrelation functions are only shown in Figure 5.3a: those for the other variables have a similar form. The magnitudes of the fluctuations in the variables and their correlations lengths are discussed in the next two sections.

The uncertainties of the root-mean-square (rms) values of various variables and the correlations lengths given in Tables 5.1, 5.3, 5.5, 5.6 and 5.7, have been obtained as 95% confidence intervals from weighted least-squares fitting of equation (5.5), or for the gas density equation (5.6). The weights used are the uncertainties of the values of the correlation function rather than the standard deviations shown in the figures. Similarly, 95% confidence intervals for the uncertainties of the Taylor microscale and correlation time are obtained from least-squares fitting of equations (5.7) and (5.5), to the spatial correlation function of u' from small values of l and the temporal correlation function of u' respectively.

The uncertainties in the rms values and correlation lengths thus obtained are underestimates of the true uncertainty as they do not take into account any systematic errors, such as those arising from the uncertain value of the computed structure functions at $l \to \infty$.

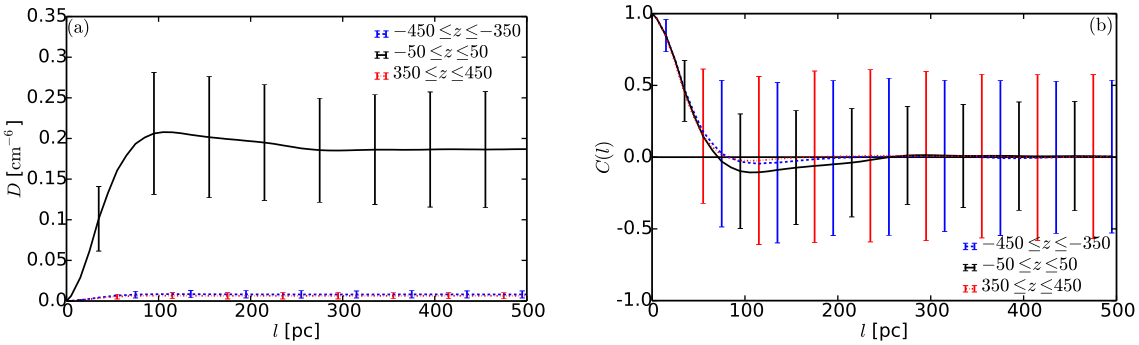

Figure 5.3: **(a)** The structure function $D(l)$ and **(b)** correlation functions $C(l)$ for density fluctuations in the warm gas, averaged about $z = -400\,\mathrm{pc}$ (blue, dashed), $z = 0\,\mathrm{pc}$ (black, solid), and $z = 400\,\mathrm{pc}$ (red, dash-dotted). The error bars denote the standard deviation of the individual measurements around their mean values, rather than the error of the mean value, as discussed in §5.2. For clarity, the error bars are only shown for every sixth bin in l, and staggered between the different curves.

5.3.1 Magnitude of the fluctuations

The rms magnitudes of the fluctuations in the warm gas are shown in Table 5.1, together with the rms values of the relative fluctuations, $\langle (f'/\langle f\rangle_\ell)^2\rangle^{1/2}$ for a variable f. The mean field $\langle f\rangle_\ell$ is obtained from Gaussian smoothing with a smoothing length $\ell = 50\,\mathrm{pc}$ (see Section 6.2.1 for further details); it should be stressed that the mean $\langle f\rangle_\ell$ is a function of position. In the case of velocity fluctuations, the average velocity, $\langle \boldsymbol{u}\rangle_\ell = 0$, refers to the sheared frame, that is, includes the systematic outflow velocity, but not the overall rotation or the shear due to the galactic differential rotation.

In the warm phase, the standard deviation of the density fluctuations decreases with $|z|$ together with the average density. The relative magnitude of the fluctuations also decreases, but more slowly.

As shown in Fig. 5.3, density fluctuations in the warm gas are weakly anti-correlated in the range of scales $80 \le l \le 250\,\mathrm{pc}$ at each height, with the modulus of negativity for $C(l)$ significantly exceeding its uncertainty (about 0.002). Therefore, the rms value and correlation length of the density fluctuations has been obtained by fitting the form in equation (5.6) to the structure function. The parameters used in the cosine function were $k(l) = 0.07l + 0.28$ at $z = 0\,\mathrm{kpc}$ and $k(l) = 0.075l + 0.4$ at $|z| = 0.4\,\mathrm{kpc}$.

A possible cause of such anti-correlation may be random shock waves propagating through the ISM. Then the density fluctuations can be expected to be correlated within distances comparable to the shock thickness (about $5\Delta x = 20\,\mathrm{pc}$ in the simulations), whereas the anti-correlation arises from the systematic rarefaction associated with a shock front. Another effect that may contribute to such anti-correlation is the presence of quasi-spherical supernova remnants (as are clearly visible in Figure 5.1), with gas density systematically lower than average within and around the bubbles and higher than average in their shells.

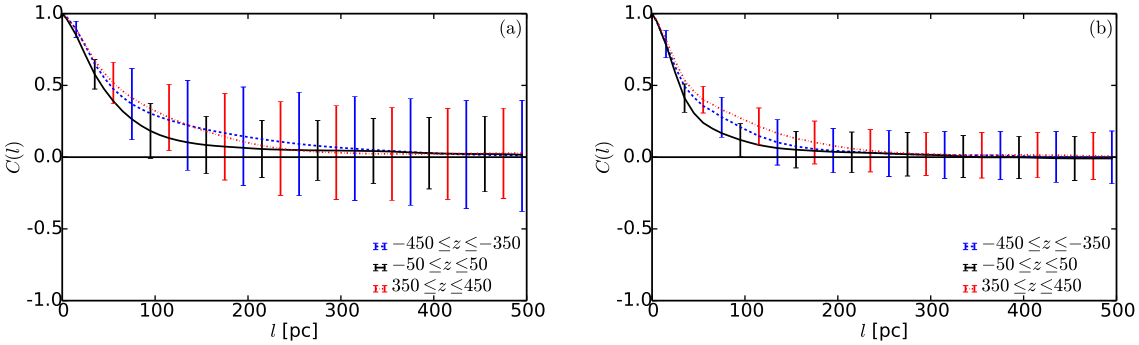

Figure 5.4: As in Fig. 5.3, but for **(a)** the random speed in the warm gas and **(b)** the modulus of the random magnetic field in the warm gas.

The rms random speed decreases with $|z|$ between $z = 0$ and $|z| = 400\,\mathrm{pc}$, as shown in Tables 5.1 and 5.3. This is understandable since the Type II supernovae, that drive most of the random flow, have a scale height of only 90 pc. At larger heights, the rms u' is $5 \pm 1\,\mathrm{km\,s^{-1}}$ in the warm phase and $11 \pm 7\,\mathrm{km\,s^{-1}}$ in the hot gas at $|z| = 0.8\,\mathrm{kpc}$.

The magnitude of σ_b in the simulations is below the typical value of $b \simeq 5\,\mu\mathrm{G}$ observed near the Sun or in external galaxies (Beck, 2016, and references therein). There could be several reasons for this, including the relatively low magnetic Reynolds numbers in the simulations reducing fluctuation dynamo efficiency, or an underestimated averaging scale ℓ. However, it is evident from Figure 6 of Gent et al. (2013a), that its underestimation would not entirely explain this discrepancy. Applying horizontal averaging, which is analogous to extending ℓ to 1 kpc, yields an increase of only 50% in the saturated magnetic energy of the fluctuation field.

5.3.2 Correlation scales

The correlation length of the density fluctuations in the warm gas shown in Table 5.1 decreases with z in the range $|z| \leq 400\,\mathrm{pc}$, in contrast to the correlation lengths of the velocity and magnetic fields.

In the simulations used here, shock-capturing diffusivities smooth shock fronts over five mesh points, i.e., 20 pc. This shock-capturing smoothing may affect the correlation lengths obtained, even though they are normally significantly larger than 20 pc. It may particularly affect the correlation length for the density fluctuations at $|z| = 400\,\mathrm{pc}$, which is only 37 pc.

The correlation length of the random velocity at the same height is significantly larger. The corresponding correlation length of the random magnetic field is intermediate between the two.

From the double rotation rate simulation, the results obtained for the correlation lengths and rms values are very similar to those in Table 5.1.

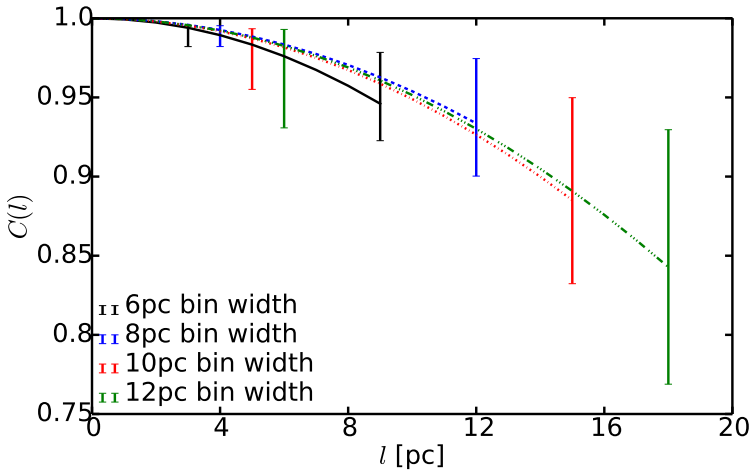

Figure 5.5: Parabolic fits to the autocorrelation function for random speed u', averaged about the mid-plane; for bin widths 6 pc (black, solid), 8 pc (blue, dashed), 10 pc (red, dash-dotted), and 12 pc (green, dash-triple-dotted). The autocorrelation function for each bin width is point plotted, with only the error bars shown.

Table 5.2: Estimates of the Taylor micro-scale obtained from fitting equation (5.7) to the autocorrelation function of the random speed at $z = 0$, for decreasing bin widths in l.

Bin width [pc]	12	10	8	6
λ [pc]	46 ± 10	45 ± 10	48 ± 8	40 ± 11

5.3.3 Taylor micro-scale and the effective Reynolds number

The Taylor micro-scale, λ, characterizes the behaviour of the correlation function at small scales, $l \to 0$, and can be obtained by fitting the correlation function near the origin to the form

$$C(l) \simeq 1 - (l/\lambda)^2 , \tag{5.7}$$

(§6.4 in Tennekes & Lumley, 1972). The associated equality $\mathrm{d}C/\mathrm{d}l = 0$ at $l = 0$ holds for the correlation functions of smooth (differentiable) random fields (Monin & Yaglom, 2007a). In numerical simulations, where the solutions at the smallest scales are controlled by the finite numerical resolution Δx, one expects $\Delta x < \lambda < l_0$ (Davidson, 2004). The Taylor micro-scale of the random speed can be used to estimate the effective Reynolds number, Re, in the simulations (e.g., §3.2 in Tennekes & Lumley, 1972),

$$\lambda \simeq 3 l_0 \mathrm{Re}^{-1/2}. \tag{5.8}$$

Such an estimate includes all dissipation effects in an averaged manner, which can be difficult to estimate otherwise because of the extreme inhomogeneity of the simulated ISM and numerical transport coefficients. Thus obtained, the Reynolds number is based on the correlation scale of the random flow; the corresponding value based on the domain size (1 kpc), often quoted in the literature, is about 400.

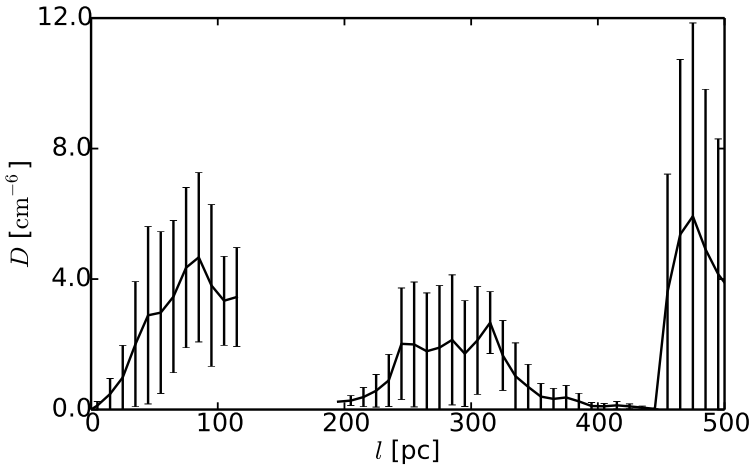

Figure 5.6: Structure function for density fluctuations in the cold phase for $|z| \leq 50$ pc (the cold gas is practically absent at larger values of $|z|$).

We fit equation (5.7) to the correlation function $C(l)$ of the random gas speed at the three smallest values of l, including $C(l) = 1$ at $l = 0$, for bin width in l of 6, 8, 10, and 12 pc. Figure 5.5 shows the correlation functions obtained at $|z| \leq 50$ pc and the fits.

The resulting estimates of λ, shown in Table 5.2, satisfy the inequalities $\Delta x < \lambda < l_0$, providing us some confidence in the estimates of the correlation lengths discussed above. For $l_0 = 60$ pc (Table 5.1) and $\lambda = 40$ pc, an estimate of the effective Reynolds number in the simulations of order 20 is obtained.

The relatively low value of the effective Reynolds number is likely to be a consequence of the shock capturing numerical scheme used in the simulations, where shock fronts are diffused over several grid points to be fully resolved. The maximum Reynolds number achievable with the numerical resolution Δx is of order $\mathrm{Re}_{\mathrm{max}} \simeq (l_0/\Delta x)^{4/3}$ (assuming a power-law turbulent spectrum with a slope of $5/3$).

With $l_0 = 50$ pc, this yields $\mathrm{Re}_{\mathrm{max}} \simeq 30$, so the effective value of Re measured directly is not much smaller than the nominal value, and is typical of the existing ISM simulations with comparable physical content at a numerical resolution of about 1 pc.

It should be noted that the value of the effective Reynolds number is likely to be much lower than local values in diffuse gas because it includes strong numerical dissipation in shocks. The correlation scale of the random flow is controlled by the energy injection mechanism rather than the Reynolds number, so the modest value of the Reynolds number that this work shares with other comparable simulations does not affect the conclusions.

5.3.4 Overall statistics and the cold and hot phases

The results presented in Sections 5.3.1, 5.3.2 and 5.3.3 are for the warm gas. The data for the cold gas at offsets beyond $l \simeq 10$–100 pc, the typical scale of the cold gas clouds, are scarce because the

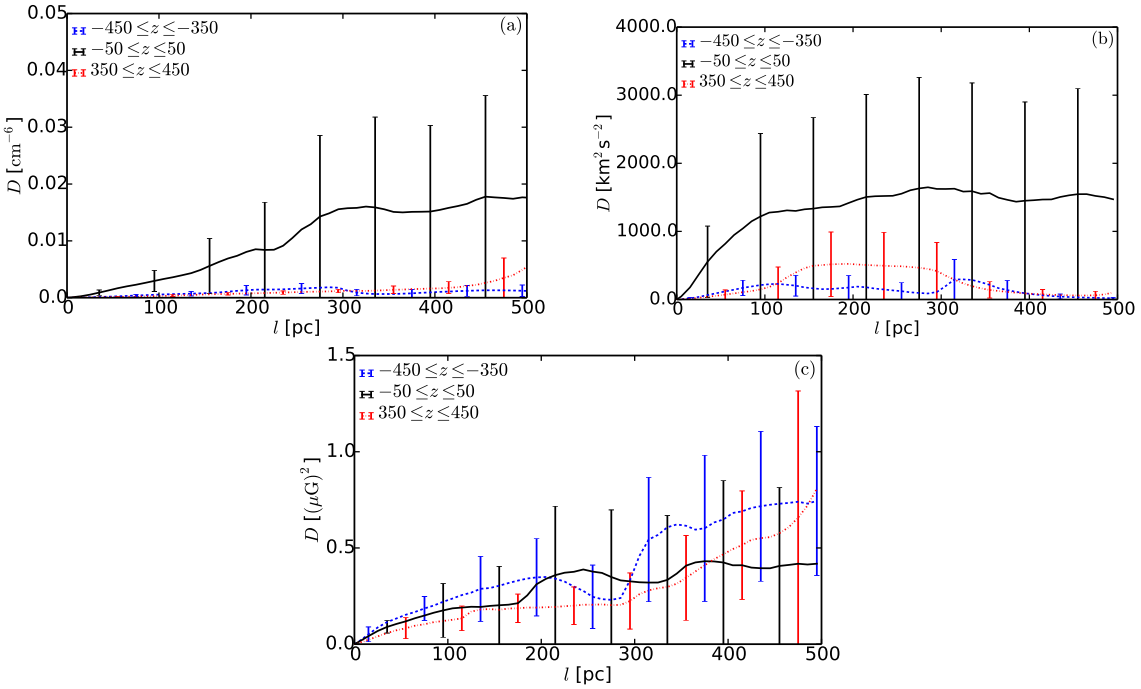

Figure 5.7: Structure functions for **(a)** density fluctuations, **(b)** random speed and **(c)** random magnetic field strength in the hot gas, averaged about $z = -400\,\mathrm{pc}$ (blue, dashed), $z = 0\,\mathrm{pc}$ (black, solid), and $z = 400\,\mathrm{pc}$ (red, dash-dotted).

cold gas occupies a small fraction of the volume. Furthermore, the numerical resolution of 4 pc in our simulations restricts the quality of the modelling of the cold phase, localized in regions of order 10 pc in size.

Figure 5.6 shows the cold phase results for the mid-plane only, since the cold gas is concentrated there, and results outside this region cannot be statistically meaningful (see Gent, 2012; Gent et al., 2013b). The structure functions for the hot phase fluctuate wildly and have large error bars (see Figure 5.7). This happens because the hot phase is extremely varied within the relatively small computational box.

As shown in Figure 5.8, the structure and correlation functions of magnetic fluctuations, b, for the whole ISM are almost identical to those in the warm phase. This is also true of the gas density fluctuations n'. This similarity is reflected in the values of l_b, $l_{n'}$, σ_b, and $\sigma_{n'}$ in Tables 5.1 and 5.3. This is, of course, largely due to the large fractional volume of the warm phase. It is worth noting, however, that the density and magnetic field strength in the hot phase are both lower than in the warm phase.

However, the values of $\sigma_{u'}$ and $l_{u'}$ for the whole ISM are significantly higher than in the warm phase. The larger values of $\sigma_{u'}$ for the whole ISM can be attributed to the contribution of the hot gas that has higher speed of sound and, correspondingly, higher random velocities.

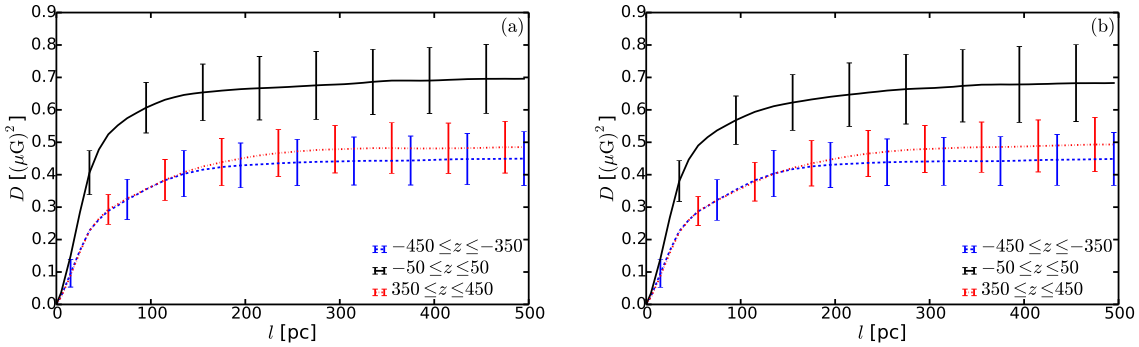

Figure 5.8: Structure functions for random magnetic field strength in: **(a)** the warm phase and **(b)** the whole ISM.

Table 5.3: The root-mean-square (rms) values of the fluctuations, the relative rms values and correlation lengths of the fluctuations in gas density, speed, and magnetic field, where no phase separation has been applied, at the mid-plane $z = 0$ and at $|z| = 400\,\mathrm{pc}$.

	n' [cm^{-3}]		u' [kms^{-1}]		b [μG]	
$\lvert z\rvert$ [pc]	0	400	0	400	0	400
rms	0.305 ± 0.001	0.0604 ± 0.0001	12.89 ± 0.03	3.65 ± 0.01	0.582 ± 0.001	0.484 ± 0.001
rms relative	0.63 ± 0.09	0.33 ± 0.03	1.0 ± 0.1	0.49 ± 0.11	0.59 ± 0.1	0.39 ± 0.05
l_0 [pc]	44 ± 2	37 ± 2	74 ± 2	117 ± 3	51 ± 1	66 ± 1
$\tilde{l}_0$ [pc]	29 ± 1	27 ± 2	63 ± 1	112 ± 2	44 ± 1	58 ± 1

5.4 Correlation time

Unlike the correlation lengths of various observable quantities in the ISM, their correlation *times* cannot be obtained from observations. Because of this, the eddy turnover time $\tau = l_0/u_0$ is universally applied to interstellar turbulence. However, the dynamics of interstellar turbulence involves a range of physical processes having distinct time scales, which may make the eddy turnover time inappropriate as an estimate of the correlation time. Non-linear Alfvén wave interactions, shock-wave turbulence and fluctuation dynamo action, among other phenomena, are likely to affect the correlation time and make it different for different variables.

Similarly to correlation lengths, the correlation times can be different in the warm and hot phases. However, this difference is harder to capture since each parcel of warm or hot gas moves around. Therefore, only correlation times averaged over the ISM phases can be obtained.

Arguably the most important of the time correlations, that of the random velocity, is considered here. For this purpose, the time series of the magnitude of the random velocity is used, measured at an array of fixed points in 32 planes in z, separated by 64 pc; within each plane, there are 64 positions separated by 100 pc in x or y.

From this data, the temporal structure function, and then the autocorrelation function $C(\tau)$ are

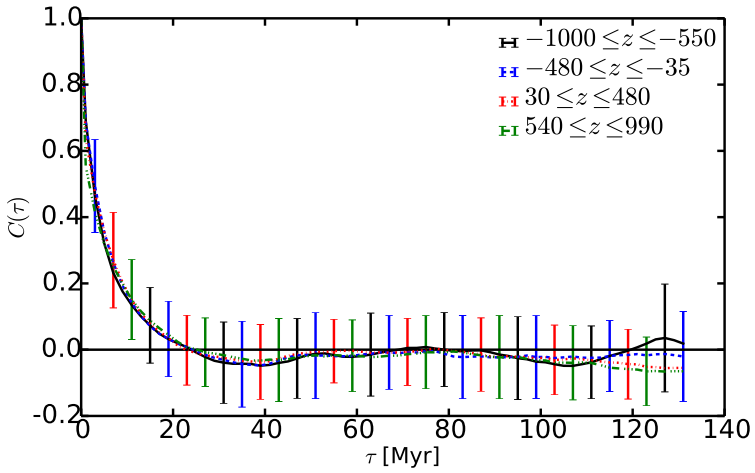

Figure 5.9: Time autocorrelation functions, $C(\tau)$, for the random speed, for $-1000 \leq z \leq -550\,\mathrm{pc}$ (black, solid), $-480 \leq z \leq -35\,\mathrm{pc}$ (blue, dashed), $30 \leq z \leq 480\,\mathrm{pc}$ (red, dash-dotted), and $540 \leq z \leq 990\,\mathrm{pc}$ (green, dash-triple-dotted). The error bars denote the standard deviation of the individual contributions to the correlation function around the mean value. For clarity, only every fourth error bar is shown at each curve.

calculated, from which the correlation time is obtained τ_0,

$$\tau_0 = \int_0^\infty C(\tau)\,\mathrm{d}\tau\,. \tag{5.9}$$

The form in equation (5.4) is fitted to $C(\tau)$ to estimate τ_0. The results shown below are from the model B1Ω.

The autocorrelation functions are shown in Figure 5.9 for four distances from the mid-plane, and the correlation times can be found in Table 5.4: $\tau_0 \approx 5\,\mathrm{Myr}$ with little variation with $|z|$. Since the fractional volumes of the warm and hot gas vary significantly with $|z|$, this suggests that both phases have similar correlation times.

With the velocity correlation length and speed in the warm gas at $z = 0$ of 60 pc and $8\,\mathrm{km\,s^{-1}}$, respectively (from Table 5.1) the kinematic time scale ('eddy turnover time') is of order $\tau_\mathrm{eddy} = l_{u'}/\sigma_{u'} \simeq 8\,\mathrm{Myr}$. At $|z| = 400\,\mathrm{pc}$, $\tau_\mathrm{eddy} \simeq 30\,\mathrm{Myr}$ in the warm gas.

According to the model of interstellar shock-wave turbulence of Bykov & Toptygin (1987), the separation of primary shock fronts driven by supernova explosions depends on their Mach number M as

$$L_\mathrm{shock} \simeq 4M^{4.5}\,\mathrm{pc}\,, \tag{5.10}$$

where the Galactic supernova rate of $0.02\,\mathrm{yr^{-1}}$ has been adopted. The primary shocks dominate over weaker secondary shocks for $M \gtrsim 1.2$, which leads to $L_\mathrm{shock} \simeq 10\,\mathrm{pc}$. The corresponding time between crossings of a given position by shock fronts, which is expected to destroy time correlations, then follows as $\tau_\mathrm{shock} = L_\mathrm{shock}/c \simeq 0.7\,\mathrm{Myr}$, where $c = 14\,\mathrm{km\,s^{-1}}$ is the magnetosonic speed in the warm gas (assuming equality of the sound and Alfvén speeds).

Table 5.4: The correlation time of the random speed at various heights in the simulation domain.

z [pc]	τ_0 [Myr]
$-1.000 \le z \le -0.550$	4.6 ± 0.6
$-0.480 \le z \le -0.035$	4.9 ± 0.5
$0.030 \le z \le 0.480$	4.9 ± 0.7
$0.540 \le z \le 0.990$	4.6 ± 1.0

Since the estimate of τ_0 does not distinguish between the hot and warm phases, it depends on both the kinematic and shock-crossing time scales in each phase (and also the Alfvén time scale, but this is close to the kinematic time scale since the magnetic and kinetic energy densities are comparable). All these time scales are of the same order of magnitude, so more careful estimates of the correlation time are required to clarify the physical nature of the time correlations in the simulated ISM.

It is plausible that the correlation time reflects both time scales and $\tau_0^{-1} \simeq \varepsilon \tau_{\rm eddy}^{-1} + (1-\varepsilon)\tau_{\rm shock}^{-1}$ with a certain constant ε. With $\tau_0 = 5\,$Myr, $\tau_{\rm eddy} = 7\,$Myr and $\tau_{\rm shock} = 1\,$Myr, $\varepsilon \simeq 0.9$, so the shock waves contribute about 10% to the random flow in this sense.

The time autocorrelation function of Fig. 5.9 appears to vary around the zero level at a time scale of about 70 Myr. Although the accuracy of the autocorrelation values is higher than suggested by the scatter of the data points around the mean values shown by the error bars, the statistical significance of these variations is unclear. Physical interpretation of the time correlation function is also hampered by the fact that there are not separate time series for the variables in the warm and hot phases separately.

We note the apparent time scale of the variations is close to the period $(2\pi\lambda/g_z)^{1/2}$ of gravity waves of wavelength $\lambda = 1\,$kpc in the Galactic gravity field, $g_z \simeq 4 \times 10^{-9}\,{\rm cm\,s^{-2}}$. Oscillatory large-scale horizontal vortical flows have been found by Käpylä et al. (2017) in similar simulations without a magnetic field. For the parameters relevant to the current study, the period of these oscillations is about 50 Myr. Extending this analysis over a range of rotation rates, SN rates and forms of the gravitational potential may clarify the significance of the pattern in the temporal correlation function apparent in Fig. 5.9.

5.5 Anisotropic Magnetic Fields

In the analysis above, any anisotropy of the random magnetic field in the horizontal planes has been neglected. This is justifiable since, at the scales of interest (from a few parsecs to about 100 pc), the expected anisotropy is only moderate (see below). However, the anisotropy of magnetic fields is of high physical significance as it reflects the dynamics of MHD turbulence with and without a global mean magnetic field (Goldreich & Sridhar (1997); Brandenburg & Lazarian (2013) and

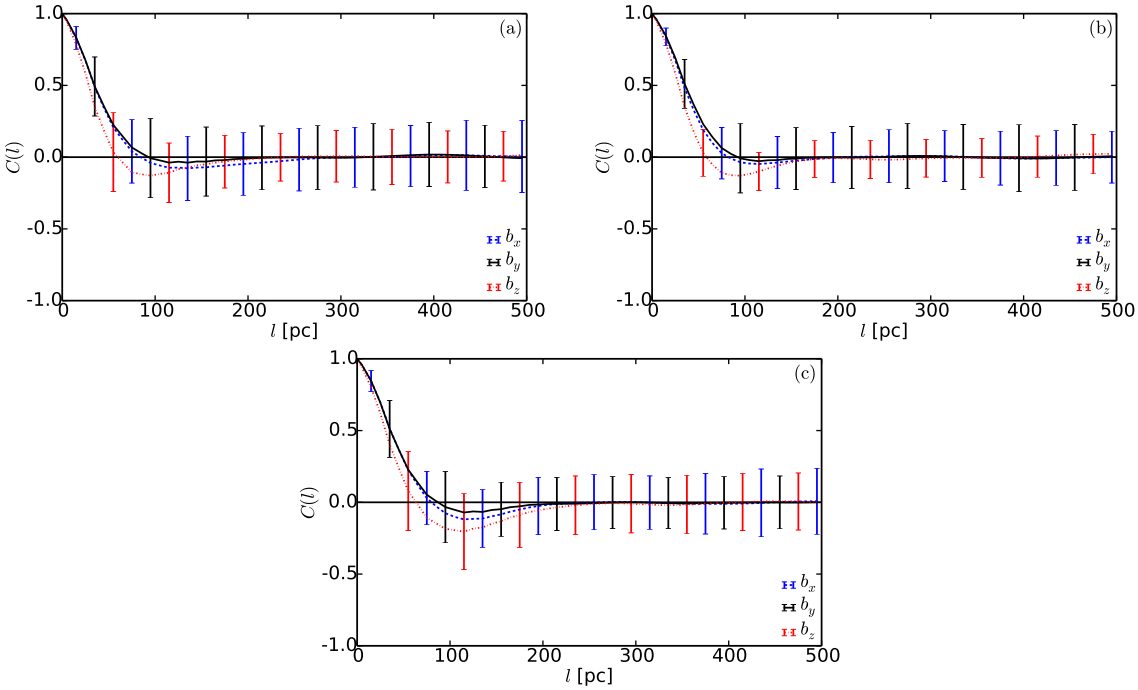

Figure 5.10: Autocorrelation functions, $C(l)$ for the magnetic field components, averaged at heights; **(a)** $z = -400\,\mathrm{pc}$, **(b)** $z = 0\,\mathrm{pc}$ and **(c)** $z = 400\,\mathrm{pc}$.

references therein; see also Cho & Vishniac (2000); Cho & Lazarian (2002a, 2003b); Mallet et al. (2016) and Oughton et al. (2016)). It also reflects the effects of galactic differential rotation and compression of the random magnetic field in shocks. The anisotropy of interstellar magnetic fields can contribute significantly to the polarized radio emission of galaxies (e.g., Sokoloff et al., 1998; Beck, 2016). In this section, using the structure and autocorrelation functions, individual components of the random magnetic field, $\boldsymbol{b} = (b_x, b_y, b_z)$ are discussed, with their rms values denoted as b_{0x}, b_{0y} and b_{0z}.

As shown in Table 5.5, the three components of $\boldsymbol{b}$ are somewhat different in magnitude. The vertical, z-components is the largest at all heights, whereas the radial (x) random field is the weakest.

All three components of magnetic field have negative autocorrelation near $l = 100\,\mathrm{pc}$, stronger for b_z than for b_x and b_y, as shown in Figure 5.10. This appears to be a consequence of the solenoidality of magnetic field: since magnetic lines must be closed, magnetic field must, on average, change its direction at a length scale comparable to its correlation length.

An enhanced azimuthal (y) component is a result of the large-scale velocity shear due to differential rotation that produces b_y from the radial field b_x, so that $\partial b_y/\partial t \simeq q\Omega b_x$ and then (e.g., Stepanov et al., 2014)

$$b_{0y} \simeq (1 + q\Omega\tau_0) b_{0x}. \tag{5.11}$$

For $q = +1$, $\Omega = 25\,\mathrm{km\,s^{-1}\,kpc^{-1}}$ and $\tau_0 = 5\,\mathrm{Myr}$, this yields $b_{0y}/b_{0x} \simeq 1.2$–1.3, in agreement

Table 5.5: The rms values for each component of the random magnetic field, denoted b_{0i} for $i \in (x,y,z)$, and their correlation lengths. The correlation lengths l_0, using Eq. (5.6), and $\tilde{l}_0$ are calculated as in Table 5.1.

	b_{0i} [nG]		l_0 [pc]		$\tilde{l}_0$ [pc]	
$\lvert z\rvert$ [pc]	0	400	0	400	0	400
b_x	549 ± 1	454 ± 1	44 ± 2	61 ± 4	33 ± 1	32 ± 1
b_y	693 ± 1	538 ± 1	42 ± 3	55 ± 4	36 ± 1	36 ± 1
b_z	735 ± 2	717 ± 4	55 ± 3	75 ± 4	16 ± 1	14 ± 1

with the estimates of Table 5.5 at $z = 0$.

The vertical component of the magnetic field is similarly enhanced due to the stretching of the horizontal magnetic field by vertical velocity u_z that varies at a scale l_0 and yet has a mean part $\overline{u}_z \simeq 2\,\mathrm{km\,s^{-1}}$ at $|z| \lesssim 200\,\mathrm{pc}$: $\partial b_z/\partial t \simeq b_x \partial u_z/\partial x + b_y \partial u_z/\partial y$. Unlike the stretching of the radial magnetic field by the large-scale velocity shear, this is a random process, so the rms vertical magnetic field grows as $t^{1/2}$. With the radial field b_x representing the isotropic background, this leads to the estimate

$$\frac{b_{0z}}{b_{0x}} \simeq \left[1 + \frac{\tau_0 \overline{u}_z}{l_0}\left(1 + \frac{b_{0x}^2}{b_{0y}^2}\right)\right]^{1/2} \simeq 1.2\,,$$

in a reasonable agreement with the estimates of Table 5.5. Since the vertical component of the random magnetic field is produced from both of its horizontal components, the z-component is the strongest one.

An important radio astronomical consequence of the magnetic anisotropy is polarization of the synchrotron emission. If our simulation domain was observed from the top or bottom (i.e., along the z direction) the observed degree of polarization due to the random magnetic field alone would be (Laing, 1981; Sokoloff et al., 1998, 1999)

$$p = p_0 \frac{|b_{0x}^2 - b_{0y}^2|}{b_{0x}^2 + b_{0y}^2} \approx 0.15,$$

where $p_0 \approx 0.7$ is the maximum intrinsic degree of polarization, and we have neglected, for the sake of the argument, both depolarization effects and the average magnetic field. Such a degree of polarization is comparable to that observed in spiral galaxies, suggesting that the anisotropy of the interstellar random magnetic fields needs to be allowed for in the interpretations of radio polarization observations of spiral galaxies (cf. Beck, 2016).

The correlation lengths of the magnetic field components are given in Table 5.5 (for comparison with Table 5.1). Because of the stretching of radial magnetic field by differential rotation that produces a stronger azimuthal field, we might expect the azimuthal correlation length to be larger than the radial one (Moffatt, 1967; Terry, 2000), contrary to the results in Table 5.5, where the correlation lengths for b_x and b_y are of similar magnitude. In particular, the correlation scales calculated using (5.6) are within errors for b_x and b_y. However, the correlation lengths were cal-

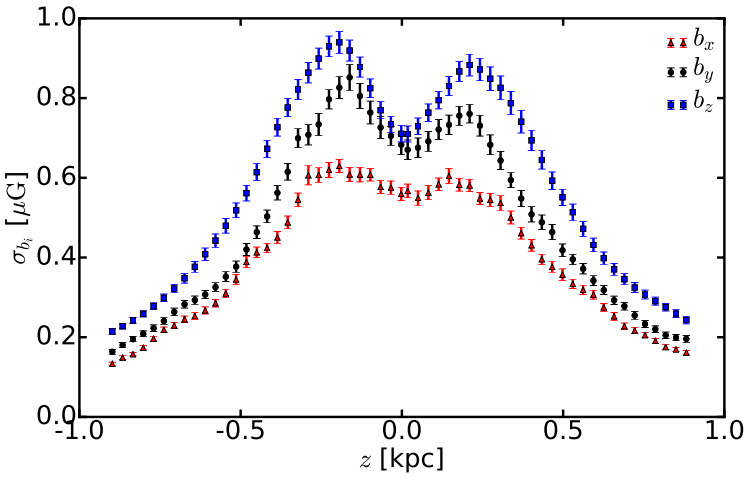

Figure 5.11: The rms values of the components of the random magnetic field vector as functions of distance to the mid-plane: the radial b_{0x} (red, triangles), azimuthal b_{0y} (black, circles), and vertical b_{0z} (blue, squares) random magnetic fields.

culated using isotropic horizontal position lags, whereas azimuthal (y) and radial (x) lags should be considered separately to detect the expected difference in the correlation lengths in the two directions. Such a refined calculation requires a larger data domain to provide sufficient statistics. Houde et al. (2013) find that $l_{0y} \approx 1.8 l_{0x}$ for the random magnetic field, i.e., the magnetic correlation length approximately along the mean-field direction (y in our case) is about twice that in the perpendicular direction, and this ratio is similar to the ratio of b_{0y}/b_{0x} found by these authors from depolarization of the synchrotron emission. The vertical magnetic field component has significant anti-correlation at $l \approx 100\,\mathrm{pc}$, shown in Figure 5.10, which results in very different values of l_0 and $\tilde{l}_0$, similar to n'.

As shown in Figure 5.11, individual components of the random magnetic field vary differently with $|z|$. The rms values first increase with distance from the mid-plane until $|z| \approx 200\,\mathrm{pc}$, and only then decrease. As suggested above, both b_y and b_z are enhanced, in comparison with b_x, by the horizontal velocity shear and random vertical flows, respectively; correspondingly, b_{0y} and b_{0z} increase with $|z|$ faster than b_{0x} at $|z| \lesssim 200\,\mathrm{pc}$, but then decrease with $|z|$ in parallel with the decrease in b_{0x}. At $|z| \geq 300\,\mathrm{pc}$, each component of $\boldsymbol{b}$ decreases roughly exponentially with the scale height of about 450 pc.

5.6 Observable quantities

The main observational tools employed in the analysis of interstellar MHD turbulence are Faraday rotation and synchrotron emission, both total and polarized. Their statistical properties and their relation to the underlying random distributions of magnetic fields, gas density and cosmic rays have received significant attention, both observationally and theoretically (see references in §5.1).

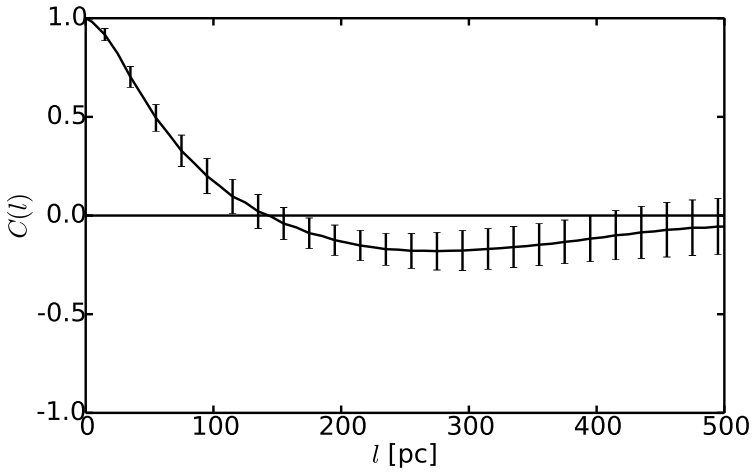

Figure 5.12: The autocorrelation function of the Faraday depth $\phi(x,y)$. The error bars represent the scatter of the data points around the mean values shown with solid line.

Here the correlation properties of the observable quantities in the simulated ISM are discussed. Given that magnetic field and gas density can have different correlation functions, and can be correlated with each other (Beck et al., 2003), statistical properties of the observable quantities are difficult to predict with confidence.

Both Faraday rotation and synchrotron emission depend on the relative orientation of the large-scale magnetic field and the line of sight. The mean magnetic field in the simulations used here is predominantly horizontal and its y-component is the strongest (Gent et al., 2013b,a). Exploring the observational appearance of the simulated volume from various vantage points will be the goal elsewhere; here the properties of fluctuations in Faraday rotation and synchrotron emission using just one direction of 'observation' are discussed.

5.6.1 Faraday depth

The Faraday depth of a magneto-ionic region is an integral along the line of sight, assumed here to be along the z-direction for convenience:

$$\phi(x,y) = 0.81 \int_{-L_z}^{L_z} n_{\rm e} \boldsymbol{B} \cdot {\rm d}\vec{z} \ {\rm rad\,m^{-2}}, \tag{5.12}$$

where $n_{\rm e}$ is the number density of thermal electrons in cm^{-3}, $\boldsymbol{B}$ is the magnetic field in μG, projected along the line-of-sight ${\rm d}\vec{z} = (0,0,{\rm d}z)$ in pc, and L_z is the half-size of the computational domain along z. Since the mean magnetic field is nearly horizontal, the mean value of B_z is close to zero together with the mean Faraday depth along this direction.

The simulations do not include gas ionization and only provide total gas density n. Since interstellar plasmas can be far from ionization equilibrium (de Avillez & Breitschwerdt, 2012b,a), the thermal electron density is obtained from a heuristic relation that ensures that the mean electron

Table 5.6: The rms values and the correlation lengths for electron density n_e.

$\lvert z\rvert$	rms	l_0
[pc]	[cm^{-3}]	[pc]
0	0.2560 ± 0.0007	59 ± 3
200	0.1665 ± 0.0008	61 ± 5
400	0.0530 ± 0.0003	80 ± 6
600	0.0208 ± 0.0002	93 ± 8
800	0.0083 ± 0.0001	83 ± 7

number density is about $0.03\,\mathrm{cm}^{-3}$ and the gas is fully ionized at $T \gtrsim 10^5\,\mathrm{K}$:

$$n_\mathrm{e} = n \left[\frac{\arctan(T/10^3\,\mathrm{K} - 10)}{\pi} + \frac{1}{2} \right]. \tag{5.13}$$

Since observations do not distinguish between different ISM phases, the Faraday depth has been computed for the whole computational domain.

The autocorrelation function of the Faraday depth is shown in Figure 5.12. Its correlation length, $l_\phi = 122 \pm 12\,\mathrm{pc}$ is significantly greater than the correlation length of electron density, 60 pc at the mid-plane increasing to 80 pc at $|z| = 800\,\mathrm{pc}$ (Table 5.6), and the vertical random magnetic field, 60 pc (Table 5.5). It should be noted that the *mean* component of B_z is negligible, so that the mean value of the Faraday depth is close to zero, $\langle \phi \rangle = 2.88 \pm 6.42\,\mathrm{rad\,m}^{-2}$.

As discussed by Beck et al. (2003), the magnitude of Faraday rotation depends on the correlation between magnetic field and thermal electron density. To clarify their relation in the simulations, the cross-correlation coefficient between n_e and B_z is computed separately for the warm and hot gas:

$$r = \frac{\overline{(n_\mathrm{e} - \overline{n}_\mathrm{e})\left(B_z - \overline{B}_z\right)}}{\overline{(n_\mathrm{e} - \overline{n}_\mathrm{e})^2}^{1/2}\,\overline{(B_z - \overline{B}_z)^2}^{1/2}} \tag{5.14}$$

where the overbar denotes an average taken over the volume occupied by the phase. The results, averaged over the snapshots, strongly suggest that the two variables are uncorrelated: $r = 0.02 \pm 0.02$ in the warm gas and 0.07 ± 0.04 in the hot phase.

The autocorrelation of ϕ is negative at $l \gtrsim 150\,\mathrm{pc}$. Both magnetic field (Section 5.5) and gas density have negative autocorrelation at these scales (Fig. 5.3). Quantitative assessment of this feature should await a more detailed analysis of the ionization structure of the modelled ISM, but this behaviour can have important implications for the interpretation of radio polarization observations of the ISM, in terms of parameters of interstellar turbulence.

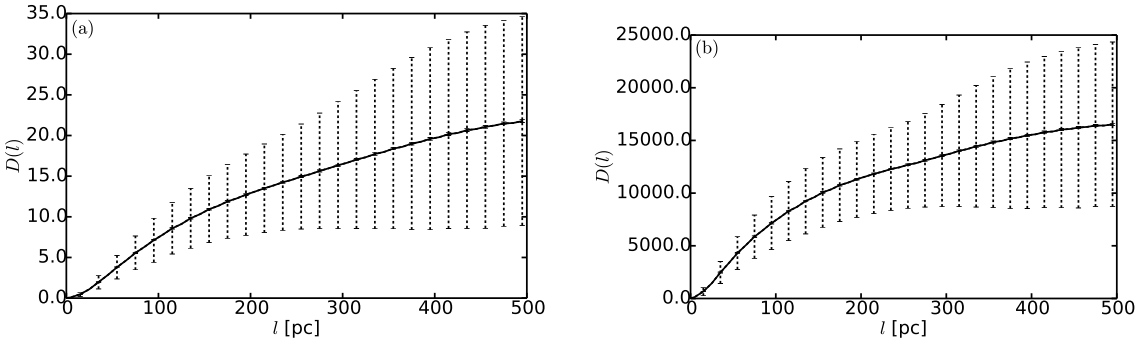

Figure 5.13: Structure functions of the synchrotron intensity assuming **(a)** constant cosmic ray density, I; and **(b)** local energy equipartition, $I_{\rm eq}$. Both structure functions are in arbitrary units. Vertical dashed lines represent the standard deviation of the individual data points around the mean value shown with solid line, whereas error bars show the accuracy of the mean. The computational volume is 'observed' at roughly the right angle to the mean magnetic field, similarly to Milky Way observations at high Galactic latitudes.

5.6.2 Synchrotron intensity

Statistical properties of the synchrotron intensity are sensitive to the relation between the distributions of cosmic ray electrons, $n_{\rm cr}$, and magnetic field. Cosmic rays (Berezinskiĭ et al., 1990) have a high diffusivity of order $3\times10^{28}\,{\rm cm^2\,s^{-1}}$, so their diffusion length over the confinement time of $10^6\,{\rm yr}$ is of order 1 kpc. Thus, it can be expected that cosmic rays are distributed much more homogeneously than magnetic fields, but the assumption of a local energy equipartition (or pressure balance) between cosmic rays and magnetic fields is often used in interpretations of synchrotron observations (e.g., Beck & Krause, 2005). The analysis of synchrotron fluctuations in spiral galaxies suggest that cosmic ray electrons and magnetic fields can be slightly anti-correlated (Stepanov et al., 2014). Fluctuations of synchrotron intensity can provide information about interstellar turbulence (Lazarian & Pogosyan, 2012, 2016). Here the synchrotron intensity fluctuations implied by ISM simulations are discussed.

The synchrotron intensity, in arbitrary units, is obtained by integration along the z-axis (so that the mean magnetic field is mostly perpendicular to the line of sight),

$$I(x,y) = \int_{-L_z}^{L_z} n_{\rm cr}\left(B_x^2 + B_y^2\right)\,{\rm d}z, \tag{5.15}$$

using two alternative assumptions about cosmic ray distribution $n_{\rm cr}$:

$$n_{\rm cr} = {\rm const}\,,$$

and

$$n_{\rm cr} \propto B^2\,,$$

i.e. the cosmic rays and magnetic field are in local energy equipartition. As with the Faraday

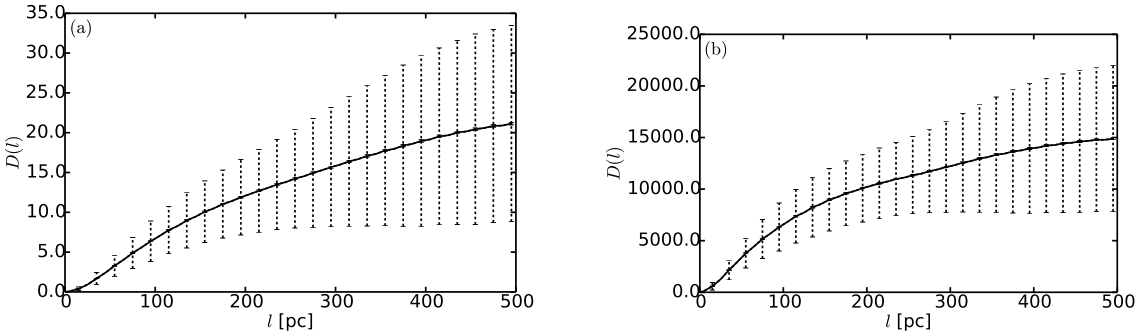

Figure 5.14: As in Figure 5.13 but for polarised intensity assuming **(a)** constant cosmic ray density, P, and **(b)** local energy equipartition, $P_{\rm eq}$.

depth, other lines of sight through the computational domain are not considered.

The Stokes parameters, at wavelengths short enough that Faraday rotation is negligible, are similarly obtained as

$$Q(x,y) = \int_{-L_z}^{L_z} \cos(2\psi_0) n_{\rm cr} (B_x^2 + B_y^2)\,{\rm d}z, \tag{5.16}$$

$$U(x,y) = \int_{-L_z}^{L_z} \sin(2\psi_0) n_{\rm cr} (B_x^2 + B_y^2)\,{\rm d}z, \tag{5.17}$$

where $\psi_0(\boldsymbol{x})$ is the intrinsic polarization angle perpendicular to the local magnetic field in the (xy)-plane, calculated as $\psi_0 = \pi/2 + \arctan(B_y/B_x)$. The polarized intensity follows as

$$P(x,y) = \sqrt{Q^2 + U^2}. \tag{5.18}$$

The structure functions of the total and polarized synchrotron intensities under both assumptions about the cosmic ray distribution are shown in Figures 5.13 and 5.14, respectively. They clearly have a more complicated form than those of the magnitude of the random magnetic field shown in Figure 5.4. This is not surprising since the mean field is a function of position, and hence contributes to the structure and correlation functions. In particular, the systematic increase of the structure function at large values of l results from this contribution. The contribution from the mean field needs to be subtracted from the structure function before any further analysis could be done. Such analysis is best postponed to simulations that include cosmic rays as a dynamical component of the ISM.

A notable feature of the results illustrated in Figures 5.13 and 5.14 is the rapid increase in the scatter of the data points and the deterioration of the accuracy of the structure function estimates as the lag l becomes larger than about 200 pc. This is understandable since the synchrotron emissivity depends on relatively high power of the fluctuating magnetic field. Observations in the Milky Way can be especially strongly affected, because even within a narrow telescope beam the divergence of the lines of sight can be as wide as hundreds of parsecs at some distance from the Sun (Cho &

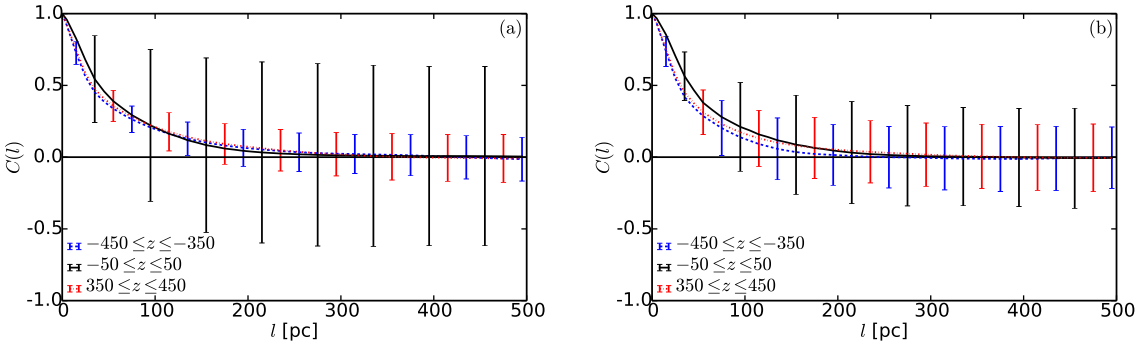

Figure 5.15: Comparison of structure functions for random magnetic field strength b, for **(a)** the standard domain and **(b)** the larger domain; averaged about $z = -400\,\mathrm{pc}$ (blue, dashed), 0 pc (black, solid), and 400 pc (red, dash-dotted). Both plots use data from the kinematic phases of the simulations.

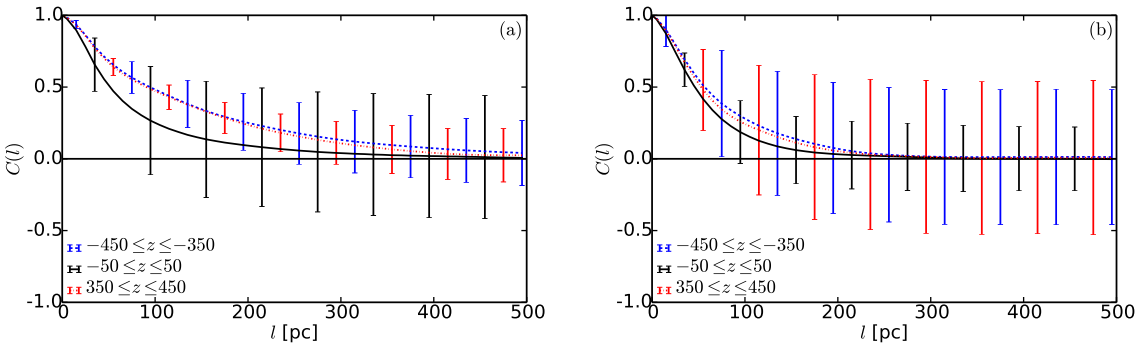

Figure 5.16: Comparison of structure functions for random speed u', comparing domain size as in Figure 5.15.

Lazarian, 2002b, 2003a, 2010).

In the case of external galaxies, a linear resolution of order a few hundred parsecs is typical of synchrotron observations. The increase in the uncertainty of the correlation function with l can cause serious complications in the analysis of interstellar turbulence using power spectra of synchrotron fluctuations (the Fourier transforms of the correlation function) as suggested by Lazarian & Pogosyan (2012, 2016) and Lee et al. (2016). This problem may not be evident when power spectra are considered because it is difficult to estimate their statistical accuracy. However, correlation analysis, with due attention to the errors, makes the problem evident.

5.7 Comparisons with similar runs

The spatial correlation results from B2Ω, a run with twice the angular velocity, are very similar to those in Section 5.3. In addition, the anisotropy results from B2Ω are very similar to those from Section 5.5, which suggests the correlation results determined here are not sensitive to the rotation rate.

In B2Ω, the velocity correlation rate and speed at the mid-plane in the warm phase change to

Table 5.7: Root-mean-square values and correlation lengths of the random magnetic and velocity fields in the standard and larger domains, for simulations in the kinematic stage of dynamo action.

		rms fluctuations		l_0 [pc]	
$\lvert z\rvert$ [pc]		0	400	0	400
b [μG]	Standard domain	0.196 ± 0.001	0.166 ± 0.001	64 ± 2	60 ± 3
	Larger domain	0.161 ± 0.001	0.123 ± 0.001	64 ± 3	49 ± 1
u' [km s^{-1}]	Standard domain	33.4 ± 0.2	16.2 ± 0.1	83 ± 4	142 ± 5
	Larger domain	11.3 ± 0.1	3.12 ± 0.04	63 ± 3	79 ± 3

58 pc and 8 km s^{-1}, resulting in the eddy turnover time of $\tau_{\rm eddy} \approx 7$ Myr, whereas $\tau_{\rm shock}$ remains unchanged.

The correlation statistics for b are very similar in both B1Ω(k) and B1ΩOoL (see Figure 5.15 and Table 5.7), but there are more significant differences for u' (see Figure 5.16 and Table 5.7).

The correlation lengths of u' are actually smaller for the larger domain, so the difference does not simply result from velocity structures having been restricted in size. In light of the differences noted above, further simulations are needed before a direct comparison can be made.

5.8 Summary

Detailed correlation analysis of the random physical fields is performed using data from an extensive suite of ISM simulations, focusing mainly on the warm gas since it occupies a larger part of the volume in these models. Statistical properties of the fluctuations in the gas are strongly non-Gaussian because of widespread filamentary and planar, small-scale structures. Such features cannot be captured by second-order correlation functions (or their equivalent, power spectra) and require other tools sensitive to all statistical moments of the random field, such as Minkowski functionals (e.g., Wilkin et al., 2007; Makarenko et al., 2015, and references therein) and topological data analysis (Adler et al., 2010; Edelsbrunner, 2014). However, careful correlation analysis remains a necessary first step in the exploration of statistical properties of random fields.

There are two difficulties in correlation analysis (and its equivalent, power spectrum analysis) that deserve special attention as they also occur in any exploration of either simulated or observational data. Correlation analysis is only meaningful when applied to a random distribution. Therefore, random fluctuations in physical parameters need to be isolated first by subtracting their averaged distributions. Averaging is straightforward in infinite domains with statistically homogeneous fluctuations. However, in reality the domain can contain only a modest number of correlation volumes, and the mean distributions of physical variables are not necessarily uniform or describable via a simple trend. The averaged distributions in this analysis are obtained using Gaussian smoothing at a scale (half-width of the Gaussian window) of 50 pc chosen carefully as in Gent et al. (2013a). Simpler procedures, for example using a uniform mean value at a given z, distort the results because of the contamination of the structure and correlation functions by

systematic and complicated non-random trends. In particular, the values of correlations lengths obtained under the assumption of horizontally uniform mean values are unphysically large, exceeding 200 pc.

Even with a correlation lengths l_0 of less than 100 pc, the finite size of the domain (of order $1\,\mathrm{kpc}^3$ in this case) can significantly affect the estimated values of l_0, as the integration in Equation (5.3) extends to infinity. This problem is resolved by fitting the measured correlation functions with physically motivated forms, which can then be integrated over an infinite range. The difference between the correlations lengths obtained with and without this fitting can be as large as a factor of two.

Given the complex structure of the simulated ISM, it is not surprising that different physical variables have different correlation functions and different correlation lengths l_0, as shown in Table 5.1. The observational estimates available for the correlations lengths in the ISM provide a wide range of values depending on the quantity observed. Conclusive comparison with observations requires detailed knowledge of the statistical properties of the random fields involved and their cross-correlations (Stepanov et al., 2014). Interstellar turbulence cannot be characterized by a single correlation length.

An estimate of the correlation time, τ_0, of the velocity fluctuations is obtained. In the simulations used here, $\tau_0 \simeq 5\,\mathrm{Myr}$ is close to both the eddy turnover time, $\tau_{\mathrm{eddy}} \simeq 8\,\mathrm{Myr}$ and the estimated time interval between the passage of shock fronts through a given position, $\tau_{\mathrm{shock}} \simeq 1\,\mathrm{Myr}$. The correlation time is likely to be sensitive to the supernova rate (and then, star formation rate) and may be closer to τ_{shock} when the supernova rate is higher. Further calculations with varying supernova rates are needed to explore under what conditions either physical process dominates the correlation time.

The random magnetic field is noticeably anisotropic, with larger rms values for azimuthal (y) and vertical (z) components in comparison to the radial (x) component, with b_z the strongest component. The enhanced y-component is produced by the action of the large-scale velocity shear on the radial turbulent magnetic field b_x, with the enhanced z component produced by stretching of the horizontal magnetic field by the random part of the vertical velocity u_z. From the rms values of b_x and b_y, an estimate is obtained of the degree of polarization of synchrotron emission of $p \approx 0.15$ that may be produced by the magnetic anisotropy.

Correlation analysis of Faraday depth is also performed along the vertical direction through the computational domain. Its correlation scale, 120 pc, is significantly larger than the correlation scales of electron density (60–90 pc) and of vertical magnetic field (60 pc). This suggests that there is no simple and universal relationship between the correlation scales of electron density, vertical magnetic field and Faraday depth.

Analysis of the total and polarized synchrotron intensities is hampered by a rapid increase of the scatter of data points around the average contributions to the structure and correlation functions. This difficulty is evident in the correlation analysis but would not be apparent in the power

spectra, where statistical errors are difficult to estimate.

Chapter 6

Mean fields and fluctuations from Gaussian smoothing

6.1 Mean-field theory in inhomogeneous turbulence

The injection of thermal and kinetic energy by stellar winds and supernova explosions drives transonic turbulence in the interstellar medium and produces an inhomogeneous, multiphase system (Elmegreen & Scalo, 2004; Scalo & Elmegreen, 2004; Mac Low & Klessen, 2004). The outer scale of turbulent motions in the ISM consistently suggested by observations, theory and simulations is of order 10–100 pc, and the turbulent scales extend to a fraction of a parsec (Armstrong et al., 1995).

Understanding the properties and nature of a turbulent flow requires the separation of mean and fluctuating quantities. Such a separation is well understood for statistically homogeneous random flows where a number of averaging procedures are available. Volume or area averaging are most important in astronomy, while numerical simulations provide a further opportunity to average over time. Under favourable conditions (defined by ergodic theorems and hypotheses), the resulting averages are equivalent to the statistical ensemble averages employed in theory (e.g., Monin & Yaglom, 2007a; Panchev, 1971; Tennekes & Lumley, 1972). The ensemble averages are rarely accessible in applications, as their calculation requires the availability of a large number of statistically independent realizations of the random processes.

Space and time averaging procedures are consistent with ensemble averaging provided they satisfy the Reynolds rules of averaging, such as $\langle f+g\rangle = \langle f\rangle + \langle g\rangle$, $\langle\langle f\rangle g\rangle = \langle f\rangle\langle g\rangle$ and $\langle\langle f\rangle\rangle = \langle f\rangle$, where f and g are random functions and angular brackets denote averaging (e.g., Sect. 3.1 in Monin & Yaglom, 2007a). Volume and time averaging only satisfy the latter Reynolds rule in an approximate manner when the scales of variations of the mean quantities and the fluctuations differ significantly (the requirement of scale separation between the averaged quantities and the fluctuations) and the averaging scale is large in comparison with the scale of the fluctuations and

small in comparison with that of the mean quantities. In practice, the mean quantities need to be homogeneous or time-independent for the ensemble and volume (or time) averages to be consistent with each other.

The outer scale of the interstellar turbulence is comparable to the scale height of the gas density distribution in spiral galaxies (about 0.1 kpc and 0.5 kpc for the cold and warm diffuse H_I, respectively). Therefore, the interstellar turbulent flow cannot be considered statistically homogeneous apart from along the horizontal directions. However, numerical simulations of the supernova-driven, multi-phase ISM have relatively small horizontal domains of order $1\,\mathrm{kpc} \times 1\,\mathrm{kpc}$ or less (e.g., Korpi et al., 1999a; Joung & Mac Low, 2006; de Avillez & Breitschwerdt, 2007, 2012b,a; Gressel et al., 2008b; Federrath et al., 2010; Hill et al., 2012; Gent et al., 2013a,b; Gressel et al., 2013; Bendre et al., 2015; Walch et al., 2015; Girichidis et al., 2016a,b). Meanwhile, the ISM has a wide range of density and velocity structures (e.g., those related to gas clouds, galactic outflows and spiral patterns) that cover continuously the range of scales from 1 pc to 10 kpc. Therefore, scale separation between the random and large-scale ISM flows is questionable at best. This poses difficulties for the interpretation of numerical simulations. Similar difficulties arise in the interpretation of observations, but numerical simulations have exposed the problems especially clearly.

The division of the Navier–Stokes and magnetohydrodynamic (MHD) equations into evolution equations for the mean flow and the fluctuations has been explored for both ensemble averaging and filtering of the fluctuations (also known as coarse-graining); i.e., volume averaging via convolution with a compact kernel. The Reynolds rules of averaging are not satisfied for this procedure but this is not an obstacle to developing a mathematically sound formalism that leads to evolution equations for averaged quantities and their moments (Germano, 1992). The most widely known application of this technique is to subgrid models for large eddy simulations of turbulent flows Meneveau (2012). Eyink (2018) and Aluie (2017) provide details and a review of this approach to hydrodynamic and MHD turbulence (see also Eyink, 1995, 2015).

An important advantage of the filtering approach is that, together with ensemble averaging, it does not require scale separation between the mean fields and their fluctuations (e.g., Aluie, 2017).

The separation of the mean and fluctuating quantities in a random flow is of crucial significance in the theory of mean-field turbulent dynamos, and the problem of averaging has been exposed in this area earlier than in other applications. The mean-field dynamo theory is based on ensemble averaging but numerical simulations rely on various volume and time averaging procedures. For example, the separation of the magnetic field into mean and fluctuating components often involves averaging over the whole computational volume or, in systems stratified along the z-direction due to gravity, averaging in the (x,y)-planes (horizontal averaging; see Brandenburg & Subramanian, 2005). The resulting mean magnetic field is either perfectly uniform or only dependent on z. However, these constraints on the form of the mean magnetic field are artificial and unphysical. An inhomogeneous system, such as the ISM, is expected to produce a spatially complex mean field, which is ignored in the simple volume of horizontal averaging techniques described above. A

further complication with horizontal averaging is the requirement that $\langle B_z \rangle$ vanishes when periodic boundary conditions are used in x and y, provided $\langle B_z \rangle = 0$ initially; otherwise the solenoidality of the mean magnetic field cannot be guaranteed (e.g., Gent et al., 2013b). Furthermore, the kinematic mean-field dynamo action, with homogeneous transport coefficients α and β, in infinite space produces an inhomogeneous mean magnetic field that varies at all wave-numbers below α/β, with the dominant mode having the wave-number $\alpha/(2\beta)$ (e.g., Sokoloff et al., 1983). *The spatial structure of any mean field is controlled by the physical properties of the system rather than by the size of the computational domain.* The only advantage of horizontal averaging is that it obeys the Reynolds rules, but this is often achieved at the expense of physical validity. Another option, consistent with the Reynolds rules, is to use azimuthal averaging to obtain an axially symmetric mean magnetic field in global simulations of dynamo action in a rotating spherical object (see Simard et al., 2016, for a review). This approach is easier to justify but still it excludes physically admissible azimuthal variations of the mean field.

In this Chapter, an alternative approach to averaging is discussed based on Gaussian smoothing as suggested by Germano (1992), and is employed to obtain the mean fields in simulations of the multi-phase, supernova-driven ISM. Averaging with a Gaussian (or another) kernel is inherent in astronomical observations, where such smoothing is applied either during data reduction or stems from the finite width of a telescope beam. This approach has been applied by Gent et al. (2013b) to the simulated magnetic field; here it is extended to the velocity and density fields and, importantly, energy densities, which represent higher-order statistical moments. In particular, kinetic energy density in a compressible flow represents a third-order statistical moment and requires special attention.

Snapshots from the model B2Ω are analysed in the range $0.8 \leq t \leq 1.725\,\mathrm{Gyr}$. Regarding the magnetic field and dynamo action, three distinct periods can be identified. For $0.8 \leq t < 1.1\,\mathrm{Gyr}$, the magnetic energy is low compared to the thermal and kinetic energies and the mean- field dynamo is in its kinematic stage. The dynamo adjusts itself to a non-linear stage at $1.1 \leq t < 1.45\,\mathrm{Gyr}$ as the magnetic energy reaches approximate equipartition with kinetic energy of the random flow. Finally, at $1.45 \leq t \leq 1.725\,\mathrm{Gyr}$, the mean-field dynamo saturates and the magnetic energy slightly exceeds the kinetic energy (see Gent et al., 2013a). Since the evolution of the magnetic field is expected to significantly affect the structure of the gas density and velocity, each period is considered independently. The results are illustrated in the figures shown below using the snapshot at $t = 1.6\,\mathrm{Gyr}$.

6.2 Mean fields and fluctuations in a compressible random flow

Averaging procedures can be used to represent a physical variable f as a superposition of a mean $\langle f \rangle$ and fluctuating f' parts, $f = \langle f \rangle + f'$. Ensemble averaging is used in most theoretical contexts. Ensemble-averaged quantities do not need to be independent of any spatial or temporal

variable. However, volume and time averaging are often the only options available in simulations and observations. For example, the average over a volume V,

$$\langle f \rangle_V = \frac{1}{V} \int_V f(\boldsymbol{x}') \, \mathrm{d}^3 \boldsymbol{x}' \,, \tag{6.1}$$

satisfies the Reynolds rules of averaging, including

$$\langle f \langle g \rangle_V \rangle_V = \langle f \rangle_V \langle g \rangle_V \,, \qquad \langle \langle f \rangle_V \rangle_V = \langle f \rangle_V \,, \tag{6.2}$$

leading to

$$\langle f' \rangle_V = 0 \,, \qquad \langle \langle f \rangle_V \, g' \rangle_V = 0 \,, \tag{6.3}$$

for the random variables f and g. This allows evolutionary equations for the central moments $\langle f'g' \rangle_V$, $\langle f'g'h' \rangle_V$ (with another random variable h), etc., to be derived by averaging the governing equations using relations such as (e.g., Monin & Yaglom, 2007a),

$$\begin{aligned} \langle u_i' u_j' \rangle_V &= \langle u_i u_j \rangle_V - \langle u_i \rangle_V \langle u_j \rangle_V \,, \\ \langle u_i' u_j' u_k' \rangle_V &= \langle u_i u_j u_k \rangle_V - \langle u_i \rangle_V \langle u_j' u_k' \rangle_V - \langle u_j \rangle_V \langle u_k' u_i' \rangle_V \\ &\quad - \langle u_k \rangle_V \langle u_i' u_j' \rangle_V - \langle u_i \rangle_V \langle u_j \rangle_V \langle u_k \rangle_V \,, \end{aligned} \tag{6.4}$$

in the case of the velocity field $\boldsymbol{u}$.

In numerical simulations, V is often the whole computational domain, or some significant part of it, or a (thin) slice parallel to one of the coordinate planes, as in averages over a horizontal plane (x,y). Another widespread averaging procedure is azimuthal averaging, appropriate when the mean quantities are axially symmetric. Such averages are restricted to be partially or fully independent of position, in all three directions in the case of volume averages, in two dimensions for horizontal averages and in the azimuth for axial averages. As discussed in Section 6.1, these constraints may be — and often are — unreasonably restrictive. Moreover, any observational data obtained with a finite resolution represent a convolution of the quantity observed with the telescope beam and are free to vary with position. It is therefore desirable to apply to numerical results an averaging procedure, compatible with the observational procedures, in a manner that does not impose unjustifiable constraints on the averaged quantities. This is the goal of this Chapter.

6.2.1 The filtering approach to averaging

A local mean part of a random field $f(\boldsymbol{x})$, denoted $\langle f \rangle_\ell$, is obtained by spatial smoothing (filtering) of its fluctuations at scales $l < \ell$, with a certain *smoothing length* ℓ, using a smoothing kernel $\mathscr{G}_\ell$:

$$\langle f(\boldsymbol{x}) \rangle_\ell = \int_V f(\boldsymbol{x}') \mathscr{G}_\ell(\boldsymbol{x} - \boldsymbol{x}') \, \mathrm{d}^3 \boldsymbol{x}' \,, \tag{6.5}$$

where integration extends over the whole volume where $f(\boldsymbol{x})$ is defined. The filtering kernel is normalized,

$$\int_V \mathcal{G}_\ell(\boldsymbol{x}-\boldsymbol{x}')\,\mathrm{d}^3\boldsymbol{x}' = 1\,,$$

and assumed to be symmetric,

$$\int_V \boldsymbol{x} G_\ell(\boldsymbol{x})\,\mathrm{d}^3\boldsymbol{x} = 0\,. \tag{6.6}$$

To ensure that fluctuations in kinetic energy density are positive definite, the kernel must be positive for all $\boldsymbol{x}$ (Aluie, 2017, and references therein). The fluctuation field is obtained as

$$f'(\boldsymbol{x}) = f(\boldsymbol{x}) - \langle f(\boldsymbol{x})\rangle_\ell\,, \tag{6.7}$$

(with the link between the prime and the scale ℓ being understood). This procedure retains the spatial structure of both the mean field and the fluctuations. Physically motivated choices for the smoothing length ℓ are discussed below.

Thus defined, the averaging procedure does not satisfy the Reynolds rules outlined in equations (6.2) and (6.3). In particular, the mean of the fluctuations does not vanish, repeated averaging affects the mean field $\langle f(\boldsymbol{x})\rangle_\ell$, and the mean and fluctuating fields are not uncorrelated:

$$\langle f'\rangle_\ell \neq 0\,, \qquad \langle\langle f\rangle_\ell\rangle_\ell \neq \langle f\rangle_\ell\,, \qquad \langle\langle f\rangle_\ell f'\rangle_\ell \neq 0\,. \tag{6.8}$$

As a consequence, the standard relations between statistical moments of total fields and their fluctuations, shown in equation (6.4), are no longer valid.

To address these complications, Germano (1992) introduced generalised statistical moments $\upsilon(f,g)\,\upsilon(f,g,h)\ \ldots$, of random fields $f(\boldsymbol{x})$, $g(\boldsymbol{x})$ and $h(\boldsymbol{x})$ to ensure that the mathematical soundness and simplicity of the averaged governing equations is regained for both the mean fields and their statistical moments. In fact, relations between the statistical moments are quite similar to the standard ones of equation (6.4). For example, the generalised statistical moments of the velocity field $\boldsymbol{u}(\boldsymbol{x})$ are defined as

$$\begin{aligned}
\upsilon(u_i,u_j) &= \langle u_i u_j\rangle_\ell - \langle u_i\rangle_\ell\langle u_j\rangle_\ell\,,\\
\upsilon(u_i,u_j,u_k) &= \langle u_i u_j u_k\rangle_\ell - \langle u_i\rangle_\ell\upsilon(u_j,u_k) - \langle u_j\rangle_\ell\upsilon(u_k,u_i)\\
&\quad - \langle u_k\rangle_\ell\upsilon(u_i,u_j) - \langle u_i\rangle_\ell\langle u_j\rangle_\ell\langle u_k\rangle_\ell\,.
\end{aligned} \tag{6.9}$$

Statistical moments of the fluctuations are obtained from the moments of the total fields and their averages as, for example,

$$\begin{aligned}
\langle u_i' u_j'\rangle_\ell &= \langle (u_i - \langle u_i\rangle_\ell)(u_j - \langle u_j\rangle_\ell)\rangle_\ell\\
&= \langle u_i u_j - \langle u_i\rangle_\ell u_j - u_i\langle u_j\rangle_\ell + \langle u_i\rangle_\ell\langle u_j\rangle_\ell\rangle_\ell\\
&= \langle u_i u_j - \langle u_i\rangle_\ell u_j' - u_i'\langle u_j\rangle_\ell - \langle u_i\rangle_\ell\langle u_j\rangle_\ell\rangle_\ell
\end{aligned}$$

$$= \langle u_i u_j \rangle_\ell - \langle \langle u_i \rangle_\ell u'_j \rangle_\ell - \langle u'_i \langle u_j \rangle_\ell \rangle_\ell - \langle \langle u_i \rangle_\ell \langle u_j \rangle_\ell \rangle_\ell \,. \tag{6.10}$$

As in equation (6.8), $\langle \langle u_i \rangle_\ell u'_j \rangle_\ell \neq 0$ and $\langle u'_i \langle u_j \rangle_\ell \rangle_\ell \neq 0$. In addition, $\langle \langle u_i \rangle_\ell \langle u_j \rangle_\ell \rangle_\ell \neq \langle u_i \rangle_\ell \langle u_j \rangle_\ell$ since $\langle \langle u_i \rangle_\ell \rangle_\ell \neq \langle u_i \rangle_\ell$. As a consequence, $\langle u'_i u'_j \rangle_\ell \neq \langle u_i u_j \rangle_\ell - \langle u_i \rangle_\ell \langle u_j \rangle_\ell = \upsilon(u_i, u_j)$. The use of generalised central moments such as $\upsilon(u_i, u_j)$, rather than the statistical moments of the fluctuations $\langle u'_i u'_j \rangle_\ell$, leads to governing equations for the fluctuations in a mathematically simple form practically identical to that obtained under ensemble averaging (see Aluie, 2017, for the case of MHD equations). The algebraic structure of the closure is the same, regardless of the choice of the filter $\mathscr{G}$. Such a property is called the averaging invariance of the turbulent equations (see Germano, 1992).

In application to the ISM simulations described in Section 4.1, the physical fields are decomposed into mean and fluctuating components with the mean fields obtained via filtering with a Gaussian kernel,

$$G_\ell(\boldsymbol{x}) = (2\pi\ell^2)^{-3/2} \exp\left[-\boldsymbol{x}^2/(2\ell^2)\right], \tag{6.11}$$

where ℓ is the smoothing length. This analysis considers the magnetic field $\boldsymbol{B}$, gas density ρ and velocity $\boldsymbol{u}$ independently. All averages are denoted with the subscript ℓ and fluctuations with the prime, with the exception of magnetic field fluctuations denoted $\boldsymbol{b}$:

$$\begin{aligned}
&\boldsymbol{B} = \boldsymbol{B}_\ell + \boldsymbol{b}, && \boldsymbol{B}_\ell = \langle \boldsymbol{B} \rangle_\ell, && \boldsymbol{b} = \boldsymbol{B} - \boldsymbol{B}_\ell, \\
&\rho = \rho_\ell + \rho', && \rho_\ell = \langle \rho \rangle_\ell, && \rho' = \rho - \rho_\ell, \\
&\boldsymbol{u} = \boldsymbol{u}_\ell + \boldsymbol{u}', && \boldsymbol{u}_\ell = \langle \boldsymbol{u} \rangle_\ell, && \boldsymbol{u}' = \boldsymbol{u} - \boldsymbol{u}_\ell .
\end{aligned} \tag{6.12}$$

6.3 The smoothing scale and Fourier spectra

The challenge in applying the filtering approach in our context is to determine an appropriate smoothing length ℓ or its admissible range. It should be noted that the mean and fluctuating parts of different variables, e.g., $\boldsymbol{B}$, ρ and $\boldsymbol{u}$, can have different spatial properties and, hence, different smoothing lengths may be required to separate the fluctuations in different variables. As demonstrated in Chapter 5, the correlation lengths of the three variables are different in the simulations discussed here. Unlike applications to subgrid turbulence models, where ℓ is identified with the spatial resolution of a simulation, the choice of ℓ in the present context is motivated by physical considerations. Following Gent et al. (2013a), the choice ℓ is motivated by the spectral structure of each variable as discussed below.

Scale separation between the mean and fluctuation fields is required neither by theory based on ensemble averages nor by the filtering technique. Nevertheless, it is natural to expect some difference in scales between the two. For example, the scale of the mean field in a turbulent dynamo is controlled by deviations of the random flow from mirror symmetry and mean velocity shear, whereas turbulent scales depend on the nature of the driving forces. Given the fundamental

Table 6.1: Notation for the total (T), mean (M) and fluctuating (F) fields and their respective Fourier spectra.

				Spectrum			Energy density			Energy		
	T	M	F	T	M	F	T	M	F	T	M	F
Magnetic field	$\boldsymbol{B}$	$\boldsymbol{B}_\ell$	$\boldsymbol{b}$	$S_B(k)$	$S_{B_\ell}(k)$	$S_b(k)$	$\langle e_B\rangle_\ell$	e_{B_ℓ}	e_b	$\mathscr{E}_B$	$\mathscr{E}_{B_\ell}$	$\mathscr{E}_b$
Gas density	ρ	ρ_ℓ	ρ'	$S_\rho(k)$	$S_{\rho_\ell}(k)$	$S_{\rho'}(k)$	—	—	—	—	—	—
Gas velocity	$\boldsymbol{u}$	$\boldsymbol{u}_\ell$	$\boldsymbol{u}'$	$S_u(k)$	$S_{u_\ell}(k)$	$S_{u'}(k)$	$\langle e_\mathrm{k}\rangle_\ell$	e_s	e_st, e_t	$\mathscr{E}_\mathrm{k}$	$\mathscr{E}_\mathrm{s}$	$\mathscr{E}_\mathrm{st}$, $\mathscr{E}_\mathrm{t}$

difference between the two groups of physical effects, it is unlikely that the two parts of magnetic field have similar scales. Since deviations from mirror symmetry are usually weak, the scale of the mean field is expected to be correspondingly large and to exceed the turbulent scale. Arguments of this kind are used to justify the two-scale approach in mean-field magnetohydrodynamics (Moffatt, 1978; Krause & Rädler, 1980; Zeldovich et al., 1983). However, numerical simulations of dynamo systems (including those discussed here) are performed in domains that are only moderately larger than the integral scale of the simulated random flow (Brandenburg & Subramanian, 2005, and references therein) which precludes any strong scale separation between the simulated mean and fluctuating fields. Nevertheless, evidence for such separation is usually sought, in the form of a pronounced minimum in the Fourier spectra at a scale exceeding the presumed integral scale of the fluctuations (often, the scale at which the random flow is driven by an explicit force) and the domain size. In application to the magnetic field, Gent et al. (2013a) demonstrate that the situation can be more subtle and, despite a pronounced difference of the two scales (by a factor of two), the Fourier spectrum of the total magnetic field may not have a noticeable minimum between them.

The Fourier spectrum of the total magnetic field $\boldsymbol{B}$ is given by

$$S_B(k) = k^2 \langle |\widehat{\boldsymbol{B}}(\boldsymbol{k})|^2 \rangle_k \,, \tag{6.13}$$

where $\widehat{\boldsymbol{B}}(\boldsymbol{k}) = \int_V \boldsymbol{B}(\boldsymbol{x}) \exp(-2\pi \mathrm{i} \boldsymbol{k}\cdot\boldsymbol{x}) \,\mathrm{d}^3\boldsymbol{x}$ is the Fourier transform of $\boldsymbol{B}$ and $\langle\cdots\rangle_k$ denotes the average value within a spherical shell of thickness δk with radius $k = |\boldsymbol{k}|$. The power spectra for the mean and random fields, $S_{B_\ell}(k)$ and $S_b(k)$, are similarly defined in terms of $\widehat{\boldsymbol{B}}_\ell(\boldsymbol{k})$ and $\widehat{\boldsymbol{b}}(\boldsymbol{k})$, the Fourier transforms of $\boldsymbol{B}_\ell$ and $\boldsymbol{b}$:

$$S_{B_\ell}(k) = k^2 \langle |\widehat{\boldsymbol{B}_\ell}(\boldsymbol{k})|^2 \rangle_k \,, \qquad S_b(k) = k^2 \langle |\widehat{\boldsymbol{b}}(\boldsymbol{k})|^2 \rangle_k \,. \tag{6.14}$$

The integral scale of each field is also considered (Sect. 12.1 in Monin & Yaglom, 2007b),

$$L = \frac{\pi}{2} \frac{\int_{2\pi/D}^{\pi/\Delta} k^{-1} S(k) \,\mathrm{d}k}{\int_{2\pi/D}^{\pi/\Delta} S(k) \,\mathrm{d}k} \,, \tag{6.15}$$

calculated using the appropriate power spectrum $S(k)$, where Δ is the grid spacing and D the size of the computational domain. Since both the mean field and the fluctuations are inhomogeneous,

equation (6.15) can be used to derive the characteristic scales of both the mean and fluctuating fields: e.g. L_{B_ℓ} for the mean magnetic field, such that $L_{B_\ell}^2 \simeq |\boldsymbol{B}_\ell|/|\nabla^2 \boldsymbol{B}_\ell|$.

As discussed in Sections 6.3.1, 6.3.2 and 6.3.3, none of the Fourier spectra of $\boldsymbol{B}$, ρ and $\boldsymbol{u}$, have a local minimum. Nonetheless, each variable has distinct, well separated length scales for the mean and fluctuating fields. The optimal smoothing scale ℓ for each variable is obtained in Section 6.3.1 from the requirements that: (i) the major maxima in the Fourier spectra of the mean field and fluctuations in each variable occur on different sides, along the wave-number axis, of the wave-number where they intersect; and (ii) that the ratio of the integral scales of the mean fields and the fluctuations is (approximately) maximized.

The spectra and lengths scales for ρ, $\boldsymbol{u}$ and their respective mean and fluctuations are defined in a similar manner and denoted $S_\rho(k)$, $S_{\rho_\ell}(k)$, $S_{\rho'}(k)$, $S_u(k)$, $S_{u_\ell}(k)$ and $S_{u'}(k)$, with the corresponding length scales L_ρ, L_{ρ_ℓ}, $L_{\rho'}$, L_u, L_{u_ℓ} and $L_{u'}$. The notation is summarized in Table 6.1.

The power spectrum $S_B(k)$ is equivalent, up to a constant factor of $1/(8\pi)$, to the magnetic energy spectrum $M(k) = S_B(k)/(8\pi)$, and the total magnetic energy can be obtained as an integral over the relevant wave-number range, $E_B = \int_k M(k)\,\mathrm{d}k$. However, unlike the case of incompressible flows, the power spectrum of the velocity field cannot be directly equated to the kinetic energy density because of the contribution from the gas density fluctuations.

Calculation of energy densities due to the mean fields and fluctuations should be done with care. To illustrate the general approach, consider magnetic energy. Although total magnetic energies can be obtained via wavenumber integrals of the power spectra, these do not always, within the filtering approach, correspond to the energies of the mean and fluctuating parts, or the sum of the latter energies. The total magnetic energy E_B satisfies $E_B = 1/(8\pi)\int_k S_B(k)\,\mathrm{d}k = \int_V e_B\,\mathrm{d}V$, where $e_B = B^2/(8\pi)$ and $\mathrm{d}V = \mathrm{d}^3\boldsymbol{x}$. And the wavenumber integral of the mean field, $E_{B_\ell} = 1/(8\pi)\int S_{B_\ell}(k)\,\mathrm{d}k$ does equal the volume integral of the relevant energy density, $\mathscr{E}_{B_\ell} = \int_V e_{B_\ell}\,\mathrm{d}V$, where $e_{B_\ell} = B_\ell^2/(8\pi)$. But the corresponding quantities for the fluctuating field, $E_b = 1/(8\pi)\int S_b(k)\,\mathrm{d}k$, and $\mathscr{E}_b = \int_V e_b\,\mathrm{d}V$, are not equal: $E_b \neq \mathscr{E}_b$. As defined, $E_b = 1/(8\pi)\int_V b^2\,\mathrm{d}V$; but as explained in more detail in section 6.4, e_b must be defined in terms of the generalised second moments with $i = j$ (from equation (6.9)): $e_b = \mu(B_i, B_j)/(8\pi)$, so that $e_b \neq b^2/(8\pi)$. Furthermore, the energies defined above do not sum: $E_B \neq E_{B_\ell} + E_b$.

In the filtering approach, the energy densities sum as required from equation (6.9), with the definitions above: $\langle e_B\rangle_\ell = e_{B_\ell} + e_b$. To avoid confusion, distinct notation is introduced for the volume integrals of these energy densities — $\mathscr{E}_B = \int_V \langle e_B\rangle_\ell\,\mathrm{d}V$, $\mathscr{E}_{B_\ell} = \int_V e_{B_\ell}\,\mathrm{d}V$, $\mathscr{E}_b = \int_V e_b\,\mathrm{d}V$ — so that the following can be written $\mathscr{E}_B = \mathscr{E}_{B_\ell} + \mathscr{E}_b$. These energy densities and their volume integrals are summarised in Table 5.1, and discussed further in Section 6.4. But note that, while $\mathscr{E}_{B_\ell} = E_{B_\ell}$, $\mathscr{E}_B \neq E_B$, and $\mathscr{E}_b \neq E_b$.

The Fourier spectra of the basic physical variables in Sections 6.3.1–6.3.3 are analysed to identify appropriate smoothing lengths ℓ, which can be different for different variables, and then use the filtering approach to derive and discuss the corresponding energy densities in Section 6.4.

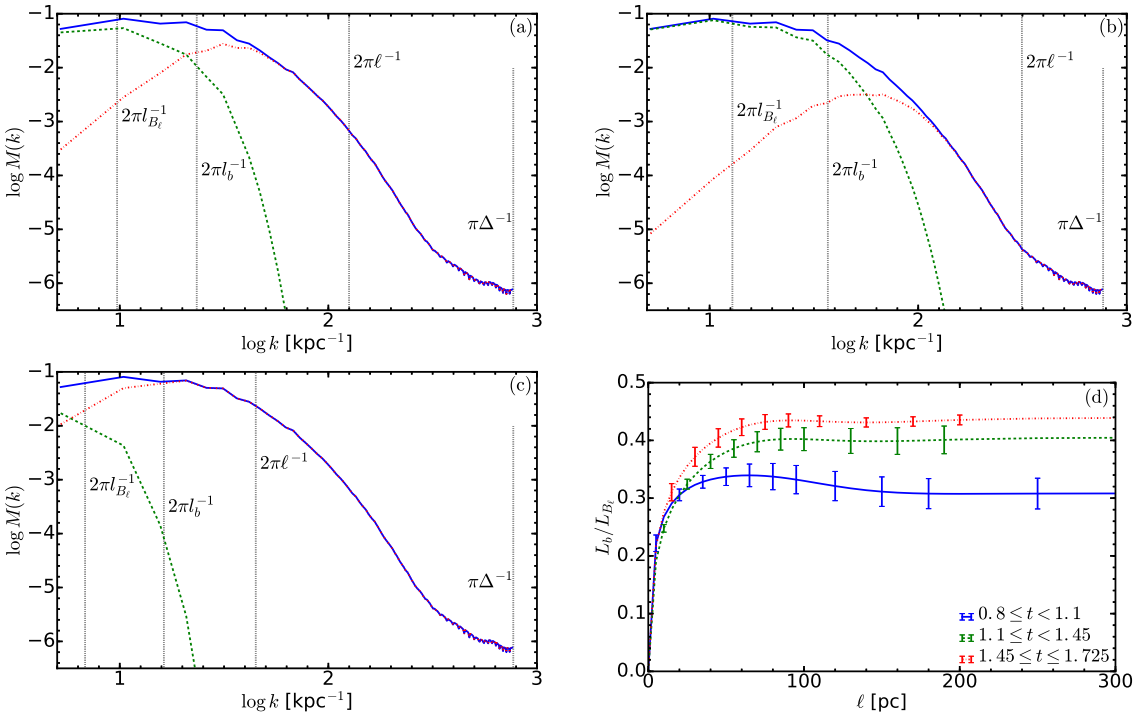

Figure 6.1: Fourier spectra of the total magnetic field $S_B(k)$ (blue, solid), its mean part $S_{B_\ell}(k)$ (green, dash-dotted) and the fluctuations $S_b(k)$ (red, dashed) at $t = 1.6$ Gyr for various values of the smoothing length ℓ: **(a)** $\ell = 50$ pc, **(b)** $\ell = 20$ pc and **(c)** $\ell = 140$ pc. The vertical dotted lines indicate (from left to right) the wave-numbers corresponding to the scale of the mean field L_{B_ℓ}, its fluctuations L_b, the smoothing length ℓ and the resolution of the simulations Δ. **(d)**: Ratio of the integral scales L_b and L_{B_ℓ} as a function of the smoothing length ℓ in the three periods of magnetic field evolution, kinematic $0.8 \le t < 1.1$ Gyr (blue, solid), transitional $1.1 \le t < 1.45$ Gyr (green, dash-dotted) and non-linear $1.45 \le t \le 1.725$ Gyr (red, dashed).

6.3.1 Magnetic field

Figures 6.1b and 6.1c show the power spectra of the total magnetic field and its mean and fluctuating parts obtained using $\ell = 20$ pc and $\ell = 140$ pc, respectively. When $\ell = 20$ pc, the integral scales of the mean field and the fluctuations are $L_{B_\ell} = 0.49$ kpc and $L_b = 0.17$ kpc, but the scale $\lambda = 0.09$ kpc where the two power spectra intersect, $S_{B_\ell}(\lambda) = S_b(\lambda)$, is smaller than the integral scale of the fluctuations, $\lambda < L_b$. This is physically inconsistent. When $\ell = 140$ pc, the opposite and equally unsatisfactory situation follows with $L_{B_\ell} = 0.92$ kpc $< \lambda = 1.09$ kpc, $L_b = 0.39$ kpc.

A more satisfactory picture emerges when $\ell = 50$ pc shown in Figure 6.1a, resulting in $L_{B_\ell} = 0.65$ kpc, $L_b = 0.27$ kpc and $\lambda = 0.3$ kpc, so that $L_b < \lambda < L_{B_\ell}$. Thus, $\ell = 50$ pc can be adopted as an appropriate smoothing length for the magnetic field: then the mean field dominates at scales around L_{B_ℓ} whereas the fluctuations contribute most of the power at scales around L_b.

The ratio of L_{B_ℓ} and l_b as a function of ℓ is shown in Figure 6.1d for the three periods of the magnetic field evolution. When magnetic field is still weak, there is a pronounced maximum at $\ell = 65$ pc which becomes less prominent as the magnetic field growth saturates. Thus, the

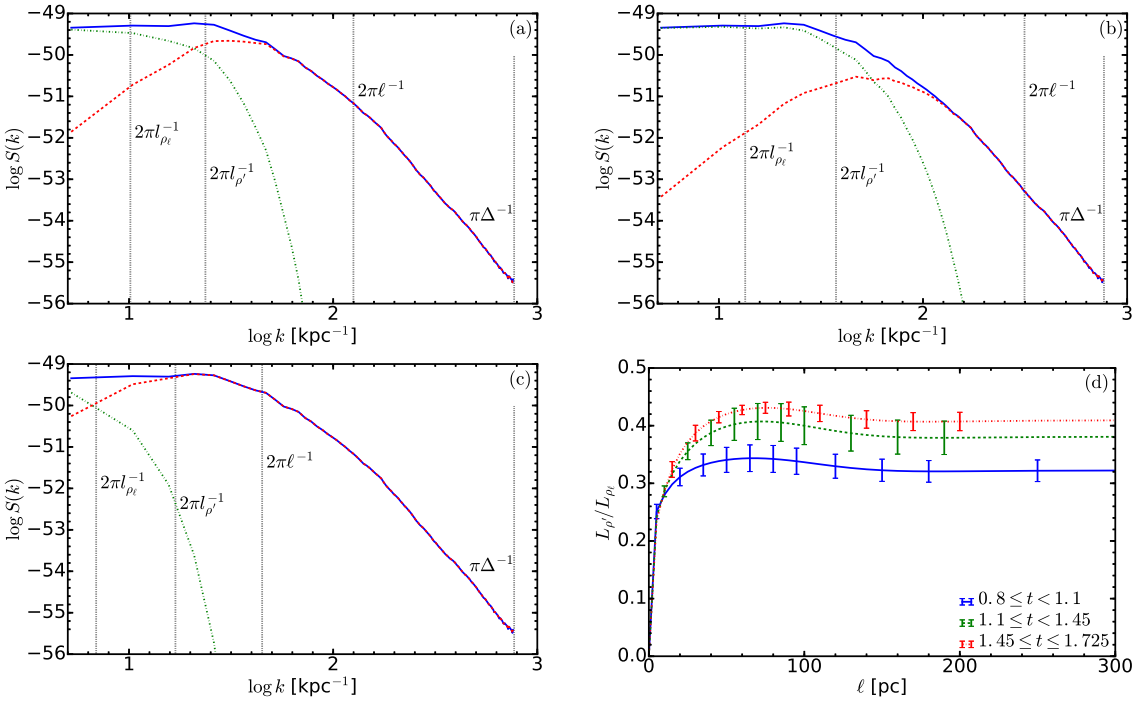

Figure 6.2: As for Figure 6.1 but for the gas density ρ (in $\mathrm{g\,cm^{-3}}$) with **(a)** $\ell = 50\,\mathrm{pc}$, **(b)** $\ell = 20\,\mathrm{pc}$ and **(c)** $\ell = 140\,\mathrm{pc}$.

requirement that $L_b < \lambda < L_{B_\ell}$ is compatible with the maximum scale separation between the mean field and the fluctuations. The ratio reaches an asymptotic value in the range 0.3–0.4 at $\ell \approx 90\,\mathrm{pc}$.

6.3.2 Gas density

Using the same arguments as for magnetic field, we conclude that $\ell = 50\,\mathrm{pc}$ is a suitable smoothing length for the density distribution, as also shown in Figure 6.2. Indeed, when $\ell = 50\,\mathrm{pc}$, we obtain $L_{\rho_\ell} = 0.62\,\mathrm{kpc}$ and $L_{\rho'} = 0.27\,\mathrm{kpc}$, with $\lambda = 0.31\,\mathrm{kpc}$. In contrast, $L_{\rho_\ell} = 0.47\,\mathrm{kpc}$ and $L_{\rho'} = 0.17\,\mathrm{kpc} > \lambda = 0.11\,\mathrm{kpc}$ for $\ell = 20\,\mathrm{pc}$, and $L_{\rho_\ell} = 0.91\,\mathrm{kpc} < \lambda = 0.95\,\mathrm{kpc}$ and $L_{\rho'} = 0.37\,\mathrm{kpc}$ for $\ell = 140\,\mathrm{pc}$.

The ratio of L_{ρ_ℓ} and $L_{\rho'}$ as a function of ℓ is shown in Figure 6.2d. Its maximum is reached at values of ℓ increasing from 65 pc to 75 pc as the magnetic field saturates, suggesting a suitable smoothing length of approximately 70 pc.

6.3.3 Gas velocity

Figures 6.3a–d illustrate similar arguments for the velocity field $\boldsymbol{u}$ (which represents deviations from the overall shearing flow and contains a systematic vertical outflow velocity). When $\ell = 50\,\mathrm{pc}$, $L_{u_\ell} = 0.66\,\mathrm{kpc}$ and $L_{u'} = 0.27\,\mathrm{kpc}$, with $\lambda = 0.3\,\mathrm{kpc}$. Conversely, $L_{u_\ell} = 0.50\,\mathrm{kpc}$, $L_{u'} =$

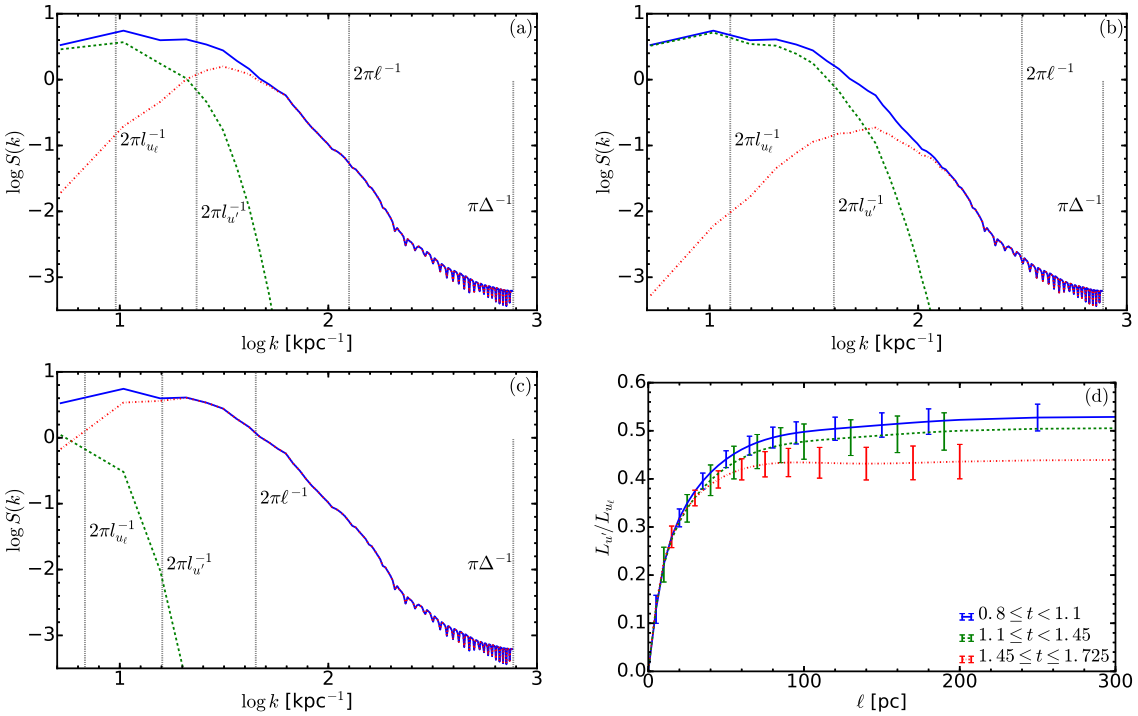

Figure 6.3: As for Figure 6.1 but for the gas velocity (in $\mathrm{km\,s^{-1}}$) with **(a)** $\ell = 50\,\mathrm{pc}$, **(b)** $\ell = 20\,\mathrm{pc}$ and **(c)** $\ell = 140\,\mathrm{pc}$.

0.16 kpc and $\lambda = 0.12\,\mathrm{kpc} < L_{u'}$ for $\ell = 20\,\mathrm{pc}$, whilst for $\ell = 140\,\mathrm{pc}$ we have $L_{u_\ell} = 0.92\,\mathrm{kpc}$, $L_{u'} = 0.39\,\mathrm{kpc}$ and $\lambda = 1.12\,\mathrm{kpc} > L_{u_\ell}$. However, the ratio of length scales in Figure 6.3d does not have any pronounced maxima, as it increases monotonically with ℓ for $t < 1.45\,\mathrm{Gyr}$,and has a very broad maximum at $\ell = 90$–$100\,\mathrm{pc}$ for $t > 1.45\,\mathrm{Gyr}$.

It is clear from each of Figures 6.1, 6.2 and 6.3, that the spectral properties of each of these fields are distinct. In addition, the properties of each field vary in time. The snapshots considered in this chapter, in the range $0.8 \le t \le 1.725\,\mathrm{Gyr}$, occur after the simulation has reached a hydrodynamic statistical state, which occurs at about 400 Myr. Thus, any changes in time result from the evolution of the mean-field dynamo, which evolves over a time-scale of order Gyr.

It would therefore seem most appropriate to select different smoothing lengths to obtain the fluctuations, depending on both the variable considered and the simulation time. However, complications would then arise with the interpretation of results obtained from such choices. The sensitivity of the results to any change in smoothing length would have to be considered. Theories based on a filtering approach to the MHD equations requires a consistent filter as the averaging operator. Hence, applying different smoothing lengths for each variable would introduce new difficulties when trying to interpret the mean fields and moments of the fluctuating fields as solutions of the filtered equations. In addition, complications could arise when selecting a smoothing scale for moments computed from multiple basic variables, such as the kinetic energy density $\frac{1}{2}\rho\boldsymbol{u}^2$. A time dependent smoothing length could be used, interpreted as a change in the grid scale of such

a simulation.

Hence, an appropriate value of ℓ that can be used as a smoothing length for all three variables throughout the times considered should be identified. $\ell = 75\,\mathrm{pc}$ is adopted as the smoothing length for magnetic field, gas density and gas velocity, since for magnetic field and gas density the local maxima in the ratios of the mean and fluctuating length scales occur close to 75 pc. For the gas velocity, the value of this ratio at 75 pc is above 90% of the asymptotic value in each period, whilst the value at 75 pc in the saturated period is very similar to the value at the broad local maximum.

6.4 Energy densities

Magnetic and kinetic energy densities have to be derived using the generalized central moments, as discussed in Section 6.2.1. The required moments are derived in Appendix B. Since the mean and fluctuating fields are sensitive to the choice of smoothing length, the resultant energies will also depend on ℓ. The maximum admissible value of ℓ is half the horizontal extent of the simulation domain. The results from the energy densities obtained with various smoothing lengths in the range $0 < \ell < 0.5\,\mathrm{kpc}$ are derived and discussed in this section. As previously, the three periods of the mean-field dynamo are considered independently and the results presented are averaged over the snapshots within each period.

6.4.1 Magnetic energy

The total magnetic energy density is given by

$$e_B = |\boldsymbol{B}|^2/(8\pi)\,,$$

with the energy density of the fluctuating magnetic field obtained as

$$e_b = \frac{1}{8\pi}\int_V |\boldsymbol{B}(\boldsymbol{x}') - \boldsymbol{B}_\ell(\boldsymbol{x})|^2\, G_\ell(\boldsymbol{x}-\boldsymbol{x}')\,\mathrm{d}^3\boldsymbol{x}'\,. \tag{6.16}$$

This ensures the energies of the mean and fluctuating magnetic fields sum to the energy of the (filtered) total magnetic energy, i.e.

$$\langle e_B\rangle_\ell = e_{B_\ell} + e_b\,, \tag{6.17}$$

where $e_{B_\ell} = |\boldsymbol{B}_\ell|^2/(8\pi)$ is the energy density of the mean magnetic field. It should be noted that $e_b \neq |\boldsymbol{b}|^2/(8\pi)$, but it can be shown, by expanding $\boldsymbol{B}(\boldsymbol{x}')$ in a Taylor series around $\boldsymbol{x}$, that $e_b = |\boldsymbol{b}|^2/(8\pi) + \mathcal{O}(\ell^2/L_{B_\ell}^2)$. Thus, the difference between the volume and filtering averages decreases as $\ell/L_{B_\ell} \to 0$. This fact, also true for any other variable, suggests one consideration for the choice of ℓ might be to maximise the ratio for L_{B_ℓ}/ℓ. In practice, however, this would simply lead to $\ell \to 0$; i.e. all the signal in the mean field, and effectively no decomposition.

The larger is ℓ, the smaller the part of the total field that is deemed to be the mean field and

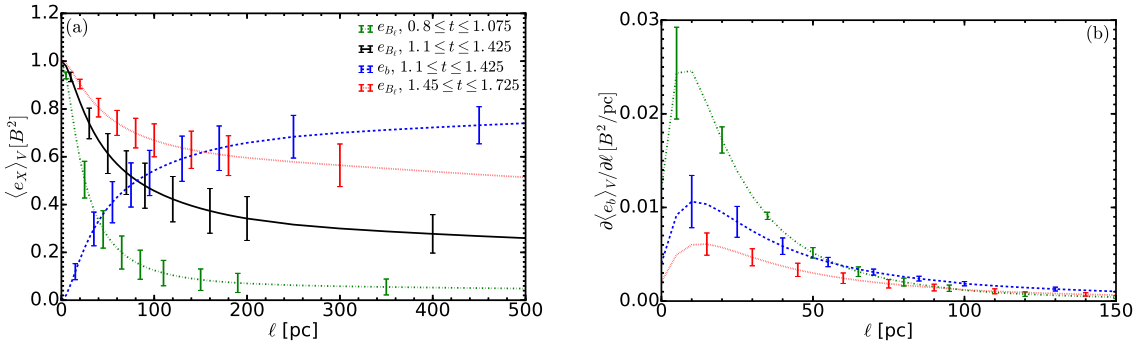

Figure 6.4: **(a)** Volume averages of the mean magnetic energy density $\langle e_{B_\ell} \rangle_V$ at times $0.8 \le t < 1.1\,\mathrm{Gyr}$ (green, dash-dotted), $1.1 \le t < 1.45\,\mathrm{Gyr}$ (black, solid) and $t \ge 1.45\,\mathrm{Gyr}$ (red, dotted); also the fluctuating magnetic energy density $\langle e_b \rangle_V$ at $1.1 \le t < 1.45\,\mathrm{Gyr}$ (blue, dashed), as functions of the smoothing length ℓ. These are normalised by the volume average of the smoothed magnetic energy density, $\langle \langle e_B \rangle_\ell \rangle_V$, with the volume averaging over the region $|z| < 0.5$. **(b)** Derivatives of $\langle e_b \rangle_V$, normalised by $\langle \langle e_B \rangle_\ell \rangle_V$, with respect to ℓ at $0.8 \le t < 1.1\,\mathrm{Gyr}$ (green, dash-dotted), $1.1 \le t < 1.45\,\mathrm{Gyr}$ (blue, dashed) and $t \ge 1.45\,\mathrm{Gyr}$ (red, dotted).

$\langle e_{B_\ell} \rangle_V$ monotonically decreases with ℓ whilst e_b monotonically increases, as shown in Fig. 6.4a. The rate of variation of $\langle e_b \rangle_V / \langle \langle e_B \rangle_\ell \rangle_V$ with ℓ, shown in Fig. 6.4b — and also of $\langle e_B \rangle_V / \langle \langle e_B \rangle_\ell \rangle_V$, not shown — becomes relatively small when $\ell > 50\,\mathrm{pc}$. This confirms that the appropriate choice for the smoothing length is $\ell > 50\,\mathrm{pc}$. (The difference between Figure 6.4a and Figure 2a of Gent et al. (2013b) is caused by a downsampling to a grid $\Delta x = 8\,\mathrm{pc}$ used in the Fourier transform for that calculation in Gent et al. (2013b).)

The mean magnetic energy grows with time due to dynamo action, and the value of ℓ for which the two energies are equal to each other increases. At late times, the mean magnetic field is energetically dominant over the fluctuating magnetic field for all ℓ.

6.4.2 Kinetic Energy

In a compressible flow, the mean kinetic energy density is represented by a third-order moment involving the density and velocity fields. Under ensemble (or volume) averaging, the mean kinetic energy density is conveniently — and physically meaningfully — represented (see Section 6.4 in Monin & Yaglom, 2007a) as

$$\begin{aligned} \langle e_K \rangle_V &= \tfrac{1}{2} \langle \rho u_i u_i \rangle_V \\ &= \tfrac{1}{2} \langle \rho \rangle_V \langle u_i \rangle_V \langle u_i \rangle_V + \langle u_i \rangle \langle \rho' u_i' \rangle_V + \tfrac{1}{2} \langle \rho u_i' u_i' \rangle_V \\ &\equiv e_s + e_{st} + e_t \,, \end{aligned} \tag{6.18}$$

where e_s is the energy density of the mean flow, e_t is the energy density of the fluctuations and e_st represents the transport of momentum $\langle \rho' u_i' \rangle$ by the mean flow (summation over repeated indices is understood here and below). An equivalent decomposition, demonstrated in detail in Appendix A

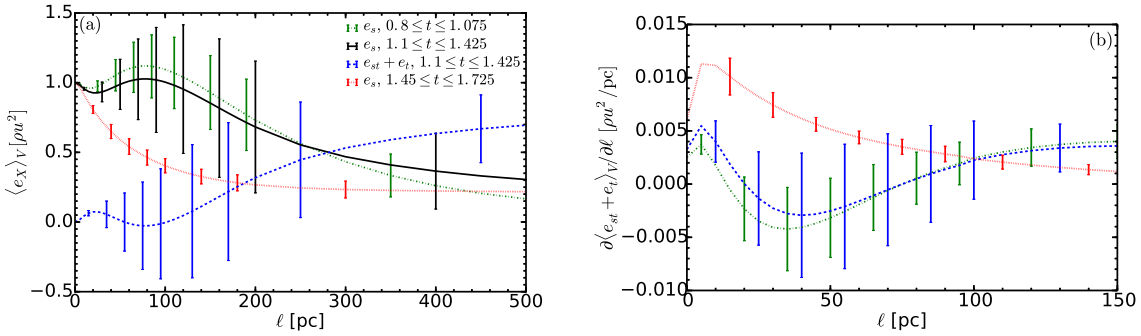

Figure 6.5: **(a)** As for Figure 6.4a but for the volume average of the mean kinetic energy density $\langle e_s \rangle_V$ at $0.8 \le t < 1.1$ Gyr (green, dash-dotted), $1.1 \le t < 1.45$ Gyr (black, solid) and $t \ge 1.45$ Gyr (red, dotted); with the volume average of the fluctuating kinetic energy density $\langle e_{st}+e_t \rangle_V$ at $1.1 \le t < 1.45$ Gyr (blue, dashed). These are normalised by the volume average of the smoothed kinetic energy $\langle \langle e_K \rangle_\ell \rangle_V$. **(b)** As Figure 6.4b but for the derivative of $\langle e_{st}+e_t \rangle_V$, with respect to ℓ (normalised by $\langle \langle e_K \rangle_\ell \rangle_V$); at $0.8 \le t < 1.1$ Gyr (green, dash-dotted), $1.1 \le t < 1.45$ Gyr (blue, dashed) and $t \ge 1.45$ Gyr (red, dotted).

is appropriate under the filtering approach as well:

$$\begin{aligned} \langle e_K \rangle_\ell &= \tfrac{1}{2} \langle \rho u_i u_i \rangle_\ell = e_s + e_{st} + e_t \,, \\ e_s &= \tfrac{1}{2} \langle \rho \rangle_\ell \langle u_i \rangle_\ell \langle u_i \rangle_\ell \,, \\ e_{st} &= \langle u_i \rangle_\ell \upsilon(\rho, u_i) \,, \\ e_t &= \langle e_K \rangle_\ell - e_s - e_{st} \\ &= \tfrac{1}{2} \langle \rho \rangle_\ell \upsilon(u_i, u_i) + \tfrac{1}{2} \upsilon(\rho, u_i, u_i) \,, \end{aligned} \tag{6.19}$$

where the moments involved are derived in Appendix B in explicit integral forms:

$$\begin{aligned} e_{st} =& \int_V \boldsymbol{u}(\boldsymbol{x}') G_\ell(\boldsymbol{x}-\boldsymbol{x}') \, \mathrm{d}^3\boldsymbol{x}' \cdot \int_V \Delta\rho_\ell(\boldsymbol{x},\boldsymbol{x}') \Delta\boldsymbol{u}_\ell(\boldsymbol{x},\boldsymbol{x}') G_\ell(\boldsymbol{x}-\boldsymbol{x}') \, \mathrm{d}^3\boldsymbol{x}' \,, \\ e_t =& \tfrac{1}{2} \int_V \rho(\boldsymbol{x}') G_\ell(\boldsymbol{x}-\boldsymbol{x}') \, \mathrm{d}^3\boldsymbol{x}' \int_V |\Delta\boldsymbol{u}_\ell(\boldsymbol{x},\boldsymbol{x}')|^2 G_\ell(\boldsymbol{x}-\boldsymbol{x}') \, \mathrm{d}^3\boldsymbol{x}' \\ &+ \tfrac{1}{2} \int_V \Delta\rho_\ell(\boldsymbol{x},\boldsymbol{x}') |\Delta\boldsymbol{u}_\ell(\boldsymbol{x},\boldsymbol{x}')|^2 G_\ell(\boldsymbol{x}-\boldsymbol{x}') \, \mathrm{d}^3\boldsymbol{x}' \,, \end{aligned} \tag{6.20}$$

where $\Delta\rho_\ell(\boldsymbol{x},\boldsymbol{x}') = \rho(\boldsymbol{x}') - \rho_\ell(\boldsymbol{x})$ and $\Delta\boldsymbol{u}_\ell(\boldsymbol{x},\boldsymbol{x}') = \boldsymbol{u}(\boldsymbol{x}') - \boldsymbol{u}_\ell(\boldsymbol{x})$.

Figure 6.5 shows how various parts of the kinetic energy density depend on the smoothing length ℓ. The behaviour of the volume averages of these contributions to the kinetic energies is much less straightforward than for magnetic energy, except for $t > 1.45$ Gyr where similar monotonic dependence on ℓ is observed. Additionally for both $0.8 \le t < 1.1$ Gyr and $1.1 \le t < 1.45$ Gyr, we observe that the fluctuating kinetic energy $e_{st}+e_t$ is equal to zero within errors for $50 \le \ell \le 100$ pc. This results from cancellation between $\langle e_{st} \rangle_V$ and $\langle e_t \rangle_V$, with $\langle e_{st} \rangle_V$ significantly negative, as confirmed by Figure 6.7. The quantity $e_{st} = \langle u_i \rangle_\ell \upsilon(\rho, u_i)$ is dominated by the contribution of the z-component of the velocity field ($i = 3$) since $\langle u_z \rangle_\ell$ is much larger than

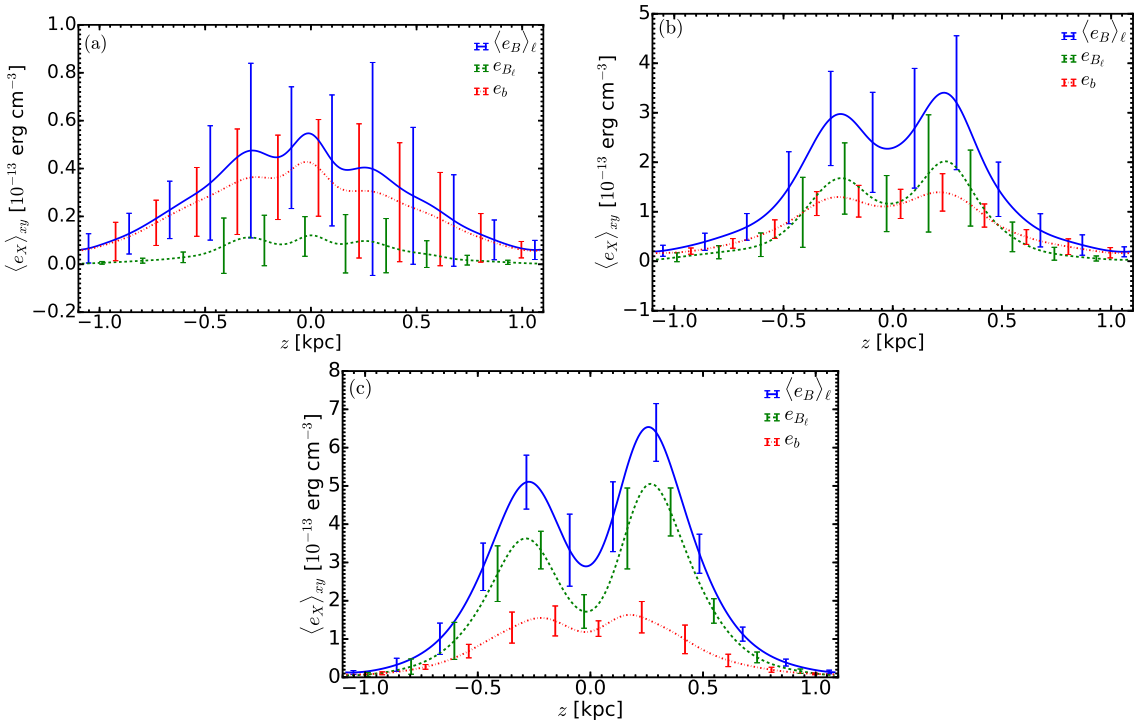

Figure 6.6: Vertical profiles of the horizontal averages of the smoothed total magnetic energy, $\langle\langle e_B\rangle_\ell\rangle_{xy}$ (blue, solid), mean magnetic energy, $\langle e_{B_\ell}\rangle_{xy}$ (green, dashed), and fluctuating magnetic energy, $\langle e_b\rangle_{xy}$ (red, dash-dotted); at times **(a)** $0.8 \leq t < 1.1\,\mathrm{Gyr}$, **(b)** $1.1 \leq t < 1.45\,\mathrm{Gyr}$ and **(c)** $t \geq 1.45\,\mathrm{Gyr}$. The smoothing length applied for each snapshot is $\ell = 75\,\mathrm{pc}$.

the x- and y- components because of a systematic gas outflow from the mid-plane.

The supernovae contain large values of $\langle u_z\rangle_\ell$ and the gas involved in the outflow is hotter and less dense than on average, leading to large negative values of $-\langle\rho\rangle_\ell\langle u_z\rangle_\ell$ for $z > 0$ and, hence, of $\langle u_z\rangle_\ell\, \upsilon(\rho, u_z) = \langle u_z\rangle_\ell\,(\langle\rho u_z\rangle_\ell - \langle\rho\rangle_\ell\langle u_z\rangle_\ell)$ (the dominant component of e_{st}).

For $z < 0\,\mathrm{kpc}$, the mean vertical velocity in the supernovae $\langle u_z\rangle_\ell$ is large and negative, resulting in large, positive values for $\upsilon(\rho, u_z) = \langle\rho u_z\rangle_\ell - \langle\rho\rangle_\ell\langle u_z\rangle_\ell$. Thus, the opposite signs of $\langle u_z\rangle_\ell$ and $\upsilon(\rho, u_z)$ result in large, negative values of e_{st} for negative z. These large, negative values for e_{st} appear to dominate the kinetic energy statistics during earlier snapshots. This is discussed in more detail below.

The variation with ℓ of the fluctuating kinetic energy produces a more complicated pattern than for fluctuating magnetic energy, see Figure 6.5. The values of ℓ for which the variation is weak are $\ell > 300\,\mathrm{pc}$. Such a smoothing length is much larger than any estimate of the correlation scale of the random motions, and the optimal smoothing lengths of both ρ or $\boldsymbol{u}$. As a result, the criterion that the variation of the fluctuating kinetic energy must be weak is not an appropriate method for choosing suitable smoothing lengths for either ρ or $\boldsymbol{u}$.

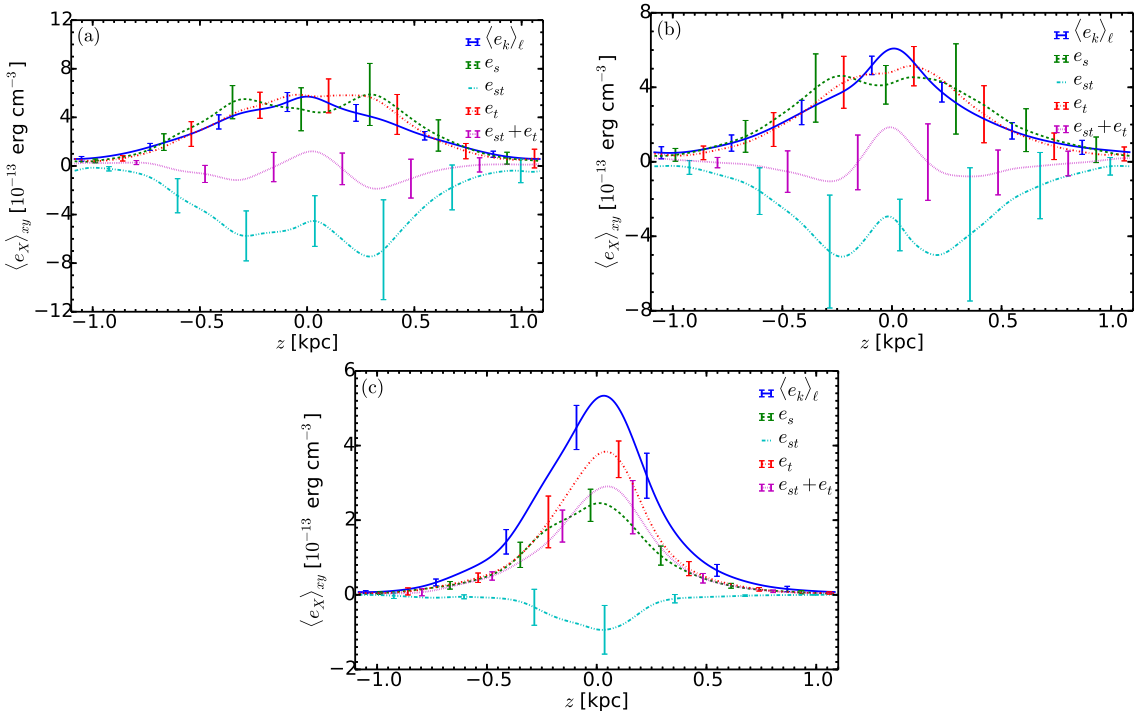

Figure 6.7: As for Figure 6.6 but for the smoothed total kinetic energy density $\langle\langle e_K\rangle_\ell\rangle_{xy}$ (blue, solid), mean kinetic energy density $\langle e_s\rangle_{xy}$ (green, dashed), 'intermediate scale' kinetic energy density $\langle e_{st}\rangle_{xy}$ (cyan, dash-dot-dotted), fluctuating kinetic energy density $\langle e_t\rangle_{xy}$ (red, dot-dashed), and the sum, $\langle e_{st}+e_t\rangle_{xy}$ (purple, dotted); at times **(a)** $0.8 \leq t < 1.1\,$Gyr, **(b)** $1.1 \leq t < 1.45\,$Gyr and **(c)** $t \geq 1.45\,$Gyr. As for Figure 6.6, the smoothing length applied is $\ell = 75\,$pc.

6.5 Influence of the mean-field dynamo

Figures 6.4 and 6.5 both suggest that the structure of magnetic and kinetic energies vary with the state of the mean-field dynamo. The vertical structure of both energies are examined, comparing the three time ranges discussed previously, to demonstrate the changes in structure caused by the dynamo.

At early times, when the fluctuating magnetic field dominates the mean field, the magnetic field is strongest at $|z| = 0.3\,$kpc where the kinetic energy is maximal, see Figures 6.6a and 6.7a.

As the mean field dynamo saturates, the mean magnetic field dominates compared to the fluctuating field. The vertical profile of the smoothed total magnetic energy corresponds to the mean magnetic energy. The peaks of the vertical profiles remain at $|z| = 0.3\,$kpc, see Figures 6.6b,c.

The increasing mean magnetic field significantly alters the vertical profile of the kinetic energy, as shown in Figures 6.7b,c. All the components in the division of kinetic energy are concentrated towards the mid-plane and the maximum value of $\langle e_K\rangle_\ell$ decreases.

Strong mean magnetic fields generated via dynamo action in the same ISM simulations have been shown to suppress outflows of hot gas (see Evirgen et al., 2017), which are associated with high values of kinetic energy. This would lead to a vertical profile of kinetic energy with the

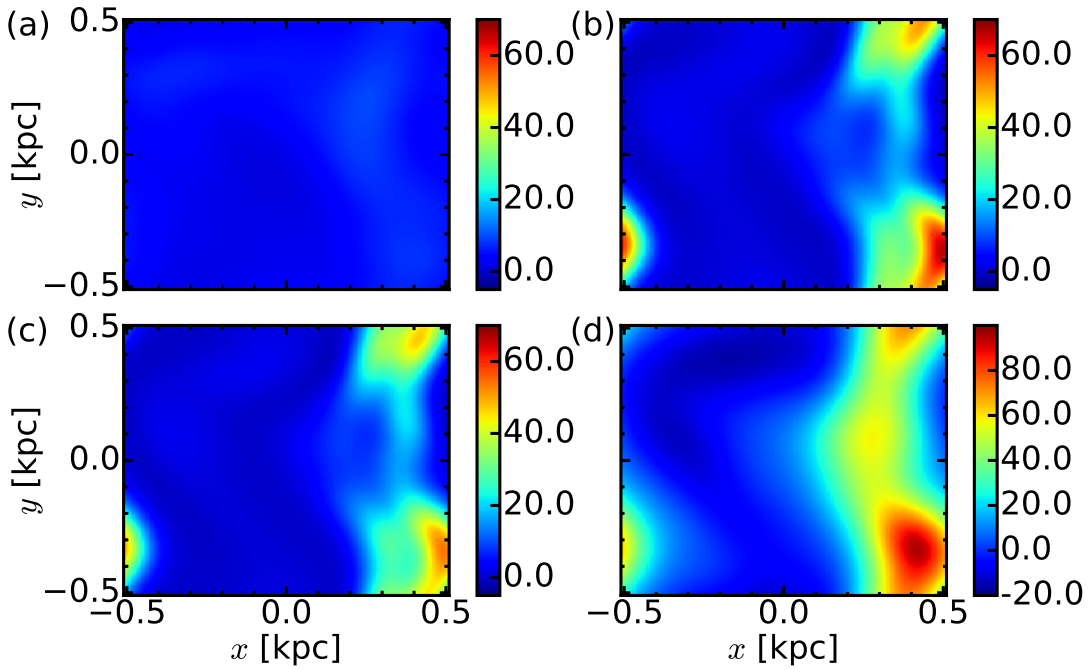

Figure 6.8: Horizontal slices of **(a)** the smoothed total kinetic energy density $\langle e_K \rangle_\ell$, **(b)** the 'intermediate-scale' kinetic energy density e_{st}, **(c)** $\langle u_z \rangle_\ell \mu(\rho, u_z)$ the vertical contribution to e_{st}, all in units of $10^{-13}\,\mathrm{erg\,cm^{-3}}$, and **(d)** the mean vertical velocity $\langle u_z \rangle_\ell$ (bottom-right panel) in $\mathrm{km\,s^{-1}}$; at $z = 290\,\mathrm{pc}$ from the snapshot $t = 0.8\,\mathrm{Gyr}$. The smoothing length used is $\ell = 75\,\mathrm{pc}$.

characteristics present in Figure 6.7c.

The most dramatic change is the effect on the 'intermediate scale' component of the kinetic energy, e_{st}. As the magnetic field strength increases, the horizontal average of e_{st} decreases significantly, becoming almost equal to zero except near to the mid-plane. As a result, the kinetic energy is approximately split between the mean and small-scale energies e_s and e_t.

As this change appears to be the most significant, particular attention is made to the horizontal planes from the snapshots $t = 0.8\,\mathrm{Gyr}$ and $t = 1.6\,\mathrm{Gyr}$, at which the vertical profiles of e_{st} shown in Figure 6.7 show the most profound differences.

In the kinematic stage of the mean-field dynamo, there are regions in which e_{st} is significantly non-zero, whilst $\langle e_K \rangle_\ell$ is uniform by comparison (see Figure 6.8). The mean and turbulent kinetic energies, e_s and e_t respectively, also exhibit highly non-zero behaviour in the same regions as e_{st}, although these are not demonstrated here. The contribution from the z–component of e_{st}, $\langle u_z \rangle_\ell \upsilon(\rho, u_z)$, comprises a large fraction of the total quantity (about 80%) and so the vertical behaviour is dominant for e_{st} at this stage. The values for which e_{st} is highest strongly coincide with regions of large positive $\langle u_z \rangle_\ell$, which are the regions of hot gas outflows. Thus, at the kinematic stage of the mean-field dynamo, e_{st} is strongly correlated with the outflows of hot gas. In this model, the mean magnetic field is absent from the regions of hot gas, as demonstrated by Evirgen et al. (2017). Thus, the mean magnetic field also avoids regions in which e_{st} is strongly non-zero.

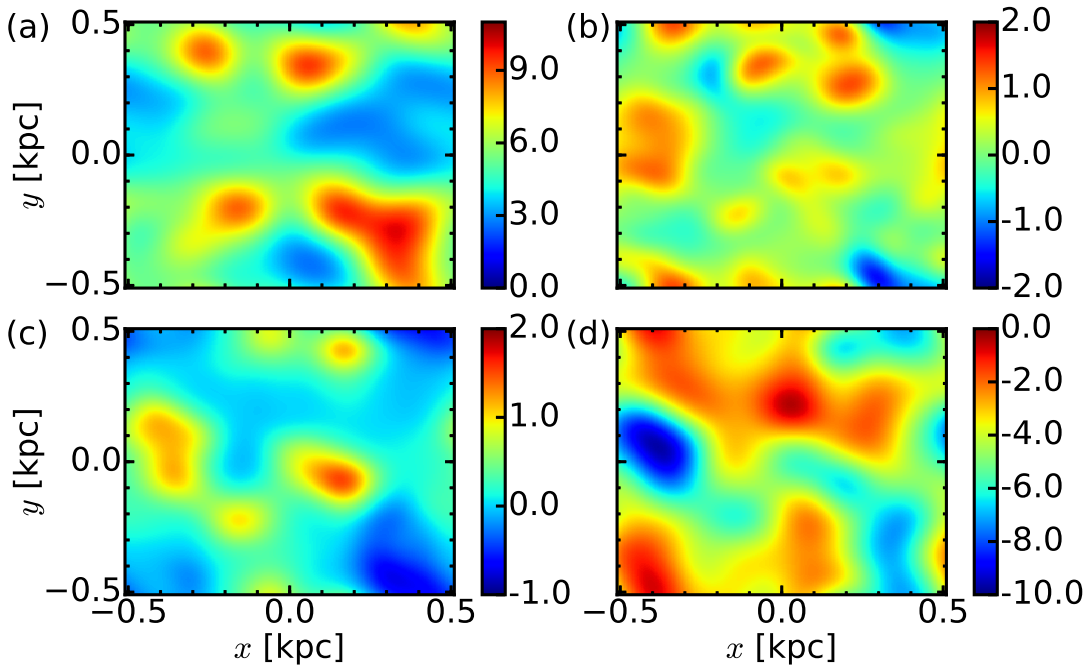

Figure 6.9: As for Figure 6.8 but in the plane $z = 30\,\mathrm{pc}$, at time $t = 1.6\,\mathrm{Gyr}$.

The action of the amplified mean magnetic field on the kinetic energies is demonstrated in Figure 6.9. The values of e_{st} are reduced significantly and e_{st} appears more uniform. By contrast, $\langle e_K \rangle_\ell$ is now more significant and the non-uniform structure of $\langle e_K \rangle_\ell$ is much more clear. The vertical contribution to e_{st} is also dramatically reduced and is no longer the dominant contribution. The mean vertical velocity is reduced both in maximal value and in the size of regions in which $\langle u_z \rangle_\ell$ is highly non-zero, indicative of the reduction of hot gas outflows. Thus, the partial suppression of the hot gas outflows by the mean magnetic field has both significantly reduced the value of e_{st} and resulted in behaviour of the overall kinetic energy becoming independent of the behaviour of e_{st}.

6.6 Discussion

Gaussian smoothing is applied to obtain mean fields for magnetic field, density and velocity. The optimal smoothing lengths were obtained by spectral analysis of each field independently. $\ell = 75\,\mathrm{pc}$ is an appropriate smoothing length to use for each of these fields.

The differing spectral behaviour of the magnetic, density and velocity fields is unsurprising, since their structures are controlled by different physical processes, even though they do not evolve independently,. The structure of the fluctuating fields, obtained using Gaussian smoothing with a filtering length of 50 pc, are distinct, as shown in Chapter 5.

The mean and fluctuating magnetic and kinetic energies are examined, using the idea of the

generalised central moments from Germano (1992) for the definitions of the fluctuating energies. The dependencies of the energies on both ℓ and the magnetic dynamo are examined.

Amplification of the mean magnetic field by dynamo action has a significant impact on the subdivisions of the magnetic and kinetic energies. As the dynamo saturates, the energy of the mean field dominates compared to the fluctuating field. Throughout the run, the magnetic field is strongest at $|z| = 300\,\mathrm{pc}$.

Increasing mean magnetic field results in the location of the maximum of the vertical profile of kinetic energy shifting from $|z| = 300\,\mathrm{pc}$ to the mid-plane. The intermediate scale kinetic energy e_{st} is closely correlated with outflows, which are partly suppressed by the growing mean magnetic field. This results in a dramatic reduction in e_{st} at late times in the simulation, when the kinetic energy is largely split between the large-scale kinetic energy, e_s, and the small-scale kinetic energy e_t.

In the simulations considered here, the intermediate kinetic energy density e_{st} is therefore a useful diagnostic for the presence of outflows; it clearly isolates an energy transfer of interest, allowing insight into some important physical processes within the system. It will therefore be of great interest to consider similar decompositions of the energy densities in other contexts, where similar insights may be possible.

Part IV

Impact of supernova rate

Chapter 7

Impact of supernova rate on the multi-phase structure

The ISM is frequently described as a multi-phase system, with thermodynamically distinct regions of cold, warm and hot gas (Field et al., 1969; Cox & Smith, 1974; McKee & Ostriker, 1977), which co-exist in pressure equilibrium. These theoretical postulations are based on the existence of distinct, thermally stable states within the interstellar gas, usually termed phases. Observations of the ISM confirm the existence of gas at the typical temperatures of the cold $T \simeq 10^2$ K, warm $T \simeq 10^4$ K and hot $T \simeq 10^6$ K phases.

Turbulence in the ISM is thought to complicate this description. Heating and shocks from supernovae generate bubbles of hot gas which ballistically propel a surrounding shell of cold, dense gas. It may be possible that the phases observed are different transients within a perturbed medium, with a random distributions of pressures, in which the regions of gas with different temperatures occupy different parts of a continuum of a qualitatively homogeneous gas.

Nonetheless, examining the ISM as distinct phases retains several advantages. Making statistical inferences on data spanning at least 6 orders in both density and temperature is highly unreliable. The assumption of phases allows for the analysis on more discrete data sets, in which the characteristics are better understood.

Thermodynamically distinct phases are found to exist within turbulent ISM simulations (see de Avillez & Breitschwerdt, 2004; Hill et al., 2012; Gent et al., 2013b, as examples), with temperature boundaries of the cold and hot gas typically occurring at $T \simeq 10^2$–10^3 K and $T \simeq 10^{5.5}$–10^6 K respectively. The fractional volumes of each phase vary with supernova rate, as demonstrated by de Avillez & Breitschwerdt (2004) who investigated supernova rates between 1 and 16 times the rate in the Solar neighbourhood. They examined the dependence of the fractional volumes of four phases; cold ($T \leq 10^3$ K), cool ($10^3 < T \leq 10^4$ K), warm ($10^4 < T \leq 10^{5.5}$ K) and hot ($T > 10^{5.5}$ K), on the supernova rate. As the supernova rate is increased from 1 to 16 times the rate in the Solar neighbourhood, the fractional volumes of the cold and cool gas decrease from 19%

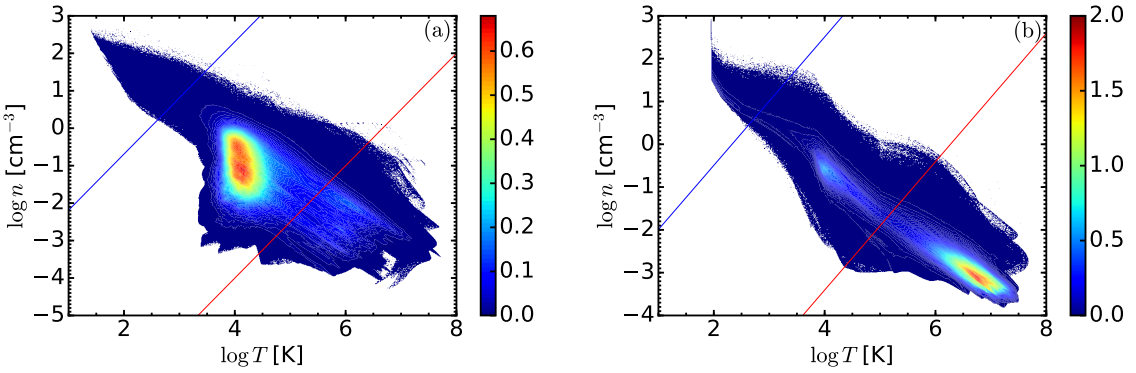

Figure 7.1: Contour plots of the two-dimensional PDFs of $\log n$ and $\log T$ from the models **(a)** H1$\Omega_{\rm ref}$ and **(b)** H1$\Omega_{\dot{\sigma}=1.0}$. In both models, the data is from 12 snapshots over an interval of 300 Myr in the statistical steady state. The blue and red lines denote the boundaries of the the cold and hot gas, corresponding to $s = 3.7 \times 10^8\,\mathrm{erg\,g^{-1}\,K^{-1}}$ and $s = 4.33 \times 10^8\,\mathrm{erg\,g^{-1}\,K^{-1}}$, and $s = 23.2 \times 10^8\,\mathrm{erg\,g^{-1}\,K^{-1}}$ and $s = 25.65 \times 10^8\,\mathrm{erg\,g^{-1}\,K^{-1}}$ respectively.

and 39% to $\approx 0\%$ and 2% respectively, whereas the fractional volumes of the warm and hot gas increase from 25% and 17% to 54% and 44% respectively. As the supernova rate increases, the cold gas is depleted by increased Lyman continuum photon absorption and shock heating, whilst the cool gas is more efficiently heated to form larger amounts of warm and hot gas.

In this chapter, I first compare the model H1$\Omega_{\dot{\sigma}=1.0}$ to reference model H1$\Omega_{\rm ref}$. I shall then report on the impact of the supernova rate on the multi-phase structure of the ISM by investigating the changes in the relative abundances of each phase, and the characteristics of each phase, with supernova rate. The multi-phase structure impacts upon the vertical structure of the ISM, and so the sensitivity of the vertical structure to the supernova rate is also discussed.

7.1 Comparison to the Previous Model

I shall first examine the distributions of number density n and temperature T, and determine if the definitions of the phases from my results are comparable to those determined previously in Gent (2012); Gent et al. (2013b).

As demonstrated in Figure 7.1, the distributions of n and T between the two reference models show dramatic difference. Whilst the peak for the warm gas in both models is at $(n,T) \simeq (10^{-1}\,\mathrm{cm^{-3}}, 10^4\,\mathrm{K})$, the modal hot gas temperature is close to $10^7\,\mathrm{K}$ in H1$\Omega_{\dot{\sigma}=1.0}$, as opposed to a value of approximately $10^6\,\mathrm{K}$ from H1$\Omega_{\rm ref}$. In addition, there appears to be much larger fraction of hot gas in H1$\Omega_{\dot{\sigma}=1.0}$, as confirmed in Figure 7.2, this is discussed in more detail in Section 7.2. H1$\Omega_{\rm ref}$ admits lower temperatures, with the minimum temperature $T \simeq 30\,\mathrm{K}$, whilst there is a cutoff at $T \simeq 10^2\,\mathrm{K}$ in H1$\Omega_{\dot{\sigma}=1.0}$, most likely related to changes in the cooling function, as highlighted in Section 7.2. However, the maximal density of the cold gas increases in H1$\Omega_{\dot{\sigma}=1.0}$ to $n \simeq 10^3\,\mathrm{cm^{-3}}$, hence the removal of the cooling cutoff in the shocks results in formation of higher

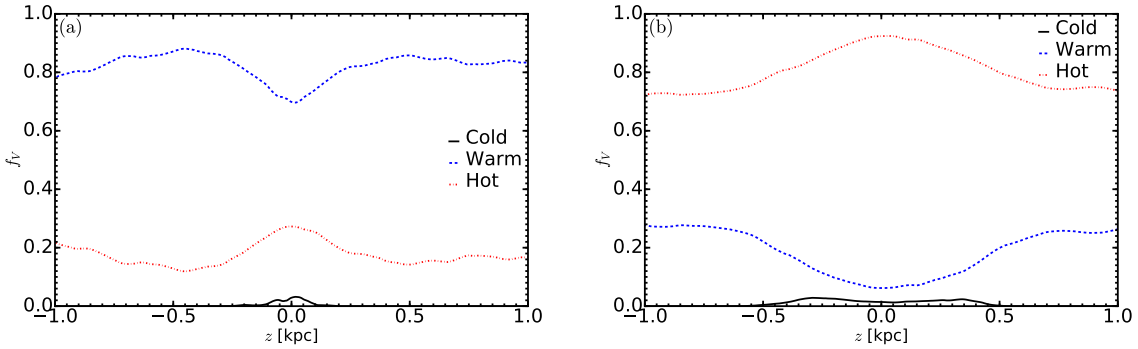

Figure 7.2: Comparison of the fractional volumes of the cold (black, solid), warm (blue, dashed) and hot (red, dot-dashed) phases as functions of height; for **(a)** H1$\Omega_{\rm ref}$ and **(b)** the model H1$\Omega_{\dot{\sigma}=1.0}$. Each plot uses data from the same snapshots as Figure 7.1.

density gas.

Despite the greater abundance of hot gas, I shall attempt to define cold, warm and hot phases in the model H1$\Omega_{\dot{\sigma}=1.0}$, similar to those determined in (Gent, 2012; Gent et al., 2013b). It was found that separation into phases by entropy leads to more stable results than using temperature, and so I shall proceed with phase definitions via entropy. Whilst specific entropy is not an observable quantity and its interpretation is much less intuitive than temperature, it can be calculated easily from simulation data. Additionally, separation by entropy allows also for the calculation of the distribution of temperature within each phase.

In an ideal gas, specific entropy is related to density and temperature via the following relation

$$s = c_v[\ln T - \ln T_0 - (\gamma - 1)(\ln \rho - \ln \rho_0)], \tag{7.1}$$

where c_v is the specific heat capacity at constant volume and $\gamma = 5/3$ is the adiabatic index. When $T = T_0$ and $\rho = \rho_0$, $s = 0$. In Figures 7.1 and 7.4, lines of constant entropy are indicated by $\log n - 1.5 \log T =$ constant. The blue and red lines mark the boundaries between the cold and warm phases and the warm and hot phases respectively, defined where the lines of constant entropy intersect the local minima, in the joint PDF of $\log n$ and $\log T$.

From the right panel of Figure 7.1, the cold phase in the model H1$\Omega_{\dot{\sigma}=1}$ is defined as $s < 4.3 \times 10^8\,\mathrm{erg\,g^{-1}\,K^{-1}}$, whilst the hot phase is defined as $s > 25.7 \times 10^8\,\mathrm{erg\,g^{-1}\,K^{-1}}$. The warm phase occupies the intermediate entropy values. These boundaries for the cold and hot phases are comparable to those in Gent (2012); Gent et al. (2013b), who determined $s < 3.7 \times 10^8\,\mathrm{erg\,g^{-1}\,K^{-1}}$ and $s > 23.2 \times 10^8\,\mathrm{erg\,g^{-1}\,K^{-1}}$ as the cold and hot phase boundaries respectively, shown in the left- and panel of Figure 7.1.

To further test the conclusions regarding the hot gas in the model H1$\Omega_{\dot{\sigma}=1.0}$, as compared to H1$\Omega_{\rm ref}$, I shall compare the fractional volumes of each of the phases in both models. The fractional

Table 7.1: The fractional volumes of the cold, warm and hot gas in the models H1$\Omega_{\rm ref}$, H1$\Omega_{\dot{\sigma}=0.5}$, H1$\Omega_{\dot{\sigma}=1.0}$ and H1$\Omega_{\dot{\sigma}=1.5}$, as a percentage of the total domain. In each model, the data is from 12 composite snapshots in an interval of 300 Myr.

Model	Fractional volume (%)		
	Cold gas	Warm gas	Hot gas
H1$\Omega_{\rm ref}$	0.2	81.8	18.0
H1$\Omega_{\dot{\sigma}=0.5}$	0.5	38.3	61.2
H1$\Omega_{\dot{\sigma}=1.0}$	0.8	19.5	79.7
H1$\Omega_{\dot{\sigma}=1.5}$	0.9	15.4	83.7

volume of the ISM occupied by a given phase i is calculated as

$$f_{V,i} = \frac{V_i}{V}, \tag{7.2}$$

where V_i is the volume occupied by phase i and V is the total volume. This can be computed easily within an ISM simulation by counting the number of mesh points each phase occupies.

Comparison of the fractional volumes for each phase are shown in Figure 7.2. In H1$\Omega_{\rm ref}$, the fractional volume of the hot gas increases moderately with height for $|z| \gtrsim 500$ pc, with a local maximum at the mid-plane resulting from a higher concentration of SN remnants. The cold gas is concentrated within 100 pc of the mid-plane. The warm phase is the most prevalent throughout the entire domain, occupying over 80% of the total volume, as shown in Table 7.1.

In contrast, for H1$\Omega_{\dot{\sigma}=1.0}$, the hot gas dominates throughout the domain, occupying roughly 80% of the total volume, with the greatest abundance at the mid-plane, again as a consequence of the greatest concentration of SNe at the mid-plane. The fractional volume of warm gas increases with height, particularly for $|z| \lesssim 500$ pc. This suggests over-heating of the gas and insufficient cooling of the hot gas, which is discussed in more detail below. The insufficient cooling likely explains the increasing fractional volume of warm gas with height, since an increased cooling time from the reduction in cooling results in the SN remnants travelling greater distances in height before the hot gas cools into warm gas. A much greater amount of cold gas is produced in H1$\Omega_{\dot{\sigma}=1.0}$ than in H1$\Omega_{\rm ref}$ (see Table 7.1), resulting from the removal of the cooling cutoff in the shocks for H1$\Omega_{\dot{\sigma}=1.0}$. The cold gas is also carried by SN remnants to much larger heights, $\gtrsim 400$ pc, since each individual remnant would travel faster through a hotter and more diffuse medium.

7.2 Fractional volume of the hot gas

From Figures 7.1 and 7.2, it is clear that the fractional volume of the hot gas and its modal temperature in the model H1$\Omega_{\dot{\sigma}=1.0}$ are both much higher than expected from either observations or previous Solar-neighbourhood ISM simulations. For example, Ferrière (1998) provide an estimate of 20% for the fractional volume of the hot gas in the Solar neighbourhood, with superbubbles

providing the largest contribution. With a supernova rate equal to the Galactic supernova rate de Avillez & Breitschwerdt (2004) find the fractional volume of the hot gas is approximately 17%. As shown in Table 7.1, the fractional volume of close to 80% for the hot gas in the model $\mathrm{H1}\Omega_{\dot{\sigma}=1.0}$, with similar fractional volumes for both $\mathrm{H1}\Omega_{\dot{\sigma}=0.5}$ and $\mathrm{H1}\Omega_{\dot{\sigma}=1.5}$, is significantly higher than in the model $\mathrm{H1}\Omega_{\mathrm{ref}}$, which has a fractional volume of hot gas of approximately 20%.

With a similar implementation using the PENCIL code able to both reproduce the Sedov-Taylor solution to reasonable accuracy and produce results of the multi-phase ISM with fractional volumes more similar to those expected (see Gent et al., 2013b), it is clear that the issue is as a result of the changes made to the numerical implementation, rather than from a physical effect such as the energy injected from SNe. Given the complexity of ISM simulations, it is perhaps unsurprising that changes to certain parameters or aspects of the numerical model can lead to some unexpected results.

These changes have resulted in increased heating of the surrounding ambient gas by the individual supernova remnants. The presence of such large regions of hot gas suggest the hot gas is also being cooled less efficiently than previously. Over time, the ISM continues to be heated to higher temperatures and so the gas within each subsequent SN remnant is cooled less before it merges with the hotter ambient medium, which results in increasing modal temperature in the hot gas until a new thermodynamic equilibrium is established. Thus, the simulations reported here cannot be interpreted as accurate representations of the ISM in the Solar neighbourhood. However, they remain useful as predictions of the effects of the supernova rate on the ISM, since all three models are comparable.

The most significant changes made were to the mean molecular weight, the thermal diffusivity and the handling of cooling and heating in the shocks. The impact of the changes in mean molecular weight and shock handling will be investigated here.

The effect of the removal of the damping of cooling in the shocks is the removal of the artificial limit of the cooling of the gas in the shocks. This would enable more cold gas to be produced and allow this gas to be more dense. However, this results in a higher proportion of the mass concentrated in a very small fraction of the volume. As a result, the thermal energy from the supernovae is injected into a smaller mass of surrounding gas, which for constant thermal energy injected per supernova results in the gas being heated to higher temperatures.

The effect of changing μ is more subtle since the code solves for entropy, rather than temperature directly. It appears in the heat equation (3.3) via the specific heat capacities;

$$c_p = \frac{\gamma R}{\mu(\gamma-1)}, \quad c_v = \frac{c_p}{\gamma}, \tag{7.3}$$

where $R = k_{\mathrm{B}}/m_u$ is the gas constant, $k_{\mathrm{B}} = 1.380658 \times 10^{-16}\,\mathrm{erg\,K^{-1}}$ the Boltzmann constant and $m_u = 1.6605402 \times 10^{-24}\,\mathrm{g}$ the atomic mass unit. Although if the unit temperature, and by association unit specific entropy, is properly scaled no significant issue should arise when computing

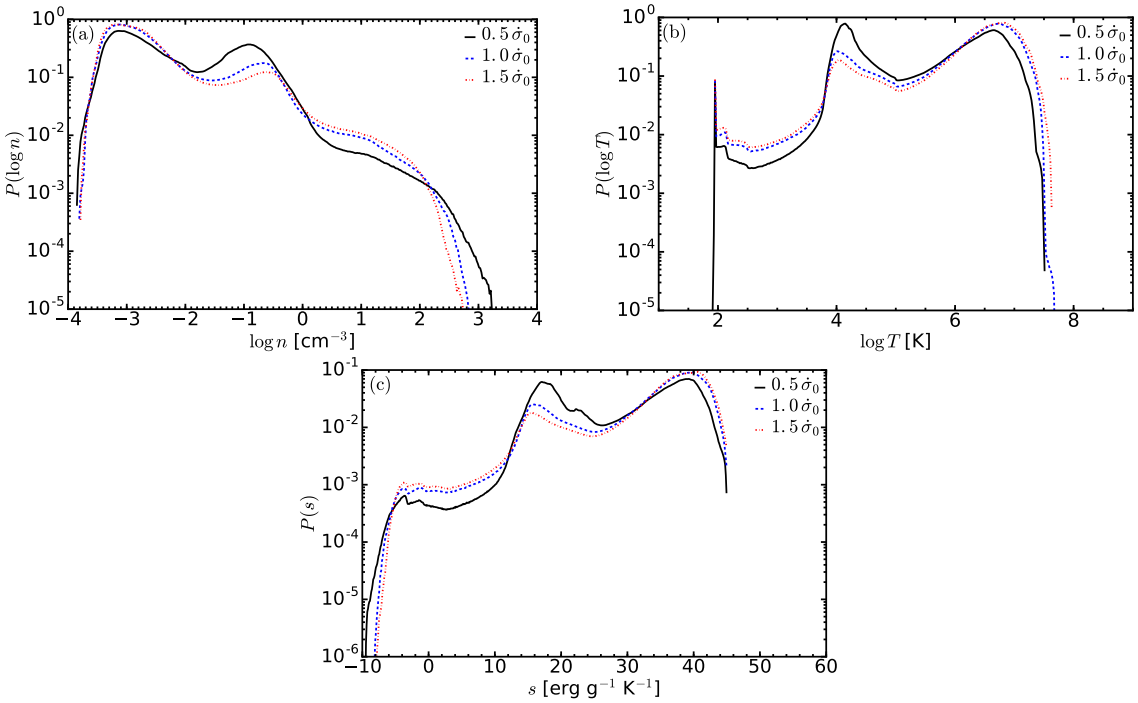

Figure 7.3: Logarithms of the PDFs of **(a)** $\log n$, **(b)** $\log T$ and **(c)** s, from the models H1$\Omega_{\dot{\sigma}=0.5}$ (black, solid), H1$\Omega_{\dot{\sigma}=1.0}$ (blue, dashed) and H1$\Omega_{\dot{\sigma}=1.5}$ (red, dot-dashed). The results are obtained from 12 composite snapshots over a time-span of 300 Myr in the statistical steady state for each model.

in code units. However, μ also appears in the cooling function, Λ, which is used in the radiative cooling term $\rho^2\Lambda$ and depends on number density squared instead of mass density squared. The WSW cooling function in Table 3.1 has been converted to be calculated for mass density instead of number density by dividing by the the square of the atomic mass $m_u = 1.6728 \times 10^{24}$ g only, which assumed $\mu = 1.0$. Hence, the values in Table 3.1 should have been multiplied by a factor of $1/\mu^2$, and so the cooling is significantly weaker than if the cooling functions had been computed using number density. Whilst this would also affect the simulations in Gressel et al. (2008a); Gent et al. (2013b,a), who use $\mu = 0.6$ and $\mu = 0.62$ respectively, this did not appear to have a significant impact on the results. Further reducing the mean molecular weight to $\mu = 0.531$ results in the cooling function being too small by a factor of approximately 3.55, instead of approximately 2.6 previously. This would result in a further reduction reduction of the radiative cooling in the hot gas. Thus, when SN remnants merge with the background ISM, the interation of the hotter interior gas with the ambient medium results in greater heating of the gas throughout the domain.

7.3 Identifying the multi-phase structure via entropy

Despite the high abundance of hot gas in the model H1$\Omega_{\dot{\sigma}=1.0}$, a multi-phase structure with the phases defined using specific entropy can be determined. Thus, by examining the PDFs of both

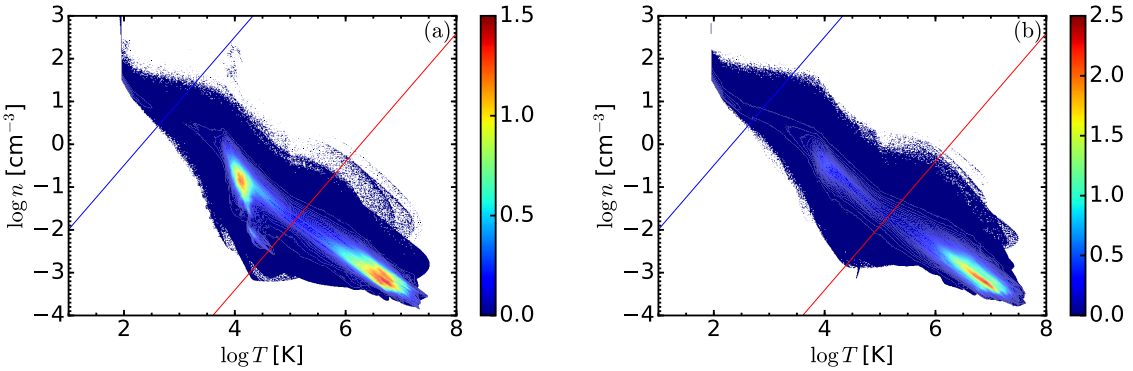

Figure 7.4: Contour plot of the two-dimensional PDF of $\log n$ versus $\log T$ from the models; **(a)** H1$\Omega_{\dot{\sigma}=0.5}$ and **(a)** H1$\Omega_{\dot{\sigma}=1.5}$. As for Figure 7.1, 12 snapshots over intervals of 300 Myr in the statistical steady state for each model are used. The blue and red lines denote the same phase boundaries as in the Figure 7.1b.

$\log n$ and $\log T$ for the models H1$\Omega_{\dot{\sigma}=0.5}$ and H1$\Omega_{\dot{\sigma}=1.5}$, it is possible to establish a definition of the cold, warm and hot phases via specific entropy that is effective regardless of supernova rate. The use of common phase boundaries for each model would be useful since it allows for a clearer comparison between the characteristic properties of the phases in each model.

The PDFs of $\log n$, $\log T$ and s shown in Figure 7.3 suggest the presence of common features in the density, temperature and entropy distributions in each model. For the model H1$\Omega_{\dot{\sigma}=0.5}$, there exists a peak at $n \simeq 10^{-0.9}\,\mathrm{cm}^{-3}$, $T \simeq 10^{4.1}\,\mathrm{K}$ and $s \simeq 17\,\mathrm{erg\,g^{-1}\,K^{-1}}$, and one at $n \simeq 10^{-3.1}\,\mathrm{cm}^{-3}$, $T \simeq 10^{6.6}\,\mathrm{K}$ and $s \simeq 39\,\mathrm{erg\,g^{-1}\,K^{-1}}$, corresponding to the warm and hot phases respectively. There also exists a minimum at $n \simeq 10^{-1.8}\,\mathrm{cm}^{-3}$, $T \simeq 10^{5.1}\,\mathrm{K}$ and $s \simeq 26\,\mathrm{erg\,g^{-1}\,K^{-1}}$, indicating a boundary between the warm and hot phases can be defined. Whilst there exist no such clear features for the cold phase and a cold/warm phase boundary in the distributions of $\log n$ and s, there exists a peak at $T \simeq 10^{2}\,\mathrm{K}$ and a minimum at $T \simeq 10^{2.5}\,\mathrm{K}$, which suggests distinct cold and warm phases can be obtained in these simulations. The shark peak near $T \simeq 10^{2}\,\mathrm{K}$ is a consequence of the truncation of the cooling function.

For the higher supernova rate runs, the peaks for the warm and hot phases are located at $n \simeq 10^{-0.5}\,\mathrm{cm}^{-3}$, $T \simeq 10^{4}\,\mathrm{K}$ and $s \simeq 16\,\mathrm{erg\,g^{-1}\,K^{-1}}$, and $n \simeq 10^{-3.1}\,\mathrm{cm}^{-3}$, $T \simeq 10^{6.8}\,\mathrm{K}$ and $s \simeq 40\,\mathrm{erg\,g^{-1}\,K^{-1}}$ respectively. The warm-hot phase boundary is located at $n \simeq 10^{-1.5}\,\mathrm{cm}^{-3}$, $T \simeq 10^{5}\,\mathrm{K}$ and $s \simeq 25\,\mathrm{erg\,g^{-1}\,K^{-1}}$. Again, no clear feature in density or entropy exists for the cold phase, although the feature in the temperature distribution indicative of the cold phase are the same as for H1$\Omega_{\dot{\sigma}=0.5}$.

The joint PDFs of $\log n$ and $\log T$ for the models H1$\Omega_{\dot{\sigma}=0.5}$ and H1$\Omega_{\dot{\sigma}=1.5}$ are shown in Figure 7.4, with the blue and red lines denoting the same phase boundaries as used for H1$\Omega_{\dot{\sigma}=1.0}$, $s < 4.3 \times 10^{8}\,\mathrm{erg\,g^{-1}\,K^{-1}}$ and $s > 25.7 \times 10^{8}\,\mathrm{erg\,g^{-1}\,K^{-1}}$ respectively. These lines intersect the minima in both figures and so these phase boundaries appear to be reasonable for each of the three models. Thus, reasonable phase boundaries defined using specific entropy can be determined independent of the supernova rate, for the three hydrodynamic models analysed.

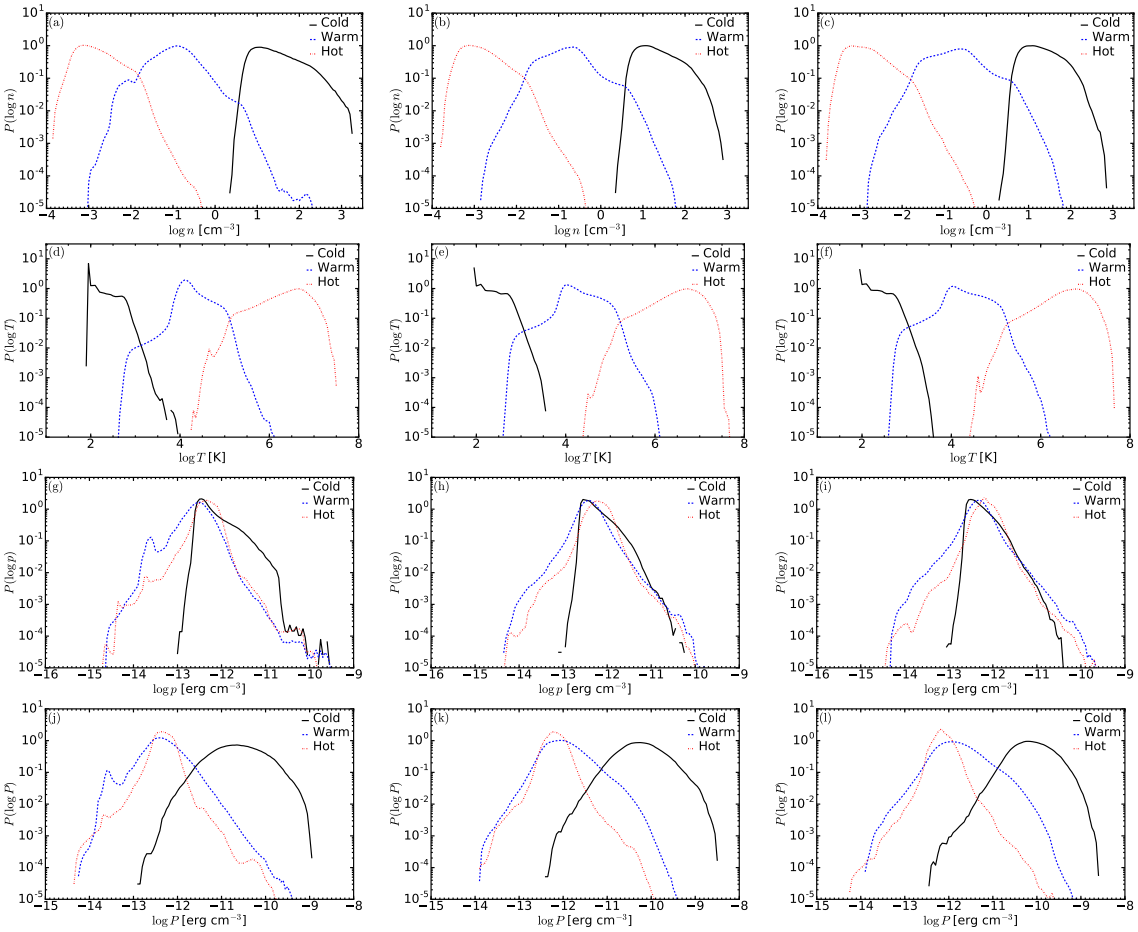

Figure 7.5: Comparisons of the log probability density functions in the cold (black, solid), warm (blue, dashed) and hot (red, dot-dashed) for the logarithms of; **(a)–(c)** gas number density, **(d)–(f)** temperature, **(g)–(i)** thermal pressure, **(j)–(l)** total pressure, between the runs H1$\Omega_{\dot{\sigma}=0.5}$ (left), H1$\Omega_{\dot{\sigma}=1.0}$ (middle) and H1$\Omega_{\dot{\sigma}=1.5}$ (right).

The probability density functions of the gas number density, temperature and the thermal and total pressure in the entropy-separated phases are shown in Figure 7.5. In each of the runs, the modal values in both number density and temperature for the cold phase, $(n, T) \simeq (10^{1.1}, 10^{1.9})$ are clearly shown. The distribution of the warm gas is bimodal with peaks at $(n, T) \simeq (10^{-0.7}, 10^{4})$ and $(n, T) \simeq (10^{-1.7}, 10^{5})$.

Increasing supernova rate results in more narrow distributions of density within each phase. For the cold and warm phases, the maximal densities decrease by about a factor of 2 between the lowest and highest supernova rates. The highest density cold and warm gas regions are formed from extended periods of cooling, which is inhibited by increased supernova heating. In the hot phase, the minimum density increases marginally, likely caused by increased compression of the hot gas by the increasing number of SNe.

In the cold and hot phases, the increasing supernova rate narrows the temperature distributions,

similar to density. The cold gas and hot gas tails almost intersect for H1$\Omega_{\dot{\sigma}=0.5}$, with the largest separation occurring for H1$\Omega_{\dot{\sigma}=1.5}$. By contrast, the temperature distribution of the warm gas broadens slightly. The most efficient cooling occurs in the shocks, which leads to production of the cold gas, particularly in shock collisions. An increased number of SN shocks leads to an increased probability of shock collisions. Hence, the maximal temperature of the cold gas produced is decreased. The increasing supernova rate increases the heating of the hot gas by supernovae which results in higher temperature hot gas. These mechanisms are likely to also result in increased amounts of cooler and hotter warm gas, which leads to the broader temperature profiles in the warm gas.

By comparison, the spread in the distributions of thermal pressure is notably smaller in each simulation, with the peaks for each phase within an order of magnitude. The overlapping distributions for each phase suggest the system is in statistical thermal pressure balance. As expected, the increased supernova rate results in increased thermal pressures throughout each phase. The distribution in each phases narrow significantly, with increased higher-pressure warm and hot gas as a result of higher temperatures in these phases, and reduced high-pressure cold gas from the lower amount of higher density cold gas.

The pressure from random motions $p_{\rm turb} = \frac{1}{3}\rho(u')^2$ is included in the total pressure P. The random motions $\boldsymbol{u}'$ are obtained by the subtraction of the mean flow $\langle \boldsymbol{u} \rangle_\ell$ from the perturbation velocity $\boldsymbol{u}$, as outlined in Chapter 6. For H1$\Omega_{\dot{\sigma}=1.0}$, the modal value of the warm gas increases by approximately 25%, whilst there is very little difference for the hot gas. The modal pressure in the cold increases by a factor of approximately 30, suggesting the cold gas is, in part, over pressured. This appears to be a result of the vertical pressure gradient. A higher proportion of the cold gas is located towards the mid-plane where there are higher turbulent pressures, relative to the warm and hot gas. These results are similar to the changes between thermal and total pressure found by Gent et al. (2013b).

The difference between the total and thermal pressures in the hot phase is more notable for H1$\Omega_{\dot{\sigma}=0.5}$ and reduces with supernova rate, suggesting the thermal pressure in the hot gas is more significantly affected by increasing supernova rate. By contrast, there is a increase in the higher-pressure warm and cold gas in the models with higher supernova rates. This increase likely results from stronger turbulent motions in these phases, which leads to higher turbulent pressures.

7.4 Impact on filling factors and fractional volumes

The phase filling factor, ϕ_i, describes how the gas is distributed within a given phase i

$$\phi_i = \frac{\overline{n_i}^2}{\overline{n_i^2}}, \tag{7.4}$$

with the bar denoting the average within the volume occupied by the phase. If $\phi_i = 1$, the gas distribution of the phase is homogeneous, whilst for $\phi_i < 1$, the gas density distribution is clumpy. The computations of both ϕ_i, and $f_{V,i}$ as defined in (7.2), are important in the analysis of the ISM, by characterising both the volume occupied by each phase and the structure of the gas within each phase. As for $f_{V,i}$, ϕ_i can be easily calculated within a simulation by computing the values of n and n^2 at individual gridpoints.

The phase filling factor is directly related to the volume filling factor, Φ_i, which is computed from ensemble averages. Thus by computing ϕ_i, an important connection can be made between the theory of turbulence and the astrophysics of the ISM.

Neither $f_{V,i}$ nor ϕ_i can be computed directly from observations of the ISM and so Φ_i is used instead. This is determined as follows

$$\Phi_i = \frac{\langle n_i \rangle_V^2}{\langle n_i^2 \rangle_V}, \tag{7.5}$$

where $\langle \rangle_V$ denotes an average computed over the whole volume. The volume filling factor and phase filling factor are directly related by the fractional volume, defined in (7.2)

$$\Phi_i = f_{V,i}\phi_i. \tag{7.6}$$

Thus, the volume occupied by a phase and the characterisation of its homogeneity are both directly related to the observable Φ_i. The relation in (7.6) is only easily understood if the ISM phase is homogeneous or if the probability density function, or similar statistical knowledge, of the phase is known.

Both filling factors and the fractional volumes of each phase are computed below for each of the supernova rates. It is expected that the fractional volume of the hot gas increases with supernova rate, however the dependence on the supernova rate for the fractional volumes of the cold and warm phases may not be as trivial. The impact of the supernova rate on the internal structure of each phase will be determined by the change in ϕ_i. The statistical properties of the gas density in each phase are not investigated here. However, the dependence of Φ will be investigated, since it allows for the investigation of the impact of the supernova rate on an observed quantity.

Each of the filling factors and the fractional volumes as functions of z are shown in Figure 7.6. Since these are functions of z, the averaging is in two dimensions. Nonetheless, the distinction between the area occupied by the phase and the entire plane is still relevant.

From Figure 7.6a–c, the phase filling factor in each phase increases from the mid-plane, the region of highest supernova activity. In each simulation, the cold phase is the closest to homogeneity, whilst the hot phase is the most clumpy. The increasing supernova rate appears to result in the cold phase becoming closer to homogeneity, most likely as a result of the reduced spread in the density distribution of the cold phase. Conversely, the warm phase appears to become more clumpy with increasing supernova rate, resulting from the reduced fractional volume, see Fig-

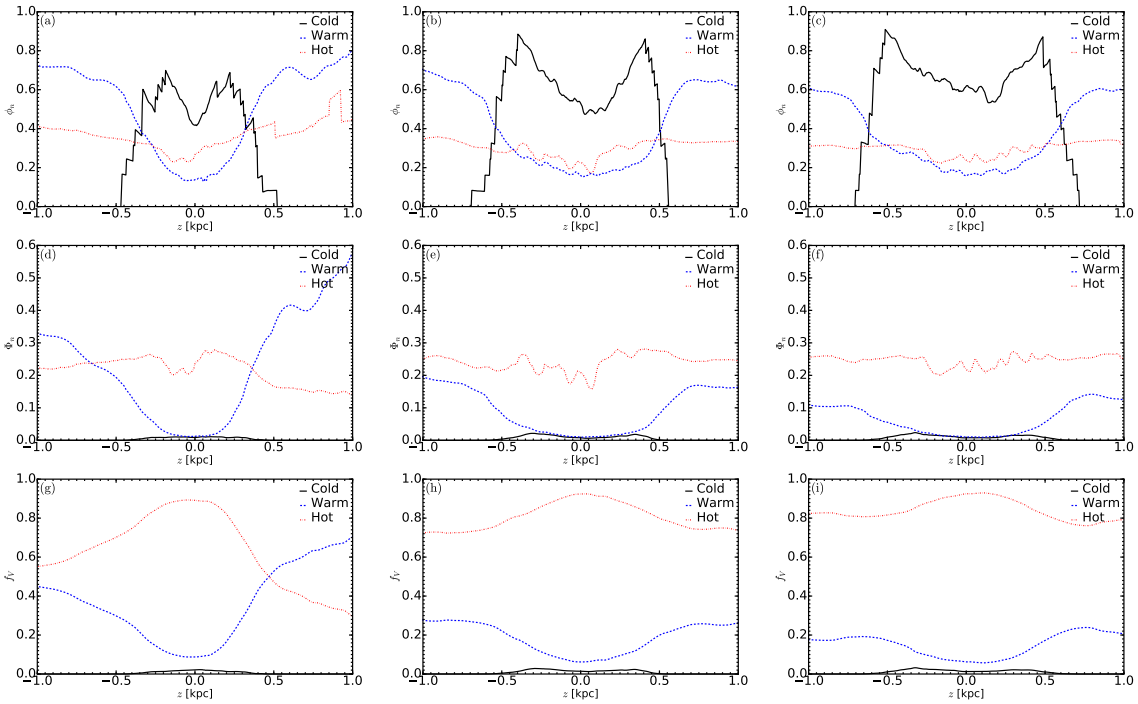

Figure 7.6: **(a)–(c)** phase filling factors, **(d)–(f)** volume filling factors and **(g)–(i)** fractional volumes in the cold (black, solid), warm (blue, dashed) and hot (red, dot-dashed) phases for the models; H1$\Omega_{\dot{\sigma}=0.5}$ (left), H1$\Omega_{\dot{\sigma}=1.0}$ (middle), H1$\Omega_{\dot{\sigma}=1.5}$ (right).

ure 7.6g–i, leading to more isolated pockets of warm gas. In addition, the heights for which the phase filling factor in the warm gas is reduced increases with supernova rate, resulting from the increased removal of warm gas close to the mid-plane. The phase filling factor of the hot gas decreases with supernova rate but only marginally.

In each model, the hot gas dominates throughout the domain, see Table 7.1. The highest fractional volumes of hot gas occur at the mid-plane, resulting from the higher concentration of SNe at the mid-plane. The fractional volume of warm gas increases with height from the cooling of SN remnants as they travel away from the mid-plane, with the abundance of the warm gas becoming comparable to the abundance of the hot gas near the vertical edge of the domain in the model H1$\Omega_{\dot{\sigma}=0.5}$. The increasing supernova rate increases the fractional volumes of both the cold and hot gas, whilst depleting the warm gas, by increased supernova heating and cooling of gas in the supernova shocks.

Figure 7.7 shows the vertical profiles of the fractional volumes of the cold gas in greater detail. As the supernova rate increases, the cold gas is propelled ballistically to greater heights, to heights of approximately 600 pc in the model H1$\Omega_{\dot{\sigma}=1.5}$. For the model H1$\Omega_{\dot{\sigma}=0.5}$, a smaller fraction of the cold gas is propelled away from the mid-plane, with the majority cold gas concentrated towards the mid-plane.

The behaviour of the volume filling factors for both the cold and warm phases appear to be

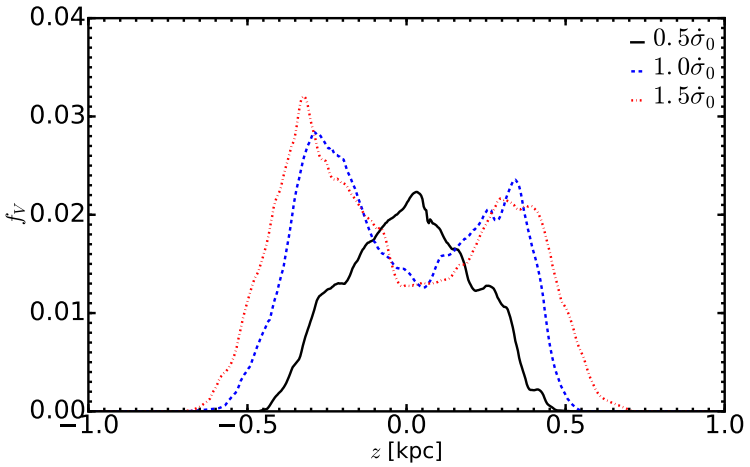

Figure 7.7: Vertical profile of the fractional volume of the cold gas in the models; $\mathrm{H1}\Omega_{\dot{\sigma}=0.5}$ (black, solid), $\mathrm{H1}\Omega_{\dot{\sigma}=1.0}$ (blue, dashed), $\mathrm{H1}\Omega_{\dot{\sigma}=1.5}$ (red, dot-dashed).

close to the behaviour of their respective fractional volumes, whereas in the hot gas, the behaviour of the volume filling factor is much closer to the behaviour of the phase filling factor; see Figure 7.6d–f. Further statistical analysis of the density within each phase would need to be performed in order to fully interpret these results.

7.5 Effects on the vertical structure

The dependence of the vertical profiles of the gas number density on the supernova rate are shown in Figure 7.8a. The peak in the vertical profile at the mid-plane broadens with supernova rate, as a result of the cold gas being distributed over a greater vertical part of domain by pressure from SNe. This also suggests an increasing disk thickness with supernova rate. The mean density in the disk is reduced, particularly at the mid-plane, from the increased abundance of low-density, hot gas and increased removal of cold gas from the mid-plane to larger heights, as shown in Figure 7.7.

The impact on the vertical structure of the temperature, shown in Figure 7.8b, is much less informative. The overall temperature increases with the supernova rate, with a slight reduction in the monotonic decrease with height, as a result of the larger injection of hot gas. The vertical distribution of temperature appears different to what would be expected from similar models, such as the 'reference' model in Gent et al. (2013b), where the temperature decreases with height for a few hundred parsecs away from the mid-plane, before then increasing with height towards the vertical edges of the domain. In addition, the average temperature is of order 10^6 K, typical of the hot gas, at all heights. This appears to be indicative of the fractional volume of the hot gas being too large for all three runs, as confirmed in Section 7.4. This is discussed in more detail in Section 7.2.

The vertical profiles of both thermal pressure $p = \rho RT$ and the total pressure, which includes

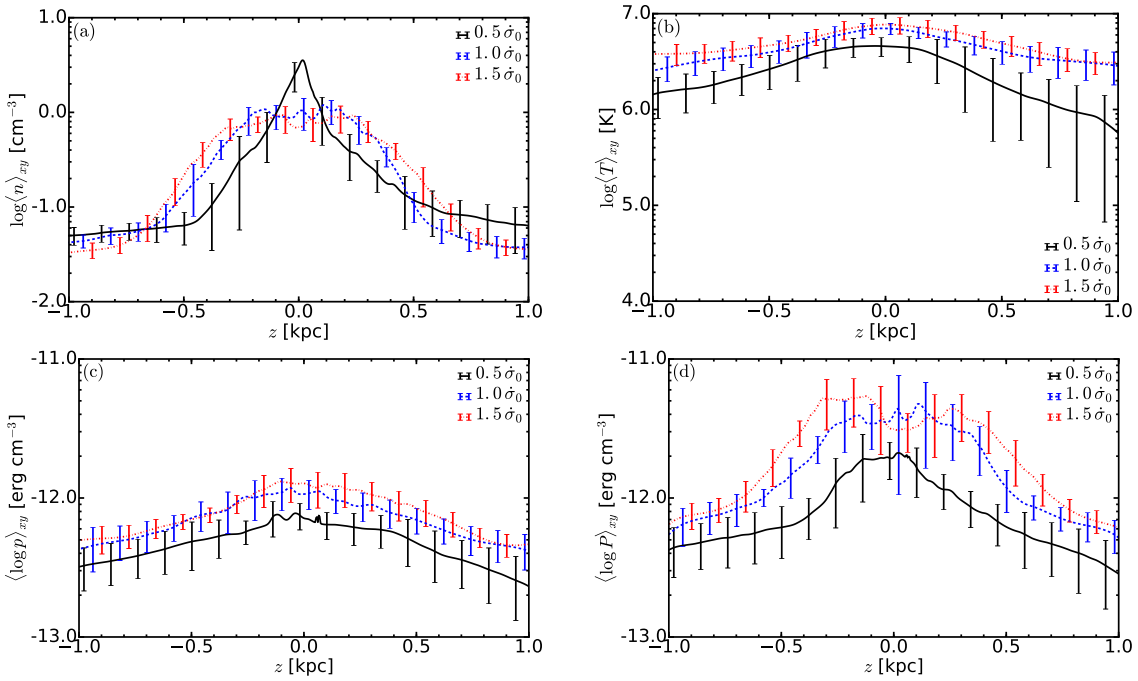

Figure 7.8: Vertical profiles of the logarithms of **(a)** gas number density, $\log n$, **(b)** gas temperature, $\log T$, **(c)** thermal pressure, $\log p$, and **(d)** total pressure, $\log P$; for the models H1$\Omega_{\dot{\sigma}=0.5}$ (black, solid), H1$\Omega_{\dot{\sigma}=1.0}$ (blue, dashed) and H1$\Omega_{\dot{\sigma}=1.5}$ (red, dot-dashed). The profiles were computed from 12 snapshots, over a period of 300 Myr, in each model. The error bars denote scatter about the mean within each horizontal plane.

the ram pressure $p_{\rm turb} = \frac{1}{3}\rho(u')^2$, are detailed in Figures 7.8c and 7.8d respectively. The mean thermal pressure is lower in H1$\Omega_{\dot{\sigma}=0.5}$, compared to the other runs, with the thermal pressure vertical profiles of the higher supernova rate runs overlapping within errors. This suggests the thermal pressure is only marginally increased as the supernova rate increases past the supernova rate in the Solar neighbourhood. In contrast, the difference in the total pressure between the runs is more significant, with increased pressure as the supernova rate increases. The scale height of the total pressure increases with supernova rate, as suggested in Figure 7.8a.

The vertical profiles of the root-mean-square of the total and turbulent velocities, and the mean vertical velocity are discussed in Figure 7.9. The rms velocity increases by approximately a factor of 2 as the supernova rate increases from $\frac{1}{2}\dot{\sigma}_0$ to $\dot{\sigma}_0$, where $\dot{\sigma}_0$ is the Solar neighbourhood supernova rate. However, as the supernova rate increases further, the increase in the root-mean-square of the total velocity is within errors. The marginally increased rms velocities appear to correlate with the increase in outflow velocity, and so the increased rms velocities are attributed to stronger vertical motions.

Similar behaviour is observed in Figure 7.9b. The rms turbulent velocities are stronger in the disk, the site of the highest supernova activity, with a more sharply pronounced structure in H1$\Omega_{\dot{\sigma}=0.5}$. Whilst there an increase in approximately 20% in the rms turbulent velocity as the

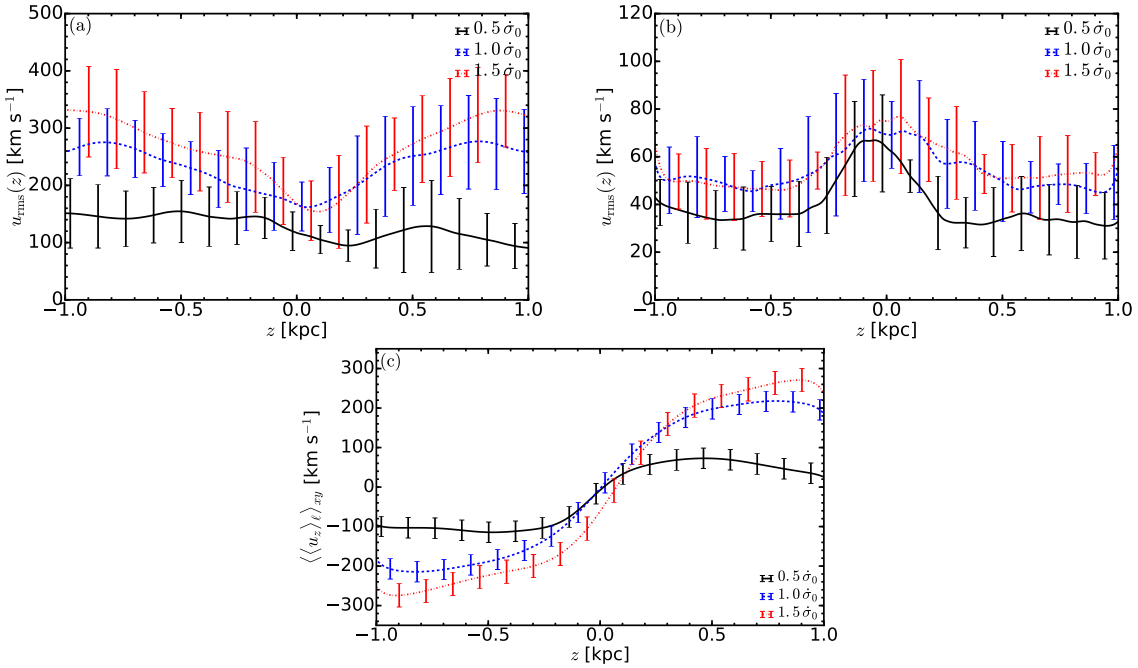

Figure 7.9: As for Figure 7.8 but for **(a)** the root-mean-square velocity $u_{\rm rms}$, **(b)** the turbulent root-mean-square velocity $u'_{\rm rms}$ and **(c)** the mean outflow velocity $\langle u_z\rangle_\ell$. The smoothing length used is $\ell = 75\,$pc.

supernova rate increases from $\frac{1}{2}\dot{\sigma}_0$ to $\dot{\sigma}_0$, the vertical profiles of $u'_{\rm rms}$ are very similar for the two higher supernova rate runs, suggesting the increased supernova activity is unable to drive stronger turbulent motions. The increased ram pressure in H1$\Omega_{\dot{\sigma}=1.5}$ is a consequence of the increased fractional volume of the cold gas, which contains higher total pressures on average, see Figure 7.5j–l.

As expected, increasing supernova rate drives stronger outflows, as shown in Figure 7.9c, in which the absolute value of $\langle\langle u_z\rangle_\ell\rangle_{xy}$ increases with supernova rate. The maximal horizontally averaged mean vertical velocity appears to approximately scale with the supernova rate. The mean vertical velocity increases away from the mid-plane for the higher supernova rates, with some moderate decrease near the vertical boundaries, likely resulting from the vertical boundary conditions. However in the model H1$\Omega_{\dot{\sigma}=0.5}$, the mean vertical velocity appears to decelerate at heights of $z > 0.5$, suggesting the outflows launched in this simulation are no longer the dominant mechanism for the vertical velocity beyond half a kiloparsec from the mid-plane.

7.6 Summary

A set of hydrodynamic simulations for which only the supernova rate varies has been investigated in order to asses the impact of the supernova rate on the physics of the ISM. The rate varies between one half and three halves the supernova rate in the Solar neighbourhood. Each of the runs

contain the unsatisfactory feature of a much larger than expected fractional volume of the hot gas, attributed to the removal of the cooling shutoff in the shocks and the change in the value of the mean molecular weight μ, and so neither run can be viewed as an accurate description of the Solar neighbourhood of the ISM. Nonetheless, comparisons between each of these simulations can be instructive to assess the qualitative impact of the supernova rate.

Despite the higher than expected abundance of the hot gas, a multi-phase structure can still be identified. The cold-warm and warm-hot boundaries, identified using specific entropy, are found to be appropriate for each of the simulations analysed. These boundaries are $s < 4.3 \times 10^8\,\mathrm{erg\,g^{-1}\,K^{-1}}$ and $s > 25.7 \times 10^8\,\mathrm{erg\,g^{-1}\,K^{-1}}$ respectively.

Clear distributions of density, temperature, and thermal and total pressures can be identified for the cold, warm and hot phases, identified by specific entropy, in each model. The increasing supernova rate narrows the density distributions in each phase, with the cold and hot phase temperature distributions also narrowed. By contrast, a broader range of temperatures are identified in the warm phase as the supernova rate increases. The thermal pressure in each phase is weakly affected by the supernova rate, with the peaks for each phase from each model within an order of magnitude. The overlapping thermal pressure distributions of each phase in each model suggest each run is in thermal pressure balance. The total pressure in the hot gas is marginally higher than the thermal pressure in each model, suggesting the turbulent pressure is less significant in the hot gas. In the cold and warm phases, the turbulent pressure is much more significant, with larger abundances of cold and warm gas at higher pressures as the supernova rate increases. The higher total pressures are likely a consequence of the increasing number of SNe driving stronger turbulent motions in these phases.

The increasing supernova rate depletes the warm gas, with greater amounts of both cold and hot gas. In addition, the cold gas is ballistically propelled to larger heights by the SNe as the supernova rate increases. The cold gas becomes closer to homogeneity, with increasing clumpy behaviour in the warm gas as the supernova rate increases. The phase filling factor of the hot gas is largely independent of the supernova rate. The behaviour of the volume filling factors of the cold and warm gas are closely associated with the behaviour of their respective fractional volumes for each model. Conversely, for each model, the volume filling factor in the hot gas is more strongly influenced by the behaviour of its phase filling factor. Further statistical analysis, such as the statistical distribution of the density within each phase, is required to fully interpret the relationship between the volume filling factor and the phase filling factor and fractional volume in each phase.

The increasing supernova rate increases the thickness of the disk and the density scale-height, as a result of increased turbulent pressure which is also increasingly significant at larger heights. The increase in turbulent pressure can be attributed to increased presence of the cold gas, which is over-pressured in the disk as a result of the vertical pressure gradient. Increased supernova heating results in marginally increased temperature and thermal pressure throughout the domain.

As expected, the mean outflow velocity increases with the supernova rate. However, as the supernova rate increases past the rate in the Solar neighbourhood, the increased number of SNe are unable to drive stronger turbulent motions. Hence, the increase in the root-mean-square of the total velocity is attributed to the stronger vertical outflows.

Chapter 8

Impact of supernova rate on correlation statistics

As demonstrated in Chapter 7, the supernova rate significantly impacts upon the multi-phase structure of the ISM, in both the distributions of the abundances of each phase and of the characteristic properties of each phase. Additionally, the vertical structure of the ISM is also markedly affected, in particular the vertical profiles of number density, turbulent pressure and outflow velocity.

It is natural to assume the supernova-driven turbulence in the ISM is also strongly dependent on the supernova rate. An increased supernova rate results in increased compression of the gas and the formation of larger amounts of cold gas, which accumulates in clouds of order 10 pc in size. Additionally, increased driving of the ISM by an increased supernova rate is expected to lead to larger turbulent velocities. Consequently, the turbulent length scales are expected to be reduced, particularly for density fluctuations, with a reduction in the time scale of turbulent motions.

These assumptions will be tested here through correlation analysis, as detailed in Chapter 5, of the hydrodynamic simulations analysed in the previous chapter. As discussed previously, whilst correlation analysis does not provide a complete picture of turbulence in the ISM, it serves as a useful basis for helping to characterise the turbulent fields.

The spatial correlations of the fluctuations of gas number density, n', and the components of the random velocity, $\boldsymbol{u}'$ are discussed in this chapter. The time correlations of the components of $\boldsymbol{u}'$ are also discussed, with the derived correlation times compared to the eddy turnover time from the spatial correlation analysis, and the time between passing shocks, as calculated in Chapter 5. No phase separation is considered here since comparisons of the correlation statistics of an individual phase between each of the models is likely to complicated by the changes in the abundances of the individual phases, particularly for the cold gas. Additionally, because of the large fractional volume of the hot gas in each run, as demonstrated in Section 7.2, the statistics within each individual phase are unlikely to be fully indicative of the statistics in the real ISM. Nonetheless, the results discussed here can still be indicative of the effects of the supernova rate on the turbulent statistics.

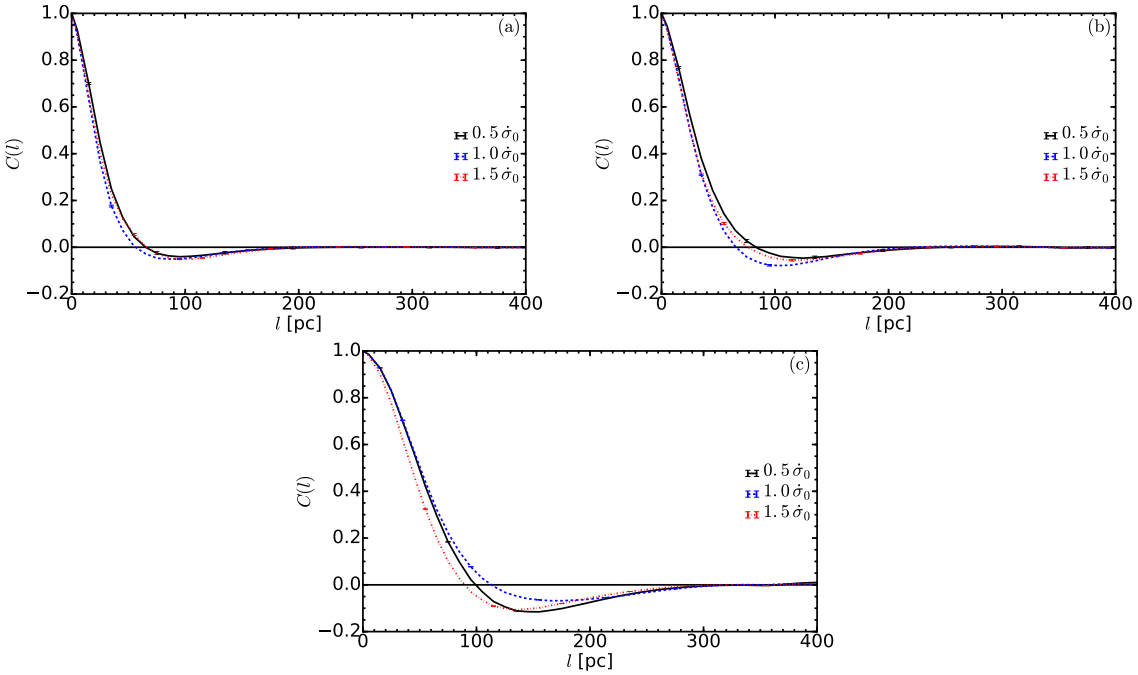

Figure 8.1: Correlation functions of the fluctuating density, n', in the models H1$\Omega_{\dot{\sigma}=0.5}$ (black, solid), H1$\Omega_{\dot{\sigma}=1.0}$ (blue, dashed), and H1$\Omega_{\dot{\sigma}=1.5}$ (red, dot-dashed), averaged in layers of thickness 100 pc in z; about heights of $|z| =$ **(a)** 0 pc, **(b)** 400 pc and **(c)** 800 pc from the mid-plane. Data from 12 snapshots, over a period of 300 Myr, was used from each model. In contrast to previous plots, the error bars denote the error of the mean, rather than scatter from the mean, since the scatter is close to 1. For clarity, every sixth error bar is shown.

The results discussed here will be compared to those in Chapter 5, with the caveat of the absence of the magnetic field and the much larger amounts of hot gas in the simulations analysed here.

8.1 Dependence of the Spatial Correlations

What is most surprising is that the correlation functions for gas number density, shown in Figure 8.1, exhibit similar behaviour to those detailed in Figure 5.3, despite the greatly reduced fractional volumes of warm gas in the hydrodynamic simulations. Whilst Figure 5.3 concerns only the warm gas in B1Ω, the correlation statistics of the total ISM are very similar to those in the warm gas for n'. Thus, for number density, the statistics for both the cold and warm phases still dominate despite the much reduced fractional volume. This arises from large density fluctuations in the cold and warm gas because of the much greater number densities in the cold and warm phases, as compared to the hot phase.

The scale of lags for which the density fluctuations becomes anti-correlated increases with height, from approximately 80 pc near the mid-plane to approximately 120 pc at height $|z| =$ 800 pc. The most rapid increase in this scale occurs for H1$\Omega_{\dot{\sigma}=1.0}$, further suggesting the anti-

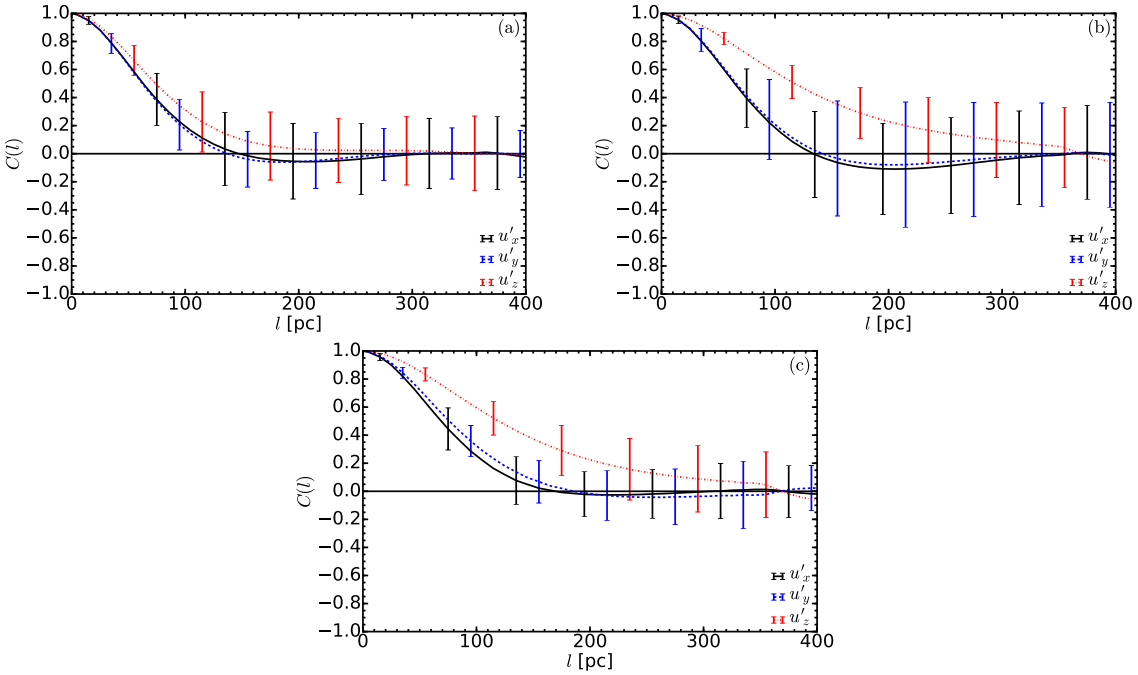

Figure 8.2: Correlation functions of the components of the random velocity u'_x (black, solid), u'_y (blue, dashed) and u'_z (red, dot-dashed) in the model H1$\Omega_{\tilde{\sigma}=1.0}$, averaged in z within layers of 100 pc about heights of $|z| =$; **(a)** 0 pc, **(b)** 400 pc and **(c)** 800 pc from the mid-plane. As for Figure 8.1, the data used is from 12 snapshots, over a period of 300 Myr. In contrast to Figure 8.1, the error bars denote scatter about the mean, rather than error. As for Figure 8.1, every sixth error bar is shown.

correlation is linked to systematic rarefraction within shock fronts, which in all models become more rarefied with height since most SN explode near the mid-plane.

Comparisons between the statistics of the random speed u' between the warm phase and the total statistics, as shown in Section 5.3, suggest the hot phase more strongly impacts the correlation statistics of the turbulent velocity, because of stronger turbulent motions in the hot gas. The smooth behaviour of the correlation functions in Figures 8.2–8.4, despite the much larger fractional volumes of hot gas in all three models, occurs because of the measurement of the ambient, mostly hot gas surrounding SN remnants. This is in contrast to the highly fluctuating behaviour in Figure 5.7, which results from the structure functions for the hot gas measuring only the behaviour within isolated regions.

Thus, as a result of the smooth behaviour of the correlation functions and the corresponding structure functions from which they are derived, the reliability of the statistics obtained from the correlation analysis in this chapter is confirmed.

Impact on rms fluctuations

The rms values of the density fluctuations and the components of the random velocity for each model are listed in Table 8.1 and are illustrated Figure 8.5a. The strength of the density fluctu-

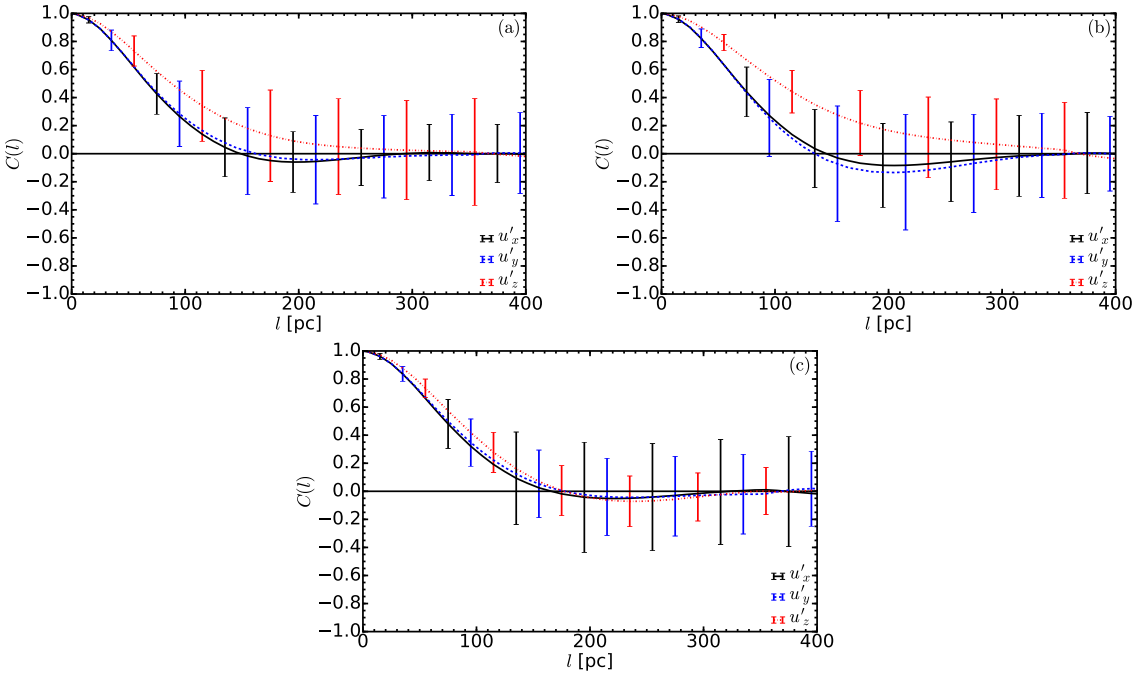

Figure 8.3: As for Figure 8.2 but for the model H1$\Omega_{\dot{\sigma}=0.5}$.

ations in the mid-plane drastically decreases with increasing supernova rate, by approximately a factor of 3 as $\dot{\sigma}$ increases from half to one times the Solar neighbourhood rate, with a decrease of approximately 25% as $\dot{\sigma}$ increases further. In contrast for $|z| = 200\,\mathrm{pc}$, rms values increase by a factor of 2–3 as the supernova rate increases, suggesting an increase in the disk thickness as indicated in Figure 7.8a.

The rms density fluctuations decrease with height in each model, with the most rapid reduction occurring in H1$\Omega_{\dot{\sigma}=0.5}$. In addition, for $|z| > 400\,\mathrm{pc}$, the density fluctuations are strongest in the model with the highest supernova rate This corresponds to the behaviour in Figure 7.8a. This is a consequence from the increased amount of cold gas, in which the density fluctuations are strongest, being generated in shocks and then propelled to greater heights as the supernova rate increases.

The rms values of the density fluctuations for each of the three hydrodynamic models are two orders of magnitude higher than those for B1Ω reported in Chapter 5 at the same heights. This results from the reduced fractional volume of the cold gas as the magnetic field strength increases. Hence, the rms values listed in Chapter 5 are more indicative of the warm gas, whose density fluctuations are much weaker due the orders of magnitude lower densities in the warm (as compared to the cold) gas.

The rms values of the turbulent velocity components, listed in Table 8.1, are further illustrated in Figure 8.5b–d. For both horizontal components, the rms values decrease with height in each model, indicating in the reduction of the driving of horizontal turbulent motions by SNe, since

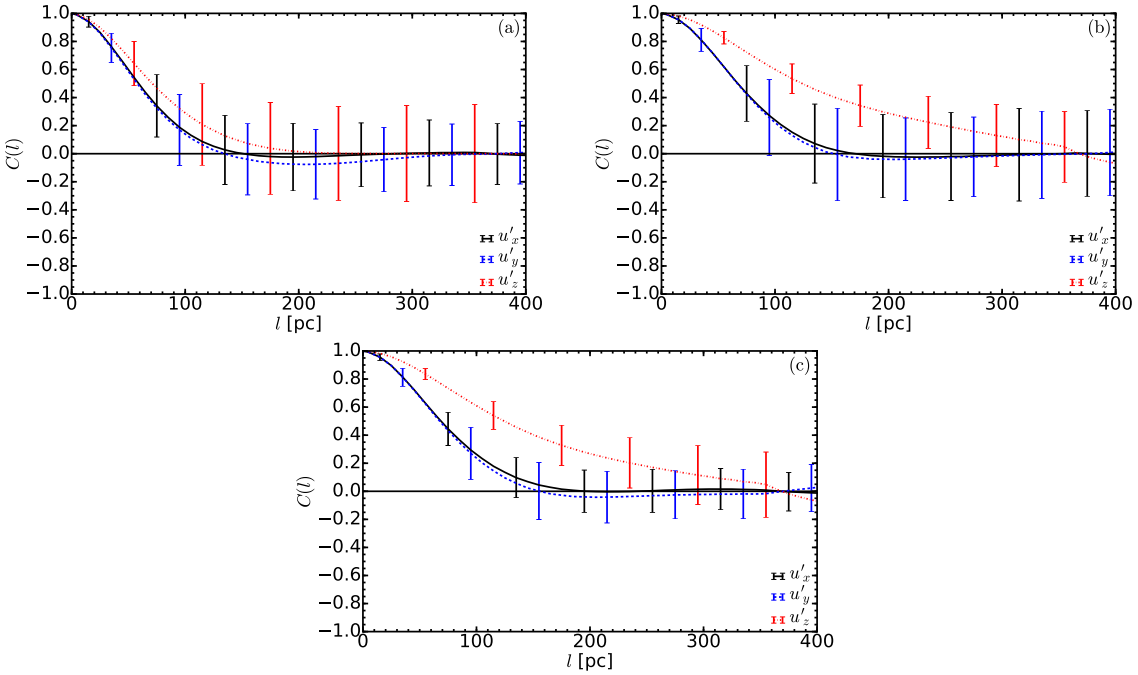

Figure 8.4: As previously but for the model H1$\Omega_{\dot{\sigma}=1.5}$.

the density of SNe decreases with height. Whilst the rms values of the two horizontal velocity components are different outside of errors, these values are still reasonably similar, suggesting the assumption of horizontal isotropy is reasonable. As the supernova rate increases from one half to one times the Solar neighbourhood rate, the rms values of both u'_x and u'_y increase, with a reduction in this difference with height, again suggesting the effect of the change in the density of SN remnants. However, the vertical profiles of the rms values of both u'_x and u'_y for both H1$\Omega_{\dot{\sigma}=1.0}$ and H1$\Omega_{\dot{\sigma}=1.5}$ almost overlap, again suggesting the highest supernova rate is unable to drive stronger horizontal turbulent motions, as first indicated in Figure 7.9.

Similar to the behaviour of the mean vertical velocity in Figure 7.9c, the rms value of u'_z increases monotonically with height for each model, although this increase is very marginal for H1$\Omega_{\dot{\sigma}=0.5}$, because of the weaker outflows in this model. Higher supernova rates driving stronger motions on average. The exception to this is the rms value at the mid-plane in the model H1$\Omega_{\dot{\sigma}=0.5}$. Whilst there is a systematic increase in the rms value of u'_z between the models H1$\Omega_{\dot{\sigma}=1.0}$ and H1$\Omega_{\dot{\sigma}=1.5}$, this increase is only marginal, and as such this information is likely to be lost when considering the rms values of the random speed u', hence the lack of difference in the vertical profiles of $u'_{\rm rms}$ shown in Figure 7.9c.

As for density fluctuations, the rms values of the turbulent velocity components are significantly increased in these models, as compared to B1Ω (see Table 5.3). This is a consequence of the much higher fractional volumes of hot gas in these models compared to B1Ω, which contain higher velocities and thus greater velocity fluctuations.

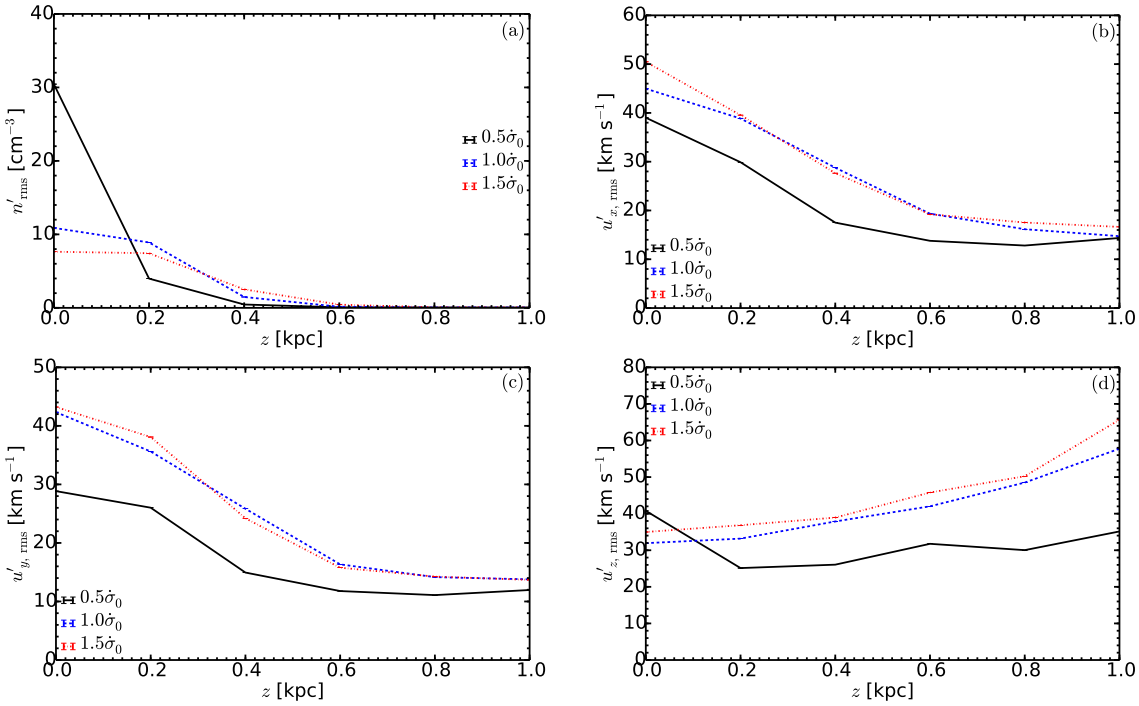

Figure 8.5: Vertical profiles of the root-mean-square values from Table 8.1 of **(a)** number density fluctuations n', and the components of the random velocity; **(b)** u'_x, **(c)** u'_y and **(d)** u'_z, from the models H1$\Omega_{\dot{\sigma}=0.5}$ (black, solid), H1$\Omega_{\dot{\sigma}=1.0}$ (blue, dashed), H1$\Omega_{\dot{\sigma}=1.5}$ (red, dot-dashed), as computed from their respective structure functions.

Impact on the correlation scales

At both $|z| = 0\,$pc and $|z| = 200\,$pc, the correlation scale of the density fluctuations is approximately 20 pc for each of the three models. With the impact of the cold gas on the correlation statistics and the presence of clouds of cold gas at both heights in all three models, this correlation scale appears to indicate the density fluctuations within cold gas regions are correlated on scales of approximately 20 pc. The marginal increase in the correlation scales in both H1$\Omega_{\dot{\sigma}=1.0}$ and H1$\Omega_{\dot{\sigma}=1.5}$ at both $|z| = 400\,$pc and $|z| = 600\,$pc, for which both models have non-trivial fractional volumes of cold gas at both heights as shown in Figure 7.6c, further suggest the correlation scales being indicative of the size of cold gas regions.

For $|z| > 200\,$pc in the model H1$\Omega_{\dot{\sigma}=0.5}$ and $|z| > 600\,$pc in both H1$\Omega_{\dot{\sigma}=1.0}$ and H1$\Omega_{\dot{\sigma}=1.5}$, the correlation scale of the density fluctuations increases significantly with height. Towards the vertical edge of the domain in each model, the fractional volumes of the warm gas increase, indicating the presence of larger regions of more diffuse warm gas, as compared to the cold gas. Above heights of 600 pc, the cold gas is absent in each model and so the correlation statistics of n' are determined by the warm phase. The correlation length of density fluctuations in the warm gas is expected to be longer than for the cold gas, since the cold gas is generated via compression of the gas by shocks. As the size of these warm regions increase, the correlation length correspondingly

Table 8.1: The root-mean-square (rms) values and the correlation lengths of the gas density fluctuations and the random velocity components, in the models H1$\Omega_{\dot{\sigma}=0.5}$, H1$\Omega_{\dot{\sigma}=1.0}$ and H1$\Omega_{\dot{\sigma}=1.5}$. The correlation lengths were calculated from integration within the range $0 \leq l \leq 400$ pc.

$\dot{\sigma}$	$\lvert z \rvert$	rms fluctuations				l_0 [pc]			
$[\dot{\sigma}_0]$	[pc]	n' [cm^{-3}]	u'_x [kms^{-1}]	u'_y [kms^{-1}]	u'_z [kms^{-1}]	n'	u'_x	u'_y	u'_z
0.5	0	30.43 ± 0.05	39.02 ± 0.02	28.85 ± 0.02	40.78 ± 0.02	22 ± 2	65 ± 1	68 ± 1	102 ± 1
	200	3.981 ± 0.004	29.89 ± 0.01	26.02 ± 0.01	25.13 ± 0.01	21 ± 1	69 ± 1	55 ± 1	103 ± 1
	400	0.4556 ± 0.0008	17.51 ± 0.01	14.94 ± 0.02	26.06 ± 0.01	28 ± 2	61 ± 1	53 ± 1	124 ± 1
	600	0.0698 ± 0.0001	13.78 ± 0.01	11.78 ± 0.01	31.76 ± 0.01	46 ± 1	74 ± 1	54 ± 1	114 ± 1
	800	0.0543 ± 0.0001	12.81 ± 0.01	11.09 ± 0.01	30.03 ± 0.01	38 ± 1	71 ± 1	74 ± 1	80 ± 1
	1000	0.0441 ± 0.0001	14.36 ± 0.01	11.96 ± 0.01	35.14 ± 0.01	58 ± 1	113 ± 1	93 ± 1	96 ± 1
1.0	0	10.88 ± 0.01	44.97 ± 0.02	42.34 ± 0.01	31.94 ± 0.01	18 ± 1	61 ± 1	59 ± 1	85 ± 1
	200	8.900 ± 0.009	38.85 ± 0.01	35.62 ± 0.01	33.18 ± 0.01	20 ± 1	61 ± 1	55 ± 1	108 ± 1
	400	1.479 ± 0.001	28.77 ± 0.01	25.84 ± 0.01	37.87 ± 0.01	21 ± 1	52 ± 1	59 ± 1	139 ± 1
	600	0.1497 ± 0.0002	19.34 ± 0.01	16.34 ± 0.01	42.01 ± 0.01	23 ± 2	55 ± 1	66 ± 1	137 ± 1
	800	0.0536 ± 0.0001	16.16 ± 0.01	14.16 ± 0.01	48.50 ± 0.01	45 ± 1	71 ± 1	76 ± 1	139 ± 1
	1000	0.0487 ± 0.0001	14.73 ± 0.01	13.78 ± 0.01	57.75 ± 0.03	49 ± 1	92 ± 1	98 ± 1	156 ± 1
1.5	0	7.641 ± 0.008	50.47 ± 0.02	43.22 ± 0.02	34.99 ± 0.02	20 ± 1	61 ± 1	51 ± 1	79 ± 1
	200	7.432 ± 0.004	39.55 ± 0.01	38.09 ± 0.01	36.84 ± 0.01	20 ± 1	51 ± 1	54 ± 1	117 ± 1
	400	2.518 ± 0.003	27.65 ± 0.01	24.21 ± 0.01	38.93 ± 0.01	23 ± 1	69 ± 1	65 ± 1	149 ± 1
	600	0.4362 ± 0.0005	19.22 ± 0.01	15.77 ± 0.01	45.78 ± 0.01	25 ± 1	52 ± 1	56 ± 1	143 ± 1
	800	0.0650 ± 0.0001	17.53 ± 0.01	14.25 ± 0.01	50.23 ± 0.01	33 ± 1	75 ± 1	66 ± 1	147 ± 1
	1000	0.0547 ± 0.0001	16.63 ± 0.01	13.69 ± 0.01	65.66 ± 0.04	38 ± 1	87 ± 1	79 ± 1	170 ± 1

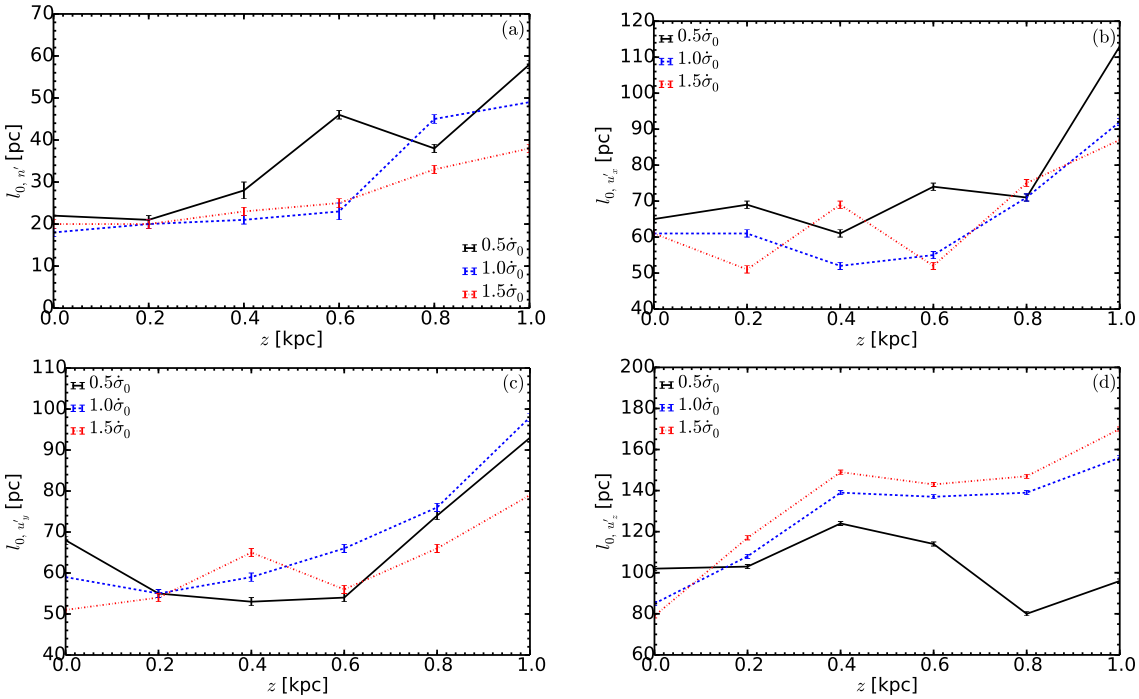

Figure 8.6: Vertical profiles of the correlation lengths from Table 8.1 of **(a)** number density fluctuations n', and the components of the random velocity; **(b)** u'_x, **(c)** u'_y and **(d)** u'_z, from the models H1$\Omega_{\dot{\sigma}=0.5}$ (black, solid), H1$\Omega_{\dot{\sigma}=1.0}$ (blue, dashed), H1$\Omega_{\dot{\sigma}=1.5}$ (red, dot-dashed), as computed from their respective correlation functions.

increases. Hence the larger correlation scales in H1$\Omega_{\dot{\sigma}=0.5}$ which contains the largest fractional volume of warm gas, as shown in Chapter 7.

In comparison to B1Ω, the correlation scale in H1$\Omega_{\dot{\sigma}=1.0}$ is decreased by approximately 50%. With the correlation statistics of B1Ω dominated by the warm phase, this again suggests the correlation scale of the density fluctuations in the cold gas is significantly shorter, since the cold phase most significantly affects the correlations of n' for $|z| \leq 600\,\mathrm{pc}$ in the model H1$\Omega_{\dot{\sigma}=1.0}$.

In contrast to the rms values, the difference in the correlation scales of the horizontal components of the random velocity suggest significant horizontal anisotropy in the random velocity within each model analysed. Thus, future correlation analysis of the random velocity components should consider the x- and y- directions independently. The correlation scales generally increase with height, resulting from the presence of fewer shocks away from the mid-plane. The vertical profiles of l_0 for both u'_x and u'_y do not show a clear behaviour with supernova rate and thus any dependence of the scale of the horizontal turbulent motions on the supernova rate is marginal.

As expected, the correlation scale of u'_z is greater than for the horizontal components, resulting from the scale of the vertical outflows exceeding the scale of the horizontal flows, since the velocity is dominated by the expanding bubbles of hot gas which rise vertically from the disk. The scale of these vertical random flows increase with height and supernova rate, with the exception of the mid-plane, as the strength of overall outflows also increase, as shown in Figure 7.9c.

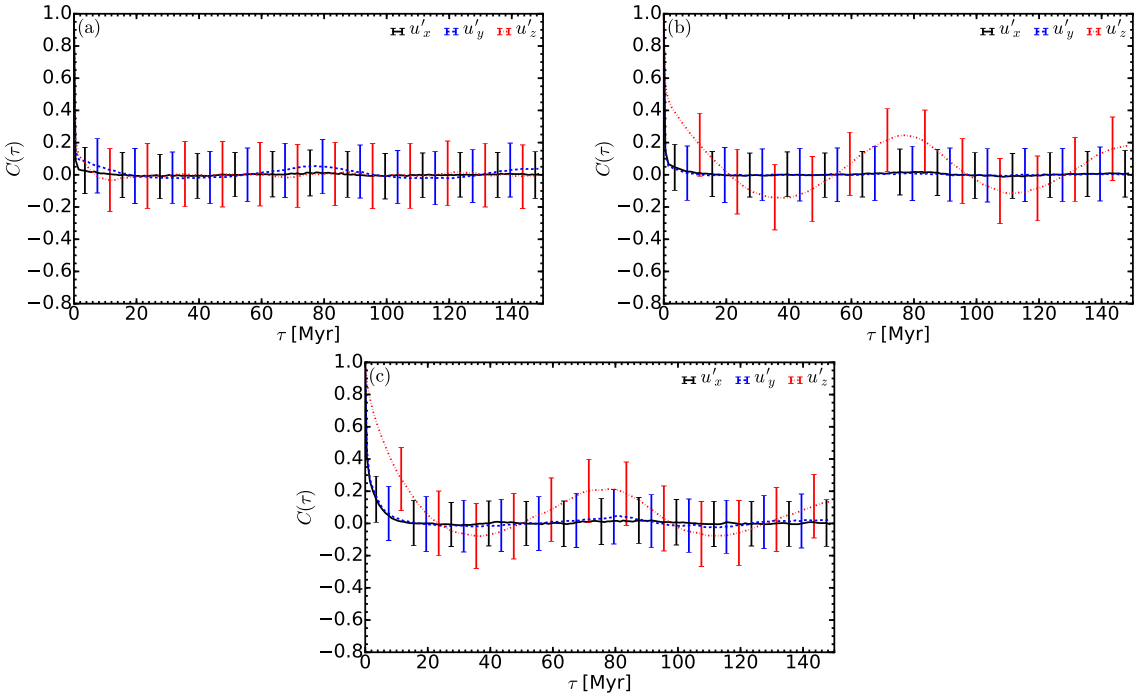

Figure 8.7: The correlation functions of the components of the random velocity; u'_x (black, solid), u'_y (blue, dashed) and u'_z (red, dot-dashed) at heights; **(a)** 0 pc, **(b)** 400 pc and **(c)** 800 pc. The data is from H1$\Omega_{\dot{\sigma}=1.0}$. As for Figures 8.2–8.4, the error bars denote standard deviation about the mean, rather than error. For clarity, every twelfth error bar is shown.

With the correlation statistics of the turbulent velocity more strongly associated with the hot phase, it is not surprising that the correlation scales of u'_z appear influenced by the outflows of hot gas, with larger outflow speeds indicative of larger regions of hot gas, hence an increase in the scale of turbulence in the z-direction. This would also explain the moderate decrease in the l_0 near the edge of the domain in the model H1$\Omega_{\dot{\sigma}=0.5}$, where a large enough fraction of the outflow gas cools resulting in a reduced outflow speed near the edge of the box. This would limit the size of the outflow regions and reduce the associated turbulent scale.

In contrast to n' the correlation scales of the turbulent velocity in the mid-plane H1$\Omega_{\dot{\sigma}=1.0}$ are comparable to those in the mid-plane of B1Ω, albeit the value in Table 5.3 is for the turbulent speed, u'. At $|z| = 400$ pc, the correlation scales for both u'_x and u'_y in H1$\Omega_{\dot{\sigma}=1.0}$ are approximately two-thirds of the u' from B1Ω, although l_0 for u'_z is roughly 50% larger than u'. However, smaller scales are expected in the horizontal components of $\boldsymbol{u}'$ compared to u', whilst larger scales are expected in u'_z. Thus, the correlation scales of both models may be regarded as comparable. Therefore, the random motions from two runs with the same supernova rate are correlated on similar scales, suggesting the correlations statistics of $\boldsymbol{u}'$ are determined more by the motions within SN remnants rather than the motions in the ambient gas, which more significantly impact the rms velocities.

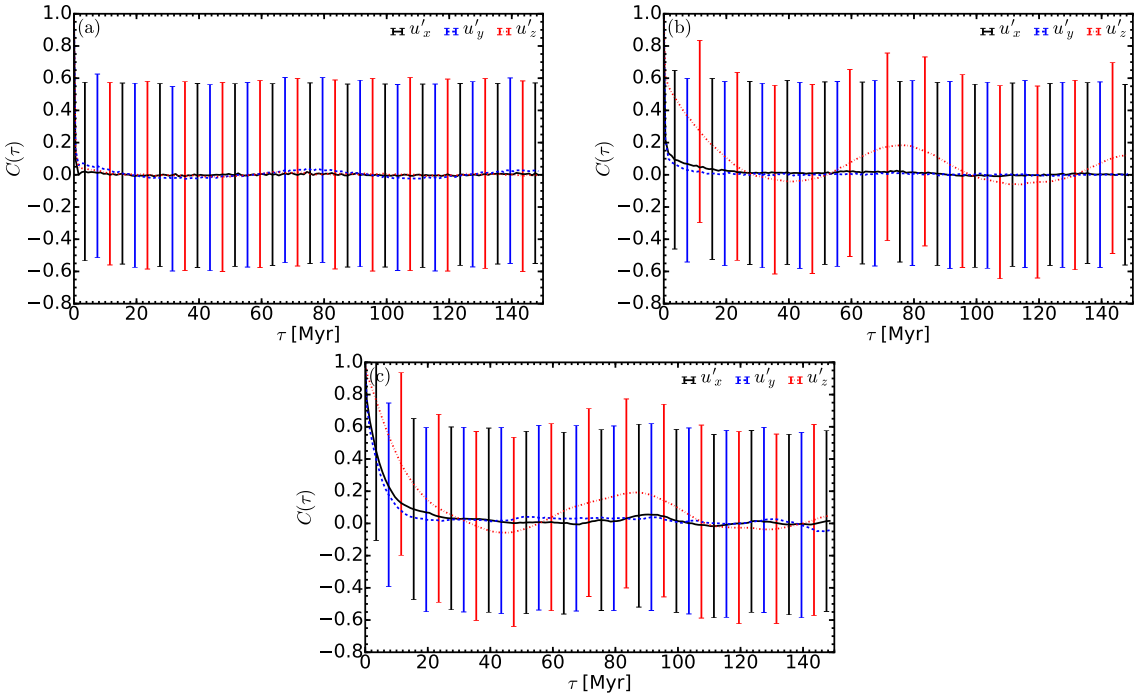

Figure 8.8: As for Figure 8.7, but for H1$\Omega_{\dot{\sigma}=0.5}$.

8.2 Impact on the correlation time

For all three models, the temporal correlation functions of both u'_x and u'_y decrease rapidly towards zero, with very minor fluctuations. However, for u'_z, $C(\tau)$ fluctuates periodically about zero for time lags greater than 20 Myr. The time period decreases with supernova rate, suggesting the periodicity in the time correlation function for u'_z is linked to the passing of rising bubbles of hot gas.

The correlation times for each of the three models, averaged about heights of 0 pc, 200 pc, 400 pc, 600 pc, 800 pc and 1000 pc, are listed in Table 8.2. For comparison, the eddy turnover times for each of the three components of u', $\tau_{\rm eddy} = l_0/u'_{\rm rms}$, are also computed in the table, using the values given in Table 8.1. These values are further illustrated in Figure 8.10.

For each model at the mid-plane, τ_0 is of order 0.1–1.0 Myr, with large errors. The correlation time for each component increases with $|z|$, increasing up to a few Myr for both u'_x and u'_y. There is some decrease with supernova rate, albeit only marginal. The differences for u'_z are much more clear than for the horizontal components. The correlation time increases up to order 10 Myr in each model, with a difference of a factor of approximately 2 at large heights between the lowest and highest supernova rates. Thus, the supernovae have a larger impact on the time-scale of the turbulence in the vertical direction. This can be explained by the fact that the motions driven by the supernovae propagate more freely in the z–direction. In the horizontal directions, the collision of shocks, which increase in probability with supernova rate, result in the cancellation of

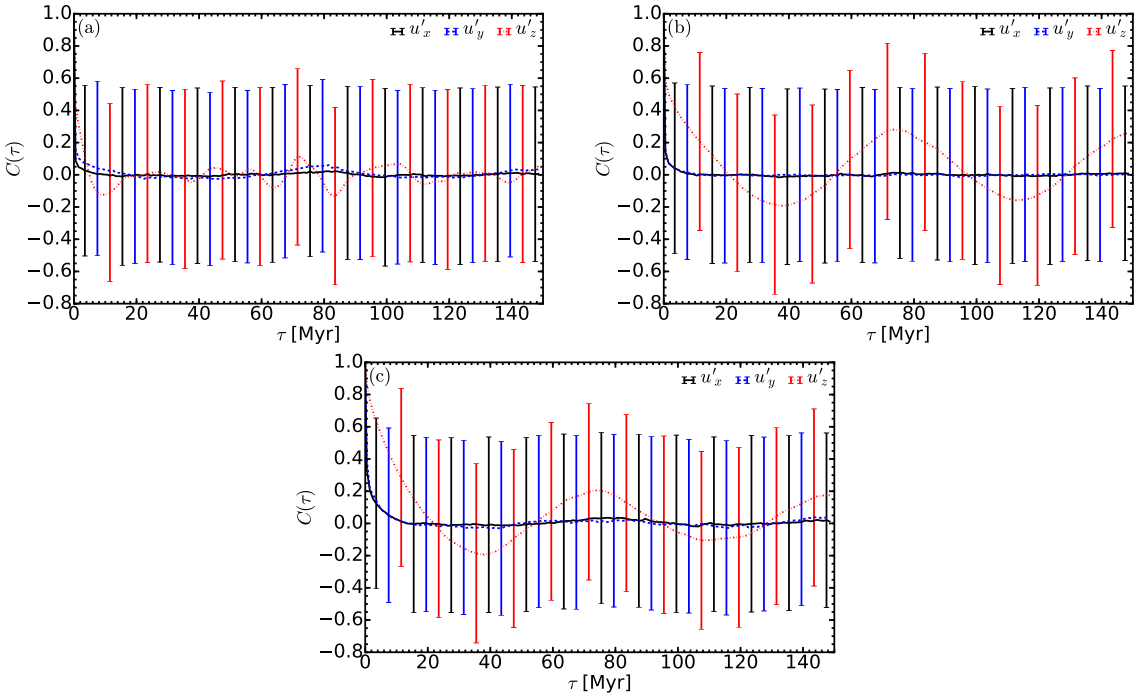

Figure 8.9: As previously, but for H1$\Omega_{\tilde{\sigma}=1.5}$.

the supernova-driven motions. Thus, the effects of increased supernova driving in the horizontal directions are suppressed by the increased number of shock collisions.

The correlation times derived in this chapter do differ from those obtained in Chapter 5. However, this is unsurprising because of the faster outflows of hot gas in the hydrodynamic simulations, as compared to B1Ω, since the SN remnants propagate through a more diffuse medium in the hydrodynamic simulations, as compared to B1Ω. Additionally, in contrast to the results from B1Ω, the correlation times for each component of the random velocity decrease away from the mid-plane. This results from the reduced driving of turbulence by a reduced frequency of supernovae away from the mid-plane. The lack of variation in the correlation times with z in Chapter 5 is likely explained by both the use of the random speed, u', and the larger z–layers used to obtain reliable statistics.

In comparison to τ_0, the eddy turnover time is affected less by the supernova rate, whilst $\tau_{\rm eddy}$ is smaller in the vertical direction, compared to the horizontal directions. The eddy turnover time appears to be a reasonable estimate for the correlation time in the horizontal directions as shown in Figures 8.10a and Figures 8.10b. However $\tau_{\rm eddy} = 2$–$3\,$Myr in the z–direction is many times smaller than the correlation time, particularly at large heights, as demonstrated in Figures 8.10c. Hence, the consideration of processes other than the turbulent eddies, such as the passage of SN remnants, is required to explain the correlation time of the vertical motions.

The separation of shocks calculated using (5.10) assumes $L_{\rm shock}$ proportional to the inverse of the supernova rate. Thus the values of $L_{\rm shock}$ are approximately 20 pc, 10 pc and 7 pc respectively,

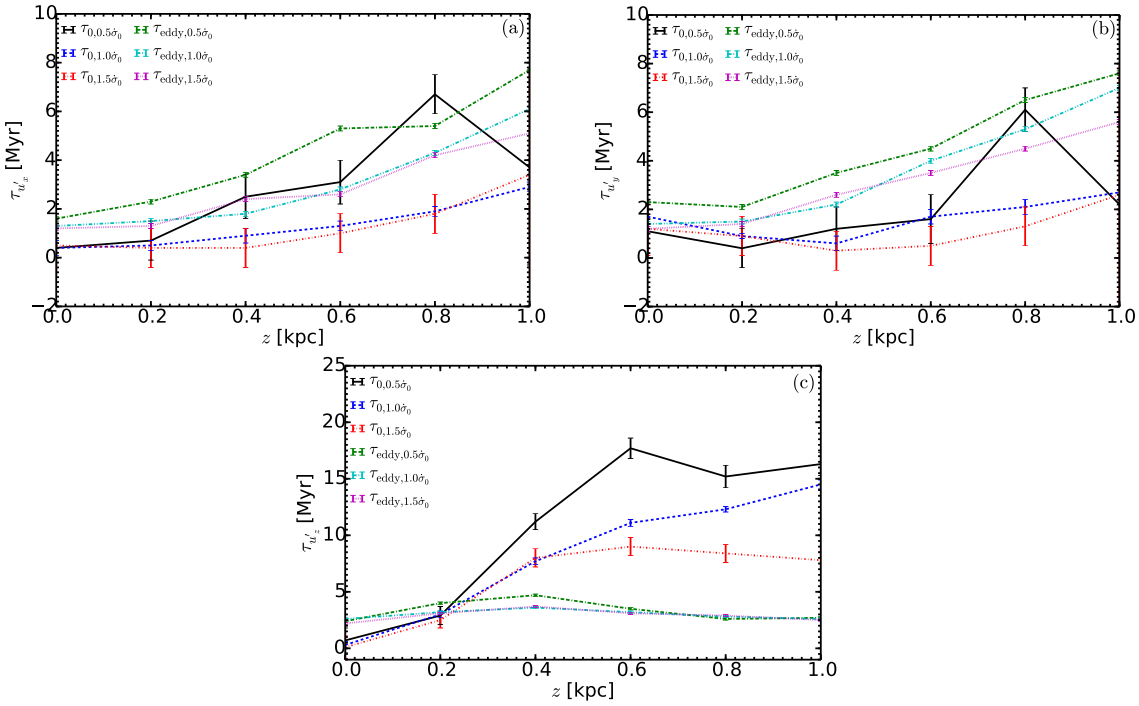

Figure 8.10: Vertical profiles of the correlation times from the models H1$\Omega_{\dot{\sigma}=0.5}$ (black, solid), H1$\Omega_{\dot{\sigma}=1.0}$ (blue, dashed) and H1$\Omega_{\dot{\sigma}=1.5}$ (red, dot-dashed), and the eddy turnover times from these models (green, dash-dash-dotted), (cyan, dash-dot-dotted) and (purple, dotted) respectively, for the components of the turbulent velocity; **(a)** u'_x, **(b)** u'_y and **(c)** u'_z. The times from are from Table 8.2.

for the different supernova rates. Assuming a speed of $c_s = 10\,\mathrm{km\,s^{-1}}$, equal to the sound speed since we do not have magnetosonic waves, the shocks times are $\tau_{\rm shock} \simeq 2\,\mathrm{Myr}$, 1 Myr and 0.7 Myr respectively. However, $\tau_{\rm shock}$ is a worse estimate than $\tau_{\rm eddy}$ for the correlation time of u'_z, particularly for the higher supernova rate models, as demonstrated in Table 8.2. Thus, the shock times are similarly useful estimates for the correlation time of the horizontal components, as compared to the eddy turnover time. Since the hot gas dominates in the hydrodynamic simulations, the estimates of the shock time listed here, using the sound speed of the warm gas, are upper limits for $\tau_{\rm shock}$.

8.3 Summary

Correlation analysis, as first detailed in Chapter 5, has been applied to both the fluctuations in gas number density, n', and the components of the random velocity, $\boldsymbol{u}'$, in order to investigate the impact of the supernova rate on the correlation statistics, which are a useful first step in characterising the turbulence in the ISM simulations.

Informative spatial and temporal correlation functions for the total statistics (i.e. no phase separation) are obtained. The correlation statistics for n' are determined by the behaviour in the

Table 8.2: The correlation time of the random speed and the eddy turnover time, obtained from the values of l_0 and $u'_{\rm rms}$ in Table 8.1, at various heights in the simulation domain. The correlation times are obtained via integration of the correlation functions in Figures 8.7–8.9, averaged over layers of 100 pc.

$\dot{\sigma}$	$\lvert z\rvert$ [pc]	τ_0 [Myr]			$\tau_{\rm eddy}$ [Myr]		
$[\dot{\sigma}_0]$		u'_x	u'_y	u'_z	u'_x	u'_y	u'_z
0.5	0	0.4 ± 1.2	1.1 ± 1.1	0.7 ± 1.1	1.6 ± 0.1	2.3 ± 0.1	2.4 ± 0.1
	200	0.7 ± 0.8	0.4 ± 0.8	2.9 ± 0.8	2.3 ± 0.1	2.1 ± 0.1	4.0 ± 0.1
	400	2.5 ± 0.9	1.2 ± 0.9	11.2 ± 0.7	3.4 ± 0.1	3.5 ± 0.1	4.7 ± 0.1
	600	3.1 ± 0.9	1.6 ± 1.0	17.7 ± 0.9	5.3 ± 0.1	4.5 ± 0.1	3.5 ± 0.1
	800	6.7 ± 0.8	6.1 ± 0.9	15.2 ± 1.0	5.4 ± 0.1	6.5 ± 0.1	2.6 ± 0.1
	1000	3.7 ± 4.0	2.2 ± 4.4	16.3 ± 1.0	7.7 ± 0.1	7.6 ± 0.1	2.7 ± 0.1
1.0	0	0.4 ± 0.3	1.7 ± 0.3	0.3 ± 0.3	1.3 ± 0.1	1.4 ± 0.1	2.6 ± 0.1
	200	0.5 ± 0.2	0.9 ± 0.1	3.0 ± 0.3	1.5 ± 0.1	1.5 ± 0.1	3.2 ± 0.1
	400	0.9 ± 0.3	0.6 ± 0.3	7.7 ± 0.3	1.8 ± 0.1	2.2 ± 0.1	3.6 ± 0.1
	600	1.3 ± 0.2	1.7 ± 0.3	11.1 ± 0.3	2.8 ± 0.1	4.0 ± 0.1	3.2 ± 0.1
	800	1.9 ± 0.2	2.1 ± 0.3	12.3 ± 0.4	4.3 ± 0.1	5.3 ± 0.1	2.8 ± 0.1
	1000	2.9 ± 0.2	2.7 ± 0.3	14.5 ± 0.4	6.1 ± 0.1	7.0 ± 0.1	2.6 ± 0.1
1.5	0	0.5 ± 1.1	1.2 ± 1.1	0.1 ± 1.0	1.2 ± 0.1	1.2 ± 0.1	2.2 ± 0.1
	200	0.4 ± 0.8	0.9 ± 0.8	2.5 ± 0.7	1.3 ± 0.1	1.4 ± 0.1	3.1 ± 0.1
	400	0.4 ± 0.8	0.3 ± 0.8	8.0 ± 0.8	2.4 ± 0.1	2.6 ± 0.1	3.7 ± 0.1
	600	1.0 ± 0.8	0.5 ± 0.8	9.0 ± 0.8	2.6 ± 0.1	3.5 ± 0.1	3.1 ± 0.1
	800	1.8 ± 0.8	1.3 ± 0.8	8.4 ± 0.8	4.2 ± 0.1	4.5 ± 0.1	2.9 ± 0.1
	1000	3.4 ± 4.4	2.6 ± 5.4	7.8 ± 0.8	5.1 ± 0.1	5.6 ± 0.1	2.5 ± 0.1

cold phase at lower heights and the warm phase towards the vertical edges, with the correlation functions for $\boldsymbol{u}'$ more indicative of the hot phase statistics.

The correlation length for fluctuations in gas number density increases with height, with the model H1$\Omega_{\dot{\sigma}=0.5}$ containing the larger correlation scales. In H1$\Omega_{\dot{\sigma}=1.0}$ and H1$\Omega_{\dot{\sigma}=1.5}$, l_0 is almost constant up to $|z| = 600$ pc but increases for large values of $|z|$. The smaller correlation scales nearer to the mid-plane are attributed to the clouds of cold gas. The larger values of l_0 near to the vertical edges of the domain result from the larger regions of more diffuse warm gas.

The correlation scales of the components of the turbulent velocity $\boldsymbol{u}'$ increase with height; this is attributed to the reduction of the number of SN remnants (leading to larger turbulent eddies) for the horizontal components, whilst the increasing scale of the vertical turbulent motions is attributed to the increasing size of outflow regions with height.

The rms values of both n' and the components of $\boldsymbol{u}'$ in each of the hydrodynamic models analysed here are significantly larger than those from the MHD B1Ω analysed in Chapter 5. The increased values of $n'_{\rm rms}$ is attributed to the larger fractional volumes of the cold gas, whilst the increase in the root-mean-square of the turbulent velocity occurs from the larger velocities in the increased abundances of hotter, more diffuse in each of the HD models analysed in this chapter.

The greater amounts of cold gas result in the reduced correlation scale of n' in the hydrodynamic models, compared to B1Ω. However, no similar systematic reduction in l_0 for the turbulent

velocity is observed. This indicates the interior motions of the SN remnants are more significant in determining the scale of the turbulent motions, compared to the surrounding gas.

In contrast to Chapter 5, the correlation times increase away from the mid-plane, attributed to the reduced driving of the turbulence caused by a reduction in the number of supernova remnants with height. The correlation times decrease with supernova rate, whilst for all models, τ_0 is larger in the z–direction, compared to the horizontal directions.

Similar dependence of the eddy turnover time on the supernova rate is observed, with smaller differences than for the correlation time. For both u'_x and u'_y, $\tau_{\rm eddy}$ is a good estimate of τ_0. However, for u'_z, the eddy turnover time is too small, by almost an order of magnitude at large heights. The time between the passing of shocks, $\tau_{\rm shock}$, provides similarly accurate estimates to those of $\tau_{\rm eddy}$. Thus, the consideration of other physical processes, such as the propagation of supernova remnants towards the vertical edges of the domain, is required to properly characterise the correlation time of the random vertical motions.

Part V

Summary of results

Chapter 9

Summary of results

9.1 Results from the Magnetised ISM

The systematic application of correlation analysis to random fields from simulations of the magnetised ISM has been performed. Given the highly non-Gaussian nature of random fields – because of widespread filamentary and planar, small-scale structures – second-order correlation functions cannot fully capture the properties of the random fields. Nonetheless, correlation analysis is an important first tool in the understanding of random fields.

Analysis of the fluctuations of the basic variables (density, magnetic field and velocity) demonstrate that ISM turbulence is not characterised by a single correlation length; the length varies between 40 pc and 90 pc depending on height and variable analysed. The fluctuating fields are obtained by subtracting mean fields obtained from Gaussian smoothing with a smoothing length of 50 pc. The larger correlation scales suggest this smoothing length does not provide an artificial limit on the correlation lengths obtained.

Time correlation analysis of the random velocity yields a correlation time of order 10^7 yr, comparable to the eddy turnover time. The correlation time was found to be independent of z, although this could be a result of the broad z–layers used in the spatial averaging.

Comparisons with a simulation with double rotation rate demonstrate the lack of sensitivity of the correlation statistics to the rotation. Additionally, comparisons to a simulation performed with the 'standard' parameters in a larger domain reveals the the domain size used does not appear to place any constraint on the correlation scales.

The random magnetic field is anisotropic, with larger rms values of the y– and z–components, compared to the x–component. The y–component is amplified by the global velocity shear, whilst the z–component is amplified by the locally inhomogeneous outflow to the galactic halo. The lack of difference between the correlation scales of the x– and y–components is attributed to the assumption of local horizontal isotropy in the calculation of the correlation functions.

The correlation scale of Faraday depth along the z–axis exceeds that of both electron density

and vertical magnetic field, suggesting a non-trivial relationship between the correlation properties of Faraday depth and the quantities from which it is calculated. The structure functions of the synchrotron intensity reveal rapidly increasing uncertainties with the scale, which can undermine the usefulness of power spectra of synchrotron intensity in studies of interstellar turbulence, since this feature is hidden within power spectra analysis.

Spectral analysis of mean and fluctuating magnetic field, gas density and gas velocity, obtained via Gaussian smoothing, was performed to determine the range of acceptable smoothing lengths that can be applied. Whilst the spectral properties of each of these fields are distinct and vary significantly with time, most likely as the result of the mean field dynamo, an acceptable range can still be determined. The most suitable compromise value for a universal smoothing length in our simulations is $\ell = 75\,\mathrm{pc}$.

Mathematically and physically meaningful second (magnetic energy) and third order moments (kinetic energy in a compressible fluid) of the fluctuations calculated from this technique can be obtained, following the approach detailed in Germano (1992). Both small-scale spatial variations of these moments and their volume averages can be discussed. Of particular interest is the kinetic energy density on 'intermediate' scales, e_{st}, which is calculated as the advection of momentum fluctuations by the mean flow. This term is closely associated with outflows of hot gas in the simulations.

The action of the mean-field dynamo significantly alters the properties of these moments and the fields from which they are calculated. As the dynamo saturates, the mean magnetic field becomes dominant over the fluctuations and the length scales of both fields in addition to the total field, increase. This is perhaps unsurprising given that we do not have a turbulent dynamo in the model due to low magnetic Reynolds numbers. Subsequently, the fluctuating magnetic field results from the tangling of mean field by turbulence. As the mean-field dynamo saturates, e_{st} is drastically reduced. This is also unsurprising since the size and velocity of outflow regions are significantly reduced by the action of the mean magnetic field. Additionally, the overall kinetic energy is reduced, albeit only fractionally.

9.2 Effects of the Supernova Rate

A comparison of hydrodynamic runs using different supernova rates, varying between one half and three halves the supernova rate in the Solar neighbourhood, has been performed. Whilst each model contains the unsatisfactory feature of a higher than expected fractional volume of hot gas, attributed to the change in mean molecular weight and the removal of the cooling and heating cutoff in the shocks, informative qualitative results were obtained which could assist in further study of the effects of the supernova rate on the ISM.

A clear multi-phase structure can be identified for each model, with common boundaries in specific entropy appropriate for each model. Increasing supernova rate narrows the distributions

of density and temperature in both the cold and hot phases. Whilst the density distribution in the warm phase also narrows, a wider range of temperatures are identified in the warm phase. The thermal pressures within each phase are weakly affected by the increasing supernova rate, with the turbulent pressure in the hot gas marginally contributing to the total pressure in the hot gas within each model. The turbulent pressure is more significant in the cold and warm phases, with increased amounts of the cold and warm gas at higher pressures in the higher supernova rate models. The increased turbulent pressures are attributed to stronger turbulent motions driven by the SNe.

As the supernova rate increases, the warm gas is depleted with greater abundances of cold and hot gas, in qualitative agreement with other models. The phase filling factor of the cold gas suggests that the cold gas becomes more homogeneous, whilst the warm gas becomes more intermittent as the supernova rate increases. The phase filling factor of the hot gas is unaffected. The volume filling factors of the cold and warm gas are closely associated with their fractional volumes, whilst the volume filling factor of the hot gas is strongly linked to its phase filling factor. Further statistical analysis is required in order to fully understand the relationship between the volume filling factor and the phase filling factor and fractional volume within each of the cold, warm and hot phases.

The increasing supernova rate increases the thickness of the disk and the density scale-height, as a result of increased turbulent pressure which is also increasingly significant at larger heights. The increase in turbulent pressure can be attributed to increased presence of the cold gas, which is over-pressured in the disk as a result of the vertical pressure gradient. Increased supernova heating results in marginally increased mean temperature and thermal pressure throughout the domain.

The increased pressures from the increasing supernova rate drive stronger outflows from the disk. However, increasing the supernova rate beyond the rate in the Solar neighbourhood does not result in faster turbulent motions. The increasing root-mean-square velocity with the supernova rate is attributed to the increased mean vertical velocities.

The dependence of the correlation statistics of both the fluctuations in gas number density, n', and the components of the turbulent velocity, $\boldsymbol{u}'$, on the supernova rate are analysed. Informative spatial and temporal correlation functions, with no phase separation applied, were computed from the simulation data, despite the higher abundance of the hot gas in the hydrodynamic simulations.

The correlation length for fluctuations in gas number density increases with height, and decreases with supernova rate. The smaller correlation scales nearer to the mid-plane are attributed to the clouds of cold gas. The increasing values of l_0 with height result from larger regions of more diffuse warm gas.

In each of the three models, the correlation scales of the components of the turbulent velocity increase with height. For the horizontal components, this is attributed to the reduction in the number of SN remnants with height. The increasing scale of the vertical turbulent motions results from the increasing size of outflow regions with height.

In comparison to the results from B1Ω, the rms values of both n' and the components of

$\boldsymbol{u}'$ in each of the three hydrodynamic models are much higher. The increased values of $n'_{\rm rms}$ are attributed to the larger fractional volumes of the cold gas, in which the variation in density fluctuations is much larger. The increase in the rms turbulent velocities results from the larger velocities in the more diffuse hot gas, with occupies a larger fractional volume in each of the hydrodynamic models analysed.

This increased fractional volume of the cold gas results in the reduced correlation scale of n' in the hydrodynamic models. However, no systematic reduction in the correlation scale of the turbulent velocity is observed. This suggests the correlation scales are more determined by the interior motions within SN remnants.

In contrast to the results from B1Ω, the correlation time τ_0 increases away from the mid-plane. The increasing correlation time is attributed to the reduced driving of turbulence by a reduced frequency of supernovae away from the mid-plane. The correlation times decrease with supernova rate, with τ_0 larger for the z–component, as compared to the horizontal components.

For both u'_x and u'_y, $\tau_{\rm eddy}$ and $\tau_{\rm shock}$ are both reasonable estimates of τ_0. However, for u'_z, both of these estimates are too small, by almost an order of magnitude at large heights. The shock time is the worse estimate in this case. Thus, the consideration of other physical processes, such as the vertical bulk motion of supernova remnants towards the vertical edges, is required to characterise the correlation time of the random vertical motions.

9.3 Further Investigation

Detailed analysis have been performed of simulations of the multi-phase ISM, which span wide ranges in density and temperature, $10^{-4} \lesssim n \lesssim 10^{2}\,{\rm cm}^{-3}$ and $10^{2} \lesssim T \lesssim 10^{8}\,{\rm K}$ respectively. A resolution of 4 pc has been demonstrated to be able to capture the physics modelled in the simulation, with results comparable to runs employing 2 pc and 1.25 pc resolutions which provide modest improvement. Progress has been made in the analysis of the different phases in the ISM, descriptions of the turbulent density, velocity and magnetic field, with some exploration of the influence of the mean-field dynamo. In addition, the influence of the supernova rate on the multi-phase structure and the correlation statistics has been investigated. The comparisons to both observations and exiting numerical models are complicated by the over abundance of hot gas, which is attributed to changes in the mean molecular weight and the removal of the cooling cut-off in the shocks. Nonetheless, the trends identified are expected to be robust within a set of simulations which have fractional volumes closer to those expected for the Solar neighbourhood.

Investigations of the effects of supernova rate in hydrodynamic simulations were performed, showing the impact on the vertical and multi-phase structures, and the correlation statistics. However, these results may not be reliable because of the much higher than expected abundance of hot gas within each of the runs. Performing a new set of hydrodynamic simulations with different supernova rates, in which the Solar neighbourhood rate parameters produce fractional volumes of

each phase closer to those observed, will be useful to test the robustness of the trends identified in this Thesis. The most significant change required is to update the cooling function to account for the value of the mean molecular weight, which would improve the efficiency of the cooling of the hot gas.

It may also be useful to extend the range of supernova rates used in order to better explore the dependence of the statistical properties of the ISM on the supernova rate.

Line-of-sight simulated observations along the z–axis were made in order to perform correlation analysis for Faraday depth and synchrotron emission. It would be useful to extend this to compute line-of-sight observations from any location in the domain, accounting for both elevation and any local bubbles, would allow for further comparison to observations. Additionally, such results would enable new interpretations of observational measurements, with regard to the underlying physics. Measurements of Faraday rotation measures of the magnetic field within the domain would be of particular interest. The models considered so far use parameters typical of the Solar neighbourhood, so comparisons between the statistics from the simulated results and the observational data should be reasonably straightforward.

Based upon the existing models and analysis performed, a number of future extensions to the model and interesting challenges present themselves.

Production of Hot Gas

As shown in Chapter 7, the fractional volume of hot gas in the hydrodynamic runs $\mathrm{H1}\Omega_{\dot{\sigma}=0.5}$, $\mathrm{H1}\Omega_{\dot{\sigma}=1.0}$ and $\mathrm{H1}\Omega_{\dot{\sigma}=1.5}$ is much higher than the fractional volumes of hot gas from observations of the Solar neighbourhood or previous ISM simulations of the Solar neighbourhood. In Section 7.2, it is speculated that this over-production of hot gas results from a reduction in the strength of the cooling function because of the reduced mean molecular weight, and the reduction of the density in the ISM surrounding supernova remnants because of the concentration of a higher proportion of the mass into cold, high density regions resulting from the removal of cooling cutoff in shocks. The effect of both of these changes needs to be tested in order to determine the necessary changes for future simulations to exhibit more fractional volumes of each of the cold, warm and hot phases.

The impact of the change in mean molecular weight on the cooling function could be tested with a simplified model using parametrised supernova heating. A comparison between two runs which explore $\mu = 0.531$ and $\mu = 0.62$ respectively will explore the impact of the reduced mean molecular weight on the temperature of the gas and the fractional volume of hot gas. In future simulations, it may also be advisable to include the factor of $1/\mu^2$ in the cooling function that has been neglected in this work and by previous authors. This would result in much greater cooling than explored by previous authors and so would also need to be tested in a simplified model before being applied to a multi-SNe ISM simulation.

The effect of the cooling cutoff in the shocks can be investigated by performing tests of a single supernova explosion. A comparison of the density and temperature of the gas in the supernova shock in runs with and without the shock cutoff will determine the importance of the removal of the cutoff in the formation of higher density cold gas, which would reduce the ambient density throughout the ISM as a whole, as explained in Section 7.2.

Parameter exploration

The testing of the effects of different parameters requires the consideration of a range of values, at least three but ideally more. The effects of varying the SN rate have been investigated here, but should be repeated for a wider range of rates. The rotation and shear rates need to also be varied independently to identify the influence of rotation and shear on the dynamics of the ISM and the mean-field dynamo.

The model has currently been tested only for parameters comparable to the Milky Way but can be extended to other galaxies at different stages of their evolution. For example, younger galaxies could be modelled using a different stellar gravitational potential and a higher proportion of ISM gas to stars.

Reynolds Numbers

The effective Reynolds number in the standard MHD model explored is of order 10, significantly smaller than the values estimated for the ISM. Whilst not measured here, it is expected that the magnetic Reynolds is of order 10–100. These result from the artificially high viscosity and diffusivities required in order to maintain numerical stability. Increasing the Reynold number would correspond to turbulent motions more similar to observations, whilst a sufficiently high magnetic Reynolds number would result in turbulent dynamo action amplifying the small-scale magnetic field. The increasing Reynolds numbers would require a reduction in the viscosity and diffusivities. However, this could create numerical instabilities. Extensive and careful testing to determine the minimum diffusivities, and refinements to the model to allow for reduced diffusivities, would need to be performed. Nonetheless, increasing Reynolds numbers are an important step in order for simulation results to be in closer agreement with observations.

Supernova Feedback and Star Formation Rates

The SN rates used in the models are implemented as a parameter, based on multiples of the observed SN rate in the Solar neighbourhood. The Kennicutt-Schmidt law details the relationship between gas surface density and star formation rate in galactic disks, from which the SN rate can be determined, and provides a reasonable fit to observations (see Kennicutt, 1998). The numerical

models of Dobbs et al. (2011) performed on the galactic scale have been able to reproduce supernova feedback and star formation rates which are in reasonable agreement with observations. In the local ISM simulations of Gatto et al. (2017), in which the SNe occur from massive stars formed from self-gravity of the cold gas rather than through SNe injection, the star formation rate was found to be in reasonable agreement with observations. The exception is the run in which stellar winds are absent, where the star formation rate was too high.

It would be useful to implement the regulation of star formation rate by SN feedback in our model, through either the processes employed by Gatto et al. (2017) or Kim & Ostriker (2017), or by other methods. Any method of SN feedback will need to respond to the mass available for star formation and the distribution of the gas between the cold and warm phases. This would result in star formation decreasing as gas is removed from the star-forming disk by hot gas outflows, before then increasing as more gas cools into dense clouds. The clustering of SNe may need to be included to better model SN feedback since SNe clustering is known to strongly drive hot gas outflows from the disk. The vertical extent would need to be increased to allow for the reasonable modelling of a fountain flow, in order for gas to be removed from the disk and then return to the mid-plane once it has cooled sufficiently. The presence of spiral arms and other effects results in the rarefaction of gas density across the disk. Thus it is not clear that we should expect to replicate the Kennicutt-Schmidt law, which is determined for whole galaxies, within a local ISM simulation. However, by considering a set of models exploring a range of gas densities modelling the spiral arm (interarm) regions, the Kennicutt-Schmidt law would be a lower (upper) bound respectively to explore the suitability of the SN feedback method implemented. An effective SN feedback method would be useful when trying to apply the model to different galaxies, which may require the use of significantly different parameters to those used to model the Galaxy.

Kennicutt-Schmidt Law

As stated above, the Kennicutt-Schmidt law provides a relationship between gas surface density and star formation rate. In each of the models explored in this Thesis, a constant star formation rate based on observations is assumed. By calculating the gas surface density in these simulations, it can be determined if our simulations satisfy the Kennicutt-Schmidt law. If these simulations do not satisfy the Kennicutt-Schmidt law, the star formation rate or the mass in the simulation would need to be adjusted. It may be more productive to implement SN feedback in our model, as discussed previously, to regulate star formation and to ensure the relationship between gas surface density and star formation rate is good fit to the Kennicutt-Schmidt law, rather than rely on achieving the desired outcome via empirical adjustments of simulation parameters

Galactic Fountain

As demonstrated by de Avillez & Breitschwerdt (2007) and similar models, a vertical extent of $z = \pm 10\,\mathrm{kpc}$ is required for the hot gas to cool and return to the mid-plane. Given the limited horizontal scales employed (up to 1 kpc), the scales of the galactic fountain have yet to be fully explored, since we cannot be confident that any effects introduced by periodic boundaries at large heights can be ignored. To explore the length and time scales of the galactic fountain, an increase in the horizontal extent is required. A varying resolution Δ with height, becoming more coarse away from the mid-plane, will be required to minimise computational expense. Given the quenching nature of the magnetic field, and the impact of cosmic rays on the velocity, density and temperature of hot gas outflows, it may be more efficient to include these effects, compared to a purely hydrodynamic model.

The inclusion of a galactic fountain flow would remove the need for the artificial replacement of mass, as detailed in Section 3.6, and so any impact of the mass replacement in the dynamics, however small, would be removed. In addition, the modelling of gas returning to the disk would be more realistic, as opposed to the inflow boundary conditions detailed in Section 3.5.

Cosmic Rays

Cosmic rays are estimated to provide about a quarter of the pressure in the ISM. They are also strongly correlated with the magnetic field. The inclusion of these will enable a more direct comparison with observations, particularly the vertical distributions of pressure, temperature and density. Additionally, the thickness of the Galactic disk is expected to be increased by cosmic ray pressure. The effects of cosmic rays in both hydrodynamic and magnetohydrodynamic kiloparsec-scale simulations of the ISM have been investigated by Girichidis et al. (2016b, 2018a); Simpson et al. (2016), which provide both a useful benchmark and motivation for the detailed analysis of simulations which include cosmic rays.

The measurement of synchrotron emission is an important tool in observations, and is dependent on the distribution of cosmic rays. Whilst calculations of synchrotron emissivity in simulations can be made, based on certain observational assumptions about the cosmic ray distribution (see Chapter 5), modelling cosmic rays directly will lead to more robust results. The ability to make direct line-of-sight measurements from simulated data is a vital step in the comparison of simulations to observations and the ability to make measurements of a more realistic simulation will improve these comparisons, in addition to allowing for the testing of the observational assumptions.

Spiral Arms

The models considered all assume the gas is located in an interarm region of the Galaxy. As the simulation box orbits the galactic centre, no density waves are encountered. The impact of arm-interarm interactions on star formation and the generation and orientation of the magnetic field remains to be investigated. Within a kiloparsec-scale model, spiral arms can be modelled as an additional gravitational potential passing through the domain periodically in time.

Magnetorotational Instability

Magnetorotational instabilities occur in plasmas as a result of differential rotation (Balbus & Hawley, 1991). It is found that these are most important in regions of galaxies where the supernova rate is low (Sellwood & Balbus, 1999). By performing simulations with and without supernova-driven turbulence in a system which includes magnetorotational instabilities, the importance of magnetorotational instabilities in driving turbulence in the ISM and any damping of magnetorotational instabilities by supernova-driven turbulence can be measured.

9.4 Review

In conclusion, detailed and systematic analysis has been performed on two sets of models; one MHD set and one hydrodynamic set. Such models are highly complex in nature due to the numerical implementation required to correctly model the physics we intend to capture. The consequences of any changes in the model can take hundreds of thousands of iterations to become apparent, and it is not always clear if the outcomes result from physical effects or from numerical artefacts. Theoretical models and observational data are incomplete and so it is not always clear if the results obtained can be fully verified by a comparison to our expectations of the ISM.

Ideally, a more comprehensive set of models which have more similar parameters, both with and without magnetic fields, would be performed and analysed. However, the expense of such models in both computational resources and time limits our ability to do this. Consequently, changes in implementation and parameters are difficult to apply retrospectively, and there are important differences between the models presented here that one must be careful to acknowledge when making inferences from the data.

Nonetheless, the results presented here provide further insight into the nature of turbulence within existing ISM models, and the impact of the supernova rate on both the large-scale and turbulent structures in the ISM. Additionally, the experience in the interpretation and reporting of results that I have gained has been reported here. The simulations presented here are a rich numerical resource that has yet to be fully explored. New simulations with extensions and improvements to the model, in addition to new analysis of ISM models built upon previous work and new analyt-

ical techniques, have the potential to explore the ISM in far greater detail than is presented here. In doing so, many new and interesting insights into both the structure and dynamics of galaxies will be obtained.

Appendix A

Derivation of the kinetic energy densities

The mean kinetic energy of a compressible flow under ensemble (or volume) averaging can be expressed in three physically meaningfully components, as demonstrated in Monin & Yaglom (2007a, Section 6.4), first shown in Chapter 6 but repeated here for convenience;

$$\begin{aligned}\langle e_K\rangle &= \frac{1}{2}\langle\rho u_i u_i\rangle \\ &= \frac{1}{2}\langle\rho\rangle\langle u_i\rangle\langle u_i\rangle + \langle u_i\rangle\langle\rho' u_i'\rangle + \frac{1}{2}\langle\rho\rangle\langle u_i' u_i'\rangle + \frac{1}{2}\langle\rho' u_i' u_i'\rangle \\ &\equiv e_s + e_{st} + e_t\,,\end{aligned} \tag{A.1}$$

where e_s is the energy density of the mean flow, e_t is the energy density of the fluctuations and e_{st} represents the transport of momentum $\langle\rho' u_i'\rangle$ by the mean flow, with repeated indices implying summation. By applying ensemble or volume averaging to the compressible Navier–Stokes equations, evolution equations can be written for each of these kinetic energy densities, as detailed in Monin & Yaglom (2007a, Section 6.4).

Applying the same reasoning as above, the averaged kinetic energy density under filtering averaging is decomposed as follows:

$$\begin{aligned}\langle e_K\rangle_\ell &= \tfrac{1}{2}\langle\rho u_i u_i\rangle_\ell \\ &= \tfrac{1}{2}\langle\rho\rangle_\ell\langle u_i\rangle_\ell\langle u_i\rangle_\ell + \langle u_i\rangle_\ell\,\upsilon(\rho, u_i) + \tfrac{1}{2}\langle\rho\rangle_\ell\,\upsilon(u_i, u_i) + \tfrac{1}{2}\upsilon(\rho, u_i, u_i) \\ &\equiv e_s + e_{st} + e_t,\end{aligned} \tag{A.2}$$

where $e_s = \frac{1}{2}\langle\rho\rangle_\ell\langle u_i\rangle_\ell\langle u_i\rangle_\ell$, $e_{st} = \langle\rho\rangle_\ell\,\upsilon(u_i, u_i)$ and $e_t = \frac{1}{2}\langle\rho\rangle_\ell\,\upsilon(u_i, u_i) + \frac{1}{2}\upsilon(\rho, u_i, u_i)$.

Using the outline from the derivation detailed in Monin & Yaglom (2007a, Section 6.4), I shall derive the evolution equations for the energy densities obtained via filtering averaging (of which Gaussian smoothing is a special case), analogous to the approach for the incompressible

Navier–Stokes equations outlined in Germano (1992). This shall demonstrate both the averaging invariance of the compressible Navier–Stokes equations and the validity of the kinetic energy densities obtained from Gaussian smoothing used in Chapter 6.

A.1 Filtering averaging

All variables will be decomposed into mean and fluctuating components as follows:

$$f = \langle f \rangle_\ell + f', \tag{A.3}$$

with $\langle\rangle_\ell$ denoting averaging with a filter of charateristic width ℓ and $'$ denoting fluctuations. Gaussian smoothing is a special case of filtering averaging, in which the filter used is a Gaussian kernel. Such averaging does not satisfy the Reynolds rules

$$\langle \langle f \rangle_\ell \rangle_\ell \neq \langle f \rangle_\ell, \quad \langle f' \rangle_\ell \neq 0, \tag{A.4}$$

and so

$$\langle \langle f \rangle_\ell \langle g \rangle_\ell \rangle_\ell \neq \langle f \rangle_\ell \langle g \rangle_\ell, \quad \langle \langle f \rangle_\ell g' \rangle_\ell \neq \langle f \rangle_\ell \langle g' \rangle_\ell. \tag{A.5}$$

We shall require the averaging operator to be linear, constant preserving

$$\langle f + g \rangle_\ell = \langle f \rangle_\ell + \langle g \rangle_\ell, \quad \langle \alpha f \rangle_\ell = \alpha \langle f \rangle_\ell \quad \text{if } \alpha = \text{constant}, \tag{A.6}$$

and commutative with derivatives

$$\left\langle \frac{\partial f}{\partial t} \right\rangle_\ell = \frac{\partial \langle f \rangle_\ell}{\partial t}, \quad \left\langle \frac{\partial f}{\partial x_i} \right\rangle_\ell = \frac{\partial \langle f \rangle_\ell}{\partial x_i}. \tag{A.7}$$

As discussed in Chapter 6, in order to regain simplicity as in the previous derivation, we introduce a new set of moments as defined in Germano (1992)

$$\begin{aligned}
\langle u_i u_j \rangle_\ell &= \langle u_i \rangle_\ell \langle u_j \rangle_\ell + \upsilon(u_i, u_j), \\
\langle u_i u_j u_k \rangle_\ell &= \langle u_i \rangle_\ell \langle u_j \rangle_\ell \langle u_k \rangle_\ell + \langle u_i \rangle_\ell \upsilon(u_j u_k) + \langle u_j \rangle_\ell \upsilon(u_k u_i) \\
&\quad + \langle u_k \rangle_\ell \upsilon(u_i u_j) + \upsilon(u_i, u_j, u_k), \\
\langle u_i u_j u_k u_p \rangle_\ell &= \langle u_i \rangle_\ell \langle u_j \rangle_\ell \langle u_k \rangle_\ell \langle u_p \rangle_\ell + \langle u_i \rangle_\ell \langle u_j \rangle_\ell \upsilon(u_k, u_p) \\
&\quad + \langle u_j \rangle_\ell \langle u_k \rangle_\ell \upsilon(u_p, u_i) + \langle u_k \rangle_\ell \langle u_p \rangle_\ell \upsilon(u_i, u_j) \\
&\quad + \langle u_p \rangle_\ell \langle u_i \rangle_\ell \upsilon(u_j, u_k) + \langle u_i \rangle_\ell \langle u_k \rangle_\ell \upsilon(u_j, u_p) \\
&\quad + \langle u_j \rangle_\ell \langle u_p \rangle_\ell \upsilon(u_i, u_k) + \langle u_i \rangle_\ell \upsilon(u_j, u_k, u_p) \\
&\quad + \langle u_j \rangle_\ell \upsilon(u_k, u_p, u_i) + \langle u_k \rangle_\ell \upsilon(u_p, u_i, u_j) \\
&\quad + \langle u_p \rangle_\ell \upsilon(u_i, u_j, u_k) + \upsilon(u_i, u_j, u_k, u_p).
\end{aligned} \tag{A.8}$$

A.2 Compressible Navier-Stokes equations

We start with the continuity equation and Navier-Stokes equations for a compressible fluid:

$$\frac{\partial \rho}{\partial t} + \frac{\partial}{\partial x_k}(\rho u_k) = 0, \tag{A.9}$$

$$\frac{\partial}{\partial t}(\rho u_i) + \frac{\partial}{\partial x_k}(\rho u_i u_k + p\,\delta_{ik} - \sigma_{ik}) = \rho X_i, \tag{A.10}$$

where X_i is the ith component of any external forces and σ_{ik} is the general viscous stress tensor, given by

$$\sigma_{ij} = \mu_v \left(\frac{\partial u_i}{\partial x_j} + \frac{\partial u_j}{\partial x_i} - \frac{2}{3}\frac{\partial u_k}{\partial x_k}\,\delta_{ij} \right) + \zeta\,\frac{\partial u_k}{\partial x_k}\,\delta_{ij}, \tag{A.11}$$

where μ_v and ζ are coefficients of viscosity. We shall also make use of the following re-arranged version of (A.10):

$$\frac{\partial u_i}{\partial t} + u_k\frac{\partial u_i}{\partial x_k} = X_i - \frac{1}{\rho}\frac{\partial p}{\partial x_i} + \frac{1}{\rho}\frac{\partial \sigma_{ik}}{\partial x_k}. \tag{A.12}$$

A.3 Total kinetic energy density

We start by deriving the equation for the total kinetic energy, which will be averaged later. The first step is to multiply (A.10) by u_j and add this to the same equation but with the indices i and j reversed:

$$u_j\frac{\partial}{\partial t}(\rho u_i) + u_j\frac{\partial}{\partial x_k}(\rho u_i u_k) + u_j\frac{\partial p}{\partial x_i} - u_j\frac{\partial \sigma_{ik}}{\partial x_k} = \rho u_j X_i, \tag{A.13}$$

$$u_i\frac{\partial}{\partial t}(\rho u_j) + u_i\frac{\partial}{\partial x_k}(\rho u_j u_k) + u_i\frac{\partial p}{\partial x_j} - u_i\frac{\partial \sigma_{jk}}{\partial x_k} = \rho u_i X_j. \tag{A.14}$$

Expanding the first two term in (A.13) and (A.14) yield

$$u_j\frac{\partial \rho}{\partial t}u_i + u_j\rho\frac{\partial u_i}{\partial t} + u_j u_i\frac{\partial}{\partial x_k}(\rho u_k) + u_j\rho u_k\frac{\partial u_i}{\partial x_k},$$
$$u_i\frac{\partial \rho}{\partial t}u_j + u_i\rho\frac{\partial u_j}{\partial t} + u_i u_j\frac{\partial}{\partial x_k}(\rho u_k) + u_i\rho u_k\frac{\partial u_j}{\partial x_k}.$$

Summing these and using (A.9) results in

$$\frac{\partial}{\partial t}(\rho u_i u_j) + u_i u_j\frac{\partial \rho}{\partial t} + \frac{\partial}{\partial x_k}(\rho u_i u_j u_k) + u_i u_j\frac{\partial}{\partial x_k}(\rho u_k) = \frac{\partial}{\partial t}(\rho u_i u_j) + \frac{\partial}{\partial x_k}(\rho u_i u_j u_k). \tag{A.15}$$

Hence, the sum of (A.13) and (A.14) yields

$$\frac{\partial}{\partial t}(\rho u_i u_j) + \frac{\partial}{\partial x_k}(\rho u_i u_j u_k) + u_j\frac{\partial p}{\partial x_i} + u_i\frac{\partial p}{\partial x_j} - u_j\frac{\partial \sigma_{ik}}{\partial x_k} - u_i\frac{\partial \sigma_{jk}}{\partial x_k} = \rho u_j X_i + \rho u_j X_j. \tag{A.16}$$

We can also re-arrange the terms involving pressure and the stress tensor:

$$u_j\frac{\partial p}{\partial x_i}=\frac{\partial}{\partial x_i}(pu_j)-p\frac{\partial u_j}{\partial x_i},\quad u_i\frac{\partial p}{\partial x_j}=\frac{\partial}{\partial x_j}(pu_i)-p\frac{\partial u_i}{\partial x_j},$$
$$u_j\frac{\partial \sigma_{ik}}{\partial x_k}=\frac{\partial}{\partial x_k}(u_j\sigma_{ik})-\frac{\partial u_j}{\partial x_k}\sigma_{ik},\quad u_i\frac{\partial \sigma_{jk}}{\partial x_k}=\frac{\partial}{\partial x_k}(u_i\sigma_{jk})-\frac{\partial u_i}{\partial x_k}\sigma_{jk}.$$

Combining this with (A.16) results in

$$\begin{aligned}\frac{\partial}{\partial t}(\rho u_iu_j)+\frac{\partial}{\partial x_k}(\rho u_iu_ju_k+pu_j\delta_{ik}+pu_i\delta_{jk}-u_j\sigma_{ik}-u_i\sigma_{jk})\\ =p\frac{\partial u_j}{\partial x_i}+p\frac{\partial u_i}{\partial x_j}-\frac{\partial u_j}{\partial x_k}\sigma_{ik}-\frac{\partial u_i}{\partial x_k}\sigma_{jk}+\rho u_jX_i+\rho u_jX_j.\end{aligned}\tag{A.17}$$

Taking $i=j$ and dividing by 2 gives the equation for the total kinetic energy $e_K=\frac{1}{2}\rho u_iu_i$

$$\frac{\partial e_K}{\partial t}+\frac{\partial}{\partial x_k}(e_Ku_k+pu_k-u_i\sigma_{ik})=p\frac{\partial u_i}{\partial x_i}-\frac{\partial u_i}{\partial x_k}\sigma_{ik}+\rho u_iX_i.\tag{A.18}$$

A.4 Kinetic Energy of the mean motion

To obtain the kinetic energy of the mean motion, we first require the filtered continuity and Navier–Stokes equations;

$$\frac{\partial\langle\rho\rangle_\ell}{\partial t}+\frac{\partial}{\partial x_k}\left[\langle\rho\rangle_\ell\langle u_k\rangle_\ell+\upsilon(\rho,u_k)\right]=0,\tag{A.19}$$

$$\begin{aligned}\frac{\partial}{\partial t}\left[\langle\rho\rangle_\ell\langle u_i\rangle_\ell+\upsilon(\rho,u_i)\right]+\frac{\partial}{\partial x_k}[\langle\rho\rangle_\ell\langle u_i\rangle_\ell\langle u_k\rangle_\ell+\langle u_i\rangle_\ell\upsilon(\rho,u_k)+\langle u_k\rangle_\ell\upsilon(\rho,u_i)\\ +\langle\rho\rangle_\ell\upsilon(u_i,u_k)+\upsilon(\rho,u_i,u_k)+\langle p\rangle_\ell\delta_{ik}-\langle\sigma_{ik}\rangle_\ell]\\ =\langle\rho\rangle_\ell\langle X_i\rangle_\ell+\upsilon(\rho,X_i),\end{aligned}\tag{A.20}$$

$$\langle\sigma_{ij}\rangle_\ell=\mu\left(\frac{\partial\langle u_i\rangle_\ell}{\partial x_j}+\frac{\partial\langle u_j\rangle_\ell}{\partial x_i}-\frac{2}{3}\frac{\partial\langle u_k\rangle_\ell}{\partial x_k}\delta_{ij}\right)+\zeta\frac{\partial\langle u_k\rangle_\ell}{\partial x_k}\delta_{ij}.\tag{A.21}$$

We shall also make use of the filtering averaged form of (A.12)

$$\frac{\partial\langle u_i\rangle_\ell}{\partial t}+\langle u_k\rangle_\ell\frac{\partial\langle u_i\rangle_\ell}{\partial x_k}+\upsilon\left(u_k,\frac{\partial u_i}{\partial x_k}\right)=\langle X_i\rangle_\ell-\left\langle\frac{1}{\rho}\frac{\partial p}{\partial x_i}\right\rangle_\ell+\left\langle\frac{1}{\rho}\frac{\partial\sigma_{ik}}{\partial x_k}\right\rangle_\ell.\tag{A.22}$$

We multiply (A.19) by $\langle u_i\rangle_\ell$ and (A.22) by $\langle\rho\rangle_\ell$, in order to determine the terms which contibute to the respective equations for the two components of momentum $\langle\rho\rangle_\ell\langle u_i\rangle_\ell$ and $\upsilon(\rho,u_i)$;

$$\langle u_i\rangle_\ell\frac{\partial\langle\rho\rangle_\ell}{\partial t}+\langle u_i\rangle_\ell\frac{\partial}{\partial x_k}[\langle\rho\rangle_\ell\langle u_k\rangle_\ell+\upsilon(\rho,u_k)]=0,\tag{A.23}$$
$$\langle\rho\rangle_\ell\frac{\partial\langle u_i\rangle_\ell}{\partial t}+\langle\rho\rangle_\ell\langle u_k\rangle_\ell\frac{\partial\langle u_i\rangle_\ell}{\partial x_k}+\langle\rho\rangle_\ell\upsilon\left(u_k,\frac{\partial u_i}{\partial x_k}\right)=\langle\rho\rangle_\ell\langle X_i\rangle_\ell$$

$$- \langle\rho\rangle_\ell \left\langle \frac{1}{\rho}\frac{\partial p}{\partial x_i} \right\rangle_\ell + \langle\rho\rangle_\ell \left\langle \frac{1}{\rho}\frac{\partial \sigma_{ik}}{\partial x_k} \right\rangle_\ell . \quad \text{(A.24)}$$

The term $\langle\rho\rangle_\ell \, \upsilon(u_k, \partial u_i/\partial x_k)$ is rewritten as follows:

$$\begin{aligned}
\langle\rho\rangle_\ell \, \upsilon\left(u_k, \frac{\partial u_i}{\partial x_k}\right) &= \langle\rho\rangle_\ell \left\langle u_k \frac{\partial u_i}{\partial x_k} \right\rangle_\ell - \langle\rho\rangle_\ell \langle u_k\rangle_\ell \frac{\partial \langle u_i\rangle_\ell}{\partial x_k} \\
&= \langle\rho\rangle_\ell \left\langle \frac{\partial}{\partial x_k}(u_i u_k) \right\rangle_\ell - \langle\rho\rangle_\ell \left\langle u_i \frac{\partial u_k}{\partial x_k} \right\rangle_\ell \\
&\quad - \langle\rho\rangle_\ell \frac{\partial}{\partial x_k}\left(\langle u_i\rangle_\ell \langle u_k\rangle_\ell\right) + \langle\rho\rangle_\ell \langle u_i\rangle_\ell \frac{\partial \langle u_k\rangle_\ell}{\partial x_k} \\
&= \langle\rho\rangle_\ell \frac{\partial}{\partial x_k}(\langle u_i u_k\rangle_\ell) - \langle\rho\rangle_\ell \frac{\partial}{\partial x_k}\left(\langle u_i\rangle_\ell \langle u_k\rangle_\ell\right) - \langle\rho\rangle_\ell \upsilon\left(u_i, \frac{\partial u_k}{\partial x_k}\right) \\
&= \langle\rho\rangle_\ell \frac{\partial}{\partial x_k}[\upsilon(u_i, u_k)] - \langle\rho\rangle_\ell \upsilon\left(u_i, \frac{\partial u_k}{\partial x_k}\right) \\
&= \frac{\partial}{\partial x_k}[\langle\rho\rangle_\ell \upsilon(u_i, u_k)] - \frac{\partial \langle\rho\rangle_\ell}{\partial x_k}\upsilon(u_i, u_k) - \langle\rho\rangle_\ell \upsilon\left(u_i, \frac{\partial u_k}{\partial x_k}\right).
\end{aligned}$$

Summing (A.23) and (A.24) gives

$$\frac{\partial}{\partial t}(\langle\rho\rangle_\ell \langle u_i\rangle_\ell) + \frac{\partial}{\partial x_k}(\langle\rho\rangle_\ell \langle u_i\rangle_\ell \langle u_k\rangle_\ell + \langle\rho\rangle_\ell \upsilon(u_i, u_k) + \langle p\rangle_\ell \delta_{ik} - \langle\sigma_{ik}\rangle_\ell) = \langle\rho\rangle_\ell \langle X_i\rangle_\ell + \phi_i, \quad \text{(A.25)}$$

where

$$\begin{aligned}
\phi_i = \frac{\partial \langle\rho\rangle_\ell}{\partial x_k}\upsilon(u_i, u_k) + \langle\rho\rangle_\ell \upsilon\left(u_i, \frac{\partial u_k}{\partial x_k}\right) - \langle u_i\rangle_\ell \frac{\partial}{\partial x_k}[\upsilon(\rho, u_k)] \\
+ \left(\frac{\partial \langle p\rangle_\ell}{\partial x_i} - \langle\rho\rangle_\ell \left\langle \frac{1}{\rho}\frac{\partial p}{\partial x_i} \right\rangle_\ell\right) + \left(\frac{\partial \langle\sigma_{ik}\rangle_\ell}{\partial x_k} - \langle\rho\rangle_\ell \left\langle \frac{1}{\rho}\frac{\partial \sigma_{ik}}{\partial x_k} \right\rangle_\ell\right). \quad \text{(A.26)}
\end{aligned}$$

It is expected that the mean pressure $\langle p\rangle_\ell$ and stress tensor $\langle\sigma_{ik}\rangle_\ell$ contribute to the mean flow, hence these are added to the left hand side of (A.25). We shall now proceed to derive the equation for the mean kinetic energy, using the same procedure as Section A.3, but using $\langle u_i\rangle_\ell$ and $\langle u_j\rangle_\ell$ instead of u_i and u_j;

$$\begin{aligned}
\langle u_j\rangle_\ell \frac{\partial}{\partial t}(\langle\rho\rangle_\ell \langle u_i\rangle_\ell) + \langle u_j\rangle_\ell \frac{\partial}{\partial x_k}(\langle\rho\rangle_\ell \langle u_i\rangle_\ell \langle u_k\rangle_\ell) + \langle u_j\rangle_\ell \frac{\partial}{\partial x_k}\left[\langle\rho\rangle_\ell \upsilon(u_i, u_k)\right] \\
+ \langle u_j\rangle_\ell \frac{\partial \langle p\rangle_\ell}{\partial x_i} - \langle u_j\rangle_\ell \frac{\partial \langle\sigma_{ik}\rangle_\ell}{\partial x_k} = \langle\rho\rangle_\ell \langle u_j\rangle_\ell \langle X_i\rangle_\ell + \langle u_j\rangle_\ell \phi_i, \quad \text{(A.27)} \\
\langle u_i\rangle_\ell \frac{\partial}{\partial t}(\langle\rho\rangle_\ell \langle u_j\rangle_\ell) + \langle u_i\rangle_\ell \frac{\partial}{\partial x_k}(\langle\rho\rangle_\ell \langle u_j\rangle_\ell \langle u_k\rangle_\ell) + \langle u_i\rangle_\ell \frac{\partial}{\partial x_k}\left[\langle\rho\rangle_\ell \upsilon(u_j, u_k)\right] \\
+ \langle u_i\rangle_\ell \frac{\partial \langle p\rangle_\ell}{\partial x_j} - \langle u_i\rangle_\ell \frac{\partial \langle\sigma_{jk}\rangle_\ell}{\partial x_k} = \langle\rho\rangle_\ell \langle u_i\rangle_\ell \langle X_j\rangle_\ell + \langle u_i\rangle_\ell \phi_j. \quad \text{(A.28)}
\end{aligned}$$

As previously, we can expand the first two terms in (A.27) and (A.28):

$$\langle u_j\rangle_\ell \frac{\partial\langle\rho\rangle_\ell}{\partial t}\langle u_i\rangle_\ell + \langle u_j\rangle_\ell\langle\rho\rangle_\ell\frac{\partial\langle u_i\rangle_\ell}{\partial t} + \langle u_j\rangle_\ell\langle u_i\rangle_\ell\frac{\partial}{\partial x_k}(\langle\rho\rangle_\ell\langle u_k\rangle_\ell) + \langle u_j\rangle_\ell\langle\rho\rangle_\ell\langle u_k\rangle_\ell\frac{\partial\langle u_i\rangle_\ell}{\partial x_k},$$
$$\langle u_i\rangle_\ell \frac{\partial\langle\rho\rangle_\ell}{\partial t}\langle u_j\rangle_\ell + \langle u_i\rangle_\ell\langle\rho\rangle_\ell\frac{\partial\langle u_j\rangle_\ell}{\partial t} + \langle u_i\rangle_\ell\langle u_j\rangle_\ell\frac{\partial}{\partial x_k}(\langle\rho\rangle_\ell\langle u_k\rangle_\ell) + \langle u_i\rangle_\ell\langle\rho\rangle_\ell\langle u_k\rangle_\ell\frac{\partial\langle u_j\rangle_\ell}{\partial x_k}.$$

The sum of these terms yields:

$$\begin{aligned}
&\frac{\partial}{\partial t}(\langle\rho\rangle_\ell\langle u_i\rangle_\ell\langle u_j\rangle_\ell) + \langle u_i\rangle_\ell\langle u_j\rangle_\ell\frac{\partial\langle\rho\rangle_\ell}{\partial t}\\
&+\frac{\partial}{\partial x_k}(\langle\rho\rangle_\ell\langle u_i\rangle_\ell\langle u_j\rangle_\ell\langle u_k\rangle_\ell) + \langle u_i\rangle_\ell\langle u_j\rangle_\ell\frac{\partial}{\partial x_k}(\langle\rho\rangle_\ell\langle u_k\rangle_\ell)\\
&=\frac{\partial}{\partial t}(\langle\rho\rangle_\ell\langle u_i\rangle_\ell\langle u_j\rangle_\ell) + \frac{\partial}{\partial x_k}(\langle\rho\rangle_\ell\langle u_i\rangle_\ell\langle u_j\rangle_\ell\langle u_k\rangle_\ell) - \langle u_i\rangle_\ell\langle u_j\rangle_\ell\frac{\partial}{\partial x_k}\left(\upsilon(\rho,u_k)\right).
\end{aligned} \tag{A.29}$$

The third terms on the LHS of (A.27) and (A.28) are rewritten as follows:

$$\langle u_j\rangle_\ell\frac{\partial}{\partial x_k}\left[\langle\rho\rangle_\ell\upsilon(u_i,u_k)\right] = \frac{\partial}{\partial x_k}\left[\langle\rho\rangle_\ell\upsilon(u_i,u_k)\,\langle u_j\rangle_\ell\right] - \langle\rho\rangle_\ell\upsilon(u_i,u_k)\,\frac{\partial\langle u_j\rangle_\ell}{\partial x_k},$$
$$\langle u_i\rangle_\ell\frac{\partial}{\partial x_k}\left[\langle\rho\rangle_\ell\upsilon(u_j,u_k)\right] = \frac{\partial}{\partial x_k}\left[\langle\rho\rangle_\ell\upsilon(u_j,u_k)\,\langle u_i\rangle_\ell\right] - \langle\rho\rangle_\ell\upsilon(u_j,u_k)\,\frac{\partial\langle u_i\rangle_\ell}{\partial x_k}.$$

The terms involving mean pressure and the mean stress tensor can also be re-arranged:

$$\begin{aligned}
\langle u_j\rangle_\ell\frac{\partial\langle p\rangle_\ell}{\partial x_i} &= \frac{\partial}{\partial x_i}(\langle p\rangle_\ell\langle u_j\rangle_\ell) - \langle p\rangle_\ell\frac{\partial\langle u_j\rangle_\ell}{\partial x_i},\\
\langle u_i\rangle_\ell\frac{\partial\langle p\rangle_\ell}{\partial x_j} &= \frac{\partial}{\partial x_j}(\langle p\rangle_\ell\langle u_i\rangle_\ell) - \langle p\rangle_\ell\frac{\partial\langle u_i\rangle_\ell}{\partial x_j},\\
\langle u_j\rangle_\ell\frac{\partial\langle\sigma_{ik}\rangle_\ell}{\partial x_k} &= \frac{\partial}{\partial x_k}(\langle\sigma_{ik}\rangle_\ell\langle u_j\rangle_\ell) - \langle\sigma_{ik}\rangle_\ell\frac{\partial\langle u_j\rangle_\ell}{\partial x_k},\\
\langle u_i\rangle_\ell\frac{\partial\langle\sigma_{jk}\rangle_\ell}{\partial x_k} &= \frac{\partial}{\partial x_k}(\langle\sigma_{jk}\rangle_\ell\langle u_i\rangle_\ell) - \langle\sigma_{jk}\rangle_\ell\frac{\partial\langle u_i\rangle_\ell}{\partial x_k}.
\end{aligned}$$

And so, the sum of (A.27) and (A.28) gives the following

$$\begin{aligned}
&\frac{\partial}{\partial t}(\langle\rho\rangle_\ell\langle u_i\rangle_\ell\langle u_j\rangle_\ell) + \frac{\partial}{\partial x_k}(\langle\rho\rangle_\ell\langle u_i\rangle_\ell\langle u_j\rangle_\ell\langle u_k\rangle_\ell) - \langle u_i\rangle_\ell\langle u_j\rangle_\ell\frac{\partial}{\partial x_k}\left(\upsilon(\rho,u_k)\right)\\
&\quad+\frac{\partial}{\partial x_k}\left(\langle\rho\rangle_\ell\upsilon(u_i,u_k)\langle u_j\rangle_\ell\right) - \langle\rho\rangle_\ell\upsilon(u_i,u_k)\frac{\partial\langle u_j\rangle_\ell}{\partial x_k}\\
&\quad+\frac{\partial}{\partial x_k}\left(\langle\rho\rangle_\ell\upsilon(u_j,u_k)\langle u_i\rangle_\ell\right) - \langle\rho\rangle_\ell\upsilon(u_j,u_k)\frac{\partial\langle u_i\rangle_\ell}{\partial x_k}\\
&\quad+\frac{\partial}{\partial x_i}(\langle p\rangle_\ell\langle u_j\rangle_\ell) - \langle p\rangle_\ell\frac{\partial\langle u_j\rangle_\ell}{\partial x_i} + \frac{\partial}{\partial x_j}(\langle p\rangle_\ell\langle u_i\rangle_\ell) - \langle p\rangle_\ell\frac{\partial\langle u_i\rangle_\ell}{\partial x_j}\\
&\quad-\frac{\partial}{\partial x_k}(\langle\sigma_{ik}\rangle_\ell\langle u_j\rangle_\ell) + \langle\sigma_{ik}\rangle_\ell\frac{\partial\langle u_j\rangle_\ell}{\partial x_k} - \frac{\partial}{\partial x_k}(\langle\sigma_{jk}\rangle_\ell\langle u_i\rangle_\ell) + \langle\sigma_{jk}\rangle_\ell\frac{\partial\langle u_i\rangle_\ell}{\partial x_k}
\end{aligned}$$

$$= \langle\rho\rangle_\ell\langle u_j\rangle_\ell\langle X_i\rangle_\ell + \langle\rho\rangle_\ell\langle u_i\rangle_\ell\langle X_j\rangle_\ell + \langle u_j\rangle_\ell\phi_i + \langle u_i\rangle_\ell\phi_j. \tag{A.30}$$

Re-arranging in an analogous manner to (A.17), we obtain

$$\begin{aligned}
&\frac{\partial}{\partial t}(\langle\rho\rangle_\ell\langle u_i\rangle_\ell\langle u_j\rangle_\ell) + \frac{\partial}{\partial x_k}(\langle\rho\rangle_\ell\langle u_i\rangle_\ell\langle u_j\rangle_\ell\langle u_k\rangle_\ell + \langle\rho\rangle_\ell\upsilon(u_i,u_k)\langle u_j\rangle_\ell \\
&\quad + \langle\rho\rangle_\ell\upsilon(u_j,u_k)\langle u_i\rangle_\ell + \langle\rho\rangle_\ell\langle u_j\rangle_\ell\,\delta_{ik} + \langle\rho\rangle_\ell\langle u_i\rangle_\ell\,\delta_{jk} - \langle u_j\rangle_\ell\langle\sigma_{ik}\rangle_\ell - \langle u_i\rangle_\ell\langle\sigma_{jk}\rangle_\ell) \\
&\quad = \langle\rho\rangle_\ell\langle u_j\rangle_\ell\langle X_i\rangle_\ell + \langle\rho\rangle_\ell\langle u_i\rangle_\ell\langle X_j\rangle_\ell - \left(\frac{\partial\langle u_j\rangle_\ell}{\partial x_k}\langle\sigma_{ik}\rangle_\ell + \frac{\partial\langle u_i\rangle_\ell}{\partial x_k}\langle\sigma_{jk}\rangle_\ell\right) \\
&\quad + \langle p\rangle_\ell\frac{\partial\langle u_j\rangle_\ell}{\partial x_i} + \langle p\rangle_\ell\frac{\partial\langle u_i\rangle_\ell}{\partial x_j} + \langle u_j\rangle_\ell\phi_i + \langle u_i\rangle_\ell\phi_j + \langle u_i\rangle_\ell\langle u_j\rangle_\ell\frac{\partial}{\partial x_k}(\upsilon(\rho,u_k)) \\
&\quad + \langle\rho\rangle_\ell\upsilon(u_j,u_k)\frac{\partial\langle u_i\rangle_\ell}{\partial x_k} + \langle\rho\rangle_\ell\upsilon(u_i,u_k)\frac{\partial\langle u_j\rangle_\ell}{\partial x_k}.
\end{aligned} \tag{A.31}$$

Thus, by setting $i = j$, dividing by 2 and using $e_s = \frac{1}{2}\langle\rho\rangle_\ell\langle u_i\rangle_\ell\langle u_i\rangle_\ell$, the equation for the kinetic energy density of the mean motion is obtained;

$$\begin{aligned}
&\frac{\partial e_s}{\partial t} + \frac{\partial}{\partial x_k}(e_s\langle u_k\rangle_\ell + \langle\rho\rangle_\ell\upsilon(u_i,u_k)\langle u_i\rangle_\ell + \langle p\rangle_\ell\langle u_k\rangle_\ell - \langle u_i\rangle_\ell\langle\sigma_{ik}\rangle_\ell) \\
&\qquad = \langle\rho\rangle_\ell\langle u_i\rangle_\ell\langle X_i\rangle_\ell - \langle\rho\rangle_\ell\varepsilon_s + \langle p\rangle_\ell\frac{\partial\langle u_i\rangle_\ell}{\partial x_i} + \langle u_i\rangle_\ell\phi_i \\
&\qquad + \frac{1}{2}\langle u_i\rangle_\ell\langle u_i\rangle_\ell\frac{\partial}{\partial x_k}[\upsilon(\rho,u_k)] + \langle\rho\rangle_\ell\upsilon(u_i,u_k)\frac{\partial\langle u_i\rangle_\ell}{\partial x_k},
\end{aligned} \tag{A.32}$$

where

$$\langle\rho\rangle_\ell\varepsilon_s = \langle\sigma_{ik}\rangle_\ell\frac{\partial\langle u_i\rangle_\ell}{\partial x_k}. \tag{A.33}$$

A.5 Transport of fluctuating momentum equation

We start by comparing (A.25) to (A.20) in order to obtain an evolution equation for the momentum $\tau(\rho,u_i)$;

$$\frac{\partial}{\partial t}[\upsilon(\rho,u_i)] + \frac{\partial}{\partial x_k}[\langle u_i\rangle_\ell\upsilon(\rho,u_k) + \langle u_k\rangle_\ell\upsilon(\rho,u_i) + \upsilon(\rho,u_i,u_k)] = \upsilon(\rho,X_i) - \phi_i. \tag{A.34}$$

We then multiply (A.34) by $\langle u_i\rangle_\ell$ and (A.22) by $\upsilon(\rho,u_i)$;

$$\begin{aligned}
&\langle u_i\rangle_\ell\frac{\partial}{\partial t}[\upsilon(\rho,u_i)] + \langle u_i\rangle_\ell\frac{\partial}{\partial x_k}[\langle u_i\rangle_\ell\upsilon(\rho,u_k)] + \langle u_i\rangle_\ell\frac{\partial}{\partial x_k}[\langle u_k\rangle_\ell\upsilon(\rho,u_i)] \\
&\qquad + \langle u_i\rangle_\ell\frac{\partial}{\partial x_k}\upsilon(\rho,u_i,u_k) = \langle u_i\rangle_\ell\upsilon(\rho,X_i) - \langle u_i\rangle_\ell\phi_i.
\end{aligned} \tag{A.35}$$

$$\upsilon(\rho,u_i)\frac{\partial\langle u_i\rangle_\ell}{\partial t} + \langle u_k\rangle_\ell\upsilon(\rho,u_i)\frac{\partial\langle u_i\rangle_\ell}{\partial x_k} + \upsilon(\rho,u_i)\upsilon\left(u_k,\frac{\partial u_i}{\partial x_k}\right)$$

$$= \upsilon(\rho,u_i)\langle X_i\rangle_\ell - \upsilon(\rho,u_i)\left\langle \frac{1}{\rho}\frac{\partial p}{\partial x_i}\right\rangle_\ell + \upsilon(\rho,u_i)\left\langle \frac{1}{\rho}\frac{\partial \sigma_{ik}}{\partial x_k}\right\rangle_\ell . \tag{A.36}$$

Summing (A.35) and (A.36) results in

$$\begin{aligned}\frac{\partial}{\partial t}[\langle u_i\rangle_\ell \upsilon(\rho,u_i)] &+ \langle u_i\rangle_\ell \frac{\partial}{\partial x_k}[\langle u_i\rangle_\ell \upsilon(\rho,u_k)] + \frac{\partial}{\partial x_k}[\langle u_i\rangle_\ell\langle u_k\rangle_\ell \upsilon(\rho,u_i)] \\ &+ \langle u_i\rangle_\ell \frac{\partial}{\partial x_k}[\upsilon(\rho,u_i,u_k)] \\ &= \langle u_i\rangle_\ell \upsilon(\rho,X_i) - \langle u_i\rangle_\ell \phi_i \\ &+ \upsilon(\rho,u_i)\left[\langle X_i\rangle_\ell - \left\langle \frac{1}{\rho}\frac{\partial p}{\partial x_i}\right\rangle_\ell + \left\langle \frac{1}{\rho}\frac{\partial \sigma_{ik}}{\partial x_k}\right\rangle_\ell - \upsilon\left(u_k,\frac{\partial u_i}{\partial x_k}\right)\right].\end{aligned} \tag{A.37}$$

We rewrite the second term in the LHS of (A.37) as

$$\begin{aligned}\langle u_i\rangle_\ell \frac{\partial}{\partial x_k}[\langle u_i\rangle_\ell \upsilon(\rho,u_k)] &= \frac{\partial}{\partial x_k}[\upsilon(\rho,u_k)]\langle u_i\rangle_\ell\langle u_i\rangle_\ell + \langle u_i\rangle_\ell \upsilon(\rho,u_k)\frac{\partial\langle u_i\rangle_\ell}{\partial x_k} \\ &= \frac{\partial}{\partial x_k}[\upsilon(\rho,u_k)]\langle u_i\rangle_\ell\langle u_i\rangle_\ell + \frac{1}{2}\upsilon(\rho,u_k)\frac{\partial}{\partial x_k}[\langle u_i\rangle_\ell\langle u_i\rangle_\ell] \\ &= \frac{1}{2}\frac{\partial}{\partial x_k}[\upsilon(\rho,u_k)\langle u_i\rangle_\ell\langle u_i\rangle_\ell] + \frac{1}{2}\frac{\partial \upsilon(\rho,u_k)}{\partial x_k}\langle u_i\rangle_\ell\langle u_i\rangle_\ell .\end{aligned}$$

The fourth term in the LHS of (A.37) is rewritten as

$$\langle u_i\rangle_\ell \frac{\partial}{\partial x_k}[\upsilon(\rho,u_i,u_k)] = \frac{\partial}{\partial x_k}[\langle u_i\rangle_\ell \upsilon(\rho,u_i,u_k)] - \upsilon(\rho,u_i,u_k)\frac{\partial\langle u_i\rangle_\ell}{\partial x_k}.$$

From (A.22), we evaluate the term in square brackets as

$$\langle X_i\rangle_\ell - \left\langle \frac{1}{\rho}\frac{\partial p}{\partial x_i}\right\rangle_\ell + \left\langle \frac{1}{\rho}\frac{\partial \sigma_{ik}}{\partial x_k}\right\rangle_\ell - \upsilon\left(u_k,\frac{\partial u_i}{\partial x_k}\right) = \frac{\partial\langle u_i\rangle_\ell}{\partial t} + \langle u_k\rangle_\ell \frac{\partial\langle u_i\rangle_\ell}{\partial x_k} = \frac{\mathrm{D}\langle u_i\rangle_\ell}{\mathrm{D}t}.$$

Thus, using $e_{st} = \langle u_i\rangle_\ell \upsilon(\rho,u_i)$, the evolution equation for the transport of the momentum $\upsilon(\rho,u_i)$ by the mean motion $\langle u_i\rangle_\ell$ is obtained

$$\begin{aligned}\frac{\partial e_{st}}{\partial t} &+ \frac{\partial}{\partial x_k}\left[e_{st}\langle u_k\rangle_\ell + \upsilon(\rho,u_i,u_k)\langle u_i\rangle_\ell + \frac{1}{2}\upsilon(\rho,u_k)\langle u_i\rangle_\ell\langle u_i\rangle_\ell\right] \\ &= \langle u_i\rangle_\ell \upsilon(\rho,X_i) - \left[\langle u_i\rangle_\ell \phi_i + \frac{1}{2}\langle u_i\rangle_\ell\langle u_i\rangle_\ell \frac{\partial}{\partial x_k}[\upsilon(\rho,u_k)]\right] \\ &+ \upsilon(\rho,u_i,u_k)\frac{\partial\langle u_i\rangle_\ell}{\partial x_k} + \upsilon(\rho,u_i)\frac{\mathrm{D}\langle u_i\rangle_\ell}{\mathrm{D}t}.\end{aligned} \tag{A.38}$$

A.6 Equation for the kinetic energy density of the fluctuations

As previously, we rearrange (A.2) to find e_t in terms of the other kinetic energy densities

$$e_t = \langle e_K \rangle_\ell - e_s - e_{st}. \tag{A.39}$$

Averaging (A.18) yields the evolution equation for $\langle e_K \rangle_\ell$

$$\frac{\partial \langle e_K \rangle_\ell}{\partial t} + \frac{\partial}{\partial x_k}[\langle e_K u_k \rangle_\ell + \langle p u_k \rangle_\ell - \langle u_i \sigma_{ik} \rangle_\ell] = \left\langle p \frac{\partial u_i}{\partial x_i} \right\rangle_\ell - \left\langle \frac{\partial u_i}{\partial x_k} \sigma_{ik} \right\rangle_\ell + \langle \rho u_i X_i \rangle_\ell. \tag{A.40}$$

The term $\langle e_K u_k \rangle_\ell$ is expanded as

$$\begin{aligned}
\langle e_K u_k \rangle_\ell &= \frac{1}{2} \langle \rho u_i u_i u_k \rangle_\ell \\
&= \frac{1}{2}[\langle \rho \rangle_\ell \langle u_i \rangle_\ell \langle u_i \rangle_\ell \langle u_k \rangle_\ell + 2 \langle \rho \rangle_\ell \langle u_i \rangle_\ell \upsilon(u_i, u_k) + \langle \rho \rangle_\ell \langle u_k \rangle_\ell \upsilon(u_i, u_i) \\
&\quad + \langle u_i \rangle_\ell \langle u_i \rangle_\ell \upsilon(\rho, u_k) + 2 \langle u_i \rangle_\ell \langle u_k \rangle_\ell \upsilon(\rho, u_i) + \langle u_k \rangle_\ell \upsilon(\rho, u_i, u_i) \\
&\quad + 2 \langle u_i \rangle_\ell \upsilon(\rho, u_i, u_k) + \langle \rho \rangle_\ell \upsilon(u_i, u_i, u_k) + \upsilon(\rho, u_i, u_i, u_k)] \\
&= \left[\frac{1}{2} \langle \rho \rangle_\ell \langle u_i \rangle_\ell \langle u_i \rangle_\ell + \langle u_i \rangle_\ell \upsilon(\rho, u_i) + \frac{1}{2} \langle \rho \rangle_\ell \upsilon(u_i, u_i) + \frac{1}{2} \upsilon(\rho, u_i, u_i) \right] \langle u_k \rangle_\ell \\
&\quad + \langle \rho \rangle_\ell \langle u_i \rangle_\ell \upsilon(u_i, u_k) + \langle u_i \rangle_\ell \upsilon(\rho, u_i, u_k) + \frac{1}{2} \langle u_i \rangle_\ell \langle u_i \rangle_\ell \upsilon(\rho, u_k) \\
&\quad + \frac{1}{2} \langle \rho \rangle_\ell \upsilon(u_i, u_i, u_k) + \frac{1}{2} \upsilon(\rho, u_i, u_i, u_k) \\
&= [e_s + e_{st} + e_t] \langle u_k \rangle_\ell + \langle \rho \rangle_\ell \langle u_i \rangle_\ell \upsilon(u_i, u_k) + \langle u_i \rangle_\ell \upsilon(\rho, u_i, u_k) \\
&\quad + \frac{1}{2} \langle u_i \rangle_\ell \langle u_i \rangle_\ell \upsilon(\rho, u_k) + \frac{1}{2} \langle \rho \rangle_\ell \upsilon(u_i, u_i, u_k) + \frac{1}{2} \upsilon(\rho, u_i, u_i, u_k).
\end{aligned}$$

Thus, (A.40) is expanded as

$$\begin{aligned}
\frac{\partial}{\partial t}[e_s + e_{st} + e_t] &+ \frac{\partial}{\partial x_k}[(e_s + e_{st} + e_t) \langle u_k \rangle_\ell + \langle \rho \rangle_\ell \langle u_i \rangle_\ell \upsilon(u_i, u_k)] \\
&+ \frac{\partial}{\partial x_k} \left[\langle u_i \rangle_\ell \upsilon(\rho, u_i, u_k) + \frac{1}{2} \langle u_i \rangle_\ell \langle u_i \rangle_\ell \upsilon(\rho, u_k) \right] \\
&+ \frac{\partial}{\partial x_k} \left[\frac{1}{2} \langle \rho \rangle_\ell \upsilon(u_i, u_i, u_k) + \frac{1}{2} \upsilon(\rho, u_i, u_i, u_k) \right] \\
&+ \frac{\partial}{\partial x_k}[\langle p \rangle_\ell \langle u_k \rangle_\ell + \upsilon(p, u_k) - \langle u_i \rangle_\ell \langle \sigma_{ik} \rangle_\ell - \upsilon(u_i, \sigma_{ik})] \\
&= \langle p \rangle_\ell \frac{\partial \langle u_i \rangle_\ell}{\partial x_i} + \upsilon \left(p, \frac{\partial u_i}{\partial x_i} \right) - \langle \rho \rangle_\ell \varepsilon_s \\
&- \upsilon \left(\frac{\partial u_i}{\partial x_k}, \sigma_{ik} \right) + \langle \rho \rangle_\ell \langle u_i \rangle_\ell \langle X_i \rangle_\ell + \langle \rho \rangle_\ell \upsilon(u_i, X_i) \\
&+ \langle u_i \rangle_\ell \upsilon(\rho, X_i) + \langle X_i \rangle_\ell \upsilon(\rho, u_i) + \upsilon(\rho, u_i, X_i).
\end{aligned} \tag{A.41}$$

We now compare (A.41) to (A.32) and (A.38). As before, the latter two equations have been repeated below for convenience

$$\begin{aligned}
&\frac{\partial e_s}{\partial t}+\frac{\partial}{\partial x_k}(e_s\langle u_k\rangle_\ell+\langle\rho\rangle_\ell\upsilon(u_i,u_k)\langle u_i\rangle_\ell+\langle p\rangle_\ell\langle u_k\rangle_\ell-\langle u_i\rangle_\ell\langle\sigma_{ik}\rangle_\ell)\\
&\quad=\langle\rho\rangle_\ell\langle u_i\rangle_\ell\langle X_i\rangle_\ell-\langle\rho\rangle_\ell\varepsilon_s+\langle p\rangle_\ell\frac{\partial\langle u_i\rangle_\ell}{\partial x_i}+\langle u_i\rangle_\ell\phi_i\\
&\quad+\frac{1}{2}\langle u_i\rangle_\ell\langle u_i\rangle_\ell\frac{\partial}{\partial x_k}[\upsilon(\rho,u_k)]+\langle\rho\rangle_\ell\upsilon(u_i,u_k)\frac{\partial\langle u_i\rangle_\ell}{\partial x_k},\\
&\frac{\partial e_{st}}{\partial t}+\frac{\partial}{\partial x_k}\left[e_{st}\langle u_k\rangle_\ell+\upsilon(\rho,u_i,u_k)\langle u_i\rangle_\ell+\frac{1}{2}\upsilon(\rho,u_k)\langle u_i\rangle_\ell\langle u_i\rangle_\ell\right]\\
&\quad=\langle u_i\rangle_\ell\upsilon(\rho,X_i)-\left[\langle u_i\rangle_\ell\phi_i+\frac{1}{2}\frac{\partial}{\partial x_k}[\upsilon(\rho,u_k)]\langle u_i\rangle_\ell\langle u_i\rangle_\ell\right]\\
&\quad+\upsilon(\rho,u_i,u_k)\frac{\partial\langle u_i\rangle_\ell}{\partial x_k}+\upsilon(\rho,u_i)\frac{\mathrm{D}\langle u_i\rangle_\ell}{\mathrm{D}t}.
\end{aligned}$$

The subtraction of (A.32) from (A.41) yields

$$\begin{aligned}
&\frac{\partial}{\partial t}(e_{st}+e_t)+\frac{\partial}{\partial x_k}\left[(e_{st}+e_t)\langle u_k\rangle_\ell+\langle u_i\rangle_\ell\upsilon(\rho,u_i,u_k)\right]\\
&\qquad+\frac{\partial}{\partial x_k}\left[\frac{1}{2}\langle u_i\rangle_\ell\langle u_i\rangle_\ell\upsilon(\rho,u_k)+\frac{1}{2}\langle\rho\rangle_\ell\upsilon(u_i,u_i,u_k)\right]\\
&\qquad+\frac{\partial}{\partial x_k}\left[\frac{1}{2}\upsilon(\rho,u_i,u_i,u_k)+\upsilon(p,u_k)-\upsilon(u_i,\sigma_{ik})\right]\\
&\qquad=\upsilon\left(p,\frac{\partial u_i}{\partial x_i}\right)-\upsilon\left(\frac{\partial u_i}{\partial x_k},\sigma_{ik}\right)+\langle\rho\rangle_\ell\upsilon(u_i,X_i)+\langle u_i\rangle_\ell\upsilon(\rho,X_i)\\
&\qquad+\langle X_i\rangle_\ell\upsilon(\rho,u_i)+\upsilon(\rho,u_i,X_i)-\left[\langle u_i\rangle_\ell\phi_i+\frac{1}{2}\frac{\partial}{\partial x_k}[\upsilon(\rho,u_k)]\langle u_i\rangle_\ell\langle u_i\rangle_\ell\right]\\
&\qquad-\langle\rho\rangle_\ell\upsilon(u_i,u_k)\frac{\partial\langle u_i\rangle_\ell}{\partial x_k}.
\end{aligned}\tag{A.42}$$

Finally, the subtraction of (A.38) from (A.42) to obtain the equation for the filtering averaged energy density of the fluctuating motion

$$\begin{aligned}
&\frac{\partial e_t}{\partial t}+\frac{\partial}{\partial x_k}\left[e_t\langle u_k\rangle_\ell+\frac{1}{2}\langle\rho\rangle_\ell\upsilon(u_i,u_i,u_k)+\frac{1}{2}\upsilon(\rho,u_i,u_i,u_k)+\upsilon(p,u_k)-\upsilon(u_i,\sigma_{ik})\right]\\
&\quad=\langle\rho\rangle_\ell\upsilon(u_i,X_i)+\langle X_i\rangle_\ell\upsilon(\rho,u_i)+\upsilon(\rho,u_i,X_i)+\upsilon\left(p,\frac{\partial u_i}{\partial x_i}\right)-\langle\rho\rangle_\ell\varepsilon_t\\
&\quad-\langle\rho\rangle_\ell\upsilon(u_i,u_k)\frac{\partial\langle u_i\rangle_\ell}{\partial x_k}-\upsilon(\rho,u_i,u_k)\frac{\partial\langle u_i\rangle_\ell}{\partial x_k}-\upsilon(\rho,u_i)\frac{\mathrm{D}\langle u_i\rangle_\ell}{\mathrm{D}t},
\end{aligned}\tag{A.43}$$

where

$$\langle\rho\rangle_\ell\varepsilon_t=\upsilon\left(\frac{\partial u_i}{\partial x_k},\sigma_{ik}\right).\tag{A.44}$$

The evolution equations of the filtering averaged energy densities detailed in (A.32), (A.38) and (A.43), have the same form as those for the averaged kinetic energy densities determined by Reynolds averaging (see Monin & Yaglom, 2007a, Section 6.4);

$$\begin{aligned}
&\frac{\partial e_s}{\partial t} + \frac{\partial}{\partial x_k}\left(e_s\langle u_k\rangle + \langle\rho\rangle\langle u_i' u_k'\rangle\langle u_i\rangle + \langle p\rangle\langle u_k\rangle - \langle u_i\rangle\langle\sigma_{ik}\rangle\right) \\
&\quad = \langle\rho\rangle\langle u_i\rangle\langle X_i\rangle - \langle\rho\rangle\varepsilon_s + \langle p\rangle\frac{\partial\langle u_i\rangle}{\partial x_i} + \langle u_i\rangle\phi_i \\
&\quad + \frac{1}{2}\langle u_i\rangle\langle u_i\rangle\frac{\partial}{\partial x_k}\left(\langle\rho' u_k'\rangle\right) + \langle\rho\rangle\langle u_i' u_k'\rangle\frac{\partial\langle u_i\rangle}{\partial x_k},
\end{aligned} \tag{A.45}$$

$$\begin{aligned}
&\frac{\partial e_{st}}{\partial t} + \frac{\partial}{\partial x_k}\left(e_{st}\langle u_k\rangle + \langle\rho' u_i' u_k'\rangle\langle u_i\rangle + \frac{1}{2}\langle\rho' u_k'\rangle\langle u_i\rangle\langle u_i\rangle\right) \\
&\quad = \langle u_i\rangle\langle\rho' X_i'\rangle - \left[\langle u_i\rangle\phi_i + \frac{1}{2}\frac{\partial}{\partial x_k}\left(\langle\rho' u_k'\rangle\right)\langle u_i\rangle\langle u_i\rangle\right] \\
&\quad + \langle\rho' u_i' u_k'\rangle\frac{\partial\langle u_i\rangle}{\partial x_k} + \langle\rho' u_i'\rangle\frac{\mathrm{D}\langle u_i\rangle}{\mathrm{D}t}.
\end{aligned} \tag{A.46}$$

$$\begin{aligned}
&\frac{\partial e_t}{\partial t} + \frac{\partial}{\partial x_k}\left[e_t\langle u_k\rangle_V + \frac{1}{2}\langle\rho\rangle\langle u_i' u_i' u_k'\rangle + \frac{1}{2}\langle\rho' u_i' u_i' u_k'\rangle + \langle p' u_k'\rangle - \langle u_i'\sigma_{ik}'\rangle\right] \\
&\quad = \langle\rho\rangle\langle u_i' X_i'\rangle + \langle\rho' u_i'\rangle\langle X_i\rangle + \langle\rho' u_i' X_i'\rangle + \left\langle p'\frac{\partial u_i'}{\partial x_i}\right\rangle - \langle\rho\rangle\varepsilon_t \\
&\quad - \langle\rho\rangle\langle u_i' u_k'\rangle\frac{\partial\langle u_i\rangle}{\partial x_k} - \langle\rho' u_i' u_k'\rangle\frac{\partial\langle u_i\rangle}{\partial x_k} - \langle\rho' u_i'\rangle\frac{\mathrm{D}\langle u_i\rangle}{\mathrm{D}t},
\end{aligned} \tag{A.47}$$

where $\langle\rangle$ denotes an averaging operator which obeys the Reynolds rules, primed variables denote fluctuations, and

$$\langle\rho\rangle\varepsilon_s = \langle\sigma_{ik}\rangle\frac{\partial\langle u_i\rangle}{\partial x_k}, \quad \langle\rho\rangle\varepsilon_t = \left\langle\frac{\partial u_i'}{\partial x_k}\sigma_{ik}'\right\rangle. \tag{A.48}$$

Thus, the averaging invariance of the compressible Navier–Stokes equations is confirmed. Therefore, the choice of the filtering averaged kinetic energy densities in (A.2) is appropriate.

Appendix B

Integral forms of the second and third order moments

B.1 Magnetic energy

The central second-order statistical moment representing the energy density of magnetic field fluctuations e_b under smoothing at a scale ℓ with a kernel $G_\ell(\boldsymbol{x}-\boldsymbol{x}')$, with $\int_V G_\ell(\boldsymbol{x}-\boldsymbol{x}')\,\mathrm{d}\boldsymbol{x}' = 1$ and $X_\ell \equiv \langle X\rangle_\ell = \int_V X(\boldsymbol{x}')G_\ell(\boldsymbol{x}-\boldsymbol{x}')\,\mathrm{d}^3\boldsymbol{x}'$ for a scalar or vectorial quantity X, is given by

$$
\begin{aligned}
8\pi e_b =& 8\pi(\langle e_B\rangle_\ell - e_{B_\ell}), \\
=& \upsilon(b_i, b_i), \\
=& \langle \boldsymbol{B}\cdot\boldsymbol{B}\rangle_\ell - \langle \boldsymbol{B}\rangle_\ell \cdot \langle \boldsymbol{B}\rangle_\ell, \\
=& \int_V B^2(\boldsymbol{x}')\, G_\ell(\boldsymbol{x}-\boldsymbol{x}')\,\mathrm{d}^3\boldsymbol{x}' - B_\ell^2(\boldsymbol{x}), \\
=& \int_V B^2(\boldsymbol{x}')\, G_\ell(\boldsymbol{x}-\boldsymbol{x}')\,\mathrm{d}^3\boldsymbol{x}' - B_\ell^2(\boldsymbol{x}) \int_V G_\ell(\boldsymbol{x}-\boldsymbol{x}')\,\mathrm{d}^3\boldsymbol{x}', \\
=& \int_V B^2(\boldsymbol{x}')\, G_\ell(\boldsymbol{x}-\boldsymbol{x}')\,\mathrm{d}^3\boldsymbol{x}' - \int_V B_\ell^2(\boldsymbol{x})\, G_\ell(\boldsymbol{x}-\boldsymbol{x}')\,\mathrm{d}^3\boldsymbol{x}', \\
=& \int_V [B^2(\boldsymbol{x}') - B_\ell^2(\boldsymbol{x})]\, G_\ell(\boldsymbol{x}-\boldsymbol{x}')\,\mathrm{d}^3\boldsymbol{x}', \\
=& \int_V \{[\boldsymbol{B}(\boldsymbol{x}') - \boldsymbol{B}_\ell(\boldsymbol{x})]\cdot[\boldsymbol{B}(\boldsymbol{x}') - \boldsymbol{B}_\ell(\boldsymbol{x})] \\
& \quad + 2\boldsymbol{B}(\boldsymbol{x}')\cdot\boldsymbol{B}_\ell(\boldsymbol{x}) - 2\boldsymbol{B}_\ell(\boldsymbol{x})\cdot\boldsymbol{B}_\ell(\boldsymbol{x})\}\, G_\ell(\boldsymbol{x}-\boldsymbol{x}')\,\mathrm{d}^3\boldsymbol{x}', \\
=& \int_V |\boldsymbol{B}(\boldsymbol{x}') - \boldsymbol{B}_\ell(\boldsymbol{x})|^2\, G_\ell(\boldsymbol{x}-\boldsymbol{x}')\,\mathrm{d}^3\boldsymbol{x}' + \int_V 2\boldsymbol{B}(\boldsymbol{x}')\cdot\boldsymbol{B}_\ell(\boldsymbol{x})\, G_\ell(\boldsymbol{x}-\boldsymbol{x}')\,\mathrm{d}^3\boldsymbol{x}' \\
& \quad - \int_V 2\boldsymbol{B}_\ell(\boldsymbol{x})\cdot\boldsymbol{B}_\ell(\boldsymbol{x})\, G_\ell(\boldsymbol{x}-\boldsymbol{x}')\,\mathrm{d}^3\boldsymbol{x}', \\
=& \int_V |\boldsymbol{B}(\boldsymbol{x}') - \boldsymbol{B}_\ell(\boldsymbol{x})|^2\, G_\ell(\boldsymbol{x}-\boldsymbol{x}')\,\mathrm{d}^3\boldsymbol{x}' + 2\boldsymbol{B}_\ell(\boldsymbol{x})\cdot\int_V \boldsymbol{B}(\boldsymbol{x}')\, G_\ell(\boldsymbol{x}-\boldsymbol{x}')\,\mathrm{d}^3\boldsymbol{x}'
\end{aligned}
\tag{B.1}
$$

$$
\begin{aligned}
&\quad - 2\boldsymbol{B}_\ell(\boldsymbol{x})\cdot\boldsymbol{B}_\ell(\boldsymbol{x}) \int_V G_\ell(\boldsymbol{x}-\boldsymbol{x}')\,\mathrm{d}^3\boldsymbol{x}',\\
&= \int_V |\boldsymbol{B}(\boldsymbol{x}')-\boldsymbol{B}_\ell(\boldsymbol{x})|^2\, G_\ell(\boldsymbol{x}-\boldsymbol{x}')\,\mathrm{d}^3\boldsymbol{x}' + 2\boldsymbol{B}_\ell(\boldsymbol{x})\cdot\boldsymbol{B}_\ell(\boldsymbol{x}) - 2\boldsymbol{B}_\ell(\boldsymbol{x})\cdot\boldsymbol{B}_\ell(\boldsymbol{x}),\\
&= \int_V |\boldsymbol{B}(\boldsymbol{x}')-\boldsymbol{B}_\ell(\boldsymbol{x})|^2\, G_\ell(\boldsymbol{x}-\boldsymbol{x}')\,\mathrm{d}^3\boldsymbol{x}'. \qquad \text{(B.2)}
\end{aligned}
$$

B.2 Kinetic energy

B.2.1 Second order moments

In a compressible flow, fluctuations in kinetic energy density involve second-order statistical moments evaluated as follows:

$$
\begin{aligned}
e_{st} =& \langle u_i\rangle_\ell\, \upsilon(\rho,u_i), \qquad \text{(B.3)}\\
=& \boldsymbol{u}_\ell\cdot\langle\rho\boldsymbol{u}\rangle_\ell - \boldsymbol{u}_\ell\cdot\rho_\ell\boldsymbol{u}_\ell,\\
=& \int_V \boldsymbol{u}(\boldsymbol{x}')\, G_\ell(\boldsymbol{x}-\boldsymbol{x}')\,\mathrm{d}^3\boldsymbol{x}'\cdot\\
&\left(\int_V \rho(\boldsymbol{x}')\,\boldsymbol{u}(\boldsymbol{x}')\, G_\ell(\boldsymbol{x}-\boldsymbol{x}')\,\mathrm{d}^3\boldsymbol{x}' - \rho_\ell(\boldsymbol{x})\boldsymbol{u}_\ell(\boldsymbol{x})\right),\\
=& \int_V \boldsymbol{u}(\boldsymbol{x}')\, G_\ell(\boldsymbol{x}-\boldsymbol{x}')\,\mathrm{d}^3\boldsymbol{x}'\cdot\\
&\left(\int_V \rho(\boldsymbol{x}')\,\boldsymbol{u}(\boldsymbol{x}')\, G_\ell(\boldsymbol{x}-\boldsymbol{x}')\,\mathrm{d}^3\boldsymbol{x}' - \rho_\ell(\boldsymbol{x})\boldsymbol{u}_\ell(\boldsymbol{x})\int_V G_\ell(\boldsymbol{x}-\boldsymbol{x}')\,\mathrm{d}^3\boldsymbol{x}'\right),\\
=& \int_V \boldsymbol{u}(\boldsymbol{x}')\, G_\ell(\boldsymbol{x}-\boldsymbol{x}')\,\mathrm{d}^3\boldsymbol{x}'\cdot\\
&\left(\int_V \rho(\boldsymbol{x}')\,\boldsymbol{u}(\boldsymbol{x}')\, G_\ell(\boldsymbol{x}-\boldsymbol{x}')\,\mathrm{d}^3\boldsymbol{x}' - \int_V \rho_\ell(\boldsymbol{x})\boldsymbol{u}_\ell(\boldsymbol{x})\, G_\ell(\boldsymbol{x}-\boldsymbol{x}')\,\mathrm{d}^3\boldsymbol{x}'\right),\\
=& \int_V \boldsymbol{u}(\boldsymbol{x}')\, G_\ell(\boldsymbol{x}-\boldsymbol{x}')\,\mathrm{d}^3\boldsymbol{x}'\cdot\left(\int_V [\rho(\boldsymbol{x}')\,\boldsymbol{u}(\boldsymbol{x}') - \rho_\ell(\boldsymbol{x})\boldsymbol{u}_\ell(\boldsymbol{x})] G_\ell(\boldsymbol{x}-\boldsymbol{x}')\,\mathrm{d}^3\boldsymbol{x}'\right),\\
=& \int_V \boldsymbol{u}(\boldsymbol{x}')\, G_\ell(\boldsymbol{x}-\boldsymbol{x}')\,\mathrm{d}^3\boldsymbol{x}'\cdot\left(\int_V \{[\rho(\boldsymbol{x}')-\rho_\ell(\boldsymbol{x})][\boldsymbol{u}(\boldsymbol{x}')-\boldsymbol{u}_\ell(\boldsymbol{x})]\right.\\
&\left. + \rho(\boldsymbol{x}')\boldsymbol{u}_\ell(\boldsymbol{x}) + \rho_\ell(\boldsymbol{x})\boldsymbol{u}(\boldsymbol{x}') - 2\rho_\ell(\boldsymbol{x})\boldsymbol{u}_\ell(\boldsymbol{x})\}\, G_\ell(\boldsymbol{x}-\boldsymbol{x}')\,\mathrm{d}^3\boldsymbol{x}'\right),\\
=& \int_V \boldsymbol{u}(\boldsymbol{x}')\, G_\ell(\boldsymbol{x}-\boldsymbol{x}')\,\mathrm{d}^3\boldsymbol{x}'\cdot\\
&\left(\int_V [\rho(\boldsymbol{x}')-\rho_\ell(\boldsymbol{x})][\boldsymbol{u}(\boldsymbol{x}')-\boldsymbol{u}_\ell(\boldsymbol{x})]\, G_\ell(\boldsymbol{x}-\boldsymbol{x}')\,\mathrm{d}^3\boldsymbol{x}' + \int_V \rho(\boldsymbol{x}')\boldsymbol{u}_\ell(\boldsymbol{x})\, G_\ell(\boldsymbol{x}-\boldsymbol{x}')\,\mathrm{d}^3\boldsymbol{x}'\right.\\
&\left. + \int_V \rho_\ell(\boldsymbol{x})\boldsymbol{u}(\boldsymbol{x}')\, G_\ell(\boldsymbol{x}-\boldsymbol{x}')\,\mathrm{d}^3\boldsymbol{x}' - 2\int_V \rho_\ell(\boldsymbol{x})\boldsymbol{u}_\ell(\boldsymbol{x})\, G_\ell(\boldsymbol{x}-\boldsymbol{x}')\,\mathrm{d}^3\boldsymbol{x}'\right),\\
=& \int_V \boldsymbol{u}(\boldsymbol{x}')\, G_\ell(\boldsymbol{x}-\boldsymbol{x}')\,\mathrm{d}^3\boldsymbol{x}'\cdot\\
&\left(\int_V [\rho(\boldsymbol{x}')-\rho_\ell(\boldsymbol{x})][\boldsymbol{u}(\boldsymbol{x}')-\boldsymbol{u}_\ell(\boldsymbol{x})]\, G_\ell(\boldsymbol{x}-\boldsymbol{x}')\,\mathrm{d}^3\boldsymbol{x}' + \boldsymbol{u}_\ell(\boldsymbol{x})\int_V \rho(\boldsymbol{x}')\, G_\ell(\boldsymbol{x}-\boldsymbol{x}')\,\mathrm{d}^3\boldsymbol{x}'\right.
\end{aligned}
$$

$$
\begin{aligned}
&+\rho_\ell(\boldsymbol{x})\int_V \boldsymbol{u}(\boldsymbol{x}')\,G_\ell(\boldsymbol{x}-\boldsymbol{x}')\,\mathrm{d}^3\boldsymbol{x}' - 2\rho_\ell(\boldsymbol{x})\boldsymbol{u}_\ell(\boldsymbol{x})\int_V G_\ell(\boldsymbol{x}-\boldsymbol{x}')\,\mathrm{d}^3\boldsymbol{x}'\Bigg),\\
&=\int_V \boldsymbol{u}(\boldsymbol{x}')\,G_\ell(\boldsymbol{x}-\boldsymbol{x}')\,\mathrm{d}^3\boldsymbol{x}'\cdot\Bigg(\int_V[\rho(\boldsymbol{x}')-\rho_\ell(\boldsymbol{x})][\boldsymbol{u}(\boldsymbol{x}')-\boldsymbol{u}_\ell(\boldsymbol{x})]\,G_\ell(\boldsymbol{x}-\boldsymbol{x}')\,\mathrm{d}^3\boldsymbol{x}'\\
&\quad+\boldsymbol{u}_\ell(\boldsymbol{x})\rho_\ell(\boldsymbol{x})+\rho_\ell(\boldsymbol{x})\boldsymbol{u}_\ell(\boldsymbol{x})-2\rho_\ell(\boldsymbol{x})\boldsymbol{u}_\ell(\boldsymbol{x})\Bigg),\\
&=\int_V \boldsymbol{u}(\boldsymbol{x}')\,G_\ell(\boldsymbol{x}-\boldsymbol{x}')\,\mathrm{d}^3\boldsymbol{x}'\cdot\Bigg(\int_V[\rho(\boldsymbol{x}')-\rho_\ell(\boldsymbol{x})][\boldsymbol{u}(\boldsymbol{x}')-\boldsymbol{u}_\ell(\boldsymbol{x})]\,G_\ell(\boldsymbol{x}-\boldsymbol{x}')\,\mathrm{d}^3\boldsymbol{x}'\Bigg). \qquad \text{(B.4)}
\end{aligned}
$$

Similarly to equations (B.1) and (B.2),

$$
\begin{aligned}
\langle\rho\rangle_\ell\,\upsilon(u_i,u_i) &= \rho_\ell\langle\boldsymbol{u}\cdot\boldsymbol{u}\rangle_\ell-\rho_\ell\boldsymbol{u}_\ell\cdot\boldsymbol{u}_\ell, \qquad \text{(B.5)}\\
&=\int_V\rho(\boldsymbol{x}')\,G_\ell(\boldsymbol{x}-\boldsymbol{x}')\,\mathrm{d}^3\boldsymbol{x}'\Bigg(\int_V u^2(\boldsymbol{x}')\,G_\ell(\boldsymbol{x}-\boldsymbol{x}')\,\mathrm{d}^3\boldsymbol{x}'-u_\ell^2(\boldsymbol{x})\Bigg),\\
&=\int_V\rho(\boldsymbol{x}')\,G_\ell(\boldsymbol{x}-\boldsymbol{x}')\,\mathrm{d}^3\boldsymbol{x}'\\
&\qquad\Bigg(\int_V u^2(\boldsymbol{x}')\,G_\ell(\boldsymbol{x}-\boldsymbol{x}')\,\mathrm{d}^3\boldsymbol{x}'-u_\ell^2(\boldsymbol{x})\int_V G_\ell(\boldsymbol{x}-\boldsymbol{x}')\,\mathrm{d}^3\boldsymbol{x}'\Bigg),\\
&=\int_V\rho(\boldsymbol{x}')\,G_\ell(\boldsymbol{x}-\boldsymbol{x}')\,\mathrm{d}^3\boldsymbol{x}'\\
&\qquad\Bigg(\int_V u^2(\boldsymbol{x}')\,G_\ell(\boldsymbol{x}-\boldsymbol{x}')\,\mathrm{d}^3\boldsymbol{x}'-\int_V u_\ell^2(\boldsymbol{x})\,G_\ell(\boldsymbol{x}-\boldsymbol{x}')\,\mathrm{d}^3\boldsymbol{x}'\Bigg),\\
&=\int_V\rho(\boldsymbol{x}')\,G_\ell(\boldsymbol{x}-\boldsymbol{x}')\,\mathrm{d}^3\boldsymbol{x}'\Bigg(\int_V[u^2(\boldsymbol{x}')-u_\ell^2(\boldsymbol{x})]G_\ell(\boldsymbol{x}-\boldsymbol{x}')\,\mathrm{d}^3\boldsymbol{x}'\Bigg),\\
&=\int_V\rho(\boldsymbol{x}')\,G_\ell(\boldsymbol{x}-\boldsymbol{x}')\,\mathrm{d}^3\boldsymbol{x}'\Bigg(\int_V\{[\boldsymbol{u}(\boldsymbol{x}')-\boldsymbol{u}_\ell(\boldsymbol{x})]\cdot[\boldsymbol{u}(\boldsymbol{x}')-\boldsymbol{u}_\ell(\boldsymbol{x})]\\
&\qquad+2\,\boldsymbol{u}_\ell(\boldsymbol{x})\cdot\boldsymbol{u}(\boldsymbol{x}')-2\,u_\ell^2(\boldsymbol{x})\}\,G_\ell(\boldsymbol{x}-\boldsymbol{x}')\,\mathrm{d}^3\boldsymbol{x}'\Bigg),\\
&=\int_V\rho(\boldsymbol{x}')\,G_\ell(\boldsymbol{x}-\boldsymbol{x}')\,\mathrm{d}^3\boldsymbol{x}'\Bigg(\int_V|\boldsymbol{u}(\boldsymbol{x}')-\boldsymbol{u}_\ell(\boldsymbol{x})|^2\,G_\ell(\boldsymbol{x}-\boldsymbol{x}')\,\mathrm{d}^3\boldsymbol{x}'\\
&\qquad+2\int_V\boldsymbol{u}(\boldsymbol{x}')\cdot\boldsymbol{u}_\ell(\boldsymbol{x})\,G_\ell(\boldsymbol{x}-\boldsymbol{x}')\,\mathrm{d}^3\boldsymbol{x}'-2\int_V u_\ell^2(\boldsymbol{x})\,G_\ell(\boldsymbol{x}-\boldsymbol{x}')\,\mathrm{d}^3\boldsymbol{x}'\Bigg),\\
&=\int_V\rho(\boldsymbol{x}')\,G_\ell(\boldsymbol{x}-\boldsymbol{x}')\,\mathrm{d}^3\boldsymbol{x}'\Bigg(\int_V|\boldsymbol{u}(\boldsymbol{x}')-\boldsymbol{u}_\ell(\boldsymbol{x})|^2\,G_\ell(\boldsymbol{x}-\boldsymbol{x}')\,\mathrm{d}^3\boldsymbol{x}'\\
&\qquad+2\boldsymbol{u}_\ell(\boldsymbol{x})\cdot\int_V\boldsymbol{u}(\boldsymbol{x}')\,G_\ell(\boldsymbol{x}-\boldsymbol{x}')\,\mathrm{d}^3\boldsymbol{x}'-2u_\ell^2(\boldsymbol{x})\int_V G_\ell(\boldsymbol{x}-\boldsymbol{x}')\,\mathrm{d}^3\boldsymbol{x}'\Bigg),\\
&=\int_V\rho(\boldsymbol{x}')\,G_\ell(\boldsymbol{x}-\boldsymbol{x}')\,\mathrm{d}^3\boldsymbol{x}'\\
&\qquad\Bigg(\int_V|\boldsymbol{u}(\boldsymbol{x}')-\boldsymbol{u}_\ell(\boldsymbol{x})|^2\,G_\ell(\boldsymbol{x}-\boldsymbol{x}')\,\mathrm{d}^3\boldsymbol{x}'+2u_\ell^2(\boldsymbol{x})-2u_\ell^2(\boldsymbol{x})\Bigg),\\
&=\int_V\rho(\boldsymbol{x}')\,G_\ell(\boldsymbol{x}-\boldsymbol{x}')\,\mathrm{d}^3\boldsymbol{x}'\Bigg(\int_V|\boldsymbol{u}(\boldsymbol{x}')-\boldsymbol{u}_\ell(\boldsymbol{x})|^2\,G_\ell(\boldsymbol{x}-\boldsymbol{x}')\,\mathrm{d}^3\boldsymbol{x}'\Bigg). \qquad \text{(B.6)}
\end{aligned}
$$

B.2.2 Third order moment

The third-order moment that appears in the kinetic energy density follows as (summation over repeated indices is understood)

$$
\begin{aligned}
\upsilon(\rho,u_i,u_i) =& \langle\rho u_i u_i\rangle_\ell - 2\langle u_i\rangle_\ell \upsilon(\rho,u_i) - \langle\rho\rangle_\ell \upsilon(u_i,u_i) - \langle\rho\rangle_\ell\langle u_i\rangle_\ell\langle u_i\rangle_\ell, \qquad \text{(B.7)}\\
=& \langle\rho u_i u_i\rangle_\ell - 2\langle u_i\rangle_\ell(\langle\rho u_i\rangle_\ell - \langle\rho\rangle_\ell\langle u_i\rangle_\ell)\\
& - \langle\rho\rangle_\ell(\langle u_i u_i\rangle_\ell - \langle u_i\rangle_\ell\langle u_i\rangle_\ell) - \langle\rho\rangle_\ell\langle u_i\rangle_\ell\langle u_i\rangle_\ell,\\
=& \langle\rho u_i u_i\rangle_\ell - 2\langle u_i\rangle_\ell\langle\rho u_i\rangle_\ell - \langle\rho\rangle_\ell\langle u_i u_i\rangle_\ell + 2\langle\rho\rangle_\ell\langle u_i\rangle_\ell\langle u_i\rangle_\ell,\\
=& \langle\rho\boldsymbol{u}\cdot\boldsymbol{u}\rangle_\ell - 2\boldsymbol{u}_\ell\cdot\langle\rho\boldsymbol{u}\rangle_\ell - \rho_\ell\langle\boldsymbol{u}\cdot\boldsymbol{u}\rangle_\ell + 2\rho_\ell\boldsymbol{u}_\ell\cdot\boldsymbol{u}_\ell,\\
=& \langle\rho u^2\rangle_\ell - 2\boldsymbol{u}_\ell\cdot\langle\rho\boldsymbol{u}\rangle_\ell - \rho_\ell\langle u^2\rangle_\ell + 2\rho_\ell u_\ell^2,\\
=& \int_V \rho(\boldsymbol{x}')u^2(\boldsymbol{x}')\,G_\ell(\boldsymbol{x}-\boldsymbol{x}')\,\mathrm{d}^3\boldsymbol{x}' - 2\boldsymbol{u}_\ell(\boldsymbol{x})\cdot\int_V \rho(\boldsymbol{x}')\boldsymbol{u}(\boldsymbol{x}')\,G_\ell(\boldsymbol{x}-\boldsymbol{x}')\,\mathrm{d}^3\boldsymbol{x}'\\
& - \rho_\ell(\boldsymbol{x})\int_V u^2(\boldsymbol{x}')\,G_\ell(\boldsymbol{x}-\boldsymbol{x}')\,\mathrm{d}^3\boldsymbol{x}' + 2\rho_\ell(\boldsymbol{x})u_\ell^2(\boldsymbol{x})\int_V G_\ell(\boldsymbol{x}-\boldsymbol{x}')\,\mathrm{d}^3\boldsymbol{x}',\\
=& \int_V \{\rho(\boldsymbol{x}')u^2(\boldsymbol{x}') - 2\boldsymbol{u}_\ell(\boldsymbol{x})\cdot\rho(\boldsymbol{x}')\boldsymbol{u}(\boldsymbol{x}')\\
& - \rho_\ell(\boldsymbol{x})u^2(\boldsymbol{x}') + 2\rho_\ell(\boldsymbol{x})u_\ell^2(\boldsymbol{x})\}\,G_\ell(\boldsymbol{x}-\boldsymbol{x}')\,\mathrm{d}^3\boldsymbol{x}',\\
=& \int_V \{[\rho(\boldsymbol{x}')-\rho_\ell(\boldsymbol{x})][u^2(\boldsymbol{x}')+u_\ell^2(\boldsymbol{x})] - \rho(\boldsymbol{x}')u_\ell^2(\boldsymbol{x})\\
& - 2\rho(\boldsymbol{x}')\boldsymbol{u}(\boldsymbol{x}')\cdot\boldsymbol{u}_\ell(\boldsymbol{x}) + 3\rho_\ell(\boldsymbol{x})u_\ell^2(\boldsymbol{x})\}\,G_\ell(\boldsymbol{x}-\boldsymbol{x}')\,\mathrm{d}^3\boldsymbol{x}',\\
=& \int_V \{[\rho(\boldsymbol{x}')-\rho_\ell(\boldsymbol{x})][u^2(\boldsymbol{x}')+u_\ell^2(\boldsymbol{x})] - \rho(\boldsymbol{x}')u_\ell^2(\boldsymbol{x}) - 2[\rho(\boldsymbol{x}')-\rho_\ell(\boldsymbol{x})]\boldsymbol{u}(\boldsymbol{x}')\cdot\boldsymbol{u}_\ell(\boldsymbol{x})\\
& - 2\rho_\ell(\boldsymbol{x})\boldsymbol{u}(\boldsymbol{x}')\cdot\boldsymbol{u}_\ell(\boldsymbol{x}) + 3\rho_\ell(\boldsymbol{x})u_\ell^2(\boldsymbol{x})\}G_\ell(\boldsymbol{x}-\boldsymbol{x}')\,\mathrm{d}^3\boldsymbol{x}',\\
=& \int_V [\rho(\boldsymbol{x}')-\rho_\ell(\boldsymbol{x})]|\boldsymbol{u}(\boldsymbol{x}')-\boldsymbol{u}_\ell(\boldsymbol{x})|^2 G_\ell(\boldsymbol{x}-\boldsymbol{x}')\,\mathrm{d}^3\boldsymbol{x}'\\
& - u_\ell^2(\boldsymbol{x})\int_V \rho(\boldsymbol{x}')G_\ell(\boldsymbol{x}-\boldsymbol{x}')\,\mathrm{d}^3\boldsymbol{x}' - 2\rho_\ell(\boldsymbol{x})\boldsymbol{u}_\ell(\boldsymbol{x})\cdot\int_V \boldsymbol{u}(\boldsymbol{x}')G_\ell(\boldsymbol{x}-\boldsymbol{x}')\,\mathrm{d}^3\boldsymbol{x}'\\
& + 3\rho_\ell(\boldsymbol{x})u_\ell^2(\boldsymbol{x})\int_V G_\ell(\boldsymbol{x}-\boldsymbol{x}')\,\mathrm{d}^3\boldsymbol{x}',\\
=& \int_V [\rho(\boldsymbol{x}')-\rho_\ell(\boldsymbol{x})]|\boldsymbol{u}(\boldsymbol{x}')-\boldsymbol{u}_\ell(\boldsymbol{x})|^2 G_\ell(\boldsymbol{x}-\boldsymbol{x}')\,\mathrm{d}^3\boldsymbol{x}' - \rho_\ell(\boldsymbol{x})\,u_\ell^2(\boldsymbol{x})\\
& - 2\rho_\ell(\boldsymbol{x})\,u_\ell^2(\boldsymbol{x}) + 3\rho_\ell(\boldsymbol{x})\,u_\ell^2(\boldsymbol{x}),\\
=& \int_V [\rho(\boldsymbol{x}')-\rho_\ell(\boldsymbol{x})]|\boldsymbol{u}(\boldsymbol{x}')-\boldsymbol{u}_\ell(\boldsymbol{x})|^2 G_\ell(\boldsymbol{x}-\boldsymbol{x}')\,\mathrm{d}^3\boldsymbol{x}'. \qquad \text{(B.8)}
\end{aligned}
$$

Appendix C

Dimensional units

By defining a set of fundamental units in the centimetres-grams-seconds (cgs) system, the dimensionless units used in a Pencil-code simulation are uniquely defined (see Mee, 2007, Appendix C). I shall detail the specified units and the units derived from these for both the MHD and HD simulations, highlighting any significant differences between the units in both sets. It should be noted that the units for the MHD simulations were detailed in Gent (2012, Appendix D). Nonetheless, these are stated here to provide further information to the reader.

The choice of code units should ideally satisfy the constraint of finite precision that variables should not differ greatly from unity. In both sets, the base units are length, velocity and density. The unit of time is derived naturally from the specification of both length and velocity. The typical time-scales in the ISM are measured in either Myr or Gyr, whilst the gas speed is usually measured in $\mathrm{km\,s^{-1}}$. Consequently, the appropriate unit of length is either pc or kpc, depending on how we wish to specify the unit of time. With an estimated mean number density at the Galactic mid-plane of approximately $1\,\mathrm{cm^{-3}}$ and the proton mass of about $1.6728\times10^{-24}\,\mathrm{g}$, a unit mass density of order $1\times10^{-24}\,\mathrm{g}$ is an appropriate choice.

It is possible to define the units of temperature and magnetic field strength independent of the specified units. However, numerical errors and code instability may occur, should the definitions of these units conflict with those already specified. The option to define unit temperature and magnetic field strength is included, since these would be necessary for models in which physics such as velocity or density are neglected. It is important to note that no more than three fundamental units can be defined independently and so it is required to derive the units of temperature and

Table C.1: Specified units for the MHD models.

Quantity	Symbol	Unit
Length	$[L]$	$3.15570\times10^{21}\,\mathrm{cm}\approx1\,\mathrm{kpc}$
Velocity	$[u]$	$10^{5}\,\mathrm{cm\,s^{-1}}=1\,\mathrm{km\,s^{-1}}$
Density	$[\rho]$	$1\times10^{-24}\,\mathrm{g\,cm^{-3}}$

Table C.2: Derived units for the MHD models.

Quantity	Symbol	Typical Derivation	Unit
Time	$[t]$	$[L][u]^{-1}$	$3.15570 \times 10^{16}\,\mathrm{s} = 1\,\mathrm{Gyr}$
Temperature	$[T]$	$\mu[u]^2\gamma^{-1}R^{-1}$	$44.74127\,\mathrm{K}$
Mass	$[m]$	$[\rho][L]^3$	$3.14256 \times 10^{40}\,\mathrm{g}$
Energy	$[E]$	$[\rho][L]^3[u]^2$	$3.14256 \times 10^{50}\,\mathrm{erg}$
Energy density	$[e_V]$	$[\rho][u]^2$	$1 \times 10^{14}\,\mathrm{erg\,cm^{-3}}$
Pressure	$[p]$	$[\rho][u]^2$	$1 \times 10^{14}\,\mathrm{dyn\,cm^{-2}}$
Magnetic field	$[B]$	$\sqrt{\mu_0}[\rho]^{\frac{1}{2}}[u]$	$3.54491 \times 10^{-7}\,\mathrm{G}$
Kinematic viscosity	$[\nu]$	$[L][u]$	$3.15570 \times 10^{26}\,\mathrm{erg\,s\,g^{-1}}$
Thermal diffusivity	$[\chi]$	$[L][u]$	$3.15570 \times 10^{26}\,\mathrm{erg\,s\,g^{-1}}$
Magnetic diffusivity	$[\eta]$	$[L][u]$	$3.15570 \times 10^{26}\,\mathrm{erg\,s\,g^{-1}}$
Specific entropy	$[s]$	$[u]^2[T]^{-1}$	$2.23507 \times 10^{8}\,\mathrm{erg\,g^{-1}\,K^{-1}}$

magnetic field strength. The specified units for both sets of simulations, with the corresponding derived units are shown below.

C.1 MHD simulations

The fundamental units for the MHD simulations are shown in Table C.1. The choice of unit velocity is $1\,\mathrm{km\,s^{-1}} = 10^5\,\mathrm{cm\,s^{-1}}$, with a unit length of $3.15570 \times 10^{21}\,\mathrm{cm} \approx 1\,\mathrm{kpc}$ ($1\,\mathrm{kpc} = 3.08573 \times 10^{21}\,\mathrm{cm}$) to ensure a derived unit time of $1\,\mathrm{Gyr} = 3.15570 \times 10^{16}\,\mathrm{s}$. The unit density employed is $1 \times 10^{24}\,\mathrm{g\,cm^{-3}}$.

The main derived units and their determination from the fundamental units are listed in Table C.2. The derivations of the units of temperature and magnetic field strength are further detailed, since their derivations from the fundamental units are less straightforward.

Unit temperature

From the equation of state, the sound speed is calculated in terms of the temperature as follows;

$$c_s^2 = \gamma\frac{p}{\rho} = \gamma\frac{k_\mathrm{B}}{m_u\mu}T, \tag{C.1}$$

where the ratio of specific heats $\gamma = 5/3$, the Boltzmann constant $k_\mathrm{B} = 1.380658 \times 10^{-16}\,\mathrm{erg\,K^{-1}}$, the atomic mass unit $m_u = 1.6605402 \times 10^{-24}\,\mathrm{g}$ and the mean molecular weight $\mu = 0.62$. The unit of temperature is then computed in terms of the unit of sound speed $c_{s0} = 1\,\mathrm{km\,s^{-1}}$ as

$$T_0 = \frac{\mu}{\gamma R}c_{s0}^2 = 44.74127\,\mathrm{K}, \tag{C.2}$$

where $R = k_\mathrm{B}/m_u$ is the gas constant.

Table C.3: Specified units for the HD models.

Quantity	Symbol	Unit
Length	$[L]$	$3.08573 \times 10^{21}\,\mathrm{cm} = 1\,\mathrm{kpc}$
Velocity	$[u]$	$9.77812 \times 10^{4}\,\mathrm{cm\,s^{-1}} \approx 1\,\mathrm{km\,s^{-1}}$
Density	$[\rho]$	$1 \times 10^{-24}\,\mathrm{g\,cm^{-3}}$

Table C.4: Derived units for the HD models.

Quantity	Symbol	Typical Derivation	Unit
Time	$[t]$	$[L][u]^{-1}$	$3.15570 \times 10^{16}\,\mathrm{s} = 1\,\mathrm{Gyr}$
Temperature	$[T]$	$\mu[u]^2\gamma^{-1}R^{-1}$	$36.63718\,\mathrm{K}$
Mass	$[m]$	$[\rho][L]^3$	$2.93800 \times 10^{40}\,\mathrm{g}$
Energy	$[E]$	$[\rho][L]^3[u]^2$	$2.80907 \times 10^{50}\,\mathrm{erg}$
Energy density	$[e_V]$	$[\rho][u]^2$	$9.56117 \times 10^{-15}\,\mathrm{erg\,cm^{-3}}$
Pressure	$[p]$	$[\rho][u]^2$	$9.56117 \times 10^{-15}\,\mathrm{dyn\,cm^{-2}}$
Kinematic viscosity	$[\nu]$	$[L][u]$	$3.01721 \times 10^{26}\,\mathrm{erg\,s\,g^{-1}}$
Thermal diffusivity	$[\chi]$	$[L][u]$	$3.01721 \times 10^{26}\,\mathrm{erg\,s\,g^{-1}}$
Specific entropy	$[s]$	$[u]^2[T]^{-1}$	$2.60968 \times 10^{8}\,\mathrm{erg\,g^{-1}\,K^{-1}}$

Unit magnetic field strength

The magnetic energy density in cgs units is $B^2/2\mu_0$, with the magnetic field is in units of Gauss [G] and $\mu_0 = 4\pi\,\mathrm{G^2\,cm^3\,erg^{-1}}$ is the vacuum permeability. Through re-arranging we determine $1\,\mathrm{G} = (\mu_0\,\mathrm{erg\,cm^{-3}})^{\frac{1}{2}}$, and so the unit of magnetic field strength is calculated as

$$B_0 = (\mu_0\rho_0 u_0^2)^{\frac{1}{2}} = 3.54491 \times 10^{-7}\,\mathrm{G}, \tag{C.3}$$

where $\rho_0 = 1 \times 10^{-24}\,\mathrm{g\,cm^{-3}}$ and $u_0 = 1 \times 10^{5}\,\mathrm{cm\,s^{-1}}$ are the unit density and velocity respectively.

C.2 HD simulations

The specified and derived units for the HD models are listed in Tables C.3 and C.4. The unit of length chosen was 1 kpc exactly, which results in a unit velocity of $9.77812 \times 10^{4}\,\mathrm{cm\,s^{-1}} \approx 1\,\mathrm{km\,s^{-1}}$ to ensure a derived unit of time of 1 Gyr. As previously, the unit density is $1 \times 10^{24}\,\mathrm{g\,cm^{-3}}$. The changes to the units of length and velocity result in only modest changes to the derived units. The exceptions are the units of temperature and specific entropy. Substituting $\mu = 0.531$ and $c_{s0} = 9.77812 \times 10^{4}\,\mathrm{cm\,s^{-1}}$ into (C.2) results in a unit of temperature $36.63718\,\mathrm{K}$, with a correpsonding derived unit of specific entropy $2.60968 \times 10^{8}\,\mathrm{erg\,g^{-1}\,K^{-1}}$.

Appendix D

A model of mean galactic magnetic fields

In this Appendix, I present my calculations of the free-decay modes of the mean magnetic field in galactic haloes, as a contribution to the model of the large-scale magnetic field in galaxies, detailed in Shukurov et al. (2018). The model is obtained from approximate solutions to the mean-field dynamo equation

$$\frac{\partial \boldsymbol{B}}{\partial t} = \nabla \times (\alpha \boldsymbol{B}) + \nabla \times (\boldsymbol{V} \times \boldsymbol{B}) + \beta \nabla^2 \boldsymbol{B}, \tag{D.1}$$

in both the disk and the halo, where $\boldsymbol{B}$ is the large-scale magnetic field, α and β are the turbulent transport coefficients representing the mean induction effects of the helical interstellar turbulence (the α-effect) and turbulent magnetic diffusion, respectively, and $\boldsymbol{V}$ is the large-scale velocity field. This model is implemented via the publicly available package GALMAG and can be applied to accretion disks, in addition to spiral galaxies.

The magnitude of the α-effect can be estimated as

$$\alpha \simeq \min\left(l^2 \Omega / h, v\right), \tag{D.2}$$

where l and v are the turbulent scale and speed, and the corresponding fiducial value is used to non-dimensionalise α:

$$\widetilde{\alpha} = \frac{\alpha}{\alpha_0}, \quad \alpha_0 = \frac{l^2 V_0}{h_0 s_0}. \tag{D.3}$$

The magnitude of α cannot exceed $\alpha = v$ because it is a measure of the helical part of the turbulent flow speed, hence α/v cannot exceed unity.

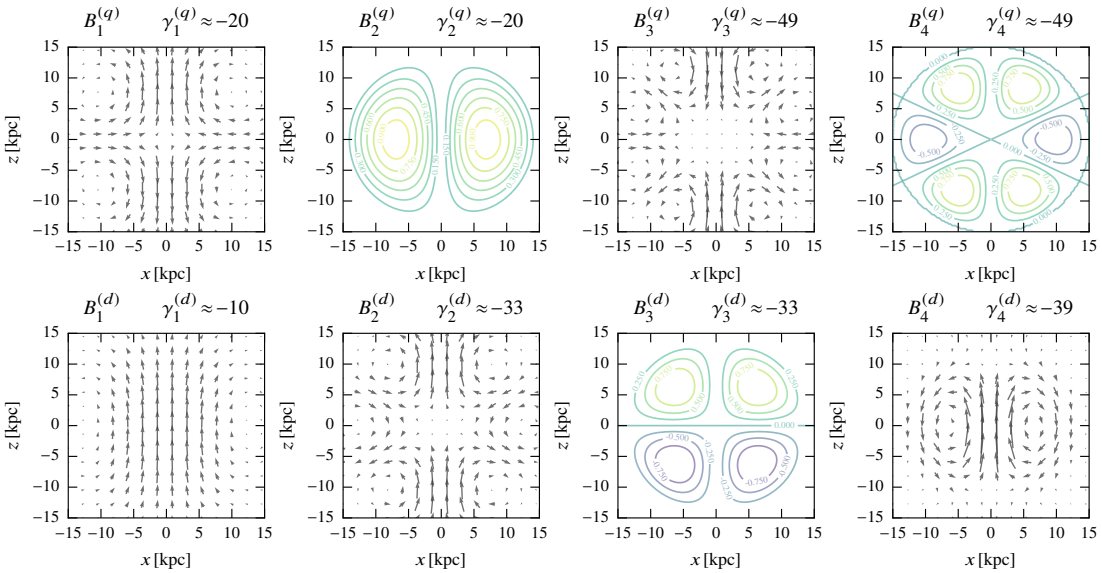

Figure D.1: The eight spherical free-decay eigenfunctions $\boldsymbol{B}_i$ of the smallest decay rates, from Shukurov et al. (2018). Each mode is either purely toroidal or purely poloidal. The top row shows the modes symmetric with respect to the mid-plane $z = 0$ (quadrupolar modes), while the modes in the bottom row are anti-symmetric (dipolar). For the poloidal modes, arrows represent the projection of the magnetic field on the (xy)-plane. For the toroidal modes, contours show the strength of the azimuthal component of the magnetic field (with arbitrary normalization). The decay rate of each mode γ is shown at the top of each panel.

D.1 Magnetic field in the halo

Magnetic field in the spherical halo is obtained as the perturbation solution of the mean-field dynamo equation with free-decay eigenfunctions as the unperturbed solutions. This approach is similar to that employed to obtain the local disc solution in Shukurov et al. (2018, Section 3.3).

In the spherical halo, it is convenient to use spherical coordinates (r, θ, ϕ). As for the disc, convenient dimensionless variables are defined, distinguished by the tilde: spherical radius and time are measured in the units of the halo radius r_h and the corresponding magnetic diffusion time,

$$\widetilde{r} = r/r_\mathrm{h} \qquad \text{and} \qquad \widetilde{t} = t\beta_\mathrm{h}/r_\mathrm{h}^2, \tag{D.4}$$

with β_h the turbulent magnetic diffusivity in the halo. The velocity field and the α-coefficient are normalised as

$$\widetilde{\alpha} = \alpha/\alpha_\mathrm{h}, \qquad \widetilde{V} = V/V_\mathrm{h}, \tag{D.5}$$

where α_h is the α-coefficient at the north pole, $(r, \theta) = (r_\mathrm{h}, 0)$, and V_h is the equatorial rotation velocity at its boundary, i.e., at $(r, \theta) = (r_\mathrm{h}, \pi/2)$.

In terms of the dimensionless variables, the mean-field dynamo equation (D.1) reduces to

$$\frac{\partial \boldsymbol{B}}{\partial \widetilde{t}} = R_{\alpha\mathrm{h}} \widetilde{\nabla} \times (\widetilde{\alpha}\boldsymbol{B}) + R_{\omega\mathrm{h}} \widetilde{\nabla} \times (\widetilde{\boldsymbol{V}} \times \boldsymbol{B}) + \widetilde{\nabla}^2 \boldsymbol{B}, \tag{D.6}$$

with the defined dynamo parameters

$$R_{\alpha \mathrm{h}} = r_{\mathrm{h}} \alpha_{\mathrm{h}} / \beta_{\mathrm{h}} \,, \qquad R_{\omega \mathrm{h}} = -r_{\mathrm{h}} V_{\mathrm{h}} / \beta_{\mathrm{h}} \,. \tag{D.7}$$

To avoid excessively heavy notation, the tilde on the dimensionless variables is suppressed. This work exclusively involves dimensionless variables unless otherwise stated.

Solutions of Eq. (D.6), growing or decaying at a rate Γ, are sought in the form of an expansion

$$\boldsymbol{B} = \exp(\Gamma t) \sum_{i=1}^{N} a_i \boldsymbol{B}_i(\vec{r}) \tag{D.8}$$

in the free-decay modes $\boldsymbol{B}_i$ which are obtained as solutions of Eq. (D.6) with $R_{\alpha \mathrm{h}} = R_{\omega \mathrm{h}} = 0$,

$$\nabla^2 \boldsymbol{B}_i = \gamma_i \boldsymbol{B}_i \,. \tag{D.9}$$

where $\gamma_i < 0$ is the rate of exponential decay of the free-decay mode $\boldsymbol{B}_i$. Outside the halo, an electromagnetic vacuum is assumed, implying a potential magnetic field, $\nabla \times \boldsymbol{B}_i = \boldsymbol{0}$. The boundary conditions that ensure a continuous matching, at the halo boundary $r = 1$, of the interior magnetic field to a potential exterior magnetic field that decays at infinity as the point dipole (the lowest magnetic multipole) are given by (Moffatt, 1978)

$$[\boldsymbol{B}_i] = 0 \text{ at } r = 1 \,, \qquad \boldsymbol{B}_i = \mathscr{O}\left(r^{-3}\right) \text{ for } r \to \infty, \tag{D.10}$$

where the square brackets denote the jump of the corresponding quantity.

The spatial form and decay rates of the spherical modes of free decay are derived in Section D.2; here their properties are briefly discussed. The free decay modes form a complete, orthonormal set of basis functions (related to spherical harmonics), each either purely poloidal (comprising the field components B_r and B_θ) or purely toroidal (consisting of B_ϕ alone). They can be divided into two classes based on their symmetry about the equator $\theta = \pi/2$: the symmetric modes are quadrupolar (indicated with superscript 'q') whereas the anti-symmetric modes have a dipolar symmetry (superscript 'd'). Their analytic forms can be found in Sections D.2.1 and D.2.2, respectively. Figure D.1 shows the structure of the four free-decay modes of each symmetry that have the largest γ_i.

D.1.1 The perturbation solution

Equation (D.6) can be conveniently written as

$$\frac{\partial \boldsymbol{B}}{\partial t} = \widehat{\mathscr{W}} \boldsymbol{B} + \nabla^2 \boldsymbol{B} \,, \tag{D.11}$$

where the perturbation operator $\widehat{\mathscr{W}}$ corresponding to the $\alpha^2\omega$-dynamo is given by

$$\widehat{\mathscr{W}}\boldsymbol{B} = R_{\alpha\mathrm{h}}\nabla\times(\alpha\boldsymbol{B}) + R_{\omega\mathrm{h}}\nabla\times(\boldsymbol{V}\times\boldsymbol{B}). \tag{D.12}$$

As discussed in Shukurov et al. (2018), GALMAG has also an option to use the $\alpha\Omega$-dynamo operator but this approximation may be questionable in the case of the halo.

By substituting Eq. (D.8) into Eq. (D.11), taking the scalar product of the result with $\boldsymbol{B}_i$ and integrating over the whole space; a homogeneous system of algebraic equations for the expansion coefficients a_i is obtained

$$a_j(\gamma_j - \Gamma) + \sum_{i=1}^{N} a_i W_{ij} = 0, \quad j = 1,2,\ldots,N, \tag{D.13}$$

where

$$W_{ij} = \int_V \boldsymbol{B}_i \cdot \widehat{\mathscr{W}}\boldsymbol{B}_j \,\mathrm{d}^3\boldsymbol{r}, \tag{D.14}$$

are the matrix elements of the perturbation operator, with integration performed over the whole space. Since the operator $\widehat{\mathscr{W}}$ transforms a poloidal field into a toroidal one and vice versa (and the two are orthogonal), it follows that $W_{ii} = 0$ and each non-vanishing matrix element involves at least one toroidal and one poloidal free-decay eigenfunction. Because the toroidal eigenfunctions vanish at $r > r_\mathrm{h}$, the integrals are in fact restricted to the interior of the halo. The solvability condition of the system of equations for a_i, the vanishing of its determinant, yields the growth rate Γ. Once the matrix elements have been computed and the system (D.13) has been solved for a_i, Eq. (D.8) yields the solution of the dynamo equation. One of the coefficients a_i remains arbitrary because the dynamo equation is linear in magnetic field and hence its solution is determined up to an arbitrary factor. This freedom is used to fix the magnetic field strength at any desired value.

D.1.2 Parameters of galactic haloes

Velocity fields in galactic haloes are poorly known. Random velocities are likely to increase with altitude, and $\mathrm{H_I}$ observations of Kalberla et al. (1998) (see also Kalberla & Kerp, 2009) suggest a three-dimensional velocity dispersion of about $100\,\mathrm{km\,s^{-1}}$, close to the sound speed at a temperature $10^6\,\mathrm{K}$. The scale of these motions is uncertain. The size of supernova remnants above the galactic disc is expected to be of order 0.3 kpc (McKee & Ostriker, 1977). The size of the hot gas bubbles rising from the disc and the scale of the Parker instability are of order 0.5–1 kpc (e.g., Rodrigues et al., 2016). Adopting the random speed and scale as $v = 100\,\mathrm{km\,s^{-1}}$ and $l = 0.5\,\mathrm{kpc}$, the turbulent diffusivity is estimated as $\beta_\mathrm{h} \simeq \frac{1}{3}lv = 5\times10^{27}\,\mathrm{cm^2\,s^{-1}}$. The corresponding magnetic diffusion time across the halo radius is $r_\mathrm{h}^2/\beta_\mathrm{h} \simeq 1.4\times10^{10}\,\mathrm{yr}$.

The knowledge of the variation of the rotation speed with position within galactic haloes is rather rudimentary. Both the rotational speed and its radial gradient decrease in spiral galaxies

with distance from the mid-plane. The typical vertical gradient within a few kiloparsecs from the mid-plane is of order $\partial V/\partial z = -(15\text{–}25)\,\mathrm{km\,s^{-1}\,kpc^{-1}}$ (Zschaechner et al., 2015). In this model, the halo is assumed to have a rotation curve of the form, in dimensional variables,

$$\boldsymbol{V}(\boldsymbol{r}) = V_\mathrm{h} f(r,\theta)\,\hat{\boldsymbol{\phi}}\,, \tag{D.15}$$

with $\hat{\boldsymbol{\phi}}$ the unit azimuthal vector and

$$f(r,\theta) = \frac{1-\exp\left(-r\sin\theta/s_\mathrm{v}\right)}{1-\exp\left(-r_\mathrm{h}/s_\mathrm{v}\right)}\,, \tag{D.16}$$

where the turnover radius is adopted as $s_\mathrm{v} = 3\,\mathrm{kpc}$, the typical value found in observations and simulations of MW-type galaxies (Reyes et al., 2011; Schaller et al., 2015). For simplicity, the rotation curve of Eqs. (D.15) and (D.16) has no z-dependence but it can easily be introduced. The role of the variation of Ω with z is to produce B_ϕ from B_z, arguably a process somewhat less important than the stretching of the radial magnetic field in the azimuthal direction at a rate $S = s\partial\Omega/\partial s$.

A simple form for the α-coefficient often used in spherical mean-field dynamo models is adopted; in dimensional variables,

$$\alpha(\boldsymbol{r}) = \alpha_\mathrm{h}\cos(\theta)\,, \tag{D.17}$$

implying the largest absolute value of α near the poles whilst α also vanishes at the equator, reflecting the fact that the mean helicity of the random flows is produced by the Coriolis force.

The magnetic field in the halo is assumed to be axially symmetric and the dynamo is assumed to operate within a region of $r_\mathrm{h} = 15\,\mathrm{kpc}$ in radius. A value of $V_\mathrm{h} = 220\,\mathrm{km\,s^{-1}}$ is used (similar to that in the disc). With the turbulent magnetic diffusivity $\beta_\mathrm{h} = 5\times10^{27}\,\mathrm{cm^2\,s^{-1}}$, this leads to $R_{\omega\mathrm{h}} \simeq 200$.

Estimating $R_{\alpha\mathrm{h}}$ in the halo is more difficult given the uncertainty of the random flow parameters. The standard estimate of Eq. (D.2) yields $\alpha_\mathrm{h} \simeq l^2\Omega/h \simeq 1\,\mathrm{km\,s^{-1}}$ and $R_{\alpha\mathrm{h}} = \alpha_\mathrm{h} r_\mathrm{h}/\beta_\mathrm{h} \simeq 1$ for $\Omega = 26\,\mathrm{km\,s^{-1}\,kpc^{-1}}$ and $h = 3\,\mathrm{kpc}$, the gas density scale height in the halo. As the fiducial value for $R_{\alpha\mathrm{h}}$, its marginal value corresponding to the vanishing dynamo growth rate is selected (see Shukurov et al., 2018, Section 4.3, for more details); $R^{(\mathrm{q})}_{\alpha\mathrm{h}} = 4.3$ for symmetric solutions and $R^{(\mathrm{d})}_{\alpha\mathrm{h}} = 8.1$ for anti-symmetric ones. The symmetric mode is preferred to the anti-symmetric one only slightly, $R^{(\mathrm{q})}_{\alpha\mathrm{h}}/R^{(\mathrm{d})}_{\alpha\mathrm{h}} \simeq 0.5$ for the marginal values. The similarity of the marginal values of $R_{\alpha\mathrm{h}}$ for the dipolar and quadrupolar magnetic structures in the halo reflects the fact that, unlike the disc dynamo, spherical dynamos usually do not exhibit strong preference of either symmetry.

Table D.1: Decay rates of spherical free-decay modes, γ_{nl}.

	$l=1$	$l=2$	$l=3$	$l=4$
$n=1$	$-\pi^2$	$-(4.493)^2$	$-(2\pi)^2$	$-(7.725)^2$
$n=2$	$-(4.493)^2$	$-(5.763)^2$	$-(7.725)^2$	$-(9.095)^2$
$n=3$	$-(5.763)^2$	$-(6.988)^2$	$-(9.095)^2$	$-(10.417)^2$
$n=4$	$-(6.988)^2$	$-(8.813)^2$	$-(10.417)^2$	$-(11.705)^2$

D.2 Spherical free-decay modes

For axisymmetric free-decay modes, a solution to Eq. (D.9) is obtained in terms of scalar potentials, as discussed by Krause & Rädler (1980) and Moffatt (1978). An outline of the solution is presented here. Magnetic field $\boldsymbol{B}$ can be represented as the sum of a poloidal field $\nabla\times\boldsymbol{A}_{\rm P}$, where $\boldsymbol{A}_{\rm P}$ is its vector potential, and a toroidal field $\boldsymbol{B}_{\rm T}$:

$$\boldsymbol{B}=\nabla\times\boldsymbol{A}_{\rm P}+\boldsymbol{B}_{\rm T}\,, \tag{D.18}$$

and $\nabla\cdot\boldsymbol{B}=0$ provided

$$\boldsymbol{A}_{\rm P}=-\boldsymbol{r}\times\nabla S\,,\qquad \boldsymbol{B}_{\rm T}=-\boldsymbol{r}\times\nabla T\,, \tag{D.19}$$

where $\boldsymbol{r}$ is the position vector normalised such that $r=1$ is the halo surface ($r=r_{\rm h}$ in dimensional variables). In terms of the scalar potentials and assuming axial symmetry, Eq. (D.9) reduces in spherical coordinates (r,θ,ϕ) to

$$\frac{1}{r^2}\frac{\partial}{\partial r}\left(r^2\frac{\partial S}{\partial r}\right)+\frac{1}{r^2\sin\theta}\frac{\partial}{\partial\theta}\left(\sin\theta\frac{\partial S}{\partial\theta}\right)=\gamma S\,, \tag{D.20}$$

$$\frac{1}{r^2}\frac{\partial}{\partial r}\left(r^2\frac{\partial T}{\partial r}\right)+\frac{1}{r^2\sin\theta}\frac{\partial}{\partial\theta}\left(\sin\theta\frac{\partial T}{\partial\theta}\right)=\gamma T\,, \tag{D.21}$$

for $r<1$ and,

$$\nabla^2 S=0\,,\qquad T=0\quad\text{for } r>1\,, \tag{D.22}$$

with the vacuum boundary conditions

$$[S]=[\partial S/\partial r]=[T]=0\text{ at }r=1 \tag{D.23}$$

where $[X]$ denotes the jump of X, and $[X]=0$ means continuity. Both potentials are also required to be finite at $r=0$.

The potentials satisfy identical equations at $r<1$, so consider this equation for G equal to either S or T,

$$\frac{1}{r^2}\frac{\partial}{\partial r}\left(r^2\frac{\partial G}{\partial r}\right)+\frac{1}{r^2\sin\theta}\frac{\partial}{\partial\theta}\left(\sin\theta\frac{\partial G}{\partial\theta}\right)-\gamma G=0\,. \tag{D.24}$$

Using separation of variables, $G(r,\theta)=R(r)\Theta(\theta)$, Bessel's equation is obtained in r and Legen-

dre's equation in θ, with the separation constant $n(n+1)$ ($n = 1,2,3,\ldots$):

$$r^2\frac{\mathrm{d}^2R}{\mathrm{d}r^2} + 2r\frac{\mathrm{d}R}{\mathrm{d}r} - [\gamma r^2 + n(n+1)]R = 0\,, \tag{D.25}$$

$$\frac{\mathrm{d}}{\mathrm{d}\theta}\left(\sin\theta\frac{\mathrm{d}\Theta}{\mathrm{d}\theta}\right) + n(n+1)\Theta\sin\theta = 0\,. \tag{D.26}$$

In terms of $x = \sqrt{-\gamma}r$ and $Q(x) = x^{1/2}R(x)$ in Eq. (D.25) and $x = \cos\theta$ in Eq. (D.26), and so

$$x^2\frac{\mathrm{d}^2Q}{\mathrm{d}x^2} + x\frac{\mathrm{d}Q}{\mathrm{d}x} + \left[x^2 - \left(n+\tfrac{1}{2}\right)^2\right]Q = 0\,, \tag{D.27}$$

$$\frac{\mathrm{d}}{\mathrm{d}x}\left[(1-x^2)\frac{\mathrm{d}\Theta}{\mathrm{d}x}\right] + n(n+1)\Theta = 0. \tag{D.28}$$

Non-singular solutions of (D.20) and (D.21) then follow as

$$T = \sum_{n=1}^{\infty}\sum_{l=1}^{\infty} c_{nl}T_{nl}(r)P_n(\cos\theta)\,, \tag{D.29}$$

$$S = r_{\mathrm{h}}\sum_{n=1}^{\infty}\sum_{l=1}^{\infty} c_{nl}S_{nl}(r)P_n(\cos\theta)\,, \tag{D.30}$$

where

$$T_{nl}(r) = S_{nl}(r) = \frac{1}{\xi_{nl}\sqrt{r}}J_{n+1/2}(\xi_{nl}r)\,,, \tag{D.31}$$

with constants c_{nl},

$$\xi_{nl} = \sqrt{-\gamma_{nl}}\,, \tag{D.32}$$

and ξ_{nl} are solutions to (D.35). The factor r_{h} in Eq. (D.30) is introduced to ensure dimensional consistency when obtaining the magnetic field from these potentials. The boundary conditions (D.23) reduce to

$$T_{nl} = 0\,, \quad S_{nl} = d_n\,, \quad \frac{\partial S_{nl}}{\partial r} = -(n+1)d_n \quad \text{at } r = 1\,, \tag{D.33}$$

where d_n are constants. Eliminating d_n, the boundary conditions for S_{nl} reduce to the recurrence relation

$$\frac{\partial S_{nl}}{\partial r} + (n+1)S_{nl} = 0 \quad \text{at } r = 1\,. \tag{D.34}$$

Together with the requirement that T_{nl} and S_{nl} do not vanish simultaneously, this gives

$$J_{n-1/2}(\xi_{nl})J_{n+1/2}(\xi_{nl}) = 0\,, \tag{D.35}$$

which determines the admissible values for ξ_{nl}, and $\gamma_{nl} = -\xi_{nl}^2$ yields the decay rates γ_{nl} given in Table D.1.

For l odd, $J_{n-1/2}(\xi_{nl}) = 0$ for all n. Hence, $T_{nl} = 0$ for l odd. Conversely, when l is even, $J_{n+1/2}(\xi_{nl}) = 0$ for all n. Hence, $S_{nl} = 0$ for l even. The solutions satisfying the boundary condi-

tions (D.33) can be written, with $j = n + l$, as follows:

$$T = \sum_{n=1}^{\infty} \sum_{l\,\text{even}} \frac{c_{nl}}{\sqrt{r}} J_{k+1/2}(\xi_{nl} r) P_n(\cos\theta)\,, \tag{D.36a}$$

$$S = \sum_{n=1}^{\infty} \sum_{l\,\text{odd}} \frac{d_{nl}}{\sqrt{r}} J_{k+1/2}(\xi_{nl} r) P_n(\cos\theta)\,, \tag{D.36b}$$

where $c_{k(j-k)}$ and $d_{k(j-k)}$ are constants. Individual terms in the sums are arranged according to increasing magnitude of the decay rates, $|\gamma_{nl}|$.

The free-decay modes form two separate families based on their symmetry about the equator $\theta = \pi/2$, the anti-symmetric (dipolar) and symmetric (quadrupolar) ones. The anti-symmetric modes, denoted with superscript (d), occur when both n and l are either odd or even, whilst the symmetric modes that have superscript (q) occur otherwise.

Explicit forms of a few lowest free-decay modes are given in the next section, each normalised to $\int_V |\boldsymbol{B}_n|^2 \,\mathrm{d}^3\boldsymbol{r} = 1$, where the integral is taken over the sphere $r \le 1$, to form an orthonormal set. Although each eigenmode is either poloidal or toroidal, their superpositions (D.36) necessarily contain both poloidal and toroidal parts: purely toroidal and purely poloidal fields cannot sustain Ohmic dissipation and unavoidably decay.

D.2.1 Symmetric modes

The four leading quadrupolar free-decay modes are shown in the upper row of Fig. D.1. The quadrupolar mode of the slowest decay has $(n,l) = (2,1)$ and is poloidal,

$$\boldsymbol{B}_1^{(\mathrm{q})} = A_1 \left(\frac{P_1(r)}{r} (3\cos^2\theta - 1)\,,\; -\frac{\sin\theta\,\cos\theta}{r} \frac{\mathrm{d}}{\mathrm{d}r}[r P_1(r)]\,,\; 0 \right), \tag{D.37}$$

where $A_1 \approx 0.662$ and

$$P_1(r) = \begin{cases} r^{-1/2} J_{5/2}(q_1 r)\,, & r \le 1\,, \\ r^{-3} J_{5/2}(q_1)\,, & r > 1\,, \end{cases} \qquad q_1 \approx 4.493\,. \tag{D.38}$$

The next mode, $(n,l) = (1,2)$, is toroidal and has the same eigenvalue,

$$\boldsymbol{B}_2^{(\mathrm{q})} = A_2\,(0,\; 0,\; P_2(r)\sin\theta)\,, \tag{D.39}$$

where $A_2 \approx 1.330$ and

$$P_2(r) = \begin{cases} r^{-1/2} J_{3/2}(q_1 r)\,, & r \le 1\,, \\ r^{-2} J_{3/2}(q_1 r)\,, & r > 1\,. \end{cases} \tag{D.40}$$

The modes $\boldsymbol{B}_3^{(\mathrm{q})}$ and $\boldsymbol{B}_4^{(\mathrm{q})}$, poloidal and toroidal respectively, also form a doublet with the common eigenvalue and correspond to $(n,l)=(4,1)$ and $(n,l)=(3,2)$, respectively:

$$\boldsymbol{B}_3^{(\mathrm{q})} = A_3 \left(-20\frac{P_3(r)}{r} S_1(\theta)\,,\ -r^{-1}\frac{\mathrm{d}}{\mathrm{d}r}[rP_3(r)]\frac{\mathrm{d}S_1(\theta)}{\mathrm{d}\theta}\,,\ 0 \right), \tag{D.41}$$

where $A_3 \approx 0.133$, $S_1(\theta) = 35\cos^4\theta - 30\cos^2\theta + 3$ and

$$P_3(r) = \begin{cases} r^{-1/2} J_{9/2}(q_3 r)\,, & r \le 1\,, \\ r^{-5} J_{9/2}(q_3)\,, & r > 1\,, \end{cases} \qquad q_3 \approx 6.988\,, \tag{D.42}$$

and

$$\boldsymbol{B}_4^{(\mathrm{q})} = A_4 \left(0,\ 0,\ -P_4(r)\frac{\mathrm{d}S_2(\theta)}{\mathrm{d}\theta} \right), \tag{D.43}$$

where $A_4 \approx 0.763$, $S_2(\theta) = 5\cos^3\theta - 3\cos\theta$ and

$$P_4(r) = \begin{cases} r^{-1/2} J_{7/2}(q_3 r)\,, & r \le 1\,, \\ r^{-4} J_{7/2}(q_3)\,, & r > 1\,. \end{cases} \tag{D.44}$$

D.2.2 Anti-symmetric modes

The spherical components of magnetic field in a few leading anti-symmetric modes have the following form, illustrated in the bottom row of Fig. D.1.

The mode that decays most slowly is poloidal, with $(n,l)=(1,1)$:

$$\boldsymbol{B}_1^{(\mathrm{d})} = C_1 \left(\frac{2}{r} Q_1(r)\cos\theta,\ -\frac{\sin\theta}{r}\frac{\mathrm{d}}{\mathrm{d}r}[rQ_1(r)],\ 0 \right), \tag{D.45}$$

where $C_1 \approx 0.346$ and

$$Q_1(r) = \begin{cases} r^{-1/2} J_{3/2}(k_1 r)\,, & r \le 1\,, \\ r^{-2} J_{3/2}(k_1)\,, & r > 1\,. \end{cases} \qquad k_1 = \pi\,. \tag{D.46}$$

The next two modes $\boldsymbol{B}_2^{(\mathrm{d})}$ and $\boldsymbol{B}_3^{(\mathrm{d})}$, poloidal and toroidal with $(n,l)=(3,1)$ and $(n,l)=(2,2)$, respectively, form a degenerate pair:

$$\boldsymbol{B}_2^{(\mathrm{d})} = C_2 \left(\frac{2\cos\theta}{r}(5\cos 2\theta - 1)Q_2(r), -\frac{\sin\theta}{r}\left(5\cos^2\theta - 1\right)\frac{\mathrm{d}}{\mathrm{d}r}\left[rQ_2(r)\right],\ 0 \right), \tag{D.47}$$

where $C_2 \approx 0.250$ and

$$Q_2(r) = \begin{cases} r^{-1/2} J_{7/2}(k_2 r)\,, & r \leq 1\,, \\ r^{-4} J_{7/2}(k_2)\,, & r > 1\,, \end{cases} \qquad k_2 \approx 5.763\,. \tag{D.48}$$

The toroidal mode of the doublet has the form

$$\boldsymbol{B}_3^{(\mathrm{d})} = C_3\,(0\,,\ 0\,,\ Q_3(r)\sin\theta\cos\theta)\,, \tag{D.49}$$

where $C_3 \approx 3.445$ and

$$Q_3(r) = \begin{cases} r^{-1/2} J_{5/2}(k_2 r)\,, & r \leq 1\,, \\ r^{-3} J_{5/2}(k_2 r)\,, & r > 1,. \end{cases} \tag{D.50}$$

The fourth antisymmetric mode is also a singular poloidal mode, with $(n,l) = (1,3)$:

$$\boldsymbol{B}_4^{(\mathrm{d})} = C_4 \left(\frac{2}{r} Q_4(r)\, P_1(\cos\theta),\ \frac{1}{r}\frac{\mathrm{d}}{\mathrm{d}r}[r Q_4(r)]\,\frac{\mathrm{d}}{\mathrm{d}\theta} P_1(\cos\theta),\ 0 \right)\,, \tag{D.51}$$

where $P_1(\cos\theta) = \cos\theta$, $C_4 \approx 0.244$ and

$$Q_4(r) = \begin{cases} r^{-1/2} J_{3/2}(k_4 r)\,, & r \leq 1\,, \\ r^{-2} J_{3/2}(k_4)\,, & r > 1\,, \end{cases} \qquad k_4 = 2\pi\,. \tag{D.52}$$

Bibliography

Adler R. J., Bobrowski O., Borman M. S., Subag E., Weinberger S., 2010, in Borrowing Strength: Theory Powering Applications. p. 124–143

Aluie H., 2017, New J. Phys., 19, 025008

Armstrong J. W., Rickett B. J., Spangler S. R., 1995, ApJ, 443, 209

Balbus S. A., Hawley J. F., 1991, ApJ, 376, 214

Balsara D. S., Kim J., 2005, ApJ, 634, 390

Balsara D. S., Kim J., Mac Low M.-M., Mathews G. J., 2004, ApJ, 617, 339

Beck R., 2016, A&A Rev., 24, 4

Beck R., Krause M., 2005, Astronomische Nachrichten, 326, 414

Beck R., Shukurov A., Sokoloff D., Wielebinski R., 2003, A&A, 411, 99

Beck R., Fletcher A., Shukurov A., Snodin A., Sokoloff D. D., Ehle M., Moss D., Shoutenkov V., 2005, A&A, 444, 739

Bendre A., Gressel O., Elstner D., 2015, AN, 336, 991

Berezinskiĭ V. S., Bulanov S. V., Dogiel V. A., Ginzburg V. L. e., Ptuskin V. S., 1990, Astrophysics of Cosmic Rays.. North Holland, Amsterdam

Binney J., Tremaine S., 1987, Galactic dynamics

Blitz L., 1993, in Levy E. H., Lunine J. I., eds, Protostars and Planets III. pp 125–161

Brandenburg A., Lazarian A., 2013, Space Sci. Rev., 178, 163

Brandenburg A., Subramanian K., 2005, Phys. Rep., 417, 1

Brandenburg A., Korpi M. J., Mee A. J., 2007, ApJ, 654, 945

Bregman J. N., 1980, ApJ, 236, 577

Brown J. C., Taylor A. R., 2001, ApJ, 563, L31

Bykov A. M., Toptygin I. N., 1987, ApSS, 138, 341

Cappellari M., et al., 2011, MNRAS, 416, 1680

Cesarsky C. J., 1980, ARA&A, 18, 289

Chandrasekhar S., 1931, MNRAS, 91, 456

Chiang W.-H., Prendergast K. H., 1985, ApJ, 297, 507

Cho J., Lazarian A., 2002a, Physical Review Letters, 88, 245001

Cho J., Lazarian A., 2002b, ApJ, 575, L63

Cho J., Lazarian A., 2003a, New A Rev., 47, 1143

Cho J., Lazarian A., 2003b, MNRAS, 345, 325

Cho J., Lazarian A., 2010, ApJ, 720, 1181

Cho J., Vishniac E. T., 2000, ApJ, 539, 273

Cioffi D. F., McKee C. F., Bertschinger E., 1988, ApJ, 334, 252

Clemens D. P., Sanders D. B., Scoville N. Z., 1988, ApJ, 327, 139

Cohen R. S., Spitzer L., Routly P. M., 1950, Phys. Rev., 80, 230

Cowie L. L., Songaila A., York D. G., 1979, ApJ, 230, 469

Cowie L. L., McKee C. F., Ostriker J. P., 1981, ApJ, 247, 908

Cox D. P., 2005, ARA&A, 43, 337

Cox D. P., Smith B. W., 1974, ApJ, 189, L105

Davidson P. A., 2004, Turbulence : an introduction for scientists and engineers. OUP Oxford

Dobbs C. L., Price D. J., 2008, MNRAS, 383, 497

Dobbs C. L., Pringle J. E., 2010, MNRAS, 409, 396

Dobbs C. L., Burkert A., Pringle J. E., 2011, MNRAS, 417, 1318

Draine B. T., 2011, Physics of the Interstellar and Intergalactic Medium

Dyson J. E., Williams D. A., 1997, The physics of the interstellar medium

Edelsbrunner H., 2014, A Short Course in Computational Geometry and Topology. Springer, Berlin

Elmegreen B. G., Scalo J., 2004, ARA&A, 42, 211

Evirgen C. C., Gent F. A., Shukurov A., Fletcher A., Bushby P., 2017, MNRAS, 464, L105

Eyink G. L., 1995, J. Statist. Phys., 78, 335

Eyink G. L., 2015, ApJ, 807, 137

Eyink G. L., 2018, preprint

Federrath C., Roman-Duval J., Klessen R. S., Schmidt W., Mac Low M.-M., 2010, A&A, 512, A81

Ferrière K., 1998, ApJ, 503, 700

Ferrière K. M., 2001, Reviews of Modern Physics, 73, 1031

Field G. B., Goldsmith D. W., Habing H. J., 1969, ApJ, 155, L149

Filippenko A. V., 1997, ARA&A, 35, 309

Fletcher C. A. J., 1991, Computational techniques for fluid dynamics, 2nd ed.. edn. Springer series in computational physics, Springer-Verlag, Berlin

Fletcher A., Beck R., Shukurov A., Berkhuijsen E. M., Horellou C., 2011, MNRAS, 412, 2396

Gaensler B. M., Haverkorn M., Staveley-Smith L., Dickey J. M., McClure-Griffiths N. M., Dickel J. R., Wolleben M., 2005, Science, 307, 1610

Gatto A., et al., 2017, MNRAS, 466, 1903

Gazol-Patiño A., Passot T., 1999, ApJ, 518, 748

Gent F. A., 2012, PhD thesis, Newcastle University School of Mathematics and Statistics (http://ethos.bl.uk/OrderDetails.do?uin=uk.bl.ethos.576746)

Gent F. A., Shukurov A., Sarson G. R., Fletcher A., Mantere M. J., 2013a, MNRAS, 430, L40

Gent F. A., Shukurov A., Fletcher A., Sarson G. R., Mantere M. J., 2013b, MNRAS, 432, 1396

Gent F. A., Mac Low M.-M., Käpylä M. J., Sarson G. R., Hollins J. F., 2018, preprint

Germano M., 1992, Journal of Fluid Mechanics, 238, 325

Girichidis P., et al., 2016a, MNRAS, 456, 3432

Girichidis P., et al., 2016b, ApJ, 816, L19

Girichidis P., Naab T., Hanasz M., Walch S., 2018a, MNRAS, 479, 3042

Girichidis P., Seifried D., Naab T., Peters T., Walch S., Wünsch R., Glover S. C. O., Klessen R. S., 2018b, MNRAS, 480, 3511

Goldreich P., Sridhar S., 1997, ApJ, 485, 680

Gressel O., Ziegler U., Elstner D., Rüdiger G., 2008a, Astronomische Nachrichten, 329, 619

Gressel O., Elstner D., Ziegler U., Rüdiger G., 2008b, A&A, 486, L35

Gressel O., Bendre A., Elstner D., 2013, MNRAS, 429, 967

Hanasz M., Wóltański D., Kowalik K., 2009, ApJ, 706, L155

Haverkorn M., Spangler S. R., 2013, Space Sci. Rev., 178, 483

Haverkorn M., Gaensler B. M., McClure-Griffiths N. M., Dickey J. M., Green A. J., 2004, ApJ, 609, 776

Haverkorn M., Gaensler B. M., Brown J. C., Bizunok N. S., McClure-Griffiths N. M., Dickey J. M., Green A. J., 2006, ApJ, 637, L33

Haverkorn M., Brown J., Gaensler B., McClure N., 2008, ApJ, 680, 362

Hawley J. F., Gammie C. F., Balbus S. A., 1995, ApJ, 440, 742

Heiles C., Troland T. H., 2003, ApJ, 586, 1067

Heitsch F., Mac Low M.-M., Klessen R. S., 2001, ApJ, 547, 280

Hill A. S., Joung M. R., Mac Low M. M., Benjamin R. A., Haffner L. M., Klingenberg C., Waagan K., 2012, ApJ, 750, 104

Hollins J. F., Sarson G. R., Shukurov A., Fletcher A., Gent F. A., 2017, ApJ, 850, 4

Hollins J. F., Sarson G. R., Shukurov A., Fletcher A., Gent F. A., 2018, preprint

Houde M., Fletcher A., Beck R., Hildebrand R. H., Vaillancourt J. E., Stil J. M., 2013, ApJ, 766, 49

Hubble E. P., 1926, ApJ, 64

Iacobelli M., et al., 2013, A&A, 558, A72

Jaffe T. R., Leahy J. P., Banday A. J., Leach S. M., Lowe S. R., Wilkinson A., 2010, MNRAS, 401, 1013

Jaffe T. R., Banday A. J., Leahy J. P., Leach S., Strong A. W., 2011, MNRAS, 416, 1152

Jaffe T. R., et al., 2013, MNRAS, 431, 683

Jansson R., Farrar G. R., 2012a, ApJ, 757, 14

Jansson R., Farrar G. R., 2012b, ApJ, 761, L11

Joung M. K. R., Mac Low M.-M., 2006, ApJ, 653, 1266

Joung M. R., Mac Low M.-M., Bryan G. L., 2009, ApJ, 704, 137

Joung M. R., Bryan G. L., Putman M. E., 2012, ApJ, 745, 148

Kalberla P. M. W., Kerp J., 2009, ARA&A, 47, 27

Kalberla P. M. W., Westphalen G., Mebold U., Hartmann D., Burton W. B., 1998, A&A, 332, L61

Kaplan S. A., 1966, Interstellar Gas Dynamics. Pergamon, Oxford

Käpylä M. J., Gent F. A., Väisälä M. S., Sarson G. R., 2017, preprint

Kennicutt Jr. R. C., 1998, ApJ, 498, 541

Kim C.-G., Ostriker E. C., 2017, ApJ, 846, 133

Kim C.-G., Ostriker E. C., 2018, ApJ, 853, 173

Klessen R. S., Heitsch F., Mac Low M.-M., 2000, ApJ, 535, 887

Korpi M. J., Brandenburg A., Shukurov A., Tuominen I., 1999a, A&A, 350, 230

Korpi M. J., Brandenburg A., Shukurov A., Tuominen I., Nordlund Å., 1999b, ApJ, 514, L99

Krause F., Rädler K.-H., 1980, Mean-Field Magnetohydrodynamics and Dynamo Theory. Pergamon Press, Oxford

Kuijken K., Gilmore G., 1989a, MNRAS, 239, 571

Kuijken K., Gilmore G., 1989b, MNRAS, 239, 605

Kulesza-Żydzik B., Kulpa-Dybeł K., Otmianowska-Mazur K., Kowal G., Soida M., 2009, A&A, 498, L21

Laing R. A., 1981, ApJ, 248, 87

Lazarian A., Pogosyan D., 2012, ApJ, 747, 5

Lazarian A., Pogosyan D., 2016, ApJ, 818, 178

Lazaryan A. L., Shutenkov V. P., 1990, Soviet Astronomy Letters, 16, 297

Lee H., Lazarian A., Cho J., 2016, ApJ, 831, 77

Lequeux J., 2005, The Interstellar Medium

Mac Low M.-M., Klessen R. S., 2004, Rev. Mod. Phys., 76, 125

Mac Low M.-M., Balsara D. S., Kim J., de Avillez M. A., 2005, ApJ, 626, 864

Makarenko I., Fletcher A., Shukurov A., 2015, MNRAS, 447, L55

Mallet A., Schekochihin A. A., Chandran B. D. G., Chen C. H. K., Horbury T. S., Wicks R. T., Greenan C. C., 2016, MNRAS, 459, 2130

McKee C. F., 1995, in Ferrara A., McKee C. F., Heiles C., Shapiro P. R., eds, Astronomical Society of the Pacific Conference Series Vol. 80, The Physics of the Interstellar Medium and Intergalactic Medium. p. 292

McKee C. F., Ostriker J. P., 1977, ApJ, 218, 148

Mee A. J. W., 2007, PhD thesis, Newcastle University School of Mathematics and Statistics

Meneveau C., 2012, Phys. Fluids, 24, 121301

Meyer J.-P., 1979, in Boury A., Grevesse N., Remy-Battiau L., eds, Liege International Astrophysical Colloquia Vol. 22, Liege International Astrophysical Colloquia. pp 153–187

Mihalas D., Binney J., 1981, Galactic astronomy: Structure and kinematics /2nd edition/

Minter A. H., Spangler S. R., 1996, ApJ, 458, 194

Moffatt H. K., 1967, in Yanglom A. M., Tatarsky V. I., eds, Atmospheric Turbulence and Radio Wave Propagation. Nauka, Moscow, pp 139–154

Moffatt H. K., 1978, Magnetic Field Generation in Electrically Conducting Fluids. Cambridge University Press, Cambridge

Monin A. S., Yaglom A. M., 2007a, Statistical Fluid Mechanics: Mechanics of Turbulence. Vol. 1. Dover, Mineola, N.Y.

Monin A. S., Yaglom A. M., 2007b, Statistical Fluid Mechanics: Mechanics of Turbulence. Vol. 2. Dover, Mineola, N.Y.

Norman C. A., Ikeuchi S., 1989, ApJ, 345, 372

Ohno H., Shibata S., 1993, MNRAS, 262, 953

Oughton S., Matthaeus W. H., Wan M., Parashar T., 2016, Journal of Geophysical Research (Space Physics), 121, 5041

Pakmor R., Pfrommer C., Simpson C. M., Springel V., 2016, ApJ, 824, L30

Panchev S., 1971, Random Functions and Turbulence. Pergamon, Oxford

Pardi A., et al., 2017, MNRAS, 465, 4611

Parker E. N., 1966, ApJ, 145, 811

Parker E. N., 1967, ApJ, 149, 517

Parker E. N., 1969, Space Sci. Rev., 9, 651

Passot T., Vazquez-Semadeni E., Pouquet A., 1995, ApJ, 455, 536

Pfrommer C., Pakmor R., Schaal K., Simpson C. M., Springel V., 2017, in 6th International Symposium on High Energy Gamma-Ray Astronomy. p. 030003

Reyes R., Mandelbaum R., Gunn J. E., Pizagno J., Lackner C. N., 2011, MNRAS, 417, 2347

Rieder M., Teyssier R., 2016, MNRAS, 457, 1722

Rodrigues L. F. S., Sarson G. R., Shukurov A., Bushby P. J., Fletcher A., 2016, ApJ, 816, 2

Rosen A., Bregman J. N., 1995, ApJ, 440, 634

Rosen A., Bregman J. N., Norman M. L., 1993, ApJ, 413, 137

Rosen A., Bregman J. N., Kelson D. D., 1996, ApJ, 470, 839

Sánchez-Salcedo F. J., Vázquez-Semadeni E., Gazol A., 2002, ApJ, 577, 768

Sarazin C. L., White III R. E., 1987, ApJ, 320, 32

Scalo J., Elmegreen B. G., 2004, ARA&A, 42, 275

Schaller M., et al., 2015, MNRAS, 451, 1247

Sedov L. I., 1959, Similarity and Dimensional Methods in Mechanics

Sellwood J. A., Balbus S. A., 1999, ApJ, 511, 660

Shapiro P. R., Field G. B., 1976, ApJ, 205, 762

Shneider C., Haverkorn M., Fletcher A., Shukurov A., 2014, A&A, 568, A83

Shukurov A., Rodrigues L. F. S., Bushby P. J., Hollins J., Rachen J. P., 2018, preprint

Simard C., Charbonneau P., Dubé C., 2016, Adv. Space Res., 58, 1522

Simpson C. M., Pakmor R., Marinacci F., Pfrommer C., Springel V., Glover S. C. O., Clark P. C., Smith R. J., 2016, ApJ, 827, L29

Slyz A. D., Kranz T., Rix H.-W., 2003, MNRAS, 346, 1162

Slyz A. D., Devriendt J. E. G., Bryan G., Silk J., 2005, MNRAS, 356, 737

Sokoloff D., Shukurov A., Ruzmaikin A., 1983, Geophys. Astrophys. Fluid Dyn., 25, 293

Sokoloff D. D., Bykov A. A., Shukurov A., Berkhuijsen E. M., Beck R., Poezd A. D., 1998, MNRAS, 299, 189

Sokoloff D. D., Bykov A. A., Shukurov A., Berkhuijsen E. M., Beck R., Poezd A. D., 1999, MNRAS, 303, 207

Solomon P. M., Rivolo A. R., Barrett J., Yahil A., 1987, ApJ, 319, 730

Spitzer Jr. L., 1990, ARA&A, 28, 71

Spitzer L., Härm R., 1953, Phys. Rev., 89, 977

Stepanov R., Shukurov A., Fletcher A., Beck R., La Porta L., Tabatabaei F., 2014, MNRAS, 437, 2201

Tammann G. A., Loeffler W., Schroeder A., 1994, ApJS, 92, 487

Taylor G., 1950, Proceedings of the Royal Society of London Series A, 201, 159

Tennekes H., Lumley J. L., 1972, First Course in Turbulence. MIT Press

Terry P. W., 2000, Reviews of Modern Physics, 72, 109

Tomisaka K., 1998, MNRAS, 298, 797

Vázquez-Semadeni E., 2015, in Lazarian A., de Gouveia Dal Pino E. M., Melioli C., eds, Astrophysics and Space Science Library Vol. 407, Magnetic Fields in Diffuse Media. p. 401

Vázquez-Semadeni E., Passot T., Pouquet A., 1995, ApJ, 441, 702

Wada K., Norman C. A., 1999, ApJ, 516, L13

Wada K., Norman C. A., 2001, ApJ, 547, 172

Wada K., Norman C. A., 2007, ApJ, 660, 276

Wada K., Meurer G., Norman C. A., 2002, ApJ, 577, 197

Walch S., et al., 2015, MNRAS, 454, 238

Wang K., Testi L., Burkert A., Walmsley C. M., Beuther H., Henning T., 2016, ApJS, 226, 9

Weiler K. W., Sramek R. A., 1988, ARA&A, 26, 295

Whelan J., Iben Jr. I., 1973, ApJ, 186, 1007

Wilkin S. L., Barenghi C. F., Shukurov A., 2007, Physical Review Letters, 99, 134501

Williams J. P., Blitz L., McKee C. F., 2000, Protostars and Planets IV, p. 97

Wisdom J., Tremaine S., 1988, AJ, 95, 925

Wolfire M. G., Hollenbach D., McKee C. F., Tielens A. G. G. M., Bakes E. L. O., 1995, ApJ, 443, 152

Zeldovich Y. B., Ruzmaikin A. A., Sokoloff D. D., 1983, Magnetic Fields in Astrophysics. Gordon and Breach

Zschaechner L. K., Rand R. J., Walterbos R., 2015, ApJ, 799, 61

de Avillez M. A., 2000, MNRAS, 315, 479

de Avillez M. A., Berry D. L., 2001, MNRAS, 328, 708

de Avillez M. A., Breitschwerdt D., 2004, A&A, 425, 899

de Avillez M. A., Breitschwerdt D., 2005a, A&A, 436, 585

de Avillez M. A., Breitschwerdt D., 2005b, ApJ, 634, L65

de Avillez M. A., Breitschwerdt D., 2007, ApJ, 665, L35

de Avillez M. A., Breitschwerdt D., 2012a, ApJ, 756, L3

de Avillez M. A., Breitschwerdt D., 2012b, ApJ, 761, L19

de Avillez M. A., Mac Low M.-M., 2001, ApJ, 551, L57

de Avillez M. A., Mac Low M.-M., 2002, ApJ, 581, 1047

van den Bergh S., 1976, ApJ, 206, 883